UiO **: University of Oslo**

Robert Wissing

Simulating Galactic Dynamo Processes with Smoothed Particle Magnetohydrodynamics

Thesis submitted for the degree of Philosophiae Doctor

Institute of Theoretical Astrophysics
Faculty of Mathematics and Natural Sciences

2022

Smoothed Particle Hydrodynamics or:
How I Learned to Stop Worrying and Love the Lagrangian.
Daniel Price

Preface

This thesis is submitted in partial fulfillment of the requirements for the degree of *Philosophiae Doctor* at the University of Oslo. The research presented here was conducted at the Institute of Theoretical Astrophysics (ITA), at the University of Oslo, under the supervision of associate professor Sijing Shen and professor David F. Mota.

The aim of this thesis was to develop a numerical scheme for galaxy simulations that can properly model magnetic fields, which remain one of the most often neglected parts. This likely stems from the complexity and technical difficulties associated with them. The numerical framework of smoothed-particle hydrodynamics(SPH) is particularly ideal in simulations of galaxy formation due to its inherent conservative and adaptive properties. This thesis is a collection of three papers, that go through the development of the SPMHD method and its application to the magnetized core-collapse, magneto-rotational instability and galaxy formation. The introductory chapters will serve to provide both a motive and a comprehensive background to the numerical method and physics involved in the three papers.

In Chapter 1, I will provide the purpose and a general introduction to the areas covering my work.

In Chapter 2, I will go through the details of the SPH method, presenting it in a more generalized manner to understand the assumptions and advantages/disadvantages of the method and to more clearly introduce the possible avenues of improvements that exist.

In Chapter 3, I will go through the details of the magneto-hydrodynamic implementation within SPH. Discussing the challenges of numerical magneto-hydrodynamics and the different ways that we can overcome these.

In Chapter 4, I will present an introduction to numerical simulations of galaxies, which include the different kind of physics needed to model galaxies and how these are implemented in modern numerical codes. The topic of magnetic fields in galaxies are covered in detail in paper 3 in this thesis and thus omitted from this introduction section.

In Chapter 5, I will summarise the main research results and discuss the future work to be done in the field of numerical methods, dynamo theory and galaxy formation.

Acknowledgements

I would first like to thank my supervisor Sijing Shen that have provided invaluable guidance and support during my PhD. Allowing me to pursue the research avenues that I was interested in, while keeping me focused on the work that needed be done. I am sure that we will keep having fruitful discussions and collaborations in the future as-well.

I would also like to thank the Institute of Theoretical Astrophysics and the friendly people that work there for making my stay in Norway truly a wonderful experience.

Finally I would like to thank all my family and friends for their everlasting support.

Robert Wissing
Oslo, August 2022

List of Papers

Paper I

Wissing, R. and Shen, S. "Smoothed particle magnetohydrodynamics with the geometric density average force expression". In: *Astronomy & Astrophysics*. Vol. 638, no. A140 (2020), pp. 18 pp. DOI: 10.1051/0004-6361/201936739.

Paper II

Wissing, R. and Shen, S. and Wadsley, J. and Quinn, T. "Magnetorotational instability with smoothed particle hydrodynamics". In: *Astronomy & Astrophysics*. Vol. 659, no. A91 (2022), pp. 21 pp. DOI: 10.1051/0004-6361/202141206.

Paper III

Wissing, R. and Shen, S. "Numerical dependencies of the galactic dynamo in isolated galaxies with SPH". *To be submitted* .

Contents

Contents

List of Figures

Chapter 1

Introduction

Figure 1.1: All-sky view of the magnetic field and total intensity of synchrotron emission measured by the Planck satellite, displaying the structure and strength of the magnetic field within the Milky Way. Here the colors from blue to orange represent the total intensity. The orientation of the projected magnetic field is indicated by the "drapery" feature shown in the figure. This figure is from the (Planck Collaboration et al., 2016).

Magnetic fields are a ubiquitous part of our universe and play an important role in a wide array of different astrophysical systems. They govern the many interesting phenomena of our Sun and determine the dynamic behavior of its birth and death in the star formation process. Magnetic fields are also critical in the launching of astrophysical jets, the transport of angular momentum in disks, and the merging process of compact stars, to just name a few. In recent years magnetic fields have also become a big subject of interest in regard to galaxy formation. Observation has shown that many galaxies exhibit strong magnetic fields, with strengths from around several μG for the Milky Way and nearby galaxies (Opher et al., 2009; Fletcher, 2010; Burlaga et al., 2013; Beck, 2015) up to several mG in starburst galaxies (Chyży and Beck, 2004; Heesen et al., 2011; Adebahr et al., 2013; Robishaw et al., 2008). The magnetic energy in these galaxies are found to be close to equipartition with the thermal and turbulent energies (Boulares and Cox, 1990; Beck et al., 1996; Taylor et al., 2009), meaning that they are strong enough to dynamically affect the galaxy. Furthermore, it has been observed that the morphology of the magnetic field

within disk galaxies exhibits a large-scale spiral structure (Beck and Wielebinski, 2013). In disk galaxies with a strong density wave structure, the magnetic field tightly coincides with the optical spiral arms, as in M51 and M83 with a strength of around $20 - 30\mu G$ (Fletcher et al., 2011; Frick et al., 2016).For galaxies with weaker density structure, the magnetic field can instead form large-scale magnetic arms not coinciding with the optical spiral arms, like in NGC6946 (Beck, 2007).

The strong magnetic fields observed can contribute a significant non-thermal pressure component to the galaxy, which can suppress star-formation rates and heavily affect the structure of the interstellar medium (Pakmor and Springel, 2013; Birnboim et al., 2015). Within the ISM the magnetic field also plays an important role in the dynamics of molecular clouds, where strong fields can lead to more massive but fewer cloud cores (Vázquez-Semadeni et al., 2005; Price and Bate, 2008). Another interesting aspect of magnetic fields within galaxies is that they can suppress the development of fluid instabilities (Jun et al., 1995; McCourt et al., 2015). This can allow for cold gas to survive longer within the predominately hot galactic outflows, which could provide a possible explanation for the observational significant component of cold molecular gas seen in galactic outflows (Chen et al., 2010; Cicone et al., 2014; Leroy et al., 2015; Martini et al., 2018). The strength and structure of magnetic fields in galaxies also determine the transport of cosmic rays (CRs), which together with magnetic fields can efficiently drive galactic outflows (Uhlig et al., 2012; Booth et al., 2013; Pakmor et al., 2016a; Butsky and Quinn, 2018).

Due to astronomy being an observational science, an important approach to testing astrophysical theories is through the use of numerical simulations. This gives us a 'virtual' lab to understand how the system will react to a range set of conditions and assumptions. It also allows us to predict the future evolution of physical systems. Due to the limitation of computation, we cannot model the motion of individual atoms. Instead, we require approximations and discretization of the physical system to be able to model the system within the limitations of computation. Within the macroscopic theory of fluids, a fluid can be described as a continuum medium with macroscopic properties that vary with position. Then whether you want to simulate gas, liquids, solids, dark matter, or et cetera, a system of equations is required that describes how these macroscopic properties will change in time. For an adiabatic inviscid fluid, the hydrodynamic system can simply be described by the famous Euler equations. This system of equations will involve both spatial and temporal derivatives that need to be solved, to do this we need to discretize the system in question. Maybe the most natural way to spatially discretize the fluid is by simply dividing up the system volume into a regular spatial grid, where each grid cell (resolution element) contains a volume average value of the macroscopic property. Then the derivatives can be computed using developed finite difference/volume schemes. However, in astrophysical fluids, we are often working on density scales that vary over many orders of magnitude and require us to resolve physical processes

over a wide range of spatial scales. This makes adaptivity of the resolution a crucial component for any numerical scheme trying to model galaxies. The adaptive mesh refinement (AMR) can be seen as an extension of the regular spatial grid method, which adds additional levels of refinement to the grid where it is desired (Berger and Oliger, 1984; Klein, 1999; Teyssier, 2002). Another option to the fixed/Eulerian grid method is to instead use a Lagrangian grid method, where the grid deforms according to the fluid flow (Pen, 1998; Springel, 2010). We can also instead of discretizing the fluid with respect to volume, discretize the fluid with respect to mass. This results in a method where the fluid properties are carried by a set of moving interpolation points (referred to as particles) that follow the underlying fluid motion. Derivatives are given by interpolation schemes over the neighbouring particles (particle method) (Gingold and Monaghan, 1977; Lucy, 1977) or via interpolation from an overlaid grid (particle-in-cell method) (Dawson, 1983).

Chapter 2

Smoothed particle hydrodynamics
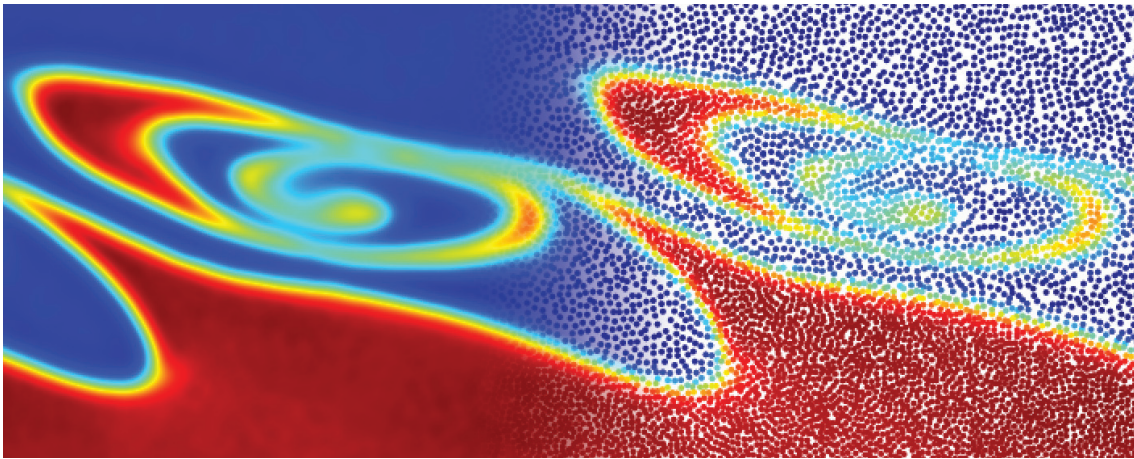
Figure 2.1: A visual representation of how a continuous fluid is modeled with smoothed particle hydrodynamics, where the fluid is completely described by a finite amount of interpolation points/particles. The figure shows the development of the Kelvin-Helmholtz instability.

Any numerical method brings forth both advantages and disadvantages depending on the system that you want to study. It is crucial that this is taken into account when one is evaluating the quality of numerical methods. Smoothed-particle hydrodynamics (SPH) is perhaps one of the most simple and elegant numerical methods that one can derive. Given solely a density estimate for an arbitrary distribution of mass particles representing the fluid, the equations of hydrodynamics can be constructed from the least-action principle (Price and Monaghan, 2004b). The Lagrangian properties present in the derivation ensure that the equations of motion obey the symmetries and conservation properties of the system (energy, momentum, and entropy). The Lagrangian nature means that the method is fully Galilean invariant. The mass particles represent the resolution elements of the method, this makes the resolution adaptive by nature and concentrates the resolution in high-density regions while spending less computational effort in empty regions of the simulation. No global boundary needs to be set up in systems involving free boundaries and SPH couple naturally to gravitational N-body codes. All of these strengths make the method ideal for many astrophysical systems. However, as with any numerical method, there are also weaknesses. In some systems, the resolution adaptivity with density is undesirable if the point of interest occurs in the lower density regions of the system, for example in the low-density mass transfer of two close binaries (Church et al., 2009). There are also some challenges in handling discontinuities

in SPH, which is something that every numerical scheme needs to consider. In finite-volume grid schemes, we have discontinuities in fluid variables between neighboring cells, which are handled by limiting the flux across the boundaries. In SPH there is an assumption that fluid variables vary smoothly along with any pair of particles, meaning that the variables are assumed to be differentiable. This means that there is a loss of information whenever the fluid properties become discontinuous, reducing the accuracy of the method. To remain accurate fluid properties need to be smoothed out on the scale of the resolution length to adhere to this condition. This is done most often through dissipation terms in SPH. The key issue in using dissipation terms to handle discontinuities is that it can be hard to avoid excessive dissipation of gradients that are not purely discontinuous. Due to the lack of consistent surfaces, SPH is limited in its application of many flux-conserving methods developed for grid codes (Evans and Hawley, 1988; Gardiner and Stone, 2005). Finally, the accuracy of the SPH method is highly tied to how the particles are distributed within the interpolation region of each particle. If the distribution is very asymmetric the accuracy of the method will be reduced. Many of these disadvantages have been tackled in recent years leading to more and more robust methods for SPH (Wadsley et al., 2017; Price et al., 2018).

One of the main topics of this thesis regards the development of a new SPMHD method that tries to improve on the traditional SPH method. It thus becomes interesting to explore what the consequences are when we modify the traditional SPH method. In this chapter, I will attempt to introduce the equations of SPH in a more generalized matter. This is to highlight the assumptions and advantages/disadvantages of the method and to more clearly introduce the possible avenues of improvements that exist. The chapter is outlined as follows: In Section 2.1 we present the equations that lay the foundation of the SPH method; Section 2.2 we discuss the function of the smoothing kernel in SPH; Section 2.2 we derive the SPH equations from the Euler equations and show the conservative properties of the method; Section 2.4 we discuss thermodynamic consistency in SPH; Section 2.5 second-order gradients in SPH; Section 2.6 derivation of the generalized SPH equation from the variational principal; Section 2.7 we present the shock/discontinuity capture methods used in SPH; Section 2.8 we present the timestepping algorithm used in the Gasoline2 code used for all our simulations; And finally Section 2.9 we discuss the differences and similarities to the moving mesh and SPH-ALE methods.

2.1 Foundation of SPH

Within the macroscopic theory of fluids we can describe a fluid as a continuous field with variable values at set coordinates.

$$A(r) = \int_V A(r')\delta(r - r')dV'. \tag{2.1}$$

We want to discretize our continuous fluid into a finite number of interpolation points. In SPH we discretize the fluid into mass elements called particles, with a given volume/weight ($dV = V_b$). In addition, we want to be able to interpolate the field values in between these particles, giving information about the field at all points. In order to do so we can approximate the delta function in the above integral with an interpolation/smoothing kernel with the following properties:

$$\lim_{h \to 0} W(r, h) = \delta(r), \tag{2.2}$$

$$\int_V W(r, h) dr = 1. \tag{2.3}$$

Here h is the smoothing length, which describes the characteristic length of the interpolation. These are the essential properties required by the smoothing kernel for approximating the delta function in Eq.2.1. However, when interpolating physical fields (such as density) three additional properties are desirable. The first is that the smoothing kernel is differentiable and the other two are positivity and symmetry:

$$W(r, h) \geq 0, \tag{2.4}$$

$$W(r, h) = W(-r, h). \tag{2.5}$$

We can then approximate the integral (Eq.2.1) and expand A(r') about r to give us (Benz, 1990; Monaghan, 1992):

$$A(r) = \int_V A(r')W(r - r', h)dV' = A(r) \int_V W(r - r', h)dV'.$$

$$+ \nabla^\alpha \nabla^\beta A(r) \int_V \delta r^\alpha \delta r^\beta W(r - r', h) dV' + O(h^4). \tag{2.6}$$

The odd error terms vanish due to the symmetry of the kernel. The second-order error of the interpolant could potentially be removed as well by reconstructing the kernel (Monaghan, 1985). However, these kernels do not ensure the positivity constraint (Eq.2.4) and could lead to negative densities. These errors are often of less concern compared to the errors that arise from the discretization as we will see. Discretizing the above equation ($dV = V_b$) gives:

$$A(r) \approx \sum_b V_b A(r_b) W(r - r_b, h). \tag{2.7}$$

This interpolant forms the foundation of all SPH formalisms. The errors of the discretized interpolant can be shown by expanding A_b in the above equation in a Taylor series around r:

$$A_a \approx \sum_b V_b A_b W_{ab} = A_a \sum_b V_b W_{ab} + \nabla_\alpha A_a \cdot \sum_b V_b (r_b - r_a)^\alpha W_{ab}$$

$$+ \frac{1}{2} \nabla^2_{\beta\gamma} A_a \cdot \sum_b V_b (r_b - r_a)^\beta (r_b - r_a)^\gamma W_{ab} + O(h^3). \tag{2.8}$$

As we can see from the errors, the accuracy of the interpolate will depend heavily on the given particle distribution, the chosen volume element, and the smoothing kernel. The leading order error $E_0 = \sum_b V_b W_{ab} \approx 1$ describes the accuracy of the volume partitioning, or in other words how well the normalization of the discrete sum captures the normalization of the continuous integral ($\int_V W dV' = 1$). A potential fix to this error is to simply normalize the smoothing kernel ($W_{ab,new} = \frac{W_{ab}}{\sum_b V_b W_{ab}}$), however, there are potential downsides to using this sort of normalization when it comes to the hydrodynamic equations which we will discuss further in Section 2.3.

A simple gradient estimate in SPH can be found by taking the spatial derivative of our expression Eq.2.7:

$$\nabla A(r) = \int_V \nabla A(r') W(r - r', h) dV'. \tag{2.9}$$

If we assume that the kernel is differentiable we can rewrite this equation using integration by parts:

$$\nabla A(r) = \int_V \nabla A(r') W(r - r', h) dV'$$

$$= \int_V \nabla \left[A(r') W(r - r', h) \right] dV' - \int_V A(r') \nabla W(r - r', h) dV'$$

$$= \int_S \left[A(r') W(r - r', h) \right] \cdot dS' + \int_V A(r') \nabla W(r - r', h) dV'. \tag{2.10}$$

The surface term that appears in the above term will in general vanish where the field A is differentiable. Assuming that A is differentiable we can write the gradient as:

$$\nabla A(r) \approx \sum_b V_b A(r_b) \nabla W(r - r_b, h). \tag{2.11}$$

The errors for the discretized gradient estimate will then be:

$$\nabla_a A_a \approx \sum_b V_b A_b \nabla_a W_{ab} = A_a \sum_b V_b \nabla_a W_{ab} + \nabla_\alpha A_a \cdot \sum_b V_b (r_b - r_a)^\alpha \nabla_a W_{ab}$$

$$+ \frac{1}{2} \nabla^2_{\beta\gamma} A_a \cdot \sum_b V_b (r_b - r_a)^\beta (r_b - r_a)^\gamma \nabla_a W_{ab} + O(h^3). \tag{2.12}$$

We can see that we have similar errors as for the regular interpolant function. We will talk more about how we can construct new gradient operators for our equations in Section 2.3.

From this point on differences between SPH methods will usually arise depending on the desired qualities. We will begin by looking at the choice of the smoothing kernel and smoothing length.

2.2 Smoothing Kernel
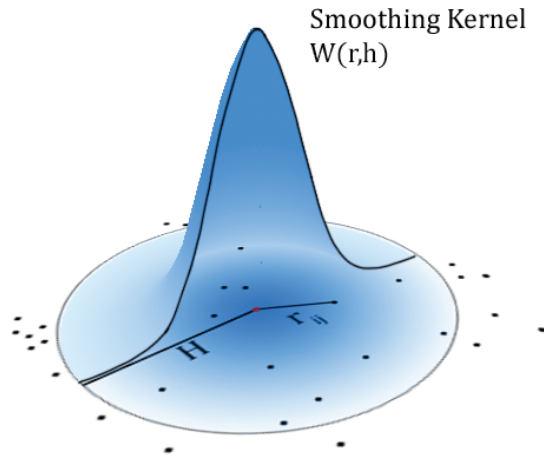
Figure 2.2: Illustration of the C4 Wendland kernel in 2D. The 3D projection shows how the smoothing kernel weight declines with radius. H represents the compact support length of the kernel and is usually taken to be some multiple of the smoothing length ($H = nh$). r_{ij} is the distance between the particle in the centre (i) and its neighbor (j).

As we saw in the above section the smoothing kernel is one of the key factors determining the accuracy of the SPH method. Apart from the conditions stated in the previous section, the smoothing kernel is often assumed to be a spherically symmetric function:

$$W(x, h) = W(y, h) = W(z, h) \tag{2.13}$$

While spherical symmetry is not a requirement it is often desirable as asymmetric kernel functions are prone to suffer inconsistencies and angular momentum issues. We can write a symmetric kernel in the form of:

$$W(r, h) = \frac{\sigma}{h^v} f(q) \tag{2.14}$$

Here σ is the normalization factor following Eq.2.3 and v is the spatial dimension and $q = r/h$. The Gaussian fits this description along with the other conditions. However, as the interpolation spans the entire volume, it is an unpractical kernel function for numerical simulations (cost goes as $O(N^2)$). As contributions from neighboring particles fall off quickly on the scale of the smoothing length, it is suitable to introduce truncated kernels, which go to zero at a finite radius (the compact radius H).

$$W(r, h) = 0 \quad |r| > H = nh \tag{2.15}$$

This H is often taken to be some multiple of the smoothing length h. This reduces the cost of our SPH calculation $O(N_{neigh}N)$, where N_{neigh} is the number of neighbors within the compact radius. The standard truncated kernels used for SPH have for a very long time been within the B-spline family (Schoenberg, 1946),

with the cubic kernel often being represented as the standard SPH kernel (since Monaghan and Lattanzio (1985)). The kernel bias/errors at a given neighbor number are strongly linked to the Fourier transform of the kernel. Because the Fourier transform of B-spline kernels falls rapidly with wave number they quickly become suitable for interpolation at low neighbor numbers. At higher wavenumbers, the Fourier transform of the B-spline kernel oscillates around zero with an amplitude that becomes smaller and smaller. Negative modes within the Fourier transform have however been shown to be quite problematic when increasing the number of neighbors above a certain critical value (Dehnen and Aly, 2012). Above this critical value, the so-called pairing instability can occur, in which particles start to merge, consequentially degrading the resolution of the simulation (Thomas and Couchman, 1992; Morris, 1996; Børve et al., 2004; Price, 2012; Dehnen and Aly, 2012). This will depend on the kernel, but for the cubic kernel it lies in the region of $N_{neigh} = 50$. Depending on the wavenumber of these negative modes and the size of their region will determine the sensitivity to the pairing instability. A family of kernel functions that ensure a positive Fourier transform is the Wendland kernels (Wendland, 1995). The family of Wendland kernel functions for 3D is defined as:

$$W(r) = C\phi_{k+2,k}(r) \quad \phi_{l,k} = I_k(1-r)^l_+ \tag{2.16}$$

with $(.)_+ = max(0,.)$ and linear operator

$$I[f](r) = \int_r^\infty sf(s)ds \tag{2.17}$$

The resulting kernel turn out to have a polynomial representation within $r = 0, 1$ while going to zero outside of this region. The second order Wendland kernel $\phi_{4,2}$ (known as the Wendland C4 kernel) can be written as:

$$W_{ab} = \frac{\sigma}{h^3} \begin{cases} (1-q)^6(1+6(1-q)+\frac{35}{3}(1-q)^2) & \text{for } 0 < q < 2, \\ 0 & \text{for } q > 2 \end{cases} \tag{2.18}$$

$$q = r/h$$

Its gradient then becomes:

$$\nabla W_{ab} = \frac{\sigma}{h^4}\hat{\mathbf{r}} \begin{cases} (1-q)^5(1+5(1-q)) & \text{for } 0 < q < 2, \\ 0 & \text{for } q > 2 \end{cases} \tag{2.19}$$

Higher-order kernels have smoother derivatives, which in combination with higher neighbor numbers act to decrease the sensitivity to particle disorder. The trade-off of using a higher-order kernel is often that it becomes less accurate than its lower-order counterpart at low neighbor numbers(Monaghan, 1992; Rosswog, 2015). The Wendland kernel produces a general over-bias in its estimation, which become more prominent at low neighbor numbers, as the bias is due to

self contribution (at $N_{neigh} = 200$ this is negligible). To improve the estimate we correct for the self contribution(Dehnen and Aly, 2012)[1]:

$$W_{ab} = W_{ab} - \epsilon W(0, h_a) \tag{2.20}$$

$$\epsilon = 0.01342(\frac{N_{neigh}}{100})^{1.579}$$

Which gives a very nice estimate over a wide range of N_{neigh} values. This is the default smoothing kernel of the Gasoline2 code (Wadsley et al., 2017) and the one we have used in all papers included within this thesis.

Another interesting family of kernels is the sinc kernels (Cabezón et al., 2008). These are susceptible to the pairing instability but can be avoided by choosing a high enough kernel index for the chosen number of neighbors. What makes these kernels interesting is the property of kernel separability, defined as:

$$W_3(r, h) = W_1(x, h)W_1(y, h)W_1(z, h)$$

Separability of the kernel guarantees consistency in a simulation involving planar symmetry, giving identical results regardless of running the simulation in 3D, 2D, or 1D (given that the resolution is the same). This is a property that the Gaussian kernel holds, but which is not withheld by truncated kernel functions. The sinc kernel can however be shown to approach separability as $n \to \infty$ (Cabezón et al., 2017). And is much closer to fulfilling this property than other kernel families such as the Wendland kernels, where increasing the order does not help in improving this property. The consequences of this property are something that has not been readily researched by the SPH community and is something that would be worth exploring more about in the future [2].

2.3 Hydrodynamic equations

The Euler equations represent the conservation laws for mass, momentum and energy for hydrodynamics and forms a system of partial hyperbolic differential equations. In compact form this is often written as:

$$\frac{\partial \mathbf{U}}{\partial t} - \nabla \cdot (\mathbf{F} - \mathbf{v_f} \otimes \mathbf{U}) = 0 \tag{2.21}$$

Here $\mathbf{U}$ represents the conserved variables $\mathbf{U} = [\rho, \rho\mathbf{v}, \rho u + \rho\mathbf{v}^2/2]$, F represent the flux of these variables $\mathbf{F} = [\rho\mathbf{v}, \rho\mathbf{v} \otimes \mathbf{v} + P, (P + \rho u + \rho\mathbf{v}^2/2)\mathbf{v}]$ in a frame of

---

[1] ϵ will depend on the kernel and N_{neigh}, we have taken the simple power-law given by Dehnen and Aly (2012) for the Wendland C4 kernel

[2] This is a nice property to introduce asymmetry within the kernel to improve linear errors. $W_3(r, h) = W_1(x, h_x)W_1(y, h_y)W_1(z, h_z)$ replacing the smoothing length with a vector. Previous implementations of asymmetric kernels simply modify: $q = r/h = \sqrt{x^2/h_x^2 + y^2/h_y^2 + z^2/h_z^2}$ which can be seen as the semimajor axes of the smoothing ellipsoid centered on position r (Shapiro et al., 1996).

reference moving with the velocity $\mathbf{v_f}$. The integral of $\mathbf{U}$ over the volume gives us the conserved quantities of mass, momentum, and energy. As SPH represents a fully Lagrangian method, the velocity of the frame of reference is equal to the fluid velocity ($\mathbf{v_f} = \mathbf{v}$). This allows us to express the Euler equation in a Lagrangian form, evolving the primitive variables($\rho, \mathbf{v}, u$):

$$\frac{d\rho}{dt} = -\rho \nabla \cdot \mathbf{v} \tag{2.22}$$

$$\frac{d\mathbf{v}}{dt} = -\frac{\nabla P}{\rho} \tag{2.23}$$

$$\frac{du}{dt} = -\frac{P}{\rho} \nabla \cdot \mathbf{v} \tag{2.24}$$

From here on out we need to construct a time-stepping algorithm to integrate the equation in time (Section 2.8) and a way to discretize the spatial gradients within SPH. We already saw a simple way to construct gradients for SPH in Section 2.1:

$$\frac{d\mathbf{v}_a}{dt} = -\frac{1}{\rho_a} \sum_b V_b P_b \nabla W(r_a - r_b, h) \tag{2.25}$$

However, it is simple to see that this sort of discretization can lead to non-conservation in momentum. The force between a particle-pair should be symmetric to conform to Newtons third law:

$$m_a \frac{d\mathbf{v}_a}{dt} + m_c \frac{d\mathbf{v}_c}{dt} = V_a V_c \left(P_c \nabla W(r_a - r_c, h_a) - P_a \nabla W(r_a - r_c, h_c) \right) = 0 \tag{2.26}$$

Taking into account the errors of the gradient estimate in Eq.2.12 it is easy to see that this condition is never ensured (even in the case of constant pressure!). This can quickly lead to severe momentum errors when the particle distribution becomes disordered. To ensure that this condition is fulfilled we require a symmetric gradient estimate. Luckily, in numerical methods we do have a certain degree of freedom when determining the gradients, as long as they converge towards the same in the continuity limit. As a simple example we can take the gradient estimate:

$$\nabla A = \nabla A - A\nabla 1 \tag{2.27}$$

If we then apply the standard SPH gradient to this equation we obtain a new gradient estimate:

$$\nabla A \approx \sum_b \frac{m_b}{\rho_b} \left(A_b - A_a \right) \nabla_a W_{ab}, \tag{2.28}$$

This new gradient estimate simply removes the zeroth order error from the gradient estimate (see Eq.2.12). As we can imagine there are an infinite number of ways to construct new gradient operators following this construction. However, if we want our equations to follow the physical conservation laws certain rules must apply. To ensure the conservation of momentum we require a symmetric gradient

operator for the momentum equation, the standard type can be constructed following (Price et al., 2012):

$$\frac{\nabla A}{\rho} = \frac{\phi}{\rho}\left[\frac{A}{\phi^2}\nabla\phi + \nabla\left(\frac{A}{\phi}\right)\right] \approx \sum_b \frac{m_b}{\rho_a\rho_b}\left(A_a\frac{\phi_b}{\phi_a} + A_b\frac{\phi_a}{\phi_b}\right)\nabla_a W_{ab}, \quad (2.29)$$

Here ϕ can be any arbitrary, differentiable scalar quantity. This equation is, however, not yet fully symmetric in the case of variable smoothing lengths for individual particles. To fully symmetrize the equation, there are several options available to us. Two straightforward ways to resolve this is to either use an average smoothing length between the two interacting particle $\overline{h_{ab}} = (h_a + h_b)/2$ or use an averaged kernel ($\overline{W_{ab}} = (W_a + W_b)/2$). Another option is to use h_a for the first gradient term ($A_a\frac{\phi_b}{\phi_a}\nabla_a W_{ab}(h_a)$) and h_b for the second gradient term ($A_b\frac{\phi_a}{\phi_b}\nabla_a W_{ab}(h_b)$) in Eq.2.29. This final way is how the SPH equations arise naturally from the Euler-Lagrange equations, which we will touch on briefly in Section 2.6. But in Gasoline2 we use the symmetric kernel gradient estimate:

$$\frac{\nabla A}{\rho} = \sum_b \frac{m_b}{\rho_a\rho_b}\left(A_a\frac{\phi_b}{\phi_a} + A_b\frac{\phi_a}{\phi_b}\right)\overline{\nabla_a W_{ab}}, \quad (2.30)$$

Applying this to Eq.2.26 we can easily see that this fulfills the condition. As the force is symmetric and always along the particle-pair the angular momentum can be shown to be conserved aswell(Price, 2004):

$$\frac{d}{dt}\sum_a r_a \times m_a v_a = \sum_a m_a\left(r_a \times \frac{dv_a}{dt}\right)$$

$$= \sum_a\sum_b \frac{m_a m_b}{\rho_a\rho_b}\left(P_a\frac{\phi_b}{\phi_a} + P_b\frac{\phi_a}{\phi_b}\right)r_a \times (r_a - r_b)F_{ab}$$

$$= -\sum_a\sum_b \frac{m_a m_b}{\rho_a\rho_b}\left(P_a\frac{\phi_b}{\phi_a} + P_b\frac{\phi_a}{\phi_b}\right)r_a \times r_b F_{ab} = 0 \quad (2.31)$$

Here $F_{ab}\hat{r}_{ab} = \nabla W_{ab}$. The final expression here becomes zero because the double summation is antisymmetric in a and b.

To ensure the conservation of energy the gradient operator chosen for the momentum equation must form a conjugate pair with the operator chosen for the energy equation (Cummins and Rudman, 1999). The conjugate operator(anti-symmetric operator) of this is given by(Price et al., 2012):

$$\frac{\nabla A}{\rho} = \frac{1}{\phi\rho}\left[\nabla(\phi A) - A\nabla\phi\right] \approx \sum_b \frac{m_b}{\rho_a\rho_b}\frac{\phi_b}{\phi_a}(A_b - A_a)\overline{\nabla_a W_{ab}}, \quad (2.32)$$

Applying these operators to the Euler equations and we get:

$$\frac{d\rho}{dt} = \rho_a\sum_b \frac{m_b}{\rho_b}\frac{\phi_b}{\phi_a}(v_b - v_a)\cdot\overline{\nabla_a W_{ab}}, \quad (2.33)$$

13

$$\frac{dv}{dt} = \sum_b \frac{m_b}{\rho_a \rho_b} \left(P_a \frac{\phi_b}{\phi_a} + P_b \frac{\phi_a}{\phi_b} \right) \overline{\nabla_a W_{ab}}, \tag{2.34}$$

$$\frac{du}{dt} = \frac{P_a}{\rho_a} \sum_b \frac{m_b}{\rho_b} \frac{\phi_b}{\phi_a} (v_b - v_a) \cdot \overline{\nabla_a W_{ab}}, \tag{2.35}$$

giving us a numerical scheme for hydrodynamics that spatially conserves both momentum and energy exactly, leaving the error in conservation mainly dependent on the time integration scheme.

2.4 Thermodynamic consistency

Two additional important conservation properties for our hydrodynamic scheme still remain. The first relates to thermodynamic consistency or in other words entropy conservation:

$$T_a \frac{dS_a}{dt} = \frac{du_a}{dt} - \frac{P_a}{\rho_a^2} \frac{d\rho_a}{dt} = 0. \tag{2.36}$$

Looking at the derived Euler equations in the previous section, we can see that we fulfill this property. The final property that we want to conserve is the mass/effective volume within our numerical scheme. This is determined by the accuracy of the continuity equation, which in our case (Eq.2.33) has both spatial and temporal errors affecting its evolution. In SPH there is, however, another way to get the density that exactly conserves the mass/effective volume. This can be done through the core SPH interpolant that we introduced in Eq.2.7 using $f = \rho$. Here, we will derive a more general form of the density estimate and take a look at the advantages and disadvantages comparing to Eq.2.33. We start by setting the volume element accordingly:[3]

$$V_b = \frac{m_b}{\rho_b}. \tag{2.37}$$

Instead of setting $f = \rho$ in the SPH interpolate (Eq.2.7) we instead use $f = \frac{\rho}{\eta}$, where η is any arbitrary scalar function (as ϕ from previous section). We then get the following density estimate:

$$\rho_a = \sum_b V_b \rho_b \frac{\eta_a}{\eta_b} W_{ab} = \sum_b^N m_b \frac{\eta_a}{\eta_b} W_{ab}. \tag{2.38}$$

This represents a more generalized form of the traditional density estimate ($\eta = 1$) and represents an integral form of the continuity equation. As we are no

---

[3]It is important to note that this can simply be seen as defining a new density $\rho_{b,new} = \rho_{b,old} \frac{\eta_b}{\eta_a}$ so that we still have $V_b = m_b / \rho_{b,new}$ in the Euler equations that we derived before and will remain unchanged as there are no direct derivatives taken on V_b. But when looking at the density estimate and its time derivative it does provide a nice illustration to write it like this.

longer evolving $\frac{d\rho_a}{dt}$ in time it is useful to take a look at the time derivative of the density estimate to see how well the condition of thermodynamic consistency is withheld (Eq.2.36):

$$\frac{d\rho_a}{dt} = \frac{1}{\Omega_a} \sum_b^N m_b \frac{\eta_a}{\eta_b} v_{ab} \cdot W_{ab} + \frac{\epsilon_a}{\Omega_a}, \tag{2.39}$$

$$\epsilon_a = \sum_b^N m_b \left(\frac{\dot{\eta}_a}{\eta_a} - \frac{\dot{\eta}_b}{\eta_b} \right) \frac{\eta_a}{\eta_b} W_{ab}, \tag{2.40}$$

$$\Omega_a = 1 - \frac{\partial h_a}{\partial \rho_a} \sum_b m_b \frac{\eta_a}{\eta_b} \frac{\partial W_{ab}}{\partial h_a}. \tag{2.41}$$

Here Ω_a is the so-called grad-h term, which takes into account the contribution of varying the smoothing length(Monaghan, 2002; Springel and Hernquist, 2002). The ϵ is an additional term that arises when using non-constant η values(Read and Hayfield, 2012). Thermodynamic inconsistency can be written as an error term (writing $\frac{du_a}{dt}$ in terms of Eq.2.24 and rearranging Eq.2.36):

$$E_S = \frac{T_a \rho_a^2}{P_a} \frac{dS_a}{dt} = \frac{d\rho_a}{dt} + \rho_a \nabla \cdot \mathbf{v_a}. \tag{2.42}$$

Which is just the difference between the two terms in the continuity equation. Inserting the estimate from the time derivative of the density (Eq.2.39) and the gradient estimate of the divergence (Eq.2.33) and we get:

$$E_S = \frac{1}{\Omega_a} \sum_b^N m_b \frac{\eta_a}{\eta_b} v_{ab} \cdot \nabla_a W_{ab} + \frac{\epsilon_a}{\Omega_a} - \rho_a \sum_b \frac{m_b}{\rho_b} \frac{\phi_b}{\phi_a} v_{ab} \cdot \nabla_a W_{ab} \tag{2.43}$$

For the traditional SPH equations were we have $\eta = 1$ $\epsilon = 0$, we can make this error term equal to zero if $\phi = \rho$ and we add the grad-h term $\frac{1}{\Omega_a}$ to the gradient estimate (both the symmetric and anti-symmetric Eq.2.30 and Eq.2.32). This forms a fully spatially conservative method with mass, energy, momentum and entropy exactly conserved (up to time-step error). This is the same form derived by the least-action principle and the Euler-Lagrange equations using the density estimate with $\eta = 1$. A slight caveat here is that we have assumed that the fluid variables are differentiable in the gradient estimate $\nabla \cdot \mathbf{v}$, in cases where the fluid variables are discontinuous or at open boundaries we have an additional error term related to the surface integral described in Eq.2.10. This is because, compared to the gradient estimate, this surface term is implicitly included in the density estimate.

While traditional SPH provides astounding conservative properties, there are significant drawbacks to this method. The main issue lies in the artificial surface tension that arises near strong density gradients. This artificial surface tension force inhibits fluid mixing and suppresses hydrodynamic instabilities

(Agertz et al., 2007). This is mainly caused by the leading order errors of SPH generated by the uneven particle distribution around strong density gradients (Read and Hayfield, 2012) and discontinuities in the internal energy (Price, 2008). To see why traditional SPH has such issues here, we can take a look at the zeroth-order errors of our symmetric gradient estimate:

$$\mathbf{E}_0 = \sum_b \frac{m_b}{\rho_b} \left(\frac{\phi_a}{\phi_b} + \frac{\phi_b}{\phi_a} \right) \nabla_a \overline{W}_{ab}, \qquad (2.44)$$

For traditional SPH we have $\phi = \rho$ which means that the error will be explicitly dependent on the density gradient together with the "unevenness" of the particle distribution. A huge improvement to this error would be to instead use $\phi = 1$ which would make the error explicitly independent of the density gradient.

This is what is done within the Gasoline2 code and was seen to provide significant improvements in problems involving strong density gradients and fluid instabilities (Wadsley et al., 2017). Another option to combat the pairing instability is to add thermal conduction near strong density gradients to smooth out the thermal energy and the particle distribution within the kernel (Price, 2008). This can be an effective method but can often lead to excessive diffusion (especially with low resolution) and can lead to suppression of fluid instabilities solely due to the diffusion. There is however a trade-off in using $\phi = 1$ as we no longer fulfill the condition of thermodynamic consistency together with the regular density estimate $\eta = 1$. A potential improvement would be to instead use $\eta = \rho$ for the density estimate. Interestingly this leaves us with an implicit equation for density instead $\sum_b \frac{m_b}{\rho_b} W_{ab} = 1$, which we can see is the partition of unit condition that we discussed in Section 2.1. Using this for the density estimate would likely lead to better accuracy, however, this would require either an iteration scheme or a fully implicit method from matrix inversion[4]. These solutions methods are both too costly to consider for practical reasons and might not even lead to convergent solutions[5]. Another issue with using a different density estimate than $\eta = 1$ is the emergence of the other error term ϵ in Eq.2.40, which would require careful consideration to evaluate its impact. As such, in Gasoline2 we keep the $\eta = 1$ density estimate. To improve the entropy conservation a linear correction term can be derived(Wadsley et al., 2017). We can derive this from Eq.2.43 by expanding v_b about r_a

$$E_S = \frac{1}{\Omega_a} \left(\nabla \cdot v_a \sum_b m_b \frac{\eta_a}{\eta_b} r_{ab} \cdot \nabla W_{ab} + O(h^2) \right)$$

$$+ \frac{\rho_a}{\Omega_a} \left(\nabla \cdot v_a \sum_b \frac{m_b}{\rho_b} \frac{\phi_b}{\phi_a} r_{ab} \cdot \nabla W_{ab} + O(h^2) \right) \qquad (2.45)$$

---

[4]In addition this has the additional requirement of needing a positive solution as we cannot allow of negative densities.

[5]Though for educational purposes it might be an interesting project to consider for future work.

A first order correction would then simply be:

$$f_a = \frac{\sum_b \frac{m_b}{\rho_a} \frac{\eta_a}{\eta_b} r_{ab} \cdot \nabla W_{ab}}{\sum_b \frac{m_b}{\rho_b} \frac{\phi_b}{\phi_a} r_{ab} \cdot \nabla W_{ab}^*}$$

(2.46)

Here ∇W_{ab}^* is the choice of kernel used for the gradient estimate(for example regular ∇W_{ab} or averaged $\nabla \overline{W_{ab}}$). This correction term can be added in together with the grad-h term Ω_a. While second and higher-order errors still remain, we have observed no systematic effect caused by this error. An important constraint to consider for the correction term is how they couple to other non-hydrodynamic forces such as gravity. The correction terms can be seen to effectively alter the adiabatic index to improve the conservation of entropy for the hydrodynamic equations, however, if the correction terms become small enough these can cause rapid gravitational collapse when coupled with gravity (due to the effective adiabatic index going below $\gamma < 4/3$ together with the energy-conserving property of SPH). While this is highly unusual it can occur given a bad particle distribution. As such, we limit the correction term to not go below 5/6.

An interesting prospect for future study would be to use $\eta_a = \rho_{a,0}$ and $\eta_b = \rho_{b,0}$, which would lead to a near-consistent thermodynamic relation to-gether with $\phi = \rho/\rho_{,0}$, where $\rho_{,0} = \sum_b m_b W_{ab}$ represents the classic density estimate with $\eta = 1$. This would in theory lead to better volume partitioning while also leading to similar improvements in the gradient estimate near density gradients. This would be similar to the method proposed by García-Senz et al. (2021).

2.5   Second-order gradients

Due to the compact support of the kernel, second order spatial derivatives prove to be very noisy and sensitive to particle disorder. A better estimate for the second derivative can be gained by using the integral approximation:

$$\nabla^2 A = 2 \sum_b m_b \frac{A_a - A_b}{\rho_b} \frac{r_{ab} \cdot \nabla_a W_{ab}}{r_{ab}^2}$$

(2.47)

This is the formalism that has been commonly used for isotropic heat conduction in SPH (Brookshaw, 1985; Cleary and Monaghan, 1999; Jubelgas et al., 2004). Equation 2.47 can also be generalized for vector quantities as shown by Español and Revenga (2003). However, this method together with the direct second derivative method has shown to be unstable when applied to anisotropic heat conduction. This is because these methods do not ensure increasing entropy during transport. A stable and more accurate approach for anisotropic heat conduction was found by Biriukov and Price (2019). In this new method, the

second derivative is gained by applying two first derivatives with alternating symmetric/anti-symmetric gradient operator. While there is an increased cost to this method (two neighbor loops), it is subject to a less stringent timestep criterion (3-8 times larger).

2.6 Variational principle

In the previous sections, we have derived the SPH equation from kernel interpolation theory and the Euler equations. Another popular derivation is often given in terms of the variational principle. Here the starting point is instead the density estimate, which alone can derive the equations of motions and energy within SPH. It is instructive to see how only determining the density leads to a fully conservative method. For some additional "freshness" we will do so for the more general form of the density estimate and show why deviating from $\eta = 1$ complicates the matter. Similar to assumptions done before, derivation using the variational principle assumes that the Lagrangian is differentiable (the action goes to zero at the surface of the integration volume) and does not account for the discreetness in time. The equations of motion of a system can be derived from the principle of least action by minimizing the action:

$$S = \int L dt \tag{2.48}$$

The discrete version of the Lagrangian is given by (Eckart, 1960; Salmon, 1988; Morrison, 1998):

$$L = \sum_b m_b \left(\frac{1}{2} v_b^2 - u_b \right) \tag{2.49}$$

Minimizing the action:

$$\delta S = \int \delta L dt = 0 \tag{2.50}$$

$$\delta L = m_a v_a \cdot \delta v_a - \sum_b m_b \frac{\delta u_b}{\delta \rho_b} \delta \rho_b \tag{2.51}$$

The perturbation in both δv and $\delta \rho$ is with respect to a small change in the particle coordinates δr. We can express the change in density with coordinates in a form similar to the time derivative of the density estimate given in Eq.2.39-2.41.

$$\delta \rho_b = \frac{1}{\Omega_b} \sum_c m_c \frac{\eta_b}{\eta_c} \nabla_b W_{bc} (\delta r_b - \delta r_c) + \frac{\delta \epsilon_b}{\Omega_b} \tag{2.52}$$

$$\delta \epsilon_b = \sum_c m_c \frac{\eta_b}{\eta_c} \left(\delta \log(\eta_b) - \delta \log(\eta_c) \right) W_{bc} \tag{2.53}$$

The function that arises from $\delta \epsilon$ quickly become difficult to properly solve. For example, take $\eta = \rho$ and we can see that we get an implicit function that needs to be solved, as a small positional perturbation for a particle will effectively

change the density of all particles. Thus, we neglect the ϵ term, providing a Lagrangian solution where η is assumed to be independent of δr. We continue the derivation by putting in the change of thermal energy at constant entropy $(\partial u_b/\partial \rho_b = \frac{P}{\rho^2})$ and integrating by parts Eq.2.50, giving the equation of motion:

$$\frac{dv_a}{dt} = -\sum_b m_b \left(\frac{P_a}{\rho_a^2 \Omega_a} \frac{\eta_a}{\eta_b} \nabla W_{ab}(h_a) + \frac{P_b}{\rho_b^2 \Omega_b} \frac{\eta_b}{\eta_a} \nabla W_{ab}(h_b) \right) \qquad (2.54)$$

The internal energy equation is simply given by looking at the conservation of energy similar as in Section 2.3.

2.7 Shocks and fluid discontinuities

As we have seen in the previous sections the Euler equations represent an adiabatic reversible model of fluids, where entropy is tightly conserved. However, in real fluids, there are irreversible processes that increase the entropy of the fluid. The main one being shocks, where the fluid variables change. Shocks are not actually discontinuous in nature, they vary smoothly over the mean free path of the fluid, where particles collide and randomize their velocities, generating heat and entropy. We are, however, working with a macroscopic theory, at a much larger scale than the mean-free path. As we cannot resolve this process, we need a sub-resolution model to capture the entropy generated by this process.

In SPH shocks have been predominately handled by applying artificial viscosity(Von Neumann and Richtmyer, 1950; Richtmyer and Morton, 1967), which smooths the discontinuous shock front on the scale of the smoothing length. This is similar to what is done in nature but at an albeit much larger scale. The most popular artificial viscosity formulations used for SPH was formulated by Monaghan and Gingold (1983), which adds an extra term to the equations of motion and the internal energy equation:

$$\frac{dv_a}{dt}_{diss} = \sum_b m_b \Pi_{ab} \overline{\nabla_a W_{ab}}, \qquad (2.55)$$

$$\frac{du}{dt}_{diss} = \sum_b m_b \left(\frac{\Pi_{ab}}{2} \right) v_{ab} \cdot \overline{\nabla_a W_{ab}}, \qquad (2.56)$$

$$\Pi_{ab} = \frac{-\alpha \frac{1}{2} \left(v_{sig,a} + v_{sig,b} \right) \mu_{ab} + \beta \mu_{ab}^2}{\frac{1}{2} \left(\rho_a + \rho_b \right)} \qquad (2.57)$$

$$\mu_{ab} = \begin{cases} \frac{\frac{1}{2}(h_a+h_b)(\mathbf{v}_{ab} \cdot \mathbf{r}_{ab})}{r_{ab}^2 + 0.01(h_a+h_b)^2} & \text{for } \mathbf{v}_{ab} \cdot \mathbf{r}_{ab} < 0, \\ 0 & \text{otherwise,} \end{cases} \qquad (2.58)$$

The non-linear term comes from the Von-Neumann Richtmyer method and the linear term was added to handle post-shock oscillations. First-order accuracy at shocks is a necessary condition for eliminating post-shock oscillations

and follows from Godunov's theorem: [*Linear numerical schemes for solving partial differential equations that do not generate new extrema (i.e., preserve monotonicity), can be at most first-order accurate.* (Godunov and Bohachevsky, 1959)]. As the resolution is increased this viscosity acts on a smaller scale and becomes more accurate. However, applying the linear viscosity term everywhere can ruin the convergence of the method in smooth flows, far away from the shocks and discontinuities where we actually need it. To handle this issue, artificial switches have been developed that shut down the linear term away from shocks and activate it near shocks. Modern switches are based on the work by Morris and Monaghan (1997), where α is set individually per particle and is increased in regions undergoing compression($\nabla \cdot v$) while decaying otherwise.

Cullen and Dehnen (2010) improved on the Morris-Monaghan switch by recognizing that the time derivative of the divergence($d(\nabla \cdot v)/dt$) was better suited for shock detection, as it could better distinguish between shocks and converging flows. This is often combined with the Balsara limiter (Balsara, 1995), which reduces dissipation in the presence of shearing flows:

$$\xi_{balsara} = \frac{|\nabla \cdot v|}{|\nabla \cdot v| + |\nabla \times v|} \tag{2.59}$$

However, using the Balsara limiter has been found to lead to different shock properties in rotating systems. To avoid this a trace-free shear tensor can be used instead, as it is zero for pure rotation but still detects shear. An issue with these switches is that they are based on the divergence of the velocity, this means that even in uniform compression viscosity will be partly active. An improvement to this was presented in the Gasoline2 code paper (Wadsley et al., 2017), where the shock indicator was instead based on the velocity gradient in the direction of the pressure gradient:

$$\nabla P = (\gamma - 1) \sum_b m_b u_b \nabla_a W(r_{ab}, h_a) \tag{2.60}$$

$$\hat{n} = -\frac{\frac{dv}{dt}}{|\frac{dv}{dt}|} = \frac{\nabla P}{|\nabla P|} \tag{2.61}$$

$$\frac{dv}{dn} = \sum_{\alpha, \beta} = n_\alpha V_{\alpha\beta} n_\beta \tag{2.62}$$

To avoid miss-activation during a uniform collapse, one-third of the divergence is removed from the shock indicator, ensuring that the $\hat{n}$ direction is the dominant part of the local compression. This is the gradient-based shock detector:

$$D = \frac{3}{2}\left(\frac{dv}{dn} + max(-\frac{1}{3}\nabla \cdot v, 0)\right) \tag{2.63}$$

This shock indicator provides a more accurate estimate than the $\nabla \cdot v$ indicator. An even more accurate estimate can be made by actually using the same $\frac{dv}{dt}$ as in the equation of motion, but this would require an additional loop over

the neighbors, increasing the cost of the method. The linear term α is updated according to (same as the Cullen Dehnen method):

$$\alpha_{loc,a} = \alpha_{max} \frac{A_a}{A_a + v_{sig,a}}, where \tag{2.64}$$

$$A_a = 2h_a^2 \xi_a max(-\frac{dD}{dt}, 0) \tag{2.65}$$

The max is taken to be $\alpha_{max} = 2$ and whenever α_a is less than $\alpha_{loc,a}$ it is set to $\alpha_a = \alpha_{loc,a}$, otherwise it decays following:

$$\frac{d\alpha_a}{dt} = (\alpha_{loc,a} - \alpha_a)/\tau_a \tag{2.66}$$

$$\tau_a = \frac{h_a}{0.2 v_{sig,a}} \tag{2.67}$$

A similar limiter to the trace-free shear tensor is used for ξ:

$$\xi_a = \left(\frac{1 - R_a}{2}\right)^4 \tag{2.68}$$

$$R_a = \frac{\sum_b m_b \frac{D_b}{|T_b|} W_R}{\sum_b m_b W_R} \tag{2.69}$$

Here $T_{\alpha\beta} = \frac{1}{2}(V_{\alpha\beta} + V_{\beta\alpha})$ and the weighting W_R is chosen to be:

$$W_R = 1 - (\frac{r_{ab}}{2h_a})^4 \tag{2.70}$$

This gradient-based shock detection is very effective in reducing the viscosity away from shocks and is easily modified for additional physics such as MHD.

The major disadvantage of the artificial viscosity is that it is hard to get a good balance between less dissipation away from shocks and proper shock capture. The artificial viscosity scheme presented above handles this balance very well, but additional improvements can likely be made. In finite-volume schemes, shock capturing is often done by either restricting the magnitude of the numerical flux across the shock front (TVD schemes) or by limiting the flux using the exact solution to the Riemann problem (Godunov schemes). Artificial dissipation can in fact itself be seen as a solution to the inter-particle Riemann problem (Monaghan, 1997), which correspond to a zeroth-order/constant velocity reconstruction in finite-volume schemes. Recently Frontiere et al. (2017) and Rosswog (2020) have presented artificial viscosity methods that take advantage of higher-order velocity reconstruction and slope limiters, which shows impressive results even with a fixed linear dissipation parameter(α). Godunov-type schemes using exact Riemann solvers have also been implemented in SPH using a conservative form of the equations (Inutsuka, 2002; Cha and Whitworth, 2003;

Puri and Ramachandran, 2014).

As we have discussed in the previous sections(see Section 2.2), the SPH gradients assume that the fluid variables are differentiable. This means that discontinuities within the flow introduce a loss of information within our equations if left untreated (Price, 2008). For regular hydrodynamics, this includes velocity and internal energy discontinuities, in which artificial viscosity handles the velocity part and artificial conduction handles the internal energy part. Applying diffusion terms to the internal energy can be a sensitive thing, as the natural tendency of gradients in thermal energy is to spread out, which means that any gradient diffused will remain diffused. Proper switches are therefore very important for artificial conduction as well. In Gasoline2 the primary dissipation for internal energy is through turbulent diffusion, which is based on the local velocity shear (Wadsley et al., 2008; Shen et al., 2010):

$$\frac{du_a}{dt}\bigg|_{cond} = \sum_b m_b \frac{(d_a + d_b)(u_b - u_a)(r_{ab} \cdot \nabla W_{ab})}{\frac{1}{2}(\rho_a + \rho_b)r_{ab}^2} \tag{2.71}$$

where d_a is the diffusion coefficient of particle a. This models the unresolved turbulent transport terms, which leading order term is the turbulent diffusion($d_a = C|S|h_a^2$, $C = 0.03$). This type of modeling captures an underlying physical phenomena and resolves the mixing issue in most situations, without leading to excessive dissipation. However, there are situations especially in shocks where additional dissipation is required for the thermal energy to produce more accurate results. Here additional shock based thermal conduction can be added (Monaghan and Lattanzio, 1985; Price, 2008). However, more aggressive thermal conduction terms can easily lead to excessive dissipation in simulations involving gravity.

2.8 Time-stepping

We integrate the SPH equation within this thesis using the Kick-Drift-Kick method as described in Quinn et al. (1997); Wadsley et al. (2004). The Kick-Drift-Kick integration scheme uses a fixed global timestep where all particle quantities are synchronized. The scheme starts by updating the non-positional particle quantities (velocity, energy, etc.) to the half step (Kick), which is followed by a full step updating the particle positions (Drift) and then finally by another half-step (Kick) for the other particle quantities to synchronize them all. An arbitrary number of sub-steps with factors of two smaller can be used to integrate gas with different timestep criteria. The basic form of the integrator is given by (only gravity force calculation):

$$v^{n+\frac{1}{2}} = v^n + \frac{1}{2}\nabla t a^n \tag{2.72}$$

$$r^{n+1} = r^n + \nabla t v^{n+\frac{1}{2}} \tag{2.73}$$

$$a^{n+1} = a(r^{n+1}) \tag{2.74}$$

$$v^{n+1} = v^{n+\frac{1}{2}} + \frac{1}{2}\nabla t a^{n+1} \tag{2.75}$$

Without gas, this method is identical to the well-known leap-frog method, which possesses both a symplectic and time-reversible property. Symplectic integrators provide much better energy conservation than non-symplectic integrators which can produce significant long-term energy drift in dynamical systems. The reason why symplectic integrators provide this benefit is due to the conservation of an approximated Hamiltonian which represents a slightly perturbed version of the original Hamiltionian (Engle et al., 2005). In addition to proving better energy conservation, symplectic integrators also ensure that the phase space volume together with linear and angular momentum is conserved. The time-reversibility property simply means that particle quantities can be returned to their initial value by reversing the direction of the time integration. The scheme deviates from being strictly symplectic when particles change the number of sub-steps to adhere to their individual timestep criteria.

The time-step criterions that we apply are:

$$dt_{accel} \leq 0.3\sqrt{\frac{a}{\epsilon}} \tag{2.76}$$

$$dt_{courant} \leq 0.4\frac{h}{(1+\alpha)v_{sig} + \beta\mu_{MAX}} \tag{2.77}$$

$$dt_{thermal} \leq 0.25\sqrt{\frac{u}{du/dt}} \quad if \quad du/dt \leq 0 \tag{2.78}$$

where the smallest criterion gives the individual timestep for the particle.

As the time-step constraint is a "local" quantity of the particle, situations can occur when there are large differences in individual time steps between nearby particles. This has been shown to cause catastrophic non-conservation in energy for simulations involving strong shocks. To avoid rapid spatial variations in the individual time-step the scheme of Saitoh and Makino (2009) is applied, where a particle time-step dt_a is limited to never exceed 4 times the timestep of any of its neighbors dt_b.

$$dt_a \leq 4dt_b \tag{2.79}$$

2.9   Relation to moving mesh/SPH-ALE

In practice, there are a lot of similarities between SPH and other Lagrangian methods often grouped as Adaptive-Lagrangian-Eulerian(ALE) methods. This includes moving-mesh methods(Gressel, 2010; Pakmor et al., 2016b) and SPH-ALE/Riemann-SPH methods(Vila, 1999; Inutsuka, 2002; Puri and Ramachandran, 2014; Avesani et al., 2014; Hopkins, 2015; Oger et al., 2016). The

two major difference between ALE methods and SPH lies in the partitioning of the volume and the evolution of conserved quantities instead of primitive variables. Here the conserved quantities are exchanged between particles through fluxes over constructed surfaces. In the case of moving mesh, this occurs through the constructed surfaces of the Voronoi mesh and in SPH-ALE through surfaces computed from the kernel gradient or some particle weighted function. These methods rely on Riemann solvers to calculate the fluxes between resolution elements. These methods are quasi-Lagrangian, which degree highly depends on the assumption of the interface velocity and reconstruction procedures. One way is to assume that the interface move with the average velocity of the interface sharing neighbors. This means that mass flux through the surfaces can occur and that particle/cell velocities are not fixed to the local fluid velocity. Another way is to assume that the interface moves with a velocity that effectively cancels the mass-flux between particles/cells[6].

A recent SPH-ALE method that has become popular in astrophysics is the MFM/MFV method developed by Hopkins (2015), which is a reformulation of the Lanson and Vila (2008) method to be used in astrophysics. Compared to moving mesh, the particle volume in MFM is still calculated using the traditional SPH density estimate, meaning that the particle volumes will overlap. The difference from SPH mainly lies in the derivation of the equations of motion from a conserved variable approach. This ensures a partition of unity due to "volume" being taken into account during flux transfer between neighbors. While MFM has proclaimed itself to be in many aspects an overall improvement to the SPH method, it is not that simple, every numerical method will bring advantages/disadvantages depending on the situation.

Riemann-solvers while attractive do not always bring the advantage that is claimed, the convergence in the method will still be limited by the width of the shock front, which for any scheme can only be resolved to within a kernel width. The method is also affected by the performance of the slope-limiter used to reconstruct the particle variables at the neighboring surfaces. This can result in similar or even worse results compared to regular SPH in low-resolution cases, but with the additional computational cost of the solver (Borrow et al., 2022). MFM similar to moving mesh code requires an additional procedure to handle irregular distributions/meshes (reconstruction, splitting, local method alterations, etc.). It is also a relatively new method for astrophysics, where numerical conservation, bias, and issues remain fairly unexplored for the method. One example is in Deng et al. (2019), where the particle-pairing instability was shown for MFM using the cubic-spline kernel at high neighbor numbers.

---

[6]The velocity of the contact discontinuity within the Riemann solution. This interface velocity is, however, only fulfilled to second-order in the subsequent particle movement (Hopkins, 2015). Potentially leading to some suppression of mass-flux (in shocks for example).

Chapter 3

Smoothed particle magneto-hydrodynamics
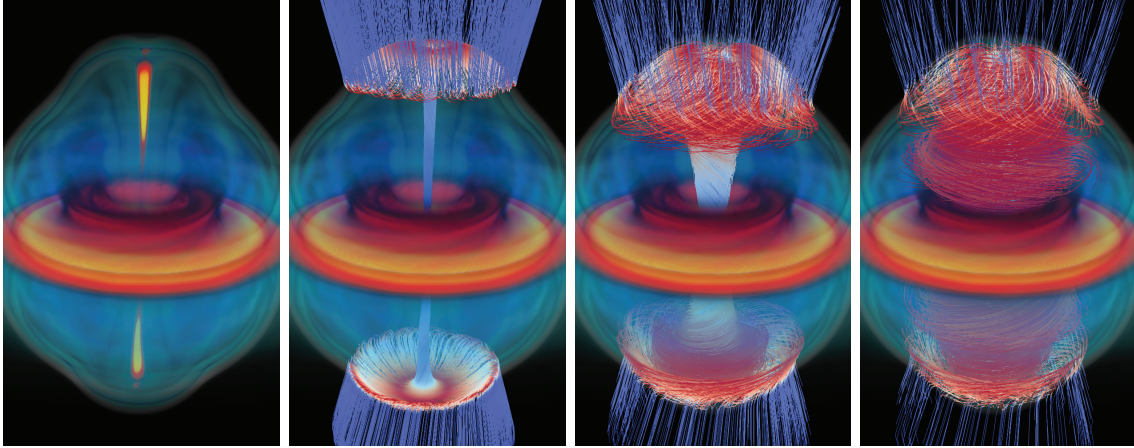
Figure 3.1: Density rendering and magnetic field structure of the jet formed from the magnetized cloud collapse. The first figure just shows the density rendering and then from left to right we visualize the different layers of the magnetic field structure going outward from the central core. The colors of the field lines represent the relative strength of the toroidal component of the magnetic field (blue to red). From this, we can see that the magnetic field structure of the jet consists of a poloidal dominated central region with a surrounding toroidal field.

Magnetized plasma within the universe can be described by the equations of magneto-hydrodynamics (MHD). In the ideal limit, the MHD equations is a result of the coupling between the Euler equations and the Maxwell equations. The equations of MHD might at first glance look relatively simple to solve. However, there is a wide range of technical difficulties involved in properly solving these equations. The first and most famous issue lies in the divergence constraint or the no-monopole condition:

$$\nabla \cdot B = 0 \qquad (3.1)$$

Divergence errors are hard to avoid as they occur naturally due to the discretization and numerical integration of the MHD equations. Numerical procedures need to be constructed for the numerical scheme to remain consistent and stable in the presence of these errors. This includes procedures that decrease the errors or limit their growth within the simulation. A second technical part of MHD is the additional complexity of shocks compared to their hydrodynamic counterpart. This is due to the additional wave types that arise in MHD,

dependent on the direction of the magnetic field along the shock front. This gives rise to different resulting shock structures that each need to be handled correctly by the numerical scheme. Third MHD introduces tension forces, this is particularly problematic for methods such as SPH. This is because in the presence of tension the particles tend to clump together, causing a so-called tensile instability (Phillips and Monaghan, 1985; Morris, 1996; Dyka et al., 1997; Monaghan, 2000). This is not too hard to understand as the regularization of SPH particles is tightly connected to the repulsive force between particles and the "zeroth-order" error, as we touched upon in the previous chapter. A negative force would remove this regularization force and simply merge particles. This tensile instability for MHD is in the end caused by the presence of divergence errors. There are, however, as we will see many ways to remove this instability from the MHD equations. Fourth: when considering systems with magnetic fields several additional conserved quantities are introduced (Morrison and Hazeltine, 1984), which needs to be considered by any numerical scheme. Fifth: There is a large resolution disparity when it comes to simulations of magnetic fields in galaxies, fluid parameters such as the magnetic Reynolds number are several magnitudes higher in reality ($Re_{mag} \approx 10^{13}$) than in numerical simulations ($Re_{mag} \approx 10 - 10000$). Amplification of the magnetic field through dynamo processes can be heavily dependent on these fluid parameters, which for numerical schemes are determined by their dissipation and resolution. Divergence errors, gradient operators, and conservation properties also play a role in correctly capturing dynamo processes in numerical schemes.

Despite all these challenges, MHD has successfully been implemented in a wide range of codes (Teyssier, 2002; Stone et al., 2008; Pakmor et al., 2011; Price et al., 2018; Pencil Code Collaboration et al., 2021), which include both Eulerian and Lagrangian codes. The first MHD implementation within SPH was included in one of the first papers on the SPH method (Gingold and Monaghan, 1977), which considered magnetic polytropes. This method did however not conserve either linear or angular momentum. This was improved upon by Phillips and Monaghan (1985), which formulated the basic SPMHD equations that modern SPMHD is based upon, these equations conserved both linear and angular momentum and were applied to simulations of star formation. An issue with this early implementation was the tensile instability, leading to particle clumping. Another early SPH MHD implementation relied on a grid to update the magnetic field, which was then interpolated onto the SPH particles (Habe et al., 1991; Mac Low, 1999). There were also applications within SPH MHD that made use of a non-conservative $J \times B$ force that ensured that the force was always perpendicular to the magnetic field (Meglicki et al., 1995; Cerqueira and de Gouveia Dal Pino, 2001), neglecting the force from any potential monopole error, which, however, showed poor performance in simulations involving shocks. The modern SPMHD method hails from the work by Price and Monaghan (2004a,b, 2005), that developed a conservative SPMHD scheme for varying smoothing lengths, that effectively prevents the tensile instability from occurring. In addition, they included improved magnetic shock capturing methods and

divergence cleaning methods. The divergence-cleaning methods were further improved upon in the work by Tricco and Price (2012); Tricco et al. (2016) and improved artificial resistivity switches have been developed (Wurster et al., 2017). This is the SPMHD scheme that the work of paper 1 was based on and further developed upon.

The chapter is outlined as follows: In Section 3.1 we go through how the continuum magnetohydrodynamics equations are derived and what assumptions are made; Section 3.2 we derive the additional kinetic waves that are generated in the fluid when subject to a magnetic field; Section 3.3 we show how the ideal MHD equations are discretized in a general form; Section 3.4 we discuss the tensile instability in MHD and how to treat it; Section 3.5 we present how magnetic field discontinuities are treated; Section 3.6 we discuss past efforts to handling the monopole error and present the method of divergence cleaning; Section 3.7 goes through the additional conservation variables that exist in MHD; Section 3.8 we present an introduction to dynamo and mean-field theory.

3.1   Continuum magnetohydrodynamics

The equations of magnetohydrodynamics is the resulting coupling of the Maxwell equations to that of hydrodynamics. The Maxwell equations are given by:

$$\nabla \times E = \frac{-\partial B}{\partial t} \tag{3.2}$$

$$\nabla \cdot E = \frac{\tau}{\epsilon_0} \tag{3.3}$$

$$\nabla \times B = \mu_0 \left(J + \epsilon_0 \frac{\partial E}{\partial t} \right) \tag{3.4}$$

$$\nabla \cdot B = 0 \tag{3.5}$$

Here, B is the magnetic field, E is the electric field, τ is the charge density, J is the current density, μ_0 is the permeability of vacuum and ϵ_0 is the permittivity of vacuum. In the ideal limit the fluid is assumed to be highly ionized (electrically neutral, ideal conductor), allowing us to neglect the effect of static electric charge within the fluid. A formulation for the induction equation can be given by taking a look at Ohm's law.

$$J' = \sigma E' \tag{3.6}$$

In a fixed frame of reference, the electric field is given by:

$$E' = E + v \times B \tag{3.7}$$

Adding this to Ohms law we can see that we can express the electric field as:

$$E = -v \times B + \frac{J}{\sigma} \tag{3.8}$$

Taking the curl of the electric field, we can insert it into the Maxwell equations to obtain the induction equation (infinite conductivity $\sigma \to \infty$):

$$\frac{\partial B}{\partial t} = \nabla \times (v \times B)$$
(3.9)

Expanding this equation gives[1]:

$$\frac{dB}{dt} = -(\nabla \cdot v)B + (B \cdot \nabla)v + (\nabla \cdot B)v$$
(3.10)

Here $(\nabla \cdot v)B$ evolves the magnetic field through shearing motion, while the $(B \cdot \nabla)v$ increases the magnetic field when undergoing compression. The final term $(\nabla \cdot B)v$ represents the monopole current, which is an unphysical term caused by the numerical divergence error. The current form of the induction equation is known as the conservative form, which exactly conserves the volume integral of the magnetic field.

$$\frac{d}{dt} \int B dV = 0$$
(3.11)

However, this form will evolve the magnetic field due to the monopole currents that can lead to a build-up of divergence-error and unphysical effects. A much more important quantity to conserve than the volume integral is the surface integral of the magnetic flux.

$$\frac{d}{dt} \int B dS = 0$$
(3.12)

By removing the monopole currents from the induction equation (($\nabla \cdot B)v$), the divergence errors are simply advected with the flow of the fluid, which ensures that the surface integral is conserved (Janhunen, 2000; Dellar, 2001).

For the equation of motion we have Lorentz Law, given by:

$$\rho \frac{\partial v}{\partial t} = \tau E + J \times B$$
(3.13)

Using the assumptions from before, Lorentz Law can be written as:

$$\rho \frac{\partial v}{\partial t} = \frac{1}{\mu_0 \rho} (\nabla \times B) \times B = \frac{1}{2\mu_0 \rho} \nabla B^2 + \frac{1}{\mu_0 \rho} (B \cdot \nabla) B$$
(3.14)

Adding the induction equation and Lorentz law to our set of hydrodynamic equations, we have the equations for SPMHD:

$$\frac{d\mathbf{v}}{dt} = \frac{\nabla \cdot \mathbf{S}}{\rho} = -\frac{1}{\rho} \nabla \left(P + \frac{\mathbf{B}^2}{2} \right) + \frac{1}{\rho} [(\mathbf{B} \cdot \nabla)\mathbf{B} + \mathbf{B}(\nabla \cdot \mathbf{B})].$$
(3.15)

---

[1]The advection term $(v \cdot \nabla)B$ is included in the Lagrangian derivative

$$\frac{d\mathbf{B}}{dt} = \nabla \times (\mathbf{v} \times \mathbf{B}) = (\mathbf{B} \cdot \nabla)\mathbf{v} - \mathbf{B}(\nabla \cdot \mathbf{v}), \tag{3.16}$$

Here S represents the stress tensor and is defined as:

$$S^{ij} = -\delta^{ij}\left(P + \frac{\mathbf{B}^2}{2}\right) + B^i B^j, \tag{3.17}$$

3.2 MHD kinetic waves

As we mentioned in the introduction, the addition of magnetic fields adds additional possible kinetic wave modes to the fluid. It is instructive to show how these wave modes arise by applying simple perturbation theory to the ideal MHD equations in the previous section. We assume that we have a uniform density field with a constant magnetic field. We then add a small perturbation $(\delta\rho, \delta v, \delta B)$ to the underlying field (ρ, v, B). Inserting this into the ideal MHD equations and considering only linear terms then give:

$$\frac{\partial \delta\rho}{\partial t} = -\rho_0 \nabla \cdot \delta v \tag{3.18}$$

$$\frac{\partial \delta v}{\partial t} = -\frac{c_s^2 \nabla \delta\rho}{\rho_0} + \frac{1}{\mu_0 \rho_0}(\nabla \times \delta B) \times B_0 \tag{3.19}$$

$$\frac{\partial \delta B}{\partial t} = \nabla \times (\delta v \times B_0) \tag{3.20}$$

The perturbations are assumed to have a wave-like solution($e^{ik\cdot r - i\omega t}$), which gives:

$$\omega\delta\rho = \rho_0 k \cdot \delta v \tag{3.21}$$

$$\omega\delta v = c_s^2\left(\frac{k \cdot \delta v}{\omega}\right)k - \frac{(B_0 \cdot k)\delta B}{\mu_0 \rho_0} + \frac{(B_0 \cdot \delta B)k}{\mu_0 \rho_0} \tag{3.22}$$

Taking the time derivative of $\omega\delta v$ and using the above relations then gives:

$$[\omega^2 - (v_A \cdot k)^2]\delta v = [(c_s^2 + v_A^2)(k \cdot \delta v) - (v_A \cdot \delta v)(k \cdot v_A)]k - [(v_A \cdot k)(k \cdot \delta v)]v_A \tag{3.23}$$

Here $v_A = \frac{B_0}{\sqrt{\mu_0 \rho_0}}$ is the Alfven speed. Assuming the magnetic field in the z-direction and wave vector in the y-z plane gives three set of equations:

$$\begin{pmatrix} \omega^2 - v_A^2 k_z^2 & 0 & 0 \\ 0 & \omega^2 - c_s^2 k_y^2 - v_A^2 k^2 & -c_s^2 k_y k_z \\ 0 & -c_s^2 k_y k_z & \omega^2 - c_s^2 k_z^2 \end{pmatrix} \delta v = \begin{pmatrix} 0 \\ 0 \\ 0 \end{pmatrix} \tag{3.24}$$

We can see that we have a velocity component in the x-direction, which is orthogonal to both the wave direction($\hat{y}, \hat{z}$) and magnetic field direction($\hat{z}$). These are transverse waves caused by the magnetic tension that travels along the magnetic field lines. They have a phase velocity of $\frac{\omega}{k_z} = v_A$ and are known

29

as Alfven waves. The longitudinal components in the y, z plane can be found from the determinant and solving for $\frac{\omega^2}{k^2}$:

$$\frac{\omega^2}{k^2} = \frac{1}{2}(c_s^2 + v_A^2) + -\frac{1}{2}\sqrt{(c_s^2 + v_A^2)^2 - 4c_s^2 v_A^2 \frac{k_z^2}{k^2}} \tag{3.25}$$

The two modes in the solution of the above equation represent the fast(+) magnetosonic waves, where pressure and magnetic fluctuations reinforce each other, and slow(-) magnetosonic waves, where pressure and magnetic fluctuations oppose each other. Given no magnetic field($v_A = 0$), we can see that we recover $\frac{\omega^2}{k^2} = c_s^2$, which are just regular sound waves.

3.3 Discretized magnetohydrodynamics

Following our discussion of SPH in the previous section, we discretize the ideal MHD equations in a similar way as the Euler equations (see Eq.2.34):

$$\frac{dv_a^i}{dt} = \sum_b \frac{m_b}{\rho_a \rho_b} \left(S_a^{ij} \frac{\phi_b}{\phi_a} + S_b^{ij} \frac{\phi_a}{\phi_b} \right) \nabla_a^j \overline{W}_{ab} \,, \tag{3.26}$$

$$\frac{d\mathbf{B}_a}{dt} = \sum_b \frac{m_b}{\rho_b} \frac{\phi_b}{\phi_a} \left[\mathbf{B}_a(\mathbf{v}_{ab} \cdot \nabla_a \overline{W}_{ab}) - \mathbf{v}_{ab}(\mathbf{B}_a \cdot \nabla_a \overline{W}_{ab}) \right] \,, \tag{3.27}$$

Similar to its hydrodynamic counterpart the symmetric operator in the equations of motions ensure that linear momentum is conserved. However, this is not the case for the angular momentum conservation, as the force is no longer ensured to be parallel between particle pairs. This is solely due to the anisotropic force term (second term in stress tensor) as both the thermal and magnetic pressure is isotropic. This can be shown clearly by considering the change in angular momentum from the stress tensor in 2D(x,y) (Price, 2004):

$$\frac{d}{dt} \sum_a (r_a \times v_a)^z = \sum_a \sum_b m_a m_b \left([\sigma_{ab}^{xx} - \sigma_{ab}^{yy}] y_{ab} x_{ab} + \sigma_{ab}^{xy} \left[y_{ab}^2 - x_{ab}^2 \right] \right) F_{ab} \tag{3.28}$$

where $\sigma_{ab}^{ij} = \frac{1}{\rho_a \rho_b} \left(S_a^{ij} \frac{\phi_b}{\phi_a} + S_b^{ij} \frac{\phi_a}{\phi_b} \right)$ and $F_{ab}\hat{r}_{ab} = \nabla W_{ab}$. We can see that it is only fully conserved if the stress is isotropic and proportional to the identity matrix. The error in angular momentum conservation will depend on the kernel errors and the force distribution. In the continuum limit, the angular momentum is conserved exactly. The error is negligible when the magnetic field is weak and usually remains small in most astrophysical simulations. There are, however, localized regions that can suffer from more non-conservation in angular momentum, for example in strong density gradients with significant angular momentum transport across it. There are potential solutions that can be applied to remedy this. As shown in Bonet (1999), the kernel gradient can be replaced

by a matrix operator to ensure the conservation, however, several other issues arise with this sort of application(noisy estimate, entropy conservation, etc.). A very interesting alternative has been presented by Müller et al. (2015), in which a spin property is introduced for the particle. This spin parameter holds the information of the orthogonal forces applied to the particle. The spin can in this case be seen as an unresolved rotation of the underlying fluid element, which effectively can interact with the surrounding particles. The spin will thus add both translational and rotational motion to nearby particles. The work from Müller et al. (2015) was done for smoothed dissipative particle dynamics to resolve the anisotropic force of physical viscosity and would be interesting to investigate its potential benefits for SPMHD in future work.

The use of the anti-symmetric operator in the induction equation ensures that the energy is conserved due to magnetic fluctuations. However, the energy conservation due to density fluctuations will depend on the choice of free parameters and consistency with the density estimate. This leads to a similar error dependence as for the entropy:

$$E_B = \frac{B^2}{\rho}(\frac{d\rho}{dt} + \nabla \cdot v) = \frac{B^2}{\rho}E_S = v_a E_S \tag{3.29}$$

Here v_a is the Alfven speed and E_S is the entropy error term from Eq.2.43. From all the test simulations presented in this thesis this spatial error always remained smaller than the time error for the conservation, which makes sense as no systematic effect was seen for the entropy conservation as well. A possibility that could be interesting to investigate is using different gradient estimates for magnetic and pressure forces, though this could potentially lead to force inconsistencies between the thermal and magnetic parts.

The discretized MHD equations are still missing a few parts to make it into a proper scheme, first the stability term against the tensile instability, second shock-capturing terms, and finally divergence cleaning procedures.

3.4   Removing the tensile instability

As we mentioned in the section introduction, we need to stabilize the equations of motions from the tensile instability, which is due to the force of the monopole error. There have been several solutions proposed to combat this issue: Murray et al. (1996) proposed using different gradient estimates for the isotropic and anisotropic parts of the stress tensor, using a symmetric term for the isotropic and anti-symmetric form for the anti-isotropic. This improves the gradient estimate for the magnetic tension term and ensures that the instability cannot occur for constant magnetic field configurations. Having less dependence on the particle configuration reduces the chance of activating the instability. This breaks momentum conservation and still allows instability to occur. Monaghan (2000) suggested adding an anti-clumping term to the force equation to prevent particles

from clumping in the presence of negative stress. Børve et al. (2001) suggested simply removing the unphysical force arising from the monopole contribution.

$$f_{divB,a}^i = -\hat{B}_a^i \sum_b \frac{m_b}{\rho_a \rho_b} \left(\mathbf{B}_a + \mathbf{B}_b\right) \cdot \nabla_a \overline{W}_{ab}. \tag{3.30}$$

This basically removes the divergence term $\left(-\frac{\mathbf{B}}{\rho} \nabla \cdot \mathbf{B}\right)$. In addition, Børve et al. (2004) showed that the instability only occurs when $\frac{1}{2}B^2 > P$. This means that we only need to activate this term within the low beta regime. Following Børve et al. (2004); Turk et al. (2012), the limiter $\hat{B}_a^i$ was introduced:

$$f_{divB,a}^i = -\hat{B}_a^i \sum_b \frac{m_b}{\rho_a \rho_b} \left(\mathbf{B}_a + \mathbf{B}_b\right) \cdot \nabla_a \overline{W}_{ab}. \tag{3.31}$$

Note that when $\beta = 1$, both the induction and momentum equations are equivalent to the Powell method (Powell et al., 1999). When this term is active, the linear momentum is no longer conserved. The degree of momentum error will depend heavily on the divergence errors present, as thus it is still important to try to reduce the divergence errors as much as possible.

It is important to note that the accuracy of the momentum equation will depend on the divergence error given by the symmetric operator while the divergence errors effect on the induction equation is given by the anti-symmetric operator. Authors that apply a more accurate gradient estimate for their divergence calculation post-simulation are not representative of the true errors that actually act in the equations during the simulation.

3.5 Shock capturing terms

To treat discontinuities in SPH we usually apply artificial dissipation terms to smooth out the fluid variables within the smoothing kernel (see Section 2.7 for more detail). For the magnetic field we add an artificial resistivity term to our equations (Price, 2004):

$$\frac{d\mathbf{B}}{dt}_{diss} = \eta \nabla^2 \mathbf{B}, \tag{3.32}$$

$$\eta = \frac{1}{2} \alpha_B v_{sig,B} |\mathbf{r}_{ab}|. \tag{3.33}$$

Here α_B is the artificial resistivity coefficient, which is a dimensionless free parameter and $v_{sig,B}$ is the signal speed chosen for the resistivity. Similar to the viscosity and conduction, switches are introduced to the resistivity to reduce dissipation away from discontinuities. Tricco and Price (2013), uses the MHD signal velocity for $v_{sig,B} = \sqrt{c_s^2 + v_a^2}$ and varies α_B following $\alpha_B = min(h_a |\nabla B_a|/|B_a|, 1)$ to ensure that resistivity is only strong where there are strong gradients in the magnetic field. Wurster et al. (2017) performed a study looking at different prescriptions of artificial resistivity, where the best

performance was seen by the method which simply used a constant α_B together with a signal speed:

$$v_{sig,B} = |\mathbf{v}_{ab} \times \hat{\mathbf{r}}_{ab}|. \tag{3.34}$$

This term ensures that there is no dissipation in constant flows and provides sufficient dissipation at magnetic discontinuities.

We discretize the second derivative in Eq.3.32 using the integral approximation(see Section 2.5):

$$\frac{d\mathbf{B}_a}{dt}_{diss} = \sum_b \frac{m_b}{\rho_b} \left(\frac{\eta_a + \eta_b}{|\mathbf{r}_{ab}|} \right) \mathbf{B}_{ab} \left(\hat{\mathbf{r}}_{ab} \cdot \nabla_a \overline{W}_{ab} \right). \tag{3.35}$$

To conserve energy we add a corresponding internal energy term:

$$\frac{du_a}{dt}_{diss} = -\frac{1}{2} \sum_b \frac{m_b}{\rho_a \rho_b} \left(\frac{\eta_a + \eta_b}{|\mathbf{r}_{ab}|} \right) \mathbf{B}_{ab}^2 \left(\hat{\mathbf{r}}_{ab} \cdot \nabla_a \overline{W}_{ab} \right). \tag{3.36}$$

Compared to artificial viscosity, artificial resistivity is applied to both approaching and receding particles as discontinuities can occur in both compressive and expansive flows. In addition, all components of the magnetic field are dissipated by the artificial resistivity as discontinuities can occur orthogonally to the direction of the shock (Price, 2004).

3.6   Divergence cleaning

As we have seen from the previous sections, a large part of the accuracy of the SPMHD method boils down to the divergence error, especially in the strong-field regime. It is, therefore, crucial to try to keep the divergence error as close to zero as possible. While grid codes have access to the constrained transport scheme (Evans and Hawley, 1988) which ensures a divergence-free field up to machine precision, it cannot easily be implemented within meshless methods, due to the absence of regular spatial grid surfaces. The generation of divergence-free fields in SPMHD has been explored in detail, however, all of them suffer from problems. The advection of divergence errors in the induction equation is sometimes known as Powell cleaning (Powell et al., 1999). However, this simply avoids the build-up of divergence errors and ensures that the surface integral of the magnetic flux is conserved. The biggest issue of this scheme is that it is zeroth-order and does not improve the divergence error with resolution. The adverse effects of this scheme are nicely laid out in Mocz et al. (2016) for moving mesh codes.

Brackbill and Barnes (1980) proposed a simple projection scheme to 'clean up' the magnetic field at each timestep.

$$B^* = \nabla \times A + \nabla\phi. \tag{3.37}$$

Taking the divergence of B^*:

$$\nabla^2 \phi = \nabla \cdot B^*, \tag{3.38}$$

after solving for ϕ we can update the magnetic field according to:

$$B = B^* - \nabla\phi. \tag{3.39}$$

The disadvantage of this approach is that it involves the solution of a Poisson equation which is computationally expensive. Another not often mentioned disadvantage is that the cross-helicity for projection methods is not conserved (Price, 2004). This is because the divergence cleaning is done independent of the velocity field, making the magnetic field lines disconnected from the velocity field lines(flux-freezing condition), which can severely affect dynamo processes.

Another option is to generate magnetic fields from Euler potentials ($B = \nabla\alpha \times \nabla\beta$), which enforce the divergence constraint by construction (Price and Rosswog, 2006). A major disadvantage of this method is that it cannot wind the magnetic field, any full turn of the magnetic field simply resets the magnetic field. It is thereby not possible to produce a dynamo with this method (Brandenburg, 2010).

Price (2010) showed that vector potential implementations ($B = \nabla \times A$) are plagued with numerical instabilities and would require stronger non-conservative forces to stabilize the method. Stasyszyn and Elstner (2015) recently showed that with additional diffusion, smoothing of the magnetic field, and enforcing the Coulomb gauge ($\nabla \cdot A = 0$), the vector potential formalism could remain stable for a handful of test cases. However, from personal tests of this vector potential formalism, the method is still subject to instabilities and requires excessive dissipation to remain stable even in the best conditions.

The best way found in SPMHD to deal with divergence error is to evolve the magnetic field via the induction equation and then to "clean" the divergence away. In general, this is done by introducing a separate scalar field that couples to the induction equation, such that it produces a damped wave equation for the divergence error. That is, the divergence is spread outward like a damped wave. The method was first developed in Dedner et al. (2002) and was improved by Tricco and Price (2012), who introduced a constrained version of the method. This makes sure that the magnetic energy is either conserved or dissipated. This was updated in Tricco et al. (2016) to correctly allow variable cleaning speed, which further improved the method. In this method, a scalar field ψ is coupled to the induction equation as follows:

$$\left(\frac{d\mathbf{B}}{dt}\right)_\psi = -\nabla\psi. \tag{3.40}$$

The scalar field ψ evolves according to:

$$\frac{d}{dt}\left(\frac{\psi}{c_h}\right) = -c_h\nabla \cdot \mathbf{B} - \frac{1}{\tau}\frac{\psi}{c_h} - \frac{1}{2}\psi(\nabla \cdot \mathbf{v}). \tag{3.41}$$

where τ is the decay time and c_h is the wave cleaning speed:

$$c_h = f_{clean}v_{mhd}, \tag{3.42}$$

$$v_{mhd} = \sqrt{c_s^2 + v_A^2}, \tag{3.43}$$

$$v_A = \sqrt{\frac{B^2}{\rho}}. \tag{3.44}$$

Here, c_s is the speed of sound, v_A the Alfvén velocity, and f_{clean} is an overcleaning factor. The f_{clean} factor can be used to increase the amount of divergence cleaning, however, this will reduce the timestep[2] according to $\Delta t \rightarrow \Delta t / f_{clean}$. Combining the cleaning equation with the induction equation produces a damped wave equation for the divergence (this form assumes constant c_h and τ):

$$\frac{\partial^2 (\nabla \cdot \mathbf{B})}{\partial t^2} - c_h^2 \nabla^2 (\nabla \cdot \mathbf{B}) + \frac{1}{\tau} \frac{\partial (\nabla \cdot \mathbf{B})}{\partial t} = 0, \tag{3.45}$$

which effectively shows that the divergence is spread out and damped. The decay time is given by:

$$\tau_a = \frac{h_a}{c_{h,a} \sigma_c}. \tag{3.46}$$

Here, σ_c is a dimensional constant, and was shown to be optimal with a value of 1 in 3D. Following Tricco and Price (2012), $\nabla \psi$ is discretized using the symmetric gradient operator (Eq.2.29) and $\nabla \cdot B$ using the anti-symmetric gradient operator (Eq.2.32). Following the previous general discretization, the cleaning equations become:

$$\left(\frac{d\mathbf{B}}{dt} \right)_{\psi,a} = - \sum_b \frac{m_b}{\rho_b} \left(\psi_a \frac{\phi_b}{\phi_a} + \psi_b \frac{\phi_a}{\phi_b} \right) \nabla_a \overline{W}_{ab}, \tag{3.47}$$

$$\frac{d}{dt} \left(\frac{\psi}{c_h} \right)_a = c_h^a \sum_b \frac{m_b}{\rho_b} \frac{\phi_b}{\phi_a} \mathbf{B}_{ab} \cdot \nabla_a \overline{W}_{ab} + \frac{\psi_a}{2 c_h^a} \sum_b \frac{m_b}{\rho_b} \frac{\phi_b}{\phi_a} \mathbf{v}_{ab} \cdot \nabla_a \overline{W}_{ab} - \frac{\psi_a}{c_h^a \tau_a}. \tag{3.48}$$

The divergence cleaning dissipates energy from the magnetic field. However, this term is so small compared to the other dissipation terms that it is not worth accounting for. We could, of course, add this energy to heat and conserve energy, however, as discussed by Tricco and Price (2012), the removal of magnetic energy and subsequent generation of thermal energy would be non-local due to the coupling of parabolic diffusion with hyperbolic transport. Due to this, we simply removed the energy.

To ensure that simulations are not affected by the divergence error, we monitor the normalized divergence error:

$$\epsilon_{divB} = \frac{h|\nabla \cdot \mathbf{B}|}{|B|}. \tag{3.49}$$

---

[2]This is a significant increase in computational cost, so it is in general not recommended to use an f_{clean} value above 1. But it does allow for a simple way to reduce the divergence error if that is required.

The mean of this quantity should preferably remain below 10^{-2}. However, regions of locally high divergence error can occur, so careful inspection of the divergence error is required to ensure the quality of simulations.

There is also a new hybrid constrained-gradient(CG) scheme developed for the MFM code (Hopkins, 2016). This iteratively approximates a globally divergence-free reconstruction of the fluid, which leads to sort of an approximate form of the traditional projection method(but at a cheaper cost). This results in lower divergence errors compared to divergence cleaning methods(albeit at a higher cost). It is unclear if this kind of method will destroy the cross-helicity conservation as seen in traditional projection methods (Price, 2004).

3.7   Additional conserved quantities

In addition, to the standard conservation laws there are additional conserved quantities within MHD (see Morrison and Hazeltine (1984)). The first is the magnetic helicity:

$$H = \int (A \cdot B) dV \tag{3.50}$$

Here A is the vector potential and is a measure of the linkage of magnetic field lines. This quantity can only be accurately tracked in numerical schemes that evolve the vector potential. Another quantity that is conserved in ideal MHD is the cross-helicity:

$$\int (B \cdot v) dV \approx \sum_b m_b \frac{B_b}{\rho_b} \cdot v_b \tag{3.51}$$

Which is a measure of the mutual linkage between the magnetic field and velocity field. This quantity is conserved due to the flux-freezing condition of MHD. The addition of diffusion adds a degree of slippage and non-conservation to this quantity. It can be used to determine how well the numerical scheme adheres to the flux-freezing condition and is likely an important quantity to correctly model dynamo effects. Due to its Lagrangian nature, this is very nicely conserved in SPH. Two other conserved quantities are the volume integral and surface integral of the magnetic field:

$$\int B dV \approx \sum_a m_a \frac{B_a}{\rho_a} \tag{3.52}$$

$$\int B \cdot dS = \int (\nabla \cdot B) dV \approx \sum_a m_a \frac{(\nabla \cdot B)_a}{\rho_a} \tag{3.53}$$

As we discussed in Section 3.1, the chosen MHD equations ensure that the surface integral is conserved, but sacrifice the conservation of the volume integral to do so. The surface integral is by far the more important quantity to correctly model (especially for shocks) (Janhunen, 2000; Price, 2004). There is an additional non-conservation error that can occur in SPH due to the discretization of the induction equation, as the anti-symmetric gradient operator is used (flux is not

symmetric between particle-pair). Non-conservation in the volume integral is usually very small but can play a role in sensitive systems such as the magneto-rotational instability simulations performed in paper 2. As this non-conservation effectively generates tiny mean-fields in the box, which in turn can induce a mean-field dynamo process (see Section 3.8). This error will mainly be dependent on the monopole error and a discussion on how to treat these errors is discussed in paper 2. Another conserved quantity relates to the MHD analog to circulation (Bekenstein and Oron, 2000). SPH has been shown to follow an approximation circulation conservation in hydrodynamics (Monaghan and Price, 2001), but this has not yet been shown to hold true for the SPMHD analog, although it might be expected to do so due to its Lagrangian nature.

3.8 Dynamo theory

A magnetic dynamo describes the exponential growth and sustenance of magnetic fields due to being stretched, twisted, and folded by the underlying fluid motions. While specific velocity field configurations can lead to dynamo action (laminar dynamo), astrophysical fluids are usually highly turbulent, where motion is chaotic across a large range of spatial scales. Dynamo action can occur across all turbulent scales, but the magnetic field is stretched faster by the smaller scale motions than the larger-scale ones, leading to a faster growth on smaller scales (known as the small-scale dynamo) (Kulsrud and Anderson, 1992; Kulsrud, 1999). In ideal MHD, the growth rate is set primarily by the viscous scale of the fluid. However, for MHD with diffusion of the magnetic field (resistivity), this is no longer necessarily true, as the magnetic fields on small scales can now be damped quickly. This makes the growth of the magnetic field more intricate, as it is determined by the relationship between the viscous scale l_v and the resistive scale l_η (Spitzer, 1962). The ratio between these two, the magnetic Prandtl number $P_m = \frac{l_v}{l_\eta}$ is thus very important in the resulting characteristic and saturation of the turbulent dynamo (Schekochihin et al., 2004). For $P_m > 1$ the quickest twisting and folding of the magnetic field is driven at the viscous scale, where the underlying velocity field is smooth as there are no smaller velocity structures in the flow at this scale. The chaotic but smooth motion at this scale lends itself to dynamo action, which means that magnetic fields can efficiently be generated (Vaĭnshteĭn and Zel'dovich, 1972; Zeldovich, 1983; Zeldovich et al., 1990). The cut-off scale of magnetic fluctuations will still be set by the resistive scale, which allows for a buildup of power within the subviscous range. With higher P_m values than one, more of the subviscous scale becomes available for magnetic field amplification (Kulsrud and Anderson, 1992; Schekochihin et al., 2004).

The small-scale dynamo has been shown to be a possible mechanism for amplifying the weak seed fields in the early universe to magnitudes observed in galaxies today (Boulares and Cox, 1990; Beck et al., 1996; Kulsrud et al., 1997). However, magnetic fields in the universe exhibit a high degree of coherence at
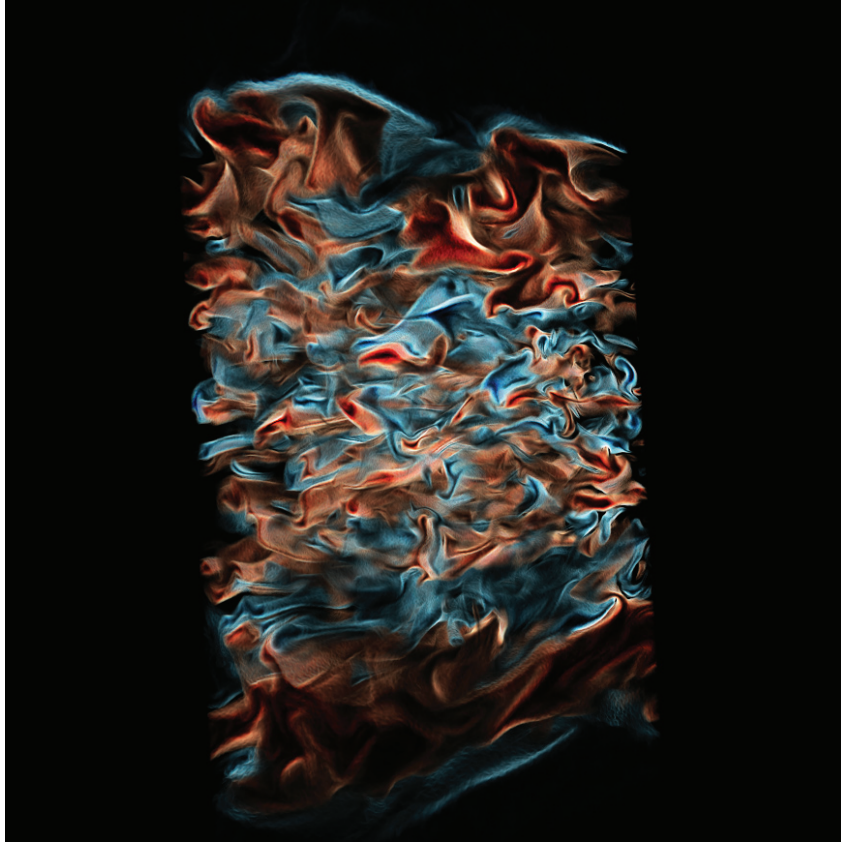
Figure 3.2: The rendering depicts the non-linear magnetic turbulence from simulations of a stratified shearing box. This is caused by the magneto-rotational instability, which destabilizes the shearing flow and generates turbulence. A feedback loop between the turbulence and magnetic field ensues due to underlying dynamo processes, leading to sustained turbulence in the box. The turbulence can subsequently act as a driver for angular momentum transport within accretion disks. Positive/negative azimuthal magnetic fields are depicted as a bluish/reddish rendering.

scales larger than the underlying turbulent motion (Beck et al., 2005; Beck, 2015). Mean-field dynamo theory is an attempt to explain how these coherent large-scale magnetic field structures can be generated in highly turbulent environments. In essence, it investigates how the small-scale kinetic and magnetic fluctuations couple to the underlying large-scale fields.

To figure out the effect of the small-scale field on the large-scale field, it is useful to introduce the formalism of mean-field theory (Moffatt, 1978; Parker, 1979; Krause and Raedler, 1980; Ruzmaikin et al., 1988; Brandenburg and Subramanian, 2005). Assuming a scale separation between the large-scale and small-scale, both the magnetic and velocity fields can be decomposed to a mean-field component ($\overline{B}$ and $\overline{U}$) and a fluctuating component (b and u):

$$B = \overline{B} + b \quad U = \overline{U} + u \tag{3.54}$$

Averaging the induction equation leads to the evolution equation for the magnetic mean-field:

$$\frac{\partial \overline{B}}{\partial t} = \nabla \times (\overline{U} \times \overline{B}) + \nabla \times \mathcal{E} + \eta \nabla^2 \overline{B} \qquad (3.55)$$

Here U represents the large-scale velocity structure, η the magnetic diffusivity and $\mathcal{E}$ is the electromotive force (EMF) produced by the fluctuating fields.

$$\mathcal{E} = \overline{u \times b} \qquad (3.56)$$

By studying how the fluctuating u and b fields reacts to an applied mean field, it can be shown that both u and b contain a component independent of the mean-field and an additional term which is linearly dependent on the applied mean-field.

$$b = b_0 + b_{\overline{B}} \quad u = u_0 + u_{\overline{B}} \qquad (3.57)$$

Assuming the indepentent terms b_0 and u_0 are uncorrelated($\mathcal{E}_0 = \overline{u_0 \times b_0} = 0$) and the assumption of scale separation, we can expand $\mathcal{E}$ in a Taylor series in $\overline{B}$ and $\overline{U}$:

$$\mathcal{E}_i = \alpha_{ij}\overline{B_j} - \eta_{ij}\overline{J_j} + \gamma_{ij}\overline{\Omega_j} + ... \qquad (3.58)$$

Here α, η and γ are the tensorial transport coefficients and $\overline{J} = \overline{\nabla \times B}$ is the mean-field current density and $\overline{\Omega} = \overline{\nabla \times U}$ is the mean-field vorticity. The first term of Eq. 3.58 is the α-effect in which the small-scale turbulence generates an EMF which is proportional to the mean-field itself. This effect, coupled together with differential rotation, can develop the well-known $\alpha\omega$ dynamo. The alpha-effect depends crucially on the small-scale helicities within the turbulent flow, which require the system to break statistical symmetry either by stratification or through having a net helicity (Pouquet et al., 1976; Moffatt, 1978; Brandenburg and Subramanian, 2005). The alpha-effect can by itself(without differential rotation) drive a dynamo, where in addition to the poloidal fields, the toroidal fields are generated by the alpha-effect as well. This is known as an α^2-dynamo. The second term in Eq. 3.58 generates an EMF in proportion to the mean-current and can act to either amplify or diffuse the mean-field. The diagonal components of η_{ij} describe the turbulent diffusion of the mean-field and the off-diagonal components η_{ij} are responsible for the dynamo produced by the $\Omega \times J$ effect (Rädler, 1969) and the shear current effect (Rogachevskii and Kleeorin, 2003), that can occur without net helicity. The last term of Eq. 3.58 is the Yoshizawa effect, which acts without the need for a large-scale magnetic field and can be seen as a turbulent battery mechanism (Yoshizawa and Yokoi, 1993; Yokoi, 2013). In addition to a mean vortical velocity component, the effect requires small-scale cross-helicity between the turbulent fields $(\overline{u \cdot b})$.

Another type of mean-field dynamo that has recently emerged as a very interesting prospect for dynamo growth within astrophysical disks, is the gravitational-instability(GI) dynamo (Riols and Latter, 2019). This is a dynamo that is sustained by the gravito-turbulence injected during spiral arm compression, which generates vertical rotating flow rolls(see Figure3.3). During compression the toroidal field is pinched, lifted, and folded by these flow

rolls, generating new radial fields. These radial fields are then sheared by the differential rotation generating toroidal fields, closing the dynamo loop. This is different than the $\alpha\Omega$ dynamo as it is governed by larger-scale motions than the turbulent helical motions. The growth rate of this dynamo seems to depend strongly on the cooling rate and the effective magnetic Reynolds number.
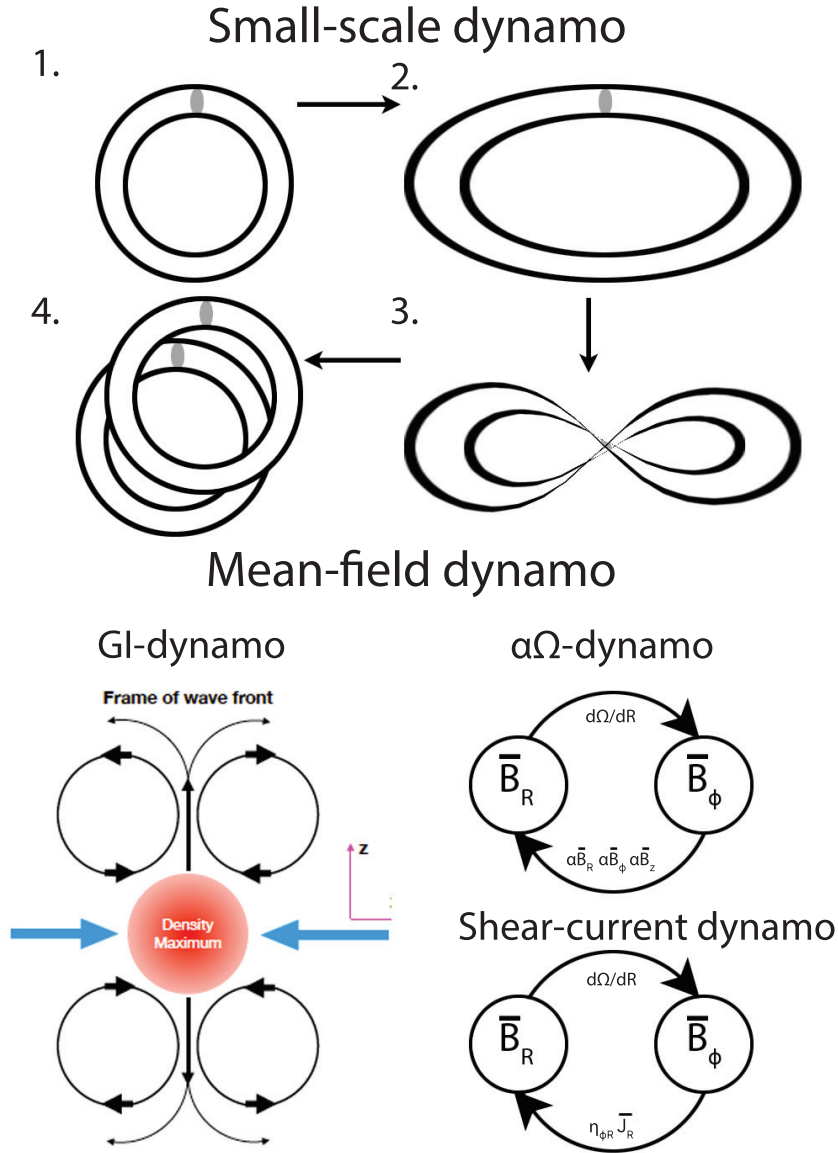
Figure 3.3: A figure diagram depicting different turbulent dynamo processes. Top figure shows the small-scale dynamo process, which include the stretching, twisting and folding of magnetic field lines due to turbulence. Right bottom figure show the classical $\alpha\Omega$-dynamo loop and the shear-current dynamo loop. Figure in the bottom left, depicting GI-dynamo is from Riols and Latter (2019). Here we can see that the compression of the spiral arm generates vertical rolls above the disk, which in turn leads to the generation of mean fields within the disk.

Chapter 4

Numerical Simulations of Galaxies
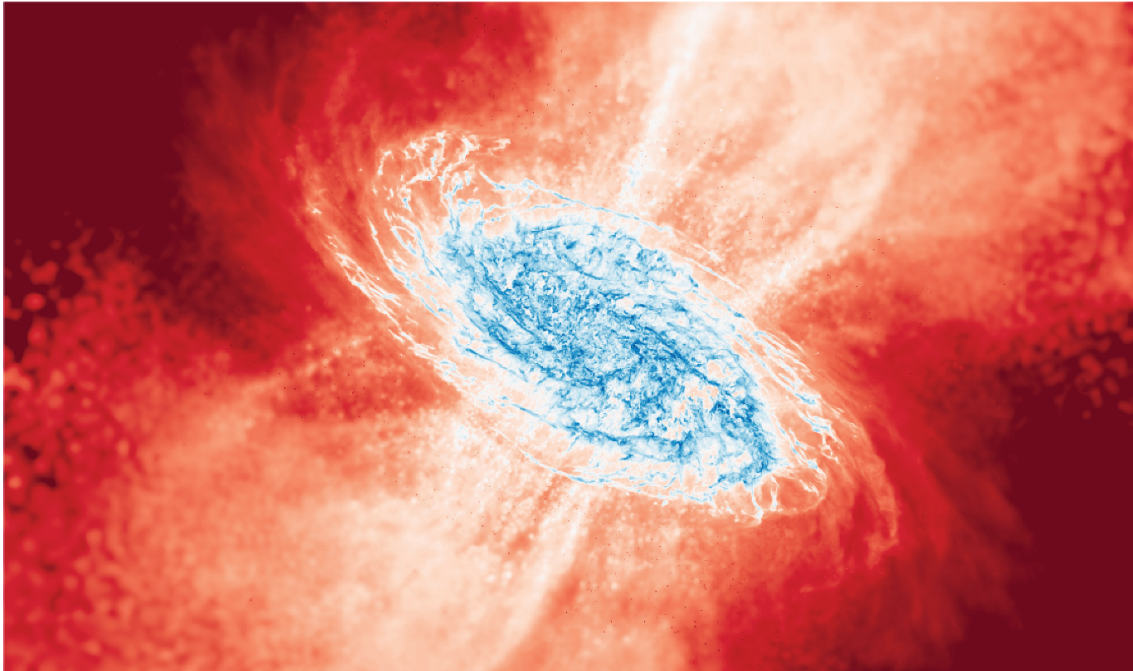
Figure 4.1: Rendering of the magnetic field strength for a simulated Milky Way-type galaxy ($M = 10^{12} M_\odot$), with a gas mass resolution of around $m = 10^2 M_\odot$. The highest magnetic field strength is dark blue; moderate strength is white and the weakest magnetic field is represented as red. From this figure, we can see that the magnetic field from the galactic disk is transported outwards to the CGM by the galactic outflows.

The first attempt to simulate a galaxy was actually not done by a numerical scheme on a digital computer. Instead, it relied on the light flux from a bunch of light bulbs to simulate the effect of gravity, both of which scale as r^{-2}. The "fluid" parcels of the galaxy were constructed of light bulbs and photocells were used to measure the collective light flux/force on each light bulb. Then a "timestep" is taken, where each of the light bulbs is moved with respect to the measured flux. Using this method, Holmberg (1941) remarkably simulated the tidal interaction between two merging galaxies. Numerical simulations on digital computers eventually came along that could model the effects of gravity. Due to the computation power at the time early simulations of galaxies could only use around 100-1000 particles. Nevertheless, these simulations were successful in showing many of the complicated morphologies that could be formed in galactic mergers/interactions (Toomre and Toomre, 1972; Eneev et al., 1973; Lauberts, 1974).

Nowadays galaxy simulations include considerably more physics and utilize millions or even billions of particles to model the galaxy. This includes the gravitational interaction between dark matter, stars and gas (Aarseth and Fall, 1980; Stadel, 2001; Dehnen, 2002); the hydrodynamic modeling of gas (Teyssier, 2002; Wadsley et al., 2004; Springel, 2010); the formation of stars (Katz, 1992); the feedback/output from supernova and stellar winds (Katz, 1992; Springel and Hernquist, 2003); the feedback/output from black holes (Di Matteo et al., 2005); the radiative cooling of gas (Marri and White, 2003; Shen et al., 2010). Simulations are also now beginning to include the modeling of the radiation field through radiative transfer (Gendelev and Krumholz, 2012; Krumholz and Thompson, 2013); non-equilibrium cooling (Capelo et al., 2018); magnetohydrodynamics (Pakmor and Springel, 2013; Rieder and Teyssier, 2017); modeling of cosmic rays (Butsky and Quinn, 2018; Thomas and Pfrommer, 2019; Hopkins et al., 2020).

Galaxy simulations provide a large tangled web of numerical complexity due to the vast amount of physical processes involved. These processes also take place over temporal and spatial scales that span many orders of magnitude. Due to our resolution constraint, some of these processes need to be resolved by so-called "sub-grid" recipes that try to model the macroscopic effects of non-resolvable processes.

The study of individual galaxies is done by either isolated galaxy simulations or zoom-in simulations. Isolated galaxy simulations are constructed from an equilibrium solution to the Jeans equation for a multi-component system including the halo, disk, and bulge (Springel et al., 2005). These simulations are easy to compare with work from other groups and can be run at very high resolution, making them ideal to investigate the internal processes within galaxies. Zoom-in simulations of galaxies re-simulate a region from a cosmological simulation at a much higher resolution. This represents more realistic initial conditions for galaxies as it takes into account the cosmological environment (Navarro and White, 1993).

The purpose of this chapter is to get an overview of the additional physics that goes into galaxy simulations. As magnetic fields in galaxies are discussed in detail in paper 3, we have omitted any discussion of the magnetic field in this chapter. The chapter is outlined as follows: In Section 4.1 we go through the implementation of gravity; Section 4.2 we discuss the gravitational softening and the issues involved in setting it; Section 4.3 we describe how star formation is implemented; Section 4.4 we discuss how radiative cooling is implemented in modern galaxy simulations; Section 4.5 we discuss the importance and the recent efforts in modeling feedback in galaxy simulations.

4.1 Gravity

The evolution of a self-gravitating fluid can be described by the coupling of the collisionless Boltzmann equation:

$$\frac{df}{dt} = \frac{\partial f}{\partial t} + v\frac{\partial f}{\partial r} - \frac{\partial \Phi}{\partial r}\frac{\partial f}{\partial v} = 0 \quad , \tag{4.1}$$

and Poisson's equation:

$$\nabla^2\Phi = 4\pi G \int f dv = 4\pi G\rho \tag{4.2}$$

Here $f(r, v, t)$ describe the phase-space distribution function of the self-gravitating fluid. To properly model the phase-space distribution (due to its dimensionality) N-body codes are used. Here the fluid is modeled using particles where the underlying distribution function is given by the phase-position of the particles. The accuracy of this will of course depends on the number of particles used to sample the phase-space distribution of the system. Finally, we need to calculate the gravitational potential to close the system. There are several ways to estimate the gravitational potential, the first and slowest way is to simply discretize the integral of the Poisson equation and solve for all particles:

$$\Phi(r) = -G\sum_{b=1}^{N}\frac{m_b}{|r - r_b|} \tag{4.3}$$

There are two major problems with this. First, the potential goes to infinity as $r- > r_b$, which results in nonphysical two-body scattering. Second, the cost of this calculation goes as $O(N^2)$, which would quickly limit the resolution that we could use for simulations involving self-gravity. The first issue can be resolved by adding a so-called softening length, which reduces the gravitational interaction between particles at small scales. The computational cost of the method can be resolved by separating the force calculation into a long-range component and a short-range component. The long-range component is solved by partitioning up the system space and using the larger-cell regions to estimate the collective gravitational interaction from that region (Barnes and Hut, 1986). The short-range force calculation is still done by regular summation, but this effectively reduces the cost of solving the gravitational potential to $O(N\log N)$.

Mesh codes instead rely on solving the differential form of the Poisson equation, which can be solved using fast Fourier transform-based methods. Here the potential is automatically softened on the scale of the grid cells and the computational cost of the method goes as $O(N\log N)$. These methods can also be combined, performing summation for the short-range component of gravity and using fast Fourier transforms for the long-range component (Efstathiou et al., 1985; Kravtsov et al., 1997; Bode and Ostriker, 2003).

4.2 Gravitational softening

The gravitational softening within N-body code and SPH warrants some more discussion. The gravitational softening can be seen as either a modification to the laws of gravity or equivalently as a smoothing of the mass (Dehnen, 2001; Barnes, 2012). One of the most simple ways to add softening is with the use of Plummer softening, where each particle is replaced with a Plummer sphere of scale ϵ.

$$\Phi(r) = -G \sum_{b=1}^{N} \frac{m_b}{\sqrt{\epsilon^2 + (r - r_b)^2}} \tag{4.4}$$

Here the mass is spread over all space with a scaling factor of ϵ. A better way to apply the softening can be obtained by instead using a softening kernel:

$$\Phi(r) = -G \sum_{b=1}^{N} m_b \phi(|r - r_b|, \epsilon) \tag{4.5}$$

Here the mass is spread within the given softening kernel(ϕ) with softening length ϵ. This will be the same or a similar kernel to the one used in SPH. This yields significantly lower force errors than the classical Plummer model(Dehnen, 2001).

The softening is introduced to reduce the fluctuations owing to shot noise, but at the same time, it biases the gravitational force within ϵ. Determining the optimal ϵ which produces the best compromise between these two effects is thus desirable. However, the choice of ϵ in simulations remains fairly arbitrary, as it can be difficult to estimate what the optimal softening for a simulation is. It might also be that there is no single constant softening that is optimal for the whole simulation. The topic of a constant softening length also plays a role when it comes to simulating self-gravity together with SPH.

The softening length can be seen as a sort of resolution length for the gravitational force, where inside the force becomes smoothed in a similar manner as the SPH force. In SPH we use a varying resolution length that depends on the density, while for gravity we use a constant resolution length. This means that there is a mismatch between the gravitational force and the SPH force. This has shown to be potentially problematic in SPH simulations involving self-gravity, leading to either suppression of collapse($\epsilon > h$) or artificial fragmentation($\epsilon < h$) (Bate and Burkert, 1997). This can be resolved by varying the softening length in the same manner as the smoothing length (Price and Monaghan, 2007). In terms of consistency, this makes a lot of sense, as it makes the hydrodynamic volume equal to the gravitational volume. However, there is an additional numerical cost involved in doing this. The first cost comes from calculating the new softening length, which if done for all particles would require a neighbor search of order ($O(N N_{neigh})$) compared to just the gas particles($O(N_{gas} N_{neigh})$). In theory, we could only use varying softening for the gas particles, as these

are the ones that need to be consistent with the hydrodynamics. However, this would mean that the effective smoothed mass density between particle species would differ, leading to a potential force bias mismatch. In addition, allowing for varying softening lengths requires additional correction factors to correctly conserve the energy of the system, which can be difficult to properly implement and adds to the numerical cost. For Gasoline2 the negative aspects of variable softening outweigh the potential gain, and a constant softening length is chosen given the highest density/smallest spacing we want to resolve in the simulation:

$$\epsilon = (m/\rho_{max})^{1/3} \tag{4.6}$$

4.3 Star formation

The resolution in galaxy simulation does not allow us to capture the formation of individual stars in molecular clouds. In fact, the molecular clouds themselves are not necessarily captured by the simulation, requiring us to construct star formation recipes that can capture the unresolved formation of stars within molecular clouds. Stellar populations within simulations are modeled using collisionless star particles. The stellar distribution of these star particles is described by an underlying initial stellar mass function (Kroupa, 2001; Chabrier, 2003). The star particles are allowed to be formed when gas within the simulations reaches a pre-determined threshold for stellar formation, in which part of the underlying gas elements can be transformed into star particles. There are many criteria that can be chosen to determine the threshold to make gas eligible for star formations. The most common ones include a density threshold (Springel and Hernquist, 2003; Stinson et al., 2006; Vogelsberger et al., 2014), Jeans-length based criteria (Teyssier et al., 2013; Trebitsch et al., 2017), molecular gas-phase requirement (Gnedin and Kravtsov, 2011; Feldmann et al., 2012; Christensen et al., 2012), converging flows (Stinson et al., 2006) or a combination of these. Gas that are eligible to become star particles do so using a probabilistic sampling scheme based on the star formation rate. The star formation rate is usually computed using the Kennicutt-Schmidt type relation (Schmidt, 1959; Kennicutt, 1998):

$$\dot{\rho_*} = \epsilon_{SF} \frac{\rho_{gas}}{t_{ff}} \tag{4.7}$$

Here ϵ_{SF} is the star formation efficiency and $t_{ff} = \frac{1}{\sqrt{4G\pi\rho_{SF}}}$ is the free fall time. The probability of forming a star particle each time step is then given by:

$$P_{SF} = 1 - \exp\left(-\frac{\epsilon_{SF}\Delta t}{t_{ff}}\right) \tag{4.8}$$

Here Δt is the length of the current timestep. From observations we have an estimated star formation efficiency in molecular gas, that is of the order 1% (Bigiel et al., 2011; Krumholz and Gnedin, 2011).

4.4 Gas cooling

Ionized gas is subject to cooling processes that dissipate the thermal energy through (collisional excitation and ionization, inverse Compton, recombination, and free-free emission). In numerical simulations, the cooling processes are included as source terms in the internal energy equation. These are determined by a so-called cooling function that is determined by the ionization fractions, density, and metallicity of the gas. Traditionally the gas has been assumed to be optically thin and in ionization equilibrium, leading to a more simple calculation of the ionization fraction (Sutherland and Dopita, 1993). In most modern simulations the ionization is determined by the background radiation field, which is assumed to be spatially uniform but redshift dependent (Wiersma et al., 2009; Shen et al., 2010). The accuracy of ionization equilibrium depends on the relation between the ionization time scale and the other dynamical time scales. For example, the assumption of equilibrium becomes bad when you have a rapidly changing radiation field or if the gas is cooling quickly. Recently there are efforts in including a self-consistent radiation field through radiation transfer codes (Petkova and Springel, 2009, 2011; Kannan et al., 2019) and non-equilibrium cooling (Richings and Schaye, 2016; Capelo et al., 2018; Kannan et al., 2020).

To save on computational cost the ionization rate is only calculated based on a handful of chemical species. The primordial elements (H,He) are the main drivers of cooling and heating in most environments, however, metal (heavier elements) cooling has shown to become dominant for a temperature of around $10^5 \leftrightarrow 10^7$ (Sutherland and Dopita, 1993; Shen et al., 2010). Following all the cooling processes would require enough resolution to resolve the multi-phase structure of the gas. The cooling functions are extracted from either cooling tables (Ferland et al., 2013) or chemical network codes (Grassi et al., 2014).

4.5 Feedback

Early simulations including gravity, star formation, and cooling resulted in significant fragmentation and unrealistically compact morphologies with star formation rates an order of magnitude higher than observed (Stinson et al., 2006; Agertz et al., 2013). This prompted the need to model the energy output processes in galaxies to suppress the excessive star formation rates and produce more realistic galaxies. These processes are known under a collective name as feedback processes, which add energy to the ISM. There are three primary ways in which feedback regulates star formation. The first is through the ejection of gas from the ISM, which depletes the "fuel" of the star formation process (Larson, 1974; Heckman et al., 1987). The gas will in most cases still be bound to the galactic halo but can take many Gyrs to return to the ISM. The second-way feedback regulates star formation is through the disruption of the cold gas clumps where stars are formed (Rogers and Pittard, 2013). The third way is

that the energy output of feedback limits the formation of cold clouds from the warmer gas by increasing the scale height of the ISM (Ostriker et al., 2010).

One of the primary sources of feedback energy in galaxies is generated by massive stars ($M > 5M$), which live short but highly-energetic lives. Producing strong stellar radiation and fast stellar winds during their lives (Weaver et al., 1977; Krumholz and Matzner, 2009) and die in a highly energetic core-collapse supernova, discharging around 10^{51} erg amount of energy to the surrounding gas (Wilson, 1985; Bethe, 1990). While smaller stars in clusters collectively produce similar energies during their lifetime, this mainly comes in the form of radiation which couple weakly with the ISM resulting in only a small deposit of energy.

The supernova explosion starts a shock expansion process, where mass from the ISM is continuously swept up by the newly formed forward shock front. Meanwhile, a reverse shock is generated which heats the inside region of the expanding shock bubble. Initially, the losses from radiation are negligible and we have an adiabatic expansion, during this phase, the momentum of the expansion is significantly boosted (Sedov-Taylor phase) (Taylor, 1950; Sedov, 1959; Chevalier, 1974). This process is diminished as a dense shell is formed at the shock front and radiative losses start to become important, transitioning from an energy-conserving to momentum-conserving evolution. Modeling the energy transfer from thermal to kinetic energy during the Sedov-Taylor phase is crucial for numerical methods to correctly model the effect from feedback. As we are often under-resolving the length-scales corresponding to the Sedov-Taylor phase, special numerical schemes are needed to correctly capture the effective momentum imparted to the ISM. In addition, as massive stars exist in tandem with each other in star clusters, the individual supernovas can interact with each other as they expand, generating a collective expansion bubble known as a superbubble (Weaver et al., 1977).

The main difficulties with including feedback in galaxy simulations relate to the resolution constraint of the Sedov-Taylor phase and getting the subgrid scheme to work properly with the rest of the physics. This is evident when combining feedback with radiative cooling at lower resolution. One of the earliest modelings of feedback did so with a thermal dump (as would be the case in a resolved case), where the star particle discharges its energy as thermal energy to nearby gas particles. However, due to the wider numerical shock widths / larger resolution lengths, the hot feedback gas will quickly mix with the cold ISM resulting in gas with short radiative cooling times. If left unhandled this can lead to complete loss of the feedback energy before it can exert momentum to the surrounding gas (Katz, 1992). This has been tackled in several ways. One way is to temporarily disable cooling for gas that is inside the approximated Sedov blast wave radius (McKee and Ostriker, 1977; Thacker and Couchman, 2000; Stinson et al., 2006). Another popular way is to instead deposit the feedback energy to kinetic energy (Navarro and White, 1994; Scannapieco et al., 2006; Dubois and Teyssier, 2008; Dalla Vecchia and Schaye, 2008). However, due to

the high-velocity gradients injected by this method, strong shocks will develop that convert the kinetic energy back to thermal energy, which can once again be efficiently radiatively cooled (Durier and Dalla Vecchia, 2012). To avoid this problem, decoupling schemes have been developed that decouple the gas affected by the feedback from interacting with the gas inside the ISM (Sun and Takayama, 2003; Vogelsberger et al., 2013). This kind of feedback depends heavily on the resolution and the numerical parameters (Dalla Vecchia and Schaye, 2008). Another alternative is to try to predict the missed momentum boost during the Sedov-Taylor phase. This is done by determining the under-resolved part of the expansion and boosting the momentum accordingly, either analytically (Hopkins et al., 2014; Kimm and Cen, 2014) or by fitting to high-resolution supernova simulations (Martizzi et al., 2015). In Gasoline2 we primarily use the superbubble feedback model from Keller et al. (2014). This separates the cold and hot phases, which effectively resolves the overcooling issue. In addition, the evolution of the superbubble is made less resolution-dependent with the help of thermal conduction and subgrid evaporation, which regulates the hot and cold phases without the need for a free parameter.

Significant feedback can also come from accreting supermassive black holes, in the form of radiation, jets, and less-collimated outflows. This feedback is often divided into two modes in numerical implementation, the quasar mode, and radio mode. The quasar mode represents the radiatively efficient part of the feedback that comes from the viscous heating and subsequent radiation of the accretion disk (Antonucci, 1993). This is often implemented similar to the SN feedback through thermal or momentum injection (Springel et al., 2005; Di Matteo et al., 2005). The radio mode feedback comes from the relativistic-collimated jets launched by the supermassive black hole. These are formed on the scale of the Schwarzschild radius but can induce a significant dynamic effect on gas that is several kpcs away from the galaxy. This means that from the scale of accretion there is a wide range of dynamic scales that needs to be correctly captured by the subgrid method (Sijacki et al., 2007; Weinberger et al., 2017; Bourne and Sijacki, 2021), which has historically made this type of feedback recipe very uncertain.

Another important component that can produce a significant feedback channel is cosmic rays (CR), which energy content has been observed to be in equipartition with the kinetic and magnetic energy within galaxies (Boulares and Cox, 1990). CR are charged particles that are accelerated to relativistic speeds in extreme astrophysical shocks (supernova explosions). Although their velocities are relativistic, CR is scattered by magnetic fields and is confined within the galaxy for tens of millions of years. The interactions with the gas provide non-thermal pressure support which can then drive galactic outflows and alter the temperature and ionization state of the gas in the CGM. CRs allow for winds that are significantly cooler than regular thermal winds, which is relevant as large reservoirs of cold ($T \sim 10^4 K$) gas are observed out to and beyond the virial radius in the CGM. Reliable modeling of CRs is, however, a complicated

matter as the physics determining their transport is governed by interactions between the CRs and Alfvén waves on the scale of the gyroradius. This is way below any attainable resolution in galaxies, as such approximations are required to capture the global transport. However, before even thinking of modeling CRs the numerical dependencies and resolution requirements of the magnetic field in galaxies should be fully explored and understood.

Chapter 5

Summary and future work

In the past chapters, we have gone through the background of the numerical methods that I used in my thesis papers and presented the physics involved in modern galaxy simulations. Below follows a short summary of the scientific work that I have done during my years as a Ph.D. student:

Paper I I have developed an MHD method for smoothed particle hydrodynamics that takes advantage of new gradient operators to improve the accuracy of the method near density discontinuities. We implement ideal MHD in the GASOLINE2 and CHANGA codes with both GDSPH and traditional SPH (TSPH) schemes. A constrained hyperbolic divergence cleaning scheme is employed to control the divergence error, and a switch for artificial resistivity with minimized dissipation is used.

We test the codes with a large suite of MHD tests and show that in all problems the results are comparable or improved over previous SPMHD implementations. While both GDSPH and TSPH perform well with relatively smooth or highly supersonic flows, GDSPH shows significant improvements in the presence of strong discontinuities and large dynamic scales. In particular, when applied to an astrophysical problem of the collapse of a magnetized cloud, GDSPH realistically captures the development of a magnetic tower and jet launching in the weak-field regime, and exhibits fast convergence with resolution, while TSPH failed to do so. Our new method shows qualitatively similar results to the ones from the meshless finite mass/volume (MFM/MFV) schemes within the GIZMO code, while remaining computationally less expensive.

Paper II The initial idea of this paper was prompted by the result from Deng et al. (2019), which showed that SPH simulations of the magneto-rotational instability(MRI) in stratified shearing boxes suffer from runaway growth and develop unphysically strong magnetic fields. This was shown to be avoided by the meshless finite mass/volume (MFM/MFV) schemes. In this paper, we showed that our method does not suffer from this runaway growth and could reproduce the characteristic "butterfly" diagram of the MRI dynamo with saturated turbulence for at least 100 orbits.

In addition, we presented a thorough numerical study on the MRI using SPMHD, looking at different initial setups and a wide range of resolution and dissipation parameters. We show, for the first time, that MRI with sustained turbulence can be simulated successfully with SPH,

with results consistent with prior work with grid-based codes, including saturation properties such as magnetic and kinetic energies and their respective stresses.

We investigated the dependency of MRI turbulence on the numerical Prandtl number(P_m) in SPH, focusing on the unstratified, zero net-flux case. We found that turbulence can only be sustained with a Prandtl number larger than ~ 2.5, similar to the critical values for the physical Prandtl number found in grid-code simulations. However, unlike grid-based codes, the numerical Prandtl number in SPH increases with resolution, and for a fixed Prandtl number, the resulting magnetic energy and stresses are independent of resolution. Due to the strong dependencies on the numerical Prandtl number, we stress that numerical analysis of the numerical Prandtl number should be done by all codes to assess its dependencies.

Mean-field analyses were performed on all simulations, and the resulting transport coefficients indicate no α-effect in the unstratified cases, but an active $\alpha\omega$ dynamo and a diamagnetic pumping effect in the stratified medium, which are generally in agreement with previous studies.

Paper III In this paper, we investigate the amplification of magnetic fields within isolated galaxy simulations. As we have seen from the previous chapter, global galaxy simulations provide a large tangled web of numerical complexity due to the vast amount of physical processes involved. Understanding the numerical dependencies that act on the galactic dynamo is a crucial step in determining what resolution and what conditions are required to properly capture the magnetic fields observed in galaxies.

The result shows that there is a strong mean-field dynamo occurring in the spiral-arm region of the disk, likely produced by an $\alpha\omega$ type dynamo. Without star formation and feedback, the amplification is highly determined by the cooling and the smallest collapse-length set by the Jeans floor. As this determines the degree of fragmentation within the disk. Amplification is driven by shear and vertical motions within the filamentary structure that forms around and between fragments($\alpha\omega$-effect).

The inclusion of feedback is seen to work in both a destructive and positive fashion for the amplification process. Destructive interference for the amplification occurs due to breakdown of filament structure in the disk, increase of turbulent diffusion, and the ejection of magnetic flux from the central plane to the CGM. The positive effect of feedback is the increase in vertical motions and the turbulent fountain flows that develop, showing a high dependence on the small-scale vertical structure and the numerical dissipation within the galaxy. Galaxies with an effective dynamo, saturate their magnetic energy density at levels between 10-30% of the thermal energy density.

Compared to the result of the MRI in the previous paper, we find that the density averaged numerical Prandtl number is below unity throughout the galaxy for all our simulations. Given a turbulent injection length of 1kpc, the numerical magnetic Reynolds number is within the range of ($Re_{mag} = 10 - 400$), indicating that some regions are below the levels required for the small-scale dynamo ($Re_{mag,crit} = 30 - 2700$) to be active.

5.1 Future work

After reading the introductory chapters and the papers in this thesis it should be clear that there is a lot of work to be done within the area of numerical methods and galaxy formation in regard to magnetic fields. I've listed some of these below:

SPH improvements :

Many improvements to the numerical method have been hinted at during the introduction chapters of this thesis. SPH is very dependent on the distribution of particles within the kernel, this means that there will always be less accuracy at density gradients/open boundaries due to the asymmetry in the particle distribution. This is improved by the GDSPH gradient operators by making the errors less sensitive to density gradients. Further improvements can potentially be made here by improving the partition of unity condition, which can be shown to directly improve the gradient estimate (García-Senz et al., 2021). In addition, this would naturally make the GDSPH method more thermodynamic consistent (see Section 2.4). The effective improvement of the method versus the potential costs of improved volume partitioning needs to be investigated further in future work.

GDSPH and improved volume partitioning are mainly improvements in regard to density gradients, there are however other consequences of asymmetry in the particle distribution. The most famous one comes from shearing flows, which add asymmetries to the particle distribution that in conjunction with the shearing flow itself result in slightly biased gradient estimates. This is most clear when looking at the divergence estimate $\nabla \cdot v$ in shearing flows, which in the presence of shear erroneously detect compression even if the velocity field is divergence-free. This is usually corrected for in the artificial viscosity by doing a linear correction to the divergence estimate (Cullen and Dehnen, 2010). However, this can also be corrected by making the gradient-operators linear-exact, this can be done by deriving the SPH gradients from an integral approach, dividing by the first-order position matrix (García-Senz et al., 2012). This can also generally improve the errors for MHD as it makes the induction

equation second-order at all times. This can in addition be combined with both GDSPH and improved volume partitioning. There exist higher-order bias errors in the gradient estimate due to the asymmetry induced by shearing flows, these can be shown to be directly proportional to the underlying particle noise. Potentially higher-order corrections can be done by reconstructing the kernel gradient taking into account higher orders of the position matrix (though the benefit vs the additional computational cost for this seems excessive).

Alternatively, some of these issues might be tackled by non-spherical smoothing kernels that can adjust their smoothing length in each direction to balance the asymmetry in the particle distribution. Though one needs to be very careful with non-spherical kernels as they can induce angular momentum errors.

In addition, it would be interesting to apply higher-order magnetic field reconstruction and slope limiters for the artificial resistivity (as was done for viscosity/conduction by Rosswog (2020)). Furthermore, an interesting avenue for solving the angular momentum loss in SPMHD due to the tension force could be by adding a spin property to the particles (Menon et al., 2015). This spin parameter holds the information that is otherwise lost by the orthogonal forces. This spin can then effectively "reintroduce" the angular momentum to the surrounding gas

Super-Lagrangian SPH :

SPH is a Lagrangian numerical method that naturally adapts its resolution with density, making high-density regions more resolved than low-density regions. While this is in the majority of cases what we want, there are circumstances/regions in which we would like to have higher resolution despite the density. One such case is for example in the CGM wherein the majority of galaxy simulations the CGM is only very coarsely resolved, which means the small-scale structure cannot be properly resolved (Hummels, 2018). This of course also means that dynamo-processes within the CGM in these simulations are severely suppressed.

Super-Lagrangian refinement in SPH is on the surface very simple, as particles can be split and merged to either generate more or fewer resolution elements. However, the accuracy of SPH can be highly degraded if the neighboring particles around it are of vastly different mass. So the tricky part of implementing super-Lagrangian refinement in SPH comes down to assuring that different regions of the simulation only contain particles of a certain mass. By implementing a transition region together with splitting and merging procedures, I believe that super-Lagrangian

refinement can be implemented in a nice way in SPH. Potentially these transition regions can take advantage of Voronoi tessellation for the merging and splitting (not the hydrodynamics), in which there already exist methods for (Springel, 2010).

Magnetic field amplification in local galactic environments :

The final paper highlights the numerical dependencies in global galaxy simulations using SPH. However, disentangling the different turbulent drivers and their resolution dependencies proves to be a difficult task. To get a better understanding of the dynamo processes induced by the supernova feedback I will in future work simulate local simulations boxes looking at the structure of the resulting turbulence and the magnetic field. Determining the effective turbulent driving length and a mixture of solenoidal-compressive modes and their dependencies on resolution. This will in addition be done in both non-stratified and stratified boxes and with and without shear to determine the effect of different environments in the galactic disk. In addition, high resolution/super-Lagrangian could be used to investigate the turbulent driving of outflow-driven gas on the CGM using local simulation boxes.

Bibliography

Aarseth, S. J. and Fall, S. M. (1980). Cosmological N-body simulations of galaxy merging. , 236:43–57.

Adebahr, B., Krause, M., Klein, U., Weżgowiec, M., Bomans, D. J., and Dettmar, R. J. (2013). <ASTROBJ>M 82</ASTROBJ> - A radio continuum and polarisation study. I. Data reduction and cosmic ray propagation. , 555:A23.

Agertz, O., Kravtsov, A. V., Leitner, S. N., and Gnedin, N. Y. (2013). Toward a Complete Accounting of Energy and Momentum from Stellar Feedback in Galaxy Formation Simulations. , 770(1):25.

Agertz, O., Moore, B., Stadel, J., Potter, D., Miniati, F., Read, J., Mayer, L., Gawryszczak, A., Kravtsov, A., Nordlund, Å., Pearce, F., Quilis, V., Rudd, D., Springel, V., Stone, J., Tasker, E., Teyssier, R., Wadsley, J., and Walder, R. (2007). Fundamental differences between SPH and grid methods. , 380:963–978.

Antonucci, R. (1993). Unified models for active galactic nuclei and quasars. , 31:473–521.

Avesani, D., Dumbser, M., and Bellin, A. (2014). A new class of Moving-Least-Squares WENO-SPH schemes. *Journal of Computational Physics*, 270:278–299.

Balsara, D. S. (1995). von Neumann stability analysis of smooth particle hydrodynamics–suggestions for optimal algorithms. *Journal of Computational Physics*, 121(2):357–372.

Barnes, J. and Hut, P. (1986). A hierarchical O(N log N) force-calculation algorithm. , 324(6096):446–449.

Barnes, J. E. (2012). Gravitational softening as a smoothing operation. , 425(2):1104–1120.

Bate, M. R. and Burkert, A. (1997). Resolution requirements for smoothed particle hydrodynamics calculations with self-gravity. , 288(4):1060–1072.

Beck, R. (2007). Magnetism in the spiral galaxy NGC 6946: magnetic arms, depolarization rings, dynamo modes, and helical fields. , 470(2):539–556.

Beck, R. (2015). Magnetic fields in spiral galaxies. , 24:4.

Beck, R., Brandenburg, A., Moss, D., Shukurov, A., and Sokoloff, D. (1996). Galactic Magnetism: Recent Developments and Perspectives. , 34:155–206.

Bibliography

Beck, R., Fletcher, A., Shukurov, A., Snodin, A., Sokoloff, D. D., Ehle, M., Moss, D., and Shoutenkov, V. (2005). Magnetic fields in barred galaxies. IV. NGC 1097 and NGC 1365. , 444(3):739–765.

Beck, R. and Wielebinski, R. (2013). *Magnetic Fields in Galaxies*, volume 5, page 641.

Bekenstein, J. D. and Oron, A. (2000). Conservation of circulation in magnetohydrodynamics. , 62(4):5594–5602.

Benz, W. (1990). Smooth Particle Hydrodynamics - a Review. In Buchler, J. R., editor, *Numerical Modelling of Nonlinear Stellar Pulsations Problems and Prospects*, page 269.

Berger, M. J. and Oliger, J. (1984). Adaptive Mesh Refinement for Hyperbolic Partial Differential Equations. *Journal of Computational Physics*, 53(3):484–512.

Bethe, H. A. (1990). Supernova mechanisms. *Reviews of Modern Physics*, 62(4):801–866.

Bigiel, F., Leroy, A. K., Walter, F., Brinks, E., de Blok, W. J. G., Kramer, C., Rix, H. W., Schruba, A., Schuster, K. F., Usero, A., and Wiesemeyer, H. W. (2011). A Constant Molecular Gas Depletion Time in Nearby Disk Galaxies. , 730(2):L13.

Biriukov, S. and Price, D. J. (2019). Stable anisotropic heat conduction in smoothed particle hydrodynamics. , 483(4):4901–4909.

Birnboim, Y., Balberg, S., and Teyssier, R. (2015). Galaxy evolution: modelling the role of non-thermal pressure in the interstellar medium. , 447(4):3678–3692.

Bode, P. and Ostriker, J. P. (2003). Tree Particle-Mesh: An Adaptive, Efficient, and Parallel Code for Collisionless Cosmological Simulation. , 145(1):1–13.

Bonet, J. (1999). Variational and momentum preservation aspects of Smooth Particle Hydrodynamic formulations. *Computer Methods in Applied Mechanics and Engineering*, 180(1-2):97–115.

Booth, C. M., Agertz, O., Kravtsov, A. V., and Gnedin, N. Y. (2013). Simulations of Disk Galaxies with Cosmic Ray Driven Galactic Winds. , 777:L16.

Borrow, J., Schaller, M., Bower, R. G., and Schaye, J. (2022). SPHENIX: smoothed particle hydrodynamics for the next generation of galaxy formation simulations. , 511(2):2367–2389.

Børve, S., Omang, M., and Trulsen, J. (2001). Regularized Smoothed Particle Hydrodynamics: A New Approach to Simulating Magnetohydrodynamic Shocks. , 561:82–93.

Børve, S., Omang, M., and Trulsen, J. (2004). Two-dimensional MHD Smoothed Particle Hydrodynamics Stability Analysis. , 153:447–462.

Boulares, A. and Cox, D. P. (1990). Galactic hydrostatic equilibrium with magnetic tension and cosmic-ray diffusion. , 365:544–558.

Bourne, M. A. and Sijacki, D. (2021). AGN jet feedback on a moving mesh: gentle cluster heating by weak shocks and lobe disruption. , 506(1):488–513.

Brackbill, J. U. and Barnes, D. C. (1980). The Effect of Nonzero $\nabla \cdot B$ on the numerical solution of the magnetohydrodynamic equations. *Journal of Computational Physics*, 35(3):426–430.

Brandenburg, A. (2010). Magnetic field evolution in simulations with Euler potentials. , 401:347–354.

Brandenburg, A. and Subramanian, K. (2005). Astrophysical magnetic fields and nonlinear dynamo theory. , 417(1-4):1–209.

Brookshaw, L. (1985). A method of calculating radiative heat diffusion in particle simulations. , 6(2):207–210.

Burlaga, L. F., Ness, N. F., and Stone, E. C. (2013). Magnetic Field Observations as Voyager 1 Entered the Heliosheath Depletion Region. *Science*, 341(6142):147–150.

Butsky, I. S. and Quinn, T. R. (2018). The Role of Cosmic-ray Transport in Shaping the Simulated Circumgalactic Medium. , 868:108.

Cabezón, R. M., García-Senz, D., and Figueira, J. (2017). SPHYNX: an accurate density-based SPH method for astrophysical applications. , 606:A78.

Cabezón, R. M., García-Senz, D., and Relaño, A. (2008). A one-parameter family of interpolating kernels for smoothed particle hydrodynamics studies. *Journal of Computational Physics*, 227(19):8523–8540.

Capelo, P. R., Bovino, S., Lupi, A., Schleicher, D. R. G., and Grassi, T. (2018). The effect of non-equilibrium metal cooling on the interstellar medium. , 475(3):3283–3304.

Cerqueira, A. H. and de Gouveia Dal Pino, E. M. (2001). Three-dimensional Magnetohydrodynamic Simulations of Radiatively Cooling, Pulsed Jets. , 560(2):779–791.

Cha, S. H. and Whitworth, A. P. (2003). Implementations and tests of Godunov-type particle hydrodynamics. , 340(1):73–90.

Chabrier, G. (2003). Galactic Stellar and Substellar Initial Mass Function. , 115(809):763–795.

Chen, Y.-M., Tremonti, C. A., Heckman, T. M., Kauffmann, G., Weiner, B. J., Brinchmann, J., and Wang, J. (2010). Absorption-line Probes of the Prevalence and Properties of Outflows in Present-day Star-forming Galaxies. , 140(2):445–461.

Chevalier, R. A. (1974). The Evolution of Supernova Remnants. Spherically Symmetric Models. , 188:501–516.

Christensen, C., Quinn, T., Governato, F., Stilp, A., Shen, S., and Wadsley, J. (2012). Implementing molecular hydrogen in hydrodynamic simulations of galaxy formation. , 425(4):3058–3076.

Church, R. P., Dischler, J., Davies, M. B., Tout, C. A., Adams, T., and Beer, M. E. (2009). Mass transfer in eccentric binaries: the new oil-on-water smoothed particle hydrodynamics technique. , 395(2):1127–1134.

Chyży, K. T. and Beck, R. (2004). Magnetic fields in merging spirals - the Antennae. , 417:541–555.

Cicone, C., Maiolino, R., Sturm, E., Graciá-Carpio, J., Feruglio, C., Neri, R., Aalto, S., Davies, R., Fiore, F., Fischer, J., García-Burillo, S., González-Alfonso, E., Hailey-Dunsheath, S., Piconcelli, E., and Veilleux, S. (2014). Massive molecular outflows and evidence for AGN feedback from CO observations. , 562:A21.

Cleary, P. W. and Monaghan, J. J. (1999). Conduction Modelling Using Smoothed Particle Hydrodynamics. *Journal of Computational Physics*, 148(1):227–264.

Cullen, L. and Dehnen, W. (2010). Inviscid smoothed particle hydrodynamics. , 408:669–683.

Cummins, S. J. and Rudman, M. (1999). An SPH Projection Method. *Journal of Computational Physics*, 152(2):584–607.

Dalla Vecchia, C. and Schaye, J. (2008). Simulating galactic outflows with kinetic supernova feedback. , 387(4):1431–1444.

Dawson, J. M. (1983). Particle simulation of plasmas. *Reviews of Modern Physics*, 55(2):403–447.

Dedner, A., Kemm, F., Kröner, D., Munz, C.-D., Schnitzer, T., and Wesenberg, M. (2002). Hyperbolic Divergence Cleaning for the MHD Equations. *Journal of Computational Physics*, 175:645–673.

Dehnen, W. (2001). Towards optimal softening in three-dimensional N-body codes - I. Minimizing the force error. , 324(2):273–291.

Dehnen, W. (2002). A Hierarchical O(N) Force Calculation Algorithm. *Journal of Computational Physics*, 179(1):27–42.

Dehnen, W. and Aly, H. (2012). Improving convergence in smoothed particle hydrodynamics simulations without pairing instability. , 425:1068–1082.

Dellar, P. J. (2001). A Note on Magnetic Monopoles and the One-Dimensional MHD Riemann Problem. *Journal of Computational Physics*, 172(1):392–398.

Deng, H., Mayer, L., Latter, H., Hopkins, P. F., and Bai, X.-N. (2019). Local Simulations of MRI turbulence with Meshless Methods. , 241(2):26.

Di Matteo, T., Springel, V., and Hernquist, L. (2005). Energy input from quasars regulates the growth and activity of black holes and their host galaxies. , 433(7026):604–607.

Dubois, Y. and Teyssier, R. (2008). On the onset of galactic winds in quiescent star forming galaxies. , 477(1):79–94.

Durier, F. and Dalla Vecchia, C. (2012). Implementation of feedback in smoothed particle hydrodynamics: towards concordance of methods. , 419(1):465–478.

Dyka, C. T., Randles, P. W., and Ingel, R. P. (1997). Stress Points for Tension Instability in SPH. *International Journal for Numerical Methods in Engineering*, 40(13):2325–2341.

Eckart, C. (1960). Variation Principles of Hydrodynamics. *Physics of Fluids*, 3(3):421–427.

Efstathiou, G., Davis, M., White, S. D. M., and Frenk, C. S. (1985). Numerical techniques for large cosmological N-body simulations. , 57:241–260.

Eneev, T. M., Kozlov, N. N., and Sunyaev, R. A. (1973). Tidal Interaction of Galaxies. , 22:41.

Engle, R. D., Skeel, R. D., and Drees, M. (2005). Monitoring energy drift with shadow Hamiltonians. *Journal of Computational Physics*, 206(2):432–452.

Español, P. and Revenga, M. (2003). Smoothed dissipative particle dynamics. , 67(2):026705.

Evans, C. R. and Hawley, J. F. (1988). Simulation of magnetohydrodynamic flows - A constrained transport method. , 332:659–677.

Feldmann, R., Gnedin, N. Y., and Kravtsov, A. V. (2012). The X-factor in Galaxies. II. The Molecular-hydrogen-Star-formation Relation. , 758(2):127.

Ferland, G. J., Porter, R. L., van Hoof, P. A. M., Williams, R. J. R., Abel, N. P., Lykins, M. L., Shaw, G., Henney, W. J., and Stancil, P. C. (2013). The 2013 Release of Cloudy. , 49:137–163.

Fletcher, A. (2010). Magnetic Fields in Nearby Galaxies. In Kothes, R., Landecker, T. L., and Willis, A. G., editors, *The Dynamic Interstellar Medium: A Celebration of the Canadian Galactic Plane Survey*, volume 438 of *Astronomical Society of the Pacific Conference Series*, page 197.

Fletcher, A., Beck, R., Shukurov, A., Berkhuijsen, E. M., and Horellou, C. (2011). Magnetic fields and spiral arms in the galaxy M51. , 412(4):2396–2416.

Frick, P., Stepanov, R., Beck, R., Sokoloff, D., Shukurov, A., Ehle, M., and Lundgren, A. (2016). Magnetic and gaseous spiral arms in M83. , 585:A21.

Frontiere, N., Raskin, C. D., and Owen, J. M. (2017). CRKSPH - A Conservative Reproducing Kernel Smoothed Particle Hydrodynamics Scheme. *Journal of Computational Physics*, 332:160–209.

García-Senz, D., Cabezón, R. M., and Escartín, J. A. (2012). Improving smoothed particle hydrodynamics with an integral approach to calculating gradients. , 538:A9.

García-Senz, D., Cabezón, R. M., and Escartín, J. A. (2021). Conservative, density-based smoothed particle hydrodynamics with improved partition of the unity and better estimation of gradients. *arXiv e-prints*, page arXiv:2101.07364.

Gardiner, T. A. and Stone, J. M. (2005). An unsplit Godunov method for ideal MHD via constrained transport. *Journal of Computational Physics*, 205:509–539.

Gendelev, L. and Krumholz, M. R. (2012). Evolution of Blister-type H II Regions in a Magnetized Medium. , 745(2):158.

Gingold, R. A. and Monaghan, J. J. (1977). Smoothed particle hydrodynamics - Theory and application to non-spherical stars. , 181:375–389.

Gnedin, N. Y. and Kravtsov, A. V. (2011). Environmental Dependence of the Kennicutt-Schmidt Relation in Galaxies. , 728(2):88.

Godunov, S. K. and Bohachevsky, I. (1959). Finite difference method for numerical computation of discontinuous solutions of the equations of fluid dynamics. *Matematičeskij sbornik*, 47(89)(3):271–306.

Grassi, T., Bovino, S., Schleicher, D. R. G., Prieto, J., Seifried, D., Simoncini, E., and Gianturco, F. A. (2014). KROME - a package to embed chemistry in astrophysical simulations. , 439(3):2386–2419.

Gressel, O. (2010). A mean-field approach to the propagation of field patterns in stratified magnetorotational turbulence. , 405(1):41–48.

Habe, A., Uchida, Y., Ikeuchi, S., and Pudritz, R. E. (1991). Triggering the Collapse of Self-Gravitating Clouds by Torsional Alfven Waves. , 43:703–718.

Heckman, T. M., Armus, L., and Miley, G. K. (1987). Evidence for Large-Scale Winds from Starburst Galaxies. II. an Optical Investigation of Powerful Far-Infrared Galaxies. , 93:276.

Heesen, V., Beck, R., Krause, M., and Dettmar, R. J. (2011). Cosmic rays and the magnetic field in the nearby starburst galaxy NGC 253 III. Helical magnetic fields in the nuclear outflow. , 535:A79.

Holmberg, E. (1941). On the Clustering Tendencies among the Nebulae. II. a Study of Encounters Between Laboratory Models of Stellar Systems by a New Integration Procedure. , 94:385.

Hopkins, P. F. (2015). A new class of accurate, mesh-free hydrodynamic simulation methods. , 450(1):53–110.

Hopkins, P. F. (2016). A constrained-gradient method to control divergence errors in numerical MHD. , 462:576–587.

Hopkins, P. F., Chan, T. K., Garrison-Kimmel, S., Ji, S., Su, K.-Y., Hummels, C. B., Kereš, D., Quataert, E., and Faucher-Giguère, C.-A. (2020). But what about...: cosmic rays, magnetic fields, conduction, and viscosity in galaxy formation. , 492(3):3465–3498.

Hopkins, P. F., Kereš, D., Oñorbe, J., Faucher-Giguère, C.-A., Quataert, E., Murray, N., and Bullock, J. S. (2014). Galaxies on FIRE (Feedback In Realistic Environments): stellar feedback explains cosmologically inefficient star formation. , 445(1):581–603.

Hummels, C. (2018). "Resolving" the Problems of the Circumgalactic Medium. In *American Astronomical Society Meeting Abstracts #231*, volume 231 of *American Astronomical Society Meeting Abstracts*, page 203.03.

Inutsuka, S.-I. (2002). Reformulation of Smoothed Particle Hydrodynamics with Riemann Solver. *Journal of Computational Physics*, 179(1):238–267.

Janhunen, P. (2000). A Positive Conservative Method for Magnetohydrodynamics Based on HLL and Roe Methods. *Journal of Computational Physics*, 160(2):649–661.

Jubelgas, M., Springel, V., and Dolag, K. (2004). Thermal conduction in cosmological SPH simulations. , 351(2):423–435.

Jun, B.-I., Norman, M. L., and Stone, J. M. (1995). A Numerical Study of Rayleigh-Taylor Instability in Magnetic Fluids. , 453:332.

Kannan, R., Marinacci, F., Vogelsberger, M., Sales, L. V., Torrey, P., Springel, V., and Hernquist, L. (2020). Simulating the interstellar medium of galaxies with radiative transfer, non-equilibrium thermochemistry, and dust. , 499(4):5732–5748.

Kannan, R., Vogelsberger, M., Marinacci, F., McKinnon, R., Pakmor, R., and Springel, V. (2019). AREPO-RT: radiation hydrodynamics on a moving mesh. , 485(1):117–149.

Katz, N. (1992). Dissipational Galaxy Formation. II. Effects of Star Formation. , 391:502.

Keller, B. W., Wadsley, J., Benincasa, S. M., and Couchman, H. M. P. (2014). A superbubble feedback model for galaxy simulations. , 442(4):3013–3025.

Kennicutt, Robert C., J. (1998). The Global Schmidt Law in Star-forming Galaxies. , 498(2):541–552.

Kimm, T. and Cen, R. (2014). Escape Fraction of Ionizing Photons during Reionization: Effects due to Supernova Feedback and Runaway OB Stars. , 788(2):121.

Klein, R. I. (1999). Star formation with 3-D adaptive mesh refinement: the collapse and fragmentation of molecular clouds. *Journal of Computational and Applied Mathematics*, 109(1):123–152.

Krause, F. and Raedler, K. H. (1980). *Mean-field magnetohydrodynamics and dynamo theory.*

Kravtsov, A. V., Klypin, A. A., and Khokhlov, A. M. (1997). Adaptive Refinement Tree: A New High-Resolution N-Body Code for Cosmological Simulations. , 111(1):73–94.

Kroupa, P. (2001). On the variation of the initial mass function. , 322(2):231–246.

Krumholz, M. R. and Gnedin, N. Y. (2011). A Comparison of Methods for Determining the Molecular Content of Model Galaxies. , 729(1):36.

Krumholz, M. R. and Matzner, C. D. (2009). The Dynamics of Radiation-pressure-dominated H II Regions. , 703(2):1352–1362.

Krumholz, M. R. and Thompson, T. A. (2013). Numerical simulations of radiatively driven dusty winds. , 434(3):2329–2346.

Kulsrud, R. M. (1999). A Critical Review of Galactic Dynamos. , 37:37–64.

Kulsrud, R. M. and Anderson, S. W. (1992). The Spectrum of Random Magnetic Fields in the Mean Field Dynamo Theory of the Galactic Magnetic Field. , 396:606.

Kulsrud, R. M., Cen, R., Ostriker, J. P., and Ryu, D. (1997). The Protogalactic Origin for Cosmic Magnetic Fields. , 480(2):481–491.

Lanson, N. and Vila, J. P. (2008). Renormalized meshfree schemes i: Consistency, stability, and hybrid methods for conservation laws. *SIAM J. Numerical Analysis*, 46:1912–1934.

Larson, R. B. (1974). Effects of supernovae on the early evolution of galaxies. , 169:229–246.

Lauberts, A. (1974). Encounters between Galaxies of Equal Size. , 33:231.

Leroy, A. K., Walter, F., Martini, P., Roussel, H., Sandstrom, K., Ott, J., Weiss, A., Bolatto, A. D., Schuster, K., and Dessauges-Zavadsky, M. (2015). The Multi-phase Cold Fountain in M82 Revealed by a Wide, Sensitive Map of the Molecular Interstellar Medium. , 814(2):83.

Lucy, L. B. (1977). A numerical approach to the testing of the fission hypothesis. , 82:1013–1024.

Mac Low, M.-M. (1999). The Energy Dissipation Rate of Supersonic, Magnetohydrodynamic Turbulence in Molecular Clouds. , 524(1):169–178.

Marri, S. and White, S. D. M. (2003). Smoothed particle hydrodynamics for galaxy-formation simulations: improved treatments of multiphase gas, of star formation and of supernovae feedback. , 345(2):561–574.

Martini, P., Leroy, A. K., Mangum, J. G., Bolatto, A., Keating, K. M., Sandstrom, K., and Walter, F. (2018). H I Kinematics along the Minor Axis of M82. , 856(1):61.

Martizzi, D., Faucher-Giguère, C.-A., and Quataert, E. (2015). Supernova feedback in an inhomogeneous interstellar medium. , 450(1):504–522.

McCourt, M., O'Leary, R. M., Madigan, A.-M., and Quataert, E. (2015). Magnetized gas clouds can survive acceleration by a hot wind. , 449:2–7.

McKee, C. F. and Ostriker, J. P. (1977). A theory of the interstellar medium: three components regulated by supernova explosions in an inhomogeneous substrate. , 218:148–169.

Meglicki, Z., Wickramasinghe, D., and Dewar, R. L. (1995). Gravitational collapse of a magnetized vortex: application to the Galactic Centre. , 272(4):717–729.

Menon, H., Wesolowski, L., Zheng, G., Jetley, P., Kale, L., Quinn, T., and Governato, F. (2015). Adaptive techniques for clustered N-body cosmological simulations. *Computational Astrophysics and Cosmology*, 2:1.

Mocz, P., Pakmor, R., Springel, V., Vogelsberger, M., Marinacci, F., and Hernquist, L. (2016). A moving mesh unstaggered constrained transport scheme for magnetohydrodynamics. , 463(1):477–488.

Moffatt, H. K. (1978). *Magnetic field generation in electrically conducting fluids.*

Monaghan, J. J. (1985). Particle methods for hydrodynamics. *Computer Physics Reports*, 3(2):71–124.

Monaghan, J. J. (1992). Smoothed particle hydrodynamics. , 30:543–574.

Monaghan, J. J. (1997). SPH and Riemann Solvers. *Journal of Computational Physics*, 136(2):298–307.

Monaghan, J. J. (2000). SPH without a Tensile Instability. *Journal of Computational Physics*, 159:290–311.

Monaghan, J. J. (2002). SPH compressible turbulence. , 335(3):843–852.

Monaghan, J. J. and Gingold, R. A. (1983). Shock Simulation by the Particle Method SPH. *Journal of Computational Physics*, 52(2):374–389.

Monaghan, J. J. and Lattanzio, J. C. (1985). A refined particle method for astrophysical problems. , 149(1):135–143.

Monaghan, J. J. and Price, D. J. (2001). Variational principles for relativistic smoothed particle hydrodynamics. , 328(2):381–392.

Morris, J. P. (1996). A study of the stability properties of smooth particle hydrodynamics. , 13(1):97–102.

Morris, J. P. and Monaghan, J. J. (1997). A Switch to Reduce SPH Viscosity. *Journal of Computational Physics*, 136(1):41–50.

Morrison, P. J. (1998). Hamiltonian description of the ideal fluid. *Reviews of Modern Physics*, 70(2):467–521.

Morrison, P. J. and Hazeltine, R. D. (1984). Hamiltonian formulation of reduced magnetohydrodynamics. *Physics of Fluids*, 27(4):886–897.

Müller, K., Fedosov, D. A., and Gompper, G. (2015). Smoothed dissipative particle dynamics with angular momentum conservation. *Journal of Computational Physics*, 281:301–315.

Murray, J., Wadsley, J., and Bond, J. R. (1996). MHD with SPH: application to the high redshift IGM. In *Bulletin of the American Astronomical Society*, volume 28, page 1413.

Navarro, J. F. and White, S. D. M. (1993). Simulations of Dissipative Galaxy Formation in Hierarchically Clustering Universes - Part One - Tests of the Code. , 265:271.

Navarro, J. F. and White, S. D. M. (1994). Simulations of dissipative galaxy formation in hierarchically clustering universes-2. Dynamics of the baryonic component in galactic haloes. , 267(2):401–412.

Oger, G., Marrone, S., Le Touzé, D., and de Leffe, M. (2016). SPH accuracy improvement through the combination of a quasi-Lagrangian shifting transport velocity and consistent ALE formalisms. *Journal of Computational Physics*, 313:76–98.

Opher, M., Bibi, F. A., Toth, G., Richardson, J. D., Izmodenov, V. V., and Gombosi, T. I. (2009). A strong, highly-tilted interstellar magnetic field near the Solar System. , 462(7276):1036–1038.

Ostriker, E. C., McKee, C. F., and Leroy, A. K. (2010). Regulation of Star Formation Rates in Multiphase Galactic Disks: A Thermal/Dynamical Equilibrium Model. , 721(2):975–994.

Pakmor, R., Bauer, A., and Springel, V. (2011). Magnetohydrodynamics on an unstructured moving grid. , 418:1392–1401.

Pakmor, R., Pfrommer, C., Simpson, C. M., and Springel, V. (2016a). Galactic Winds Driven by Isotropic and Anisotropic Cosmic-Ray Diffusion in Disk Galaxies. , 824:L30.

Pakmor, R. and Springel, V. (2013). Simulations of magnetic fields in isolated disc galaxies. , 432:176–193.

Pakmor, R., Springel, V., Bauer, A., Mocz, P., Munoz, D. J., Ohlmann, S. T., Schaal, K., and Zhu, C. (2016b). Improving the convergence properties of the moving-mesh code AREPO. , 455(1):1134–1143.

Parker, E. N. (1979). *Cosmical magnetic fields. Their origin and their activity.*

Pen, U.-L. (1998). A High-Resolution Adaptive Moving Mesh Hydrodynamic Algorithm. , 115(1):19–34.

Pencil Code Collaboration, Brandenburg, A., Johansen, A., Bourdin, P., Dobler, W., Lyra, W., Rheinhardt, M., Bingert, S., Haugen, N., Mee, A., Gent, F., Babkovskaia, N., Yang, C.-C., Heinemann, T., Dintrans, B., Mitra, D., Candelaresi, S., Warnecke, J., Käpylä, P., Schreiber, A., Chatterjee, P., Käpylä, M., Li, X.-Y., Krüger, J., Aarnes, J., Sarson, G., Oishi, J., Schober, J., Plasson, R., Sandin, C., Karchniwy, E., Rodrigues, L., Hubbard, A., Guerrero, G., Snodin, A., Losada, I., Pekkilä, J., and Qian, C. (2021). The Pencil Code, a modular MPI code for partial differential equations and particles: multipurpose and multiuser-maintained. *The Journal of Open Source Software*, 6(58):2807.

Petkova, M. and Springel, V. (2009). An implementation of radiative transfer in the cosmological simulation code GADGET. , 396(3):1383–1403.

Petkova, M. and Springel, V. (2011). A novel approach for accurate radiative transfer in cosmological hydrodynamic simulations. , 415(4):3731–3749.

Phillips, G. J. and Monaghan, J. J. (1985). A numerical method for three-dimensional simulations of collapsing, isothermal, magnetic gas clouds. , 216:883–895.

Planck Collaboration, Adam, R., Ade, P. A. R., Aghanim, N., Akrami, Y., Alves, M. I. R., Argüeso, F., Arnaud, M., Arroja, F., Ashdown, M., Aumont, J., Baccigalupi, C., Ballardini, M., Banday, A. J., Barreiro, R. B., Bartlett, J. G., Bartolo, N., Basak, S., Battaglia, P., Battaner, E., Battye, R., Benabed, K., Benoît, A., Benoit-Lévy, A., Bernard, J. P., Bersanelli, M., Bertincourt, B., Bielewicz, P., Bikmaev, I., Bock, J. J., Böhringer, H., Bonaldi, A., Bonavera, L., Bond, J. R., Borrill, J., Bouchet, F. R., Boulanger, F., Bucher, M., Burenin,

R., Burigana, C., Butler, R. C., Calabrese, E., Cardoso, J. F., Carvalho, P., Casaponsa, B., Castex, G., Catalano, A., Challinor, A., Chamballu, A., Chary, R. R., Chiang, H. C., Chluba, J., Chon, G., Christensen, P. R., Church, S., Clemens, M., Clements, D. L., Colombi, S., Colombo, L. P. L., Combet, C., Comis, B., Contreras, D., Couchot, F., Coulais, A., Crill, B. P., Cruz, M., Curto, A., Cuttaia, F., Danese, L., Davies, R. D., Davis, R. J., de Bernardis, P., de Rosa, A., de Zotti, G., Delabrouille, J., Delouis, J. M., Désert, F. X., Di Valentino, E., Dickinson, C., Diego, J. M., Dolag, K., Dole, H., Donzelli, S., Doré, O., Douspis, M., Ducout, A., Dunkley, J., Dupac, X., Efstathiou, G., Eisenhardt, P. R. M., Elsner, F., Enßlin, T. A., Eriksen, H. K., Falgarone, E., Fantaye, Y., Farhang, M., Feeney, S., Fergusson, J., Fernandez-Cobos, R., Feroz, F., Finelli, F., Florido, E., Forni, O., Frailis, M., Fraisse, A. A., Franceschet, C., Franceschi, E., Frejsel, A., Frolov, A., Galeotta, S., Galli, S., Ganga, K., Gauthier, C., Génova-Santos, R. T., Gerbino, M., Ghosh, T., Giard, M., Giraud-Héraud, Y., Giusarma, E., Gjerløw, E., González-Nuevo, J., Górski, K. M., Grainge, K. J. B., Gratton, S., Gregorio, A., Gruppuso, A., Gudmundsson, J. E., Hamann, J., Handley, W., Hansen, F. K., Hanson, D., Harrison, D. L., Heavens, A., Helou, G., Henrot-Versillé, S., Hernández-Monteagudo, C., Herranz, D., Hildebrandt, S. R., Hivon, E., Hobson, M., Holmes, W. A., Hornstrup, A., Hovest, W., Huang, Z., Huffenberger, K. M., Hurier, G., Ilić, S., Jaffe, A. H., Jaffe, T. R., Jin, T., Jones, W. C., Juvela, M., Karakci, A., Keihänen, E., Keskitalo, R., Khamitov, I., Kiiveri, K., Kim, J., Kisner, T. S., Kneissl, R., Knoche, J., Knox, L., Krachmalnicoff, N., Kunz, M., Kurki-Suonio, H., Lacasa, F., Lagache, G., Lähteenmäki, A., Lamarre, J. M., Langer, M., Lasenby, A., Lattanzi, M., Lawrence, C. R., Le Jeune, M., Leahy, J. P., Lellouch, E., Leonardi, R., León-Tavares, J., Lesgourgues, J., Levrier, F., Lewis, A., Liguori, M., Lilje, P. B., Lilley, M., Linden-Vørnle, M., Lindholm, V., Liu, H., López-Caniego, M., Lubin, P. M., Ma, Y. Z., Macías-Pérez, J. F., Maggio, G., Maino, D., Mak, D. S. Y., Mandolesi, N., Mangilli, A., Marchini, A., Marcos-Caballero, A., Marinucci, D., Maris, M., Marshall, D. J., Martin, P. G., Martinelli, M., Martínez-González, E., Masi, S., Matarrese, S., Mazzotta, P., McEwen, J. D., McGehee, P., Mei, S., Meinhold, P. R., Melchiorri, A., Melin, J. B., Mendes, L., Mennella, A., Migliaccio, M., Mikkelsen, K., Millea, M., Mitra, S., Miville-Deschênes, M. A., Molinari, D., Moneti, A., Montier, L., Moreno, R., Morgante, G., Mortlock, D., Moss, A., Mottet, S., Münchmeyer, M., Munshi, D., Murphy, J. A., Narimani, A., Naselsky, P., Nastasi, A., Nati, F., Natoli, P., Negrello, M., Netterfield, C. B., Nørgaard-Nielsen, H. U., Noviello, F., Novikov, D., Novikov, I., Olamaie, M., Oppermann, N., Orlando, E., Oxborrow, C. A., Paci, F., Pagano, L., Pajot, F., Paladini, R., Pandolfi, S., Paoletti, D., Partridge, B., Pasian, F., Patanchon, G., Pearson, T. J., Peel, M., Peiris, H. V., Pelkonen, V. M., Perdereau, O., Perotto, L., Perrott, Y. C., Perrotta, F., Pettorino, V., Piacentini, F., Piat, M., Pierpaoli, E., Pietrobon, D., Plaszczynski, S., Pogosyan, D., Pointecouteau, E., Polenta, G., Popa, L., Pratt, G. W., Prézeau, G., Prunet, S., Puget, J. L., Rachen, J. P., Racine, B., Reach, W. T., Rebolo, R., Reinecke, M., Remazeilles, M., Renault, C., Renzi, A., Ristorcelli, I., Rocha, G., Roman, M.,

Romelli, E., Rosset, C., Rossetti, M., Rotti, A., Roudier, G., Rouillé d'Orfeuil, B., Rowan-Robinson, M., Rubiño-Martín, J. A., Ruiz-Granados, B., Rumsey, C., Rusholme, B., Said, N., Salvatelli, V., Salvati, L., Sandri, M., Sanghera, H. S., Santos, D., Saunders, R. D. E., Sauvé, A., Savelainen, M., Savini, G., Schaefer, B. M., Schammel, M. P., Scott, D., Seiffert, M. D., Serra, P., Shellard, E. P. S., Shimwell, T. W., Shiraishi, M., Smith, K., Souradeep, T., Spencer, L. D., Spinelli, M., Stanford, S. A., Stern, D., Stolyarov, V., Stompor, R., Strong, A. W., Sudiwala, R., Sunyaev, R., Sutter, P., Sutton, D., Suur-Uski, A. S., Sygnet, J. F., Tauber, J. A., Tavagnacco, D., Terenzi, L., Texier, D., Toffolatti, L., Tomasi, M., Tornikoski, M., Tramonte, D., Tristram, M., Troja, A., Trombetti, T., Tucci, M., Tuovinen, J., Türler, M., Umana, G., Valenziano, L., Valiviita, J., Van Tent, F., Vassallo, T., Vibert, L., Vidal, M., Viel, M., Vielva, P., Villa, F., Wade, L. A., Walter, B., Wandelt, B. D., Watson, R., Wehus, I. K., Welikala, N., Weller, J., White, M., White, S. D. M., Wilkinson, A., Yvon, D., Zacchei, A., Zibin, J. P., and Zonca, A. (2016). Planck 2015 results. I. Overview of products and scientific results. , 594:A1.

Pouquet, A., Frisch, U., and Leorat, J. (1976). Strong MHD helical turbulence and the nonlinear dynamo effect. *Journal of Fluid Mechanics*, 77:321–354.

Powell, K. G., Roe, P. L., Linde, T. J., Gombosi, T. I., and De Zeeuw, D. L. (1999). A Solution-Adaptive Upwind Scheme for Ideal Magnetohydrodynamics. *Journal of Computational Physics*, 154(2):284–309.

Price, D. J. (2004). *Magnetic fields in Astrophysics.* PhD thesis, Institute of Astronomy, Madingley Rd, Cambridge, CB2 0HA, UK.

Price, D. J. (2008). Modelling discontinuities and Kelvin Helmholtz instabilities in SPH. *Journal of Computational Physics*, 227:10040–10057.

Price, D. J. (2010). Smoothed Particle Magnetohydrodynamics - IV. Using the vector potential. , 401:1475–1499.

Price, D. J. (2012). Smoothed particle hydrodynamics and magnetohydrodynamics. *Journal of Computational Physics*, 231:759–794.

Price, D. J. and Bate, M. R. (2008). The effect of magnetic fields on star cluster formation. , 385(4):1820–1834.

Price, D. J. and Monaghan, J. J. (2004a). Smoothed Particle Magnetohydrodynamics - I. Algorithm and tests in one dimension. , 348:123–138.

Price, D. J. and Monaghan, J. J. (2004b). Smoothed Particle Magnetohydrodynamics - II. Variational principles and variable smoothing-length terms. , 348:139–152.

Price, D. J. and Monaghan, J. J. (2005). Smoothed Particle Magnetohydrodynamics - III. Multidimensional tests and the $\nabla.B = 0 constraint.$, $364 : 384--406.$

Price, D. J. and Monaghan, J. J. (2007). An energy-conserving formalism for adaptive gravitational force softening in smoothed particle hydrodynamics and N-body codes. , 374(4):1347–1358.

Price, D. J. and Rosswog, S. (2006). Producing Ultrastrong Magnetic Fields in Neutron Star Mergers. *Science*, 312(5774):719–722.

Price, D. J., Tricco, T. S., and Bate, M. R. (2012). Collimated jets from the first core. , 423(1):L45–L49.

Price, D. J., Wurster, J., Tricco, T. S., Nixon, C., Toupin, S., Pettitt, A., Chan, C., Mentiplay, D., Laibe, G., Glover, S., Dobbs, C., Nealon, R., Liptai, D., Worpel, H., Bonnerot, C., Dipierro, G., Ballabio, G., Ragusa, E., Federrath, C., Iaconi, R., Reichardt, T., Forgan, D., Hutchison, M., Constantino, T., Ayliffe, B., Hirsh, K., and Lodato, G. (2018). Phantom: A Smoothed Particle Hydrodynamics and Magnetohydrodynamics Code for Astrophysics. , 35:e031.

Puri, K. and Ramachandran, P. (2014). Approximate Riemann solvers for the Godunov SPH (GSPH). *Journal of Computational Physics*, 270:432–458.

Quinn, T., Katz, N., Stadel, J., and Lake, G. (1997). Time stepping N-body simulations. *arXiv e-prints*, pages astro–ph/9710043.

Rädler, K. H. (1969). Zur Elektrodynamik in turbulenten, Coriolis-Kräften unterworfenen leitenden Medien. *Monatsber. Deutsch. Akad Wissenschaftliche Berlin*, 11:194–201.

Read, J. I. and Hayfield, T. (2012). SPHS: smoothed particle hydrodynamics with a higher order dissipation switch. , 422(4):3037–3055.

Richings, A. J. and Schaye, J. (2016). The effects of metallicity, UV radiation and non-equilibrium chemistry in high-resolution simulations of galaxies. , 458(1):270–292.

Richtmyer, R. D. and Morton, K. W. (1967). *Difference methods for initial-value problems.*

Rieder, M. and Teyssier, R. (2017). A small-scale dynamo in feedback-dominated galaxies - II. The saturation phase and the final magnetic configuration. , 471(3):2674–2686.

Riols, A. and Latter, H. (2019). Gravitoturbulent dynamos in astrophysical discs. , 482(3):3989–4008.

Robishaw, T., Quataert, E., and Heiles, C. (2008). Extragalactic Zeeman Detections in OH Megamasers. , 680(2):981–998.

Rogachevskii, I. and Kleeorin, N. (2003). Electromotive force and large-scale magnetic dynamo in a turbulent flow with a mean shear. , 68(3):036301.

Rogers, H. and Pittard, J. M. (2013). Feedback from winds and supernovae in massive stellar clusters - I. Hydrodynamics. , 431(2):1337–1351.

Rosswog, S. (2015). Boosting the accuracy of SPH techniques: Newtonian and special-relativistic tests. , 448:3628–3664.

Rosswog, S. (2020). The Lagrangian hydrodynamics code MAGMA2. , 498(3):4230–4255.

Ruzmaikin, A. A., Sokolov, D. D., and Shukurov, A. M. (1988). *Magnetic Fields of Galaxies*, volume 133.

Saitoh, T. R. and Makino, J. (2009). A Necessary Condition for Individual Time Steps in SPH Simulations. , 697:L99–L102.

Salmon, R. (1988). Hamiltonian fluid mechanics. *Annual Review of Fluid Mechanics*, 20:225–256.

Scannapieco, C., Tissera, P. B., White, S. D. M., and Springel, V. (2006). Feedback and metal enrichment in cosmological SPH simulations - II. A multiphase model with supernova energy feedback. , 371(3):1125–1139.

Schekochihin, A. A., Cowley, S. C., Taylor, S. F., Maron, J. L., and McWilliams, J. C. (2004). Simulations of the Small-Scale Turbulent Dynamo. , 612(1):276–307.

Schmidt, M. (1959). The Rate of Star Formation. , 129:243.

Schoenberg, I. J. (1946). Contributions to the problem of approximation of equidistant data by analytic functions: Part a.—on the problem of smoothing or graduation. a first class of analytic approximation formulae. *Quarterly of Applied Mathematics*, 4(1):45–99.

Sedov, L. I. (1959). *Similarity and Dimensional Methods in Mechanics.*

Shapiro, P. R., Martel, H., Villumsen, J. V., and Owen, J. M. (1996). Adaptive Smoothed Particle Hydrodynamics, with Application to Cosmology: Methodology. , 103:269.

Shen, S., Wadsley, J., and Stinson, G. (2010). The enrichment of the intergalactic medium with adiabatic feedback - I. Metal cooling and metal diffusion. , 407:1581–1596.

Sijacki, D., Springel, V., Di Matteo, T., and Hernquist, L. (2007). A unified model for AGN feedback in cosmological simulations of structure formation. , 380(3):877–900.

Spitzer, L. (1962). *Physics of Fully Ionized Gases.*

Springel, V. (2010). E pur si muove: Galilean-invariant cosmological hydrodynamical simulations on a moving mesh. , 401(2):791–851.

Springel, V., Di Matteo, T., and Hernquist, L. (2005). Modelling feedback from stars and black holes in galaxy mergers. , 361(3):776–794.

Springel, V. and Hernquist, L. (2002). Cosmological smoothed particle hydrodynamics simulations: the entropy equation. , 333:649–664.

Springel, V. and Hernquist, L. (2003). Cosmological smoothed particle hydrodynamics simulations: a hybrid multiphase model for star formation. , 339(2):289–311.

Stadel, J. G. (2001). *Cosmological N-body simulations and their analysis.* PhD thesis, University of Washington, United States.

Stasyszyn, F. A. and Elstner, D. (2015). A vector potential implementation for smoothed particle magnetohydrodynamics. *Journal of Computational Physics*, 282:148–156.

Stinson, G., Seth, A., Katz, N., Wadsley, J., Governato, F., and Quinn, T. (2006). Star formation and feedback in smoothed particle hydrodynamic simulations - I. Isolated galaxies. , 373(3):1074–1090.

Stone, J. M., Gardiner, T. A., Teuben, P., Hawley, J. F., and Simon, J. B. (2008). Athena: A New Code for Astrophysical MHD. , 178:137–177.

Sun, M. and Takayama, K. (2003). Vorticity production in shock diffraction. *Journal of Fluid Mechanics*, 478:237–256.

Sutherland, R. S. and Dopita, M. A. (1993). Cooling Functions for Low-Density Astrophysical Plasmas. , 88:253.

Taylor, A. R., Stil, J. M., and Sunstrum, C. (2009). A Rotation Measure Image of the Sky. , 702(2):1230–1236.

Taylor, G. (1950). The Formation of a Blast Wave by a Very Intense Explosion. I. Theoretical Discussion. *Proceedings of the Royal Society of London Series A*, 201(1065):159–174.

Teyssier, R. (2002). Cosmological hydrodynamics with adaptive mesh refinement. A new high resolution code called RAMSES. , 385:337–364.

Teyssier, R., Pontzen, A., Dubois, Y., and Read, J. I. (2013). Cusp-core transformations in dwarf galaxies: observational predictions. , 429(4):3068–3078.

Thacker, R. J. and Couchman, H. M. P. (2000). Implementing Feedback in Simulations of Galaxy Formation: A Survey of Methods. , 545(2):728–752.

Thomas, P. A. and Couchman, H. M. P. (1992). Simulating the formation of a cluster of galaxies. , 257(1):11–31.

Thomas, T. and Pfrommer, C. (2019). Cosmic-ray hydrodynamics: Alfvén-wave regulated transport of cosmic rays. , 485(3):2977–3008.

Toomre, A. and Toomre, J. (1972). Galactic Bridges and Tails. , 178:623–666.

Trebitsch, M., Blaizot, J., Rosdahl, J., Devriendt, J., and Slyz, A. (2017). Fluctuating feedback-regulated escape fraction of ionizing radiation in low-mass, high-redshift galaxies. , 470(1):224–239.

Tricco, T. S. and Price, D. J. (2012). Constrained hyperbolic divergence cleaning for smoothed particle magnetohydrodynamics. *Journal of Computational Physics*, 231:7214–7236.

Tricco, T. S. and Price, D. J. (2013). A switch to reduce resistivity in smoothed particle magnetohydrodynamics. , 436:2810–2817.

Tricco, T. S., Price, D. J., and Bate, M. R. (2016). Constrained hyperbolic divergence cleaning in smoothed particle magnetohydrodynamics with variable cleaning speeds. *Journal of Computational Physics*, 322:326–344.

Turk, M. J., Oishi, J. S., Abel, T., and Bryan, G. L. (2012). Magnetic Fields in Population III Star Formation. , 745(2):154.

Uhlig, M., Pfrommer, C., Sharma, M., Nath, B. B., Enßlin, T. A., and Springel, V. (2012). Galactic winds driven by cosmic ray streaming. , 423:2374–2396.

Vaĭnshteĭn, S. I. and Zel'dovich, Y. B. (1972). REVIEWS OF TOPICAL PROBLEMS: Origin of Magnetic Fields in Astrophysics (Turbulent "Dynamo" Mechanisms). *Soviet Physics Uspekhi*, 15(2):159–172.

Vázquez-Semadeni, E., Kim, J., Shadmehri, M., and Ballesteros-Paredes, J. (2005). The Lifetimes and Evolution of Molecular Cloud Cores. , 618(1):344–359.

Vila, J. P. (1999). On particle weighted methods and sph. *Mathematical Models Methods in Applied Sciences - M3AS*, 09:161–209.

Vogelsberger, M., Genel, S., Sijacki, D., Torrey, P., Springel, V., and Hernquist, L. (2013). A model for cosmological simulations of galaxy formation physics. , 436(4):3031–3067.

Vogelsberger, M., Genel, S., Springel, V., Torrey, P., Sijacki, D., Xu, D., Snyder, G., Bird, S., Nelson, D., and Hernquist, L. (2014). Properties of galaxies reproduced by a hydrodynamic simulation. , 509(7499):177–182.

Von Neumann, J. and Richtmyer, R. D. (1950). A Method for the Numerical Calculation of Hydrodynamic Shocks. *Journal of Applied Physics*, 21(3):232–237.

Wadsley, J. W., Keller, B. W., and Quinn, T. R. (2017). Gasoline2: a modern smoothed particle hydrodynamics code. , 471:2357–2369.

Wadsley, J. W., Stadel, J., and Quinn, T. (2004). Gasoline: a flexible, parallel implementation of TreeSPH. , 9(2):137–158.

Wadsley, J. W., Veeravalli, G., and Couchman, H. M. P. (2008). On the treatment of entropy mixing in numerical cosmology. , 387:427–438.

Weaver, R., McCray, R., Castor, J., Shapiro, P., and Moore, R. (1977). Interstellar bubbles. II. Structure and evolution. , 218:377–395.

Weinberger, R., Springel, V., Hernquist, L., Pillepich, A., Marinacci, F., Pakmor, R., Nelson, D., Genel, S., Vogelsberger, M., Naiman, J., and Torrey, P. (2017). Simulating galaxy formation with black hole driven thermal and kinetic feedback. , 465(3):3291–3308.

Wendland, H. (1995). Piecewise polynomial, positive definite and compactly supported radial functions of minimal degree. *Advances in Computational Mathematics*, 4(1):389–396.

Wiersma, R. P. C., Schaye, J., and Smith, B. D. (2009). The effect of photoionization on the cooling rates of enriched, astrophysical plasmas. , 393(1):99–107.

Wilson, J. R. (1985). Supernovae and Post-Collapse Behavior. In *Numerical Astrophysics*, page 422.

Wurster, J., Bate, M. R., Price, D. J., and Tricco, T. S. (2017). Investigating prescriptions for artificial resistivity in smoothed particle magnetohydrodynamics. *arXiv e-prints*.

Yokoi, N. (2013). Cross helicity and related dynamo. *Geophysical and Astrophysical Fluid Dynamics*, 107(1-2):114–184.

Yoshizawa, A. and Yokoi, N. (1993). Turbulent Magnetohydrodynamic Dynamo for Accretion Disks Using the Cross-Helicity Effect. , 407:540.

Zeldovich, Y. B. (1983). *Magnetic fields in astrophysics.*

Zeldovich, Y. B., Ruzmaikin, A. A., and Sokoloff, D. D. (1990). *The almighty chance.*

Papers

Paper I

Smoothed particle magnetohydrodynamics with the geometric density average force expression

Wissing, R., Shen, S.

Astronomy & Astrophysics

Smoothed particle magnetohydrodynamics with the geometric density average force expression

Robert Wissing and Sijing Shen

Institute of Theoretical Astrophysics, University of Oslo, Postboks 1029, 0315 Oslo, Norway
e-mail: robertwi@astro.uio.no, sijing.shen@astro.uio.no

ABSTRACT

We present a novel method of magnetohydrodynamics (MHD) within the smoothed particle hydrodynamics scheme (SPMHD) using the geometric density average force expression. Geometric density average within smoothed particle hydrodynamics (GDSPH) has recently been shown to reduce the leading order errors and greatly improve the accuracy near density discontinuities, eliminating surface tension effects. Here, we extend the study to investigate how SPMHD benefits from this method. We implement ideal MHD in the Gasoline2 and Changa codes with both GDSPH and traditional smoothed particle hydrodynamics (TSPH) schemes. A constrained hyperbolic divergence cleaning scheme was employed to control the divergence error and a switch for artificial resistivity with minimized dissipation was also used. We tested the codes with a large suite of MHD tests and showed that in all problems, the results are comparable or improved over previous SPMHD implementations. While both GDSPH and TSPH perform well with relatively smooth or highly supersonic flows, GDSPH shows significant improvements in the presence of strong discontinuities and large dynamic scales. In particular, when applied to the astrophysical problem of the collapse of a magnetized cloud, GDSPH realistically captures the development of a magnetic tower and jet launching in the weak-field regime, while exhibiting fast convergence with resolution, whereas TSPH failed to do so. Our new method shows qualitatively similar results to those of the meshless finite mass/volume schemes within the Gizmo code, while remaining computationally less expensive.

Key words. methods: numerical – ISM: magnetic fields – magnetohydrodynamics (MHD)

1. Introduction

Magnetic fields are important in a wide array of different astrophysical systems. In star formation, they govern the dynamics at several stages during collapse. They are critical in the launching of jets from a broad range of sources. They also play a major role in the transport of angular momentum in ionized accretion disks due to the magnetorotational instability. Magnetic fields have been largely neglected in galaxy formation simulations, mostly due to the technical difficulties associated with them. It is only recently that researchers have begun to apply them (Wang & Abel 2009; Kotarba et al. 2011; Pakmor & Springel 2013; Rieder & Teyssier 2016; Butsky et al. 2017; Su et al. 2017; Pakmor et al. 2017; Steinwandel et al. 2019). The importance of magnetic fields in galaxy formation is clear from observations of the Milky Way and nearby galaxies, which reveal that the magnetic energy is in equipartition with the thermal and turbulent energies (Boulares & Cox 1990; Beck et al. 1996). This means that they are likely to have a large dynamical effect on the evolution of the galaxy, adding significant non-thermal pressure that can suppress star-formation (Pakmor & Springel 2013). In addition, it has been shown that magnetic fields have a strong impact on fluid instabilities (Jun et al. 1995; McCourt et al. 2015), which may affect how gas in the intergalactic medium (IGM) accretes onto galaxies and how gas in galactic outflows leaves (or cycles back to) galaxies. The strength and structure of magnetic fields in galaxies also determine the transport of cosmic rays (CRs), which has recently emerged as a promising candidate for driving galactic outflows because they have long cooling time scales (Uhlig et al. 2012; Booth et al. 2013; Pakmor et al. 2016; Butsky & Quinn 2018).

Apart from the improvements in the general method, advances have been made in the magnetohydrodynamics extension for smoothed particle hydrodynamics (SPMHD). The modern foundation of SPMHD comes largely from the work of Price & Monaghan (2004) which was built on the earlier work of Phillips & Monaghan (1985). The two main technical difficulties to overcome for SPMHD, are the handling of divergence errors and the choice of an artificial resistivity term to capture shocks and discontinuities in the magnetic field.

Artificial dissipation terms are required to smooth out discontinuities in any fluid quantity in all numerical hydrodynamics methods. In SPH, this is most commonly achieved via explicit artificial dissipation. To avoid excessive dissipation away from shocks and discontinuities, switches have been developed to limit where the artificial dissipation terms are active. For magnetic fields, newly developed artificial resistivity switches (Price et al. 2018; Tricco & Price 2013) have significantly reduced the amount of dissipation and improved the method in the weak field regime.

Unphysical divergence errors (magnetic monopoles) can arise from the discretization and numerical integration of the MHD equations. Divergence errors in SPMHD for magnetic-dominated scenarios need to be handled with care, as they can produce a negative force between particles which leads to the tensile instability (Monaghan 2000). As such, the force produced from the divergence needs to be partly removed in the strong field regime for the method to remain stable, this breaks momentum and energy conservation in proportion to the

divergence error. It is therefore crucial to try to keep the divergence error as close to zero as possible. While grid codes have access to the constrained transport scheme (Evans & Hawley 1988), which ensures a divergence free field up to machine precision, it cannot easily be implemented within meshless methods, due to the absence of regular spatial grid surfaces. Generation of divergence free fields in SPMHD have been explored in detail, however, all of them suffer from problems. Generation of magnetic fields from Euler potentials ($B = \nabla\alpha \times \nabla\beta$) cannot wind the magnetic field and thereby not produce a dynamo (Brandenburg 2010). Price (2010) showed that vector potential implementations ($B = \nabla \times A$) are plagued with numerical instabilities. However, Stasyszyn & Elstner (2015) recently showed that with additional diffusion, smoothing of the magnetic field, and enforcing the Coulomb gauge ($\nabla \cdot A = 0$), the vector potential formalism could remain stable for a handful of test cases. Additional testing would be required to determine the robustness of the method. The most popular method to deal with divergence error in meshless methods, is to evolve the magnetic field via the induction equation and then to "clean" the divergence away. In general, this is done by introducing a separate scalar field which couples to the induction equation such that it produces a damped wave equation for the divergence error, so the divergence is spread outward like a damped wave. The method was first developed in Dedner et al. (2002) and was improved by Tricco & Price (2012), who introduced a constrained version of the method. This ascertains that the magnetic energy is either conserved or dissipated. This was updated in Tricco et al. (2016) to correctly allow variable cleaning speed, which further improved the method.

These new improvements in artificial dissipation and divergence error controlling have significantly increased the accuracy and convergence of the SPMHD method. There have also been implementations of non-ideal MHD in SPMHD proposed recently (Tsukamoto et al. 2013, 2015a,b; Wurster et al. 2014, 2016; Price et al. 2018), which include Ohmic resistivity, ambipolar diffusion, and the Hall effect.

As mentioned previously, the numerical surface tension seen in traditional SPH (TSPH) can be solved by using a different gradient operator (GDSPH; Wadsley et al. 2017). This substantially improves the accuracy of pressure forces across density jumps and provides a more physical form for the internal energy equation, where it represents a direct discretization of $\frac{du}{dt} = -\frac{P}{\rho} \nabla \cdot v$ from the Euler equations while retaining all the usual conservation properties. In Wadsley et al. (2017), the authors show that GDSPH, together with an explicit turbulent diffusion term on thermal energy, yields excellent results in fluid mixing test cases, such as the Kelvin-Helmholtz instability and the blob test.

In this paper, we investigate how SPMHD benefits from the use of GDSPH. As such, we have implemented MHD within the GASOLINE2 (Wadsley et al. 2017) and CHANGA (Menon et al. 2015) codes, which both utilize the GDSPH formalism. GASOLINE2 is a highly parallel, state-of-the-art code for cosmological structure formation simulations which includes all the features of modern SPH methods. CHANGA includes all the same SPH methods as GASOLINE2, but it is written in an inherently parallel language CHARM++ (Kale & Krishnan 1993) which enables more efficient parallelization. The major difference between the two codes lies in the gravity solver, which is different in CHANGA because it uses an oct-tree, rather than an arbitrary binary KD-tree as in GASOLINE2.

This paper is organized as follows. In Sect. 2, we go through the SPMHD theory and show how the equations can be formu-

lated using the GDSPH approach. In Sect. 3, we test our implementation on a large suite of standard test cases and in Sect. 4 we apply the code to an astrophysical application: the collapse of a magnetized cloud. In Sect. 5, we discuss our results and present some concluding remarks.

2. Theory

In this section, we show how the MHD equations can be formulated in a conservative way within the GDSPH framework. The development is similar to the findings in previous work (Price & Monaghan 2004; Price 2012; Tricco et al. 2016; Price et al. 2018) and we direct the reader to these papers for additional background details.

2.1. MHD theory

The two main equations which are relevant for ideal MHD are the Lorentz force law and the induction equation. Assuming that the fluid is an ideal conductor ($E = 0$), the Lorentz force law can be written as:

$$\frac{d\mathbf{v}}{dt} = \frac{1}{\mu_0\rho}(\nabla \times \mathbf{B}) \times \mathbf{B} = \frac{1}{\mu_0\rho}\left(-\frac{1}{2}\nabla\mathbf{B}^2 + (\mathbf{B} \cdot \nabla)\mathbf{B}\right), \quad (1)$$

where $\mathbf{v}$, ρ, $\mathbf{B}$ and μ_0 is the velocity, density, magnetic field and vacuum permeability, respectively. The first term acts like an isotropic magnetic pressure term, while the other term acts as an attractive term along magnetic field lines (tension). Going forward, we define code units such that $\mu_0 = 1$. The conservative form of SPMHD is attained by using the stress tensor to describe the momentum equation. Assuming that the magnetic field is divergence free, the MHD stress tensor can be written as:

$$S^{ij} = -\delta^{ij}\left(P + \frac{\mathbf{B}^2}{2}\right) + B^i B^j, \quad (2)$$

where P is the thermal pressure and δ^{ij} is the Kronecker delta. The momentum equation can then be written as:

$$\frac{d\mathbf{v}}{dt} = \frac{\nabla \cdot \mathbf{S}}{\rho} = -\frac{1}{\rho}\nabla\left(P + \frac{\mathbf{B}^2}{2}\right) + \frac{1}{\rho}\left[(\mathbf{B} \cdot \nabla)\mathbf{B} + \mathbf{B}(\nabla \cdot \mathbf{B})\right]. \quad (3)$$

There is an extra tension force term which would normally have no effect due to the assumption $\nabla \cdot \mathbf{B} = 0$. However, as mentioned in the introduction, this constraint is usually not fully upheld in numerical codes. To avoid numerical instability within SPH, this term needs to be negated when the magnetic pressure exceeds the thermal pressure.

The change in the magnetic field is obtained from the induction equation:

$$\frac{d\mathbf{B}}{dt} = \nabla \times (\mathbf{v} \times \mathbf{B}) = (\mathbf{B} \cdot \nabla)\mathbf{v} - \mathbf{B}(\nabla \cdot \mathbf{v}), \quad (4)$$

where the first term affects the magnetic field through shearing motion, while the second will increase the magnetic field when undergoing compression. A combined effect of the two terms is to enhance the field due to compression perpendicular to the field direction (for example, $B \propto \rho^{2/3}$ for spherical collapse). Compression in the direction of the field has no effect.

2.2. SPH discretization

Derivatives within SPH can be discretized in a number of ways, and a general formulation is given by Price (2012):

$$\frac{\nabla A}{\rho} = \frac{\phi}{\rho}\left[\frac{A}{\phi^2}\nabla\phi + \nabla\left(\frac{A}{\phi}\right)\right] \approx \sum_b \frac{m_b}{\rho_a\rho_b}\left(A_a\frac{\phi_b}{\phi_a} + A_b\frac{\phi_a}{\phi_b}\right)\nabla_a\overline{W}_{ab},$$
$$(5)$$

$$\frac{\nabla A}{\rho} = \frac{1}{\phi\rho}\left[\nabla(\phi A) - A\nabla\phi\right] \approx \sum_b \frac{m_b}{\rho_a\rho_b}\frac{\phi_b}{\phi_a}\left(A_b - A_a\right)\nabla_a\overline{W}_{ab}, \quad (6)$$

where ϕ can be any arbitrary, differentiable scalar quantity. The geometric density average force formulation (GDSPH) corresponds to using $\phi = 1$ while traditional SPH corresponds to using $\phi = \rho$. GDSPH therefore gives the following symmetric and anti-symmetric gradient operators:

$$\frac{\nabla A}{\rho} \approx \frac{1}{\rho}(A\nabla 1 + \nabla A) = \sum_b \frac{m_b}{\rho_a\rho_b}\left(A_a + A_b\right)\nabla_a\overline{W}_{ab}, \quad (7)$$

$$\frac{\nabla A}{\rho} \approx \frac{1}{\rho}(\nabla A - A\nabla 1) = \sum_b \frac{m_b}{\rho_a\rho_b}\left(A_b - A_a\right)\nabla_a\overline{W}_{ab}. \quad (8)$$

Here, $\nabla_a\overline{W}_{ab}$ is a symmetric gradient of the smoothing kernel:

$$\nabla_a\overline{W}_{ab} = \frac{1}{2}\left[f_a\nabla_a W(r_{ab}, h_a) + f_b\nabla_b W(r_{ab}, h_b)\right], \quad (9)$$

where W is the smoothing kernel, h_a is the smoothing length of particle a, and $r_{ab} = |\mathbf{r_a} - \mathbf{r_b}|$ is the distance between particle a and b. Here, f_a is a correction term introduced in Wadsley et al. (2017) to ensure that internal energy and density evolve consistently, such that entropy is tightly conserved. To attain a conservative formalism for SPH, the symmetric gradient operator is applied to the equations of motion and the anti-symmetric gradient operator is applied to the internal energy equation[1]. As a consequence, zeroth order errors arise in the equations of motions which will depend on the local particle distribution[2]. A generalized error term for the zeroth order errors is given by:

$$\mathbf{E}_0 = \sum_b \frac{m_b}{\rho_b}\left(\Phi_{ab} + \Phi_{ab}^{-1}\right)\nabla_a\overline{W}_{ab}, \quad (10)$$

where $\Phi = \frac{\phi_a}{\phi_b}$ depend on the chosen scalar quantity ϕ in Eqs. (5) and (6). As shown by Read et al. (2010), in TSPH $\Phi_{ab} = \frac{\rho_a}{\rho_b}$, while in GDSPH $\Phi_{ab} = 1$. It is then evident that these errors are more severe at density gradients in TSPH than in GDSPH (where they are explicitly independent of the density gradient). A similar improvement can be seen for the linear errors.

Applying the symmetric gradient operator to the momentum equation (Eq. (3)) and the anti-symmetric gradient operator to the induction equation (Eq. (4)) gives:

$$\frac{dv_a^i}{dt} = \sum_b \frac{m_b}{\rho_a\rho_b}\left(S_a^{ij} + S_b^{ij}\right)\nabla_a^j\overline{W}_{ab} + f_{\text{div}B,a}^i, \quad (11)$$

$$\frac{d\mathbf{B}_a}{dt} = \sum_b \frac{m_b}{\rho_b}\left[\mathbf{B}_a(\mathbf{v}_{ab}\cdot\nabla_a\overline{W}_{ab}) - \mathbf{v}_{ab}(\mathbf{B}_a\cdot\nabla_a\overline{W}_{ab})\right], \quad (12)$$

---

[1] This can clearly be seen when deriving the SPH equations from the least action principle (Price 2012).
[2] This can be seen as an inherent re-meshing procedure, where the particles try to arrange themselves to maximize the sum of the particle volumes and reach a minimum energy state.

where $\mathbf{v}_{ab} = \mathbf{v}_a - \mathbf{v}_b$. The stability term $f_{\text{div}B,a}^i$ is added to avoid the tensile instability. This can occur due to divergence errors when the magnetic pressure exceeds the gas pressure ($\frac{B^2}{2} > P$) (Phillips & Monaghan 1985). The stability term is defined as:

$$f_{\text{div}B,a}^i = -\hat{B}_a^i \sum_b \frac{m_b}{\rho_a\rho_b}\left(\mathbf{B}_a + \mathbf{B}_b\right)\cdot\nabla_a\overline{W}_{ab}. \quad (13)$$

This basically removes the divergence term $\left(-\frac{\mathbf{B}}{\rho}\nabla\cdot\mathbf{B}\right)$ from Eq. (3) (Børve et al. 2001; Price 2012). Removing a term from the conservative momentum equation effectively breaks momentum conservation. However, the error introduced will be proportional to the divergence. To minimize its effect in the weak field regime, we use the scheme from Børve et al. (2004) with a factor of $\hat{B}_a^i = B_a^i$ for $\beta < 1$ as advocated by Tricco & Price (2012):

$$\hat{B}_a^i = \begin{cases} B_a^i & \beta < 1 \\ B_a^i(2-\beta) & 1 < \beta < 2 \\ 0 & \text{otherwise,} \end{cases} \quad (14)$$

where $\beta = \frac{2P}{B^2}$ is the plasma beta.

2.3. Treating discontinuities

When fluid quantities become discontinuous, they are no longer differentiable, which is problematic as differentiability is assumed by the SPMHD equations. Artificial resistivity is required to smooth out discontinuities in the magnetic field which can occur both along and orthogonal to the fluid motion and in both compression and rarefaction. The artificial resistivity can be represented as an isotropic diffusion:

$$\frac{d\mathbf{B}}{dt_{\text{diss}}} = \eta\nabla^2\mathbf{B}, \quad (15)$$

where η is a resistivity parameter. We use the Brookshaw method (Brookshaw 1985), which estimates the second derivative by using the first derivative kernel and the difference in the field divided by the particle spacing. Following the GDSPH discretization, we get:

$$\frac{d\mathbf{B}_a}{dt_{\text{diss}}} = \sum_b \frac{m_b}{\rho_b}\left(\frac{\eta_a + \eta_b}{|\mathbf{r}_{ab}|}\right)\mathbf{B}_{ab}\left(\hat{\mathbf{r}}_{ab}\cdot\nabla_a\overline{W}_{ab}\right), \quad (16)$$

where $\mathbf{B}_{ab} = \mathbf{B}_a - \mathbf{B}_b$ and $\hat{\mathbf{r}}_{ab} = \mathbf{r}_{ab}/|\mathbf{r}_{ab}|$. To conserve energy, the change in the internal energy becomes:

$$\frac{du_a}{dt_{\text{diss}}} = -\frac{1}{2}\sum_b \frac{m_b}{\rho_a\rho_b}\left(\frac{\eta_a + \eta_b}{|\mathbf{r}_{ab}|}\right)\mathbf{B}_{ab}^2\left(\hat{\mathbf{r}}_{ab}\cdot\nabla_a\overline{W}_{ab}\right). \quad (17)$$

To reduce dissipation away from shocks, we can introduce a varying and resolution dependent resistivity parameter:

$$\eta = \frac{1}{2}\alpha_B v_{\text{sig},B}|\mathbf{r}_{ab}|, \quad (18)$$

where α_B is a dimensionless coefficient and $v_{\text{sig},B}$ is the signal speed. Proper choice of α_B and $v_{\text{sig},B}$ makes the artificial resistivity second order accurate away from shocks ($\eta \propto h^2$). We choose to implement the resistivity from PHANTOM (Price et al. 2018) where the signal speed is activated following:

$$v_{\text{sig},B} = |\mathbf{v}_{ab}\times\hat{\mathbf{r}}_{ab}|. \quad (19)$$

The dimensionless coefficient α_B is set to a constant. In PHANTOM, this coefficient is set to $\alpha_B = 1$, however, from our tests we find that $\alpha_B = 0.5$ provides sufficient dissipation. This switch was shown to be the least dissipative compared to previous switches, while still capturing the correct magnetic features (Wurster et al. 2017).

2.4. Divergence cleaning

As we discussed in the introduction, divergence errors are generated by the discretization and integration of the MHD equations. Apart from creating an unphysical magnetic field, it also forces us to introduce a stability term (Eq. (13)), which breaks momentum conservation in the strong field regime. This makes it crucial to reduce the divergence errors as much as possible. The best way found in SPMHD is by introducing a divergence cleaning scheme (Tricco & Price 2012). In general, this is done by introducing a separate scalar field which couples to the induction equation, such that it produces a damped wave equation for the divergence error. That is, the divergence is spread outward like a damped wave. In our implementation, we employ the constrained hyperbolic divergence cleaning from Tricco et al. (2016), an improved version of the method presented by Dedner et al. (2002). The constrained hyperbolic divergence cleaning ensures that magnetic energy is either conserved or dissipated. In this method, a scalar field ψ is coupled to the induction equation as follows:

$$\left(\frac{\mathrm{d}\mathbf{B}}{\mathrm{d}t}\right)_{\psi} = -\nabla\psi. \tag{20}$$

The scalar field ψ evolves according to:

$$\frac{\mathrm{d}}{\mathrm{d}t}\left(\frac{\psi}{c_h}\right) = -c_h\nabla\cdot\mathbf{B} - \frac{1}{\tau}\frac{\psi}{c_h} - \frac{1}{2}\psi(\nabla\cdot\mathbf{v}). \tag{21}$$

where τ is the decay time and c_h is the wave cleaning speed:

$$c_h = f_{\text{clean}}v_{\text{mhd}}, \tag{22}$$

$$v_{\text{mhd}} = \sqrt{c_s^2 + v_A^2}, \tag{23}$$

$$v_A = \sqrt{\frac{B^2}{\rho}}. \tag{24}$$

Here, c_s is the speed of sound, v_A the Alfvén velocity, and f_{clean} is an overcleaning factor. The f_{clean} factor can be used to increase the amount of divergence cleaning, however, this will reduce the timestep[3] according to $\Delta t \rightarrow \Delta t/f_{\text{clean}}$. Combining the cleaning equation with the induction equation produces a damped wave equation for the divergence (this form assumes constant c_h and τ):

$$\frac{\partial^2(\nabla\cdot\mathbf{B})}{\partial t^2} - c_h^2\nabla^2(\nabla\cdot\mathbf{B}) + \frac{1}{\tau}\frac{\partial(\nabla\cdot\mathbf{B})}{\partial t} = 0, \tag{25}$$

which effectively shows that the divergence is spread out and damped. The decay time is given by:

$$\tau_a = \frac{h_a}{c_{h,a}\sigma_c}. \tag{26}$$

Here, σ_c is a dimensional constant, and was shown to be optimal with a value of 1 in 3D. Following Tricco & Price (2012), $\nabla\psi$ is discretized using the symmetric gradient operator (Eq. (7)) and $\nabla\cdot B$ using the anti-symmetric gradient operator (Eq. (8)). Within the GDSPH discretization, Eqs. (20) and (21) become:

$$\left(\frac{\mathrm{d}\mathbf{B}}{\mathrm{d}t}\right)_{\psi,a} = -\sum_b \frac{m_b}{\rho_b}(\psi_a + \psi_b)\nabla_a\overline{W}_{ab}, \tag{27}$$

$$\frac{\mathrm{d}}{\mathrm{d}t}\left(\frac{\psi}{c_h}\right)_a = c_h^a\sum_b\frac{m_b}{\rho_b}\mathbf{B}_{ab}\cdot\nabla_a\overline{W}_{ab} + \frac{\psi_a}{2c_h^a}\sum_b\frac{m_b}{\rho_b}\mathbf{v}_{ab}\cdot\nabla_a\overline{W}_{ab} - \frac{\psi_a}{c_h^a\tau_a}. \tag{28}$$

---

[3] This is a significant increase in computational cost, so it is in general not recommended to use an f_{clean} value above 1. But it does allows for a simple way to reduce the divergence error, if that is required.

The divergence cleaning dissipates energy from the magnetic field. However, this term is so small compared to the other dissipation terms that it is not worth accounting for. We could, of course, add this energy to heat and conserve energy, however, as discussed by Tricco & Price (2012), the removal of magnetic energy and subsequent generation of thermal energy would be non-local due to the coupling of parabolic diffusion with hyperbolic transport. Due to this, we simply removed the energy.

To ensure that simulations are not affected by the divergence error, we monitor the normalized divergence error:

$$\epsilon_{\text{div}B} = \frac{h|\nabla\cdot\mathbf{B}|}{|B|}. \tag{29}$$

The mean of this quantity should preferably remain below 10^{-2}. However, regions of locally high divergence error can occur, so careful inspection of the divergence error is required to ensure the quality of simulations.

2.5. Shock capturing

To correctly capture shocks in MHD, we need to modify the artificial viscosity term in the momentum equation (see Wadsley et al. 2017 for a detailed description of the artificial viscosity term in GASOLINE2). For MHD the sound speed is replaced by the fast magnetosonic speed (Eq. (23)). We also modify the gradient-based shock detector introduced in GASOLINE2, which determines the direction of the shock from the pressure gradient. For the MHD, we must include the Lorentz force to correctly determine the direction of the shock. A more general way to determine the direction of the shock is to estimate the acceleration of the MHD forces without the dissipation terms before the actual force calculation:

$$\hat{\mathbf{n}} = -\left(\frac{\frac{\mathrm{d}\mathbf{v}}{\mathrm{d}t}}{\left|\frac{\mathrm{d}v}{\mathrm{d}t}\right|}\right)_{\text{no diss}}. \tag{30}$$

This addition improves the behavior of shock detection in convergent flows for MHD. In GASOLINE2, the diffusion of fluid scalar variables such as thermal energy, metals and so forth are modeled using subgrid turbulent mixing (Wadsley et al. 2008; Shen et al. 2010). However, we found that in strong shocks like the MHD blastwave, the thermal dissipation is not enough and can lead to incorrect velocity profiles. As such, we add a thermal shock dissipation similar to Eqs. (4.5) with (4.8) in Monaghan (1992), however, we use $\overline{c}_{ab} = 0$ and with a larger constant (fitted parameter from the GASOLINE2 code):

$$\frac{\mathrm{d}u}{\mathrm{d}t}_{\text{shock}} = -\sum_b\frac{m_b}{\overline{\rho}_{ab}}d_{\text{shock}}u_{ab}\frac{\left(\hat{\mathbf{r}}_{ab}\cdot\nabla_a\overline{W}_{ab}\right)}{|r_{ab}|}, \tag{31}$$

$$d_{\text{shock}} = 16\overline{h}_{ab}|\mu_{ab}|, \tag{32}$$

$$\mu_{ab} = \begin{cases} \frac{\overline{h}_{ab}(\mathbf{v}_{ab}\cdot\mathbf{r}_{ab})}{r_{ab}^2+0.01\overline{h}_{ab}^2} & \text{for } \mathbf{v}_{ab}\cdot\mathbf{r}_{ab} < 0, \\ 0 & \text{otherwise.} \end{cases} \tag{33}$$

3. Test problems

In this section, we present the results from our test cases. All the simulations were run with the MHD version of GASOLINE2. To remain consistent and show the production quality of the method, we decided to run all the tests in 3D and with a default set of code parameters (described below). While glass-like initial conditions should always be used to correctly capture the

natural state of 3D SPH simulations, for the sake of comparison, we elected to follow the initial setups from other authors, which often use lattice-based initial conditions. Test cases that are originally 1D or 2D are made 3D by extending the non-active dimensions by a set number of particles. By default, GASOLINE2 sets the smoothing length based on a fixed number of neighbours. However, we found that in very uniform and precise tests, as in the circularized Alfvén wave test, this approach generates small force errors that generate perturbations in the traveling wave. As such, we made the smoothing length directly proportional to the density and simultaneously determined the density and smoothing length using an iterative summation (Springel & Hernquist 2002). We note, however, that in all other tests, no visible effect was seen. We ran simulations with both TSPH and GDSPH, and the only difference between them is the choice of ϕ in Eqs. (5) and (6); all the other numerical schemes and parameters remain the same. In many of these tests, we compare the results to the state-of-the-art SPMHD code PHANTOM (Price et al. 2018), and to the PSPH and the new meshless finite mass/volume (MFM/MFV) method of the GIZMO code (Hopkins 2015). The MFM/MFV method utilizes a Lagrangian Godunov type method that employs more complex gradient operators and calculates fluxes from Riemann solvers.

Default set of code parameters. For the smoothing kernel, we used a Wendland C4 kernel (Wendland 1995) with 200 neighbours[4]. Our artificial viscosity (AV) followed the prescription given in Wadsley et al. (2017), the AV parameters were set to $\alpha_{\max} = 4$, $\alpha_{\min} = 0$, $\tau = 0.1\frac{h}{c}$ and $\beta = 2$. The artificial resistivity (AR) followed from the method outlined in Sect. 2.2, and the AR parameter was set to $\alpha_B = 0.5$. The thermal diffusion followed the turbulent mixing model described in Wadsley et al. (2008) and Shen et al. (2010), with the turbulent diffusion coefficient set to $C = 0.03$.

3.1. Circularized polarized Alfvén wave

The circularized polarized Alfvén wave test was introduced by Tóth (2000) to serve as an analytical solution to the ideal MHD equations. Due to the waves being circularized, the gradient in magnetic pressure is zero and the wave should remain the same after each period. This proves to be a useful test for gauging the dissipation and dispersion of the MHD implementation. This test is sensitive to the tensile instability (Price & Monaghan 2005), so it also serves as a good test to see if the stability term (Eq. (13)) properly stabilizes the solution. The setup follows Gardiner & Stone (2008) and Price et al. (2018), in which the waves are traveling at an angle of $\theta = 30°$ with respect to the x axis, within a periodic box of length $L = (l, l/2, l/2)$, where $l = 3$. The transverse velocities and magnetic fields are circularized:
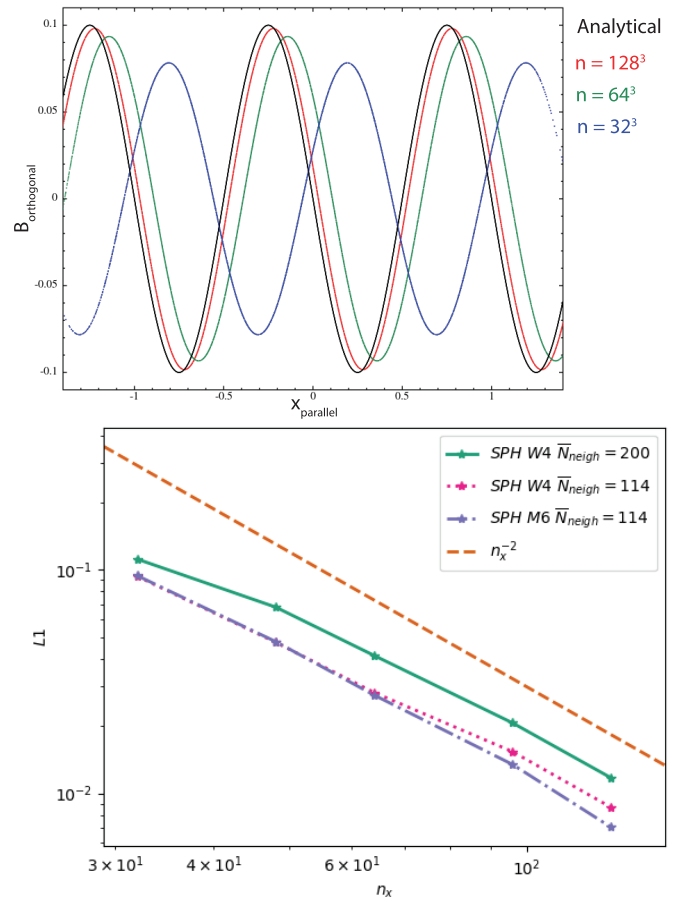
$$B_{\perp,1} = v_{\perp,1} = 0.1 \sin(2\pi x_\parallel/\lambda),$$
$$B_{\perp,2} = v_{\perp,2} = 0.1 \cos(2\pi x_\parallel/\lambda),$$

while the parallel components are set to:

$$v_\parallel = 0 \quad B_\parallel = 1.$$

Here, $x_\parallel$ is the direction of propagation, and $\lambda = 1$ is the wavelength. An adiabatic EOS ($\gamma = 5/3$) is used with uniform pressure $P = 0.1$ and density $\rho = 1.0$. The particles are

---

[4] Choice of kernel and neighbour number discussed at the end of Sect. 3.1.

Fig. 1. Results of the 3D circularly polarized Alfvén wave test. *Top panel:* transverse component of the magnetic field in the direction of propagation after five periods. The analytical/initial solution is plotted in black, and the simulation results with resolution $[n_x, n_y, n_z] = [128, 74, 78]$ in red, $[n_x, n_y, n_z] = [64, 36, 39]$ in green, and $[n_x, n_y, n_z] = [32, 18, 18]$ in blue. Both of these are with Wendland C4 kernel with 200 neighbours. *Bottom panel:* convergence study for the Alfvén wave test using different kernels and neighbour numbers. Shows how the L_1 error scales with resolution (particles along the x-axis). The code default (Wendland C4 kernel with 200 neighbours) is shown in green, Wendland C4 kernel with 114 neighbours are shown in magenta, Quintic kernel with 114 neighbours are shown in blue and the dashed brown line shows the curve for second order convergence. Convergence towards the analytical solution for all kernels are close to second order. When the smoothing length becomes comparable to half the wave length of the Alfvén wave, the MHD gradients becomes more ill defined which causes the slower convergence speed for the Wendland kernel ($\overline{N}_{\mathrm{neigh}} = 200$) at low resolution.

set up on a close-packed lattice and the simulation is run for five periods ($t = 5$). As we have uniform density, there are no differences between GDSPH and TSPH in this test case. We plot the transverse component of the magnetic field in the direction of propagation, showing the results of different resolutions $[n_x, n_y, n_z] = [128, 74, 78]$, $[64, 36, 39]$, and $[32, 18, 18]$ in the upper panel of Fig. 1. From the results, we can see that both the phase and amplitude converge towards the analytical solution as we increase resolution. For a more qualitative look at the convergence, we perform a convergence study for this test using different smoothing kernels and neighbour numbers. In the lower panel of Fig. 1, we show the L1 error norm for the transverse magnetic field at five different resolutions ($n_x = 32, 48, 64, 96, 128$), and as we can see all the kernels

exhibits second-order convergence. The major outliner is at low resolution for the Wendland C4 kernel with more neighbours. This is caused by the larger smoothing length, which at low resolution becomes comparable to half the wave length of the Alfvén wave. This makes the MHD gradients more ill defined which causes force errors that shows itself predominately as a phase shift in the Alfvén wave as time goes by. The amplitude of the wave is only weakly affected by this. From the bottom panel in Fig. 1 we can also see that the Wendland kernel has slightly lower convergence speed then the quintic kernel at higher resolution. Despite this result, we chose to go with the Wendland kernel C4 with 200 neighbors as our code default for the forthcoming tests. This is for several reasons. First, the quintic kernel is susceptible to the pairing instability whereas the Wendland kernels are not (Dehnen & Aly 2012). In addition, the Wendland kernels tend to make the particle distribution remain well ordered in dynamical conditions, which improves the overall accuracy of the method (Rosswog 2015). While the computational cost increases roughly linearly with increased neighbour number, gravity is usually the more dominant cost in astrophysical simulations, which means that the increase in cost is usually not significant. In the end, the choice of kernel and neighbour number will depend on the application at hand. However, for simulations involving subsonic flows, a high neighbour number has been shown to be preferred (as showcased by the Gresho-Chan vortex test in Dehnen & Aly 2012 and Rosswog 2015).

3.2. Advection loop

The advecting current loop test was introduced by Gardiner & Stone (2005, 2008), in which a weak magnetic loop is advected by a constant velocity field. As the ratio between the thermal pressure and magnetic pressure is massive ($\beta \approx 10^6$), the magnetic field is dynamically unimportant and should simply be advected along the velocity field. This proves to be one of the more difficult tests for grid-based code due to intrinsic dissipation during advection. We followed the setup from Gardiner & Stone (2008), Hopkins & Raives (2016) and Price et al. (2018), and initialized a 3D thin periodic box with length $L = (2, 1, 2\frac{\sqrt{6}}{n_x})$, velocity $v = (2, 1, \frac{0.1}{\sqrt{5}})$ and pressure $P = 1$. The magnetic field inside the loop was determined from the potential $A_z = A_0(R_0 - r)$, where $A_0 = 10^{-3}$, $R_0 = 0.3$, and $r^2 = x^2 + y^2$. The face-centered magnetic fields are then $\boldsymbol{B_0} = \nabla \times A_z = \frac{A_0}{r}(y, -x, 0)$ inside the loop and zero everywhere else. We set up two initial conditions, one with a uniform density $\rho = 1$ with resolution $[n_x, n_y, n_z] = [128, 74, 12]$ and another with a density gradient ($\Delta \equiv \frac{\rho_{in}}{\rho_{out}} = 2$) between the inner loop ($\rho_{in} = 2$) and outer medium ($\rho_{out} = 1$), with resolution $[n_x, n_y, n_z] = [256, 148, 12]$. The particles are set up on a close-packed lattice and the loop is advected for twenty periods with all the default dissipation and divergence cleaning terms turned on. The results of the test can be seen in Figs 2 and 3.

From the figures, we can see that in the case with uniform density the field loop is closely conserved, resulting in only 0.3% reduction in magnetic energy after twenty periods. This is a significant improvement from the advection loop presented in Price et al. (2018), which starts to degrade after five periods. We have also tested this case using a quintic spline kernel, a smaller number of neighbours and an $\alpha_B = 1$ for the AR similar to Price et al. (2018), while a little more degradation can be seen, the difference in magnetic energy is still small after twenty periods (1% instead of a 0.3% decrease in magnetic energy). Without any dissipation and divergence cleaning the advection loop
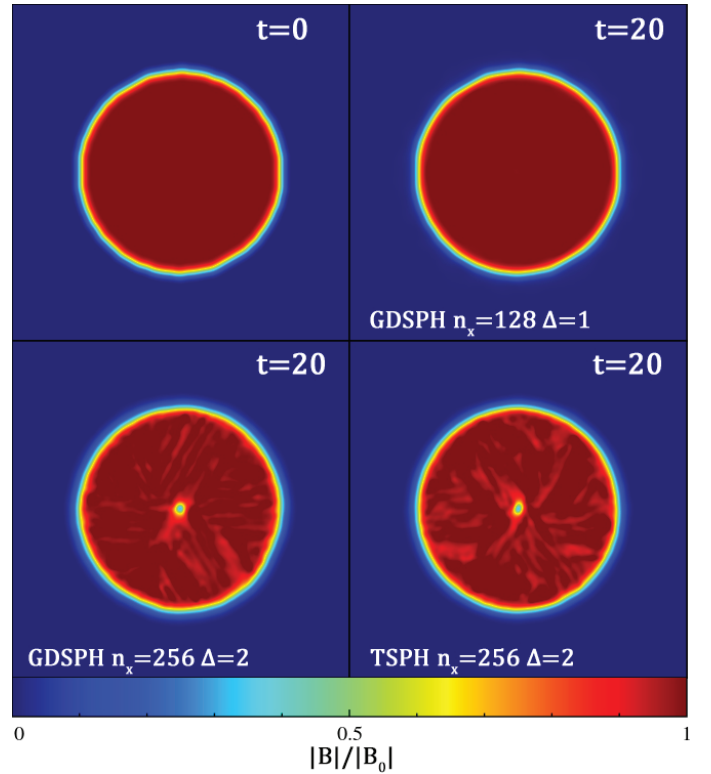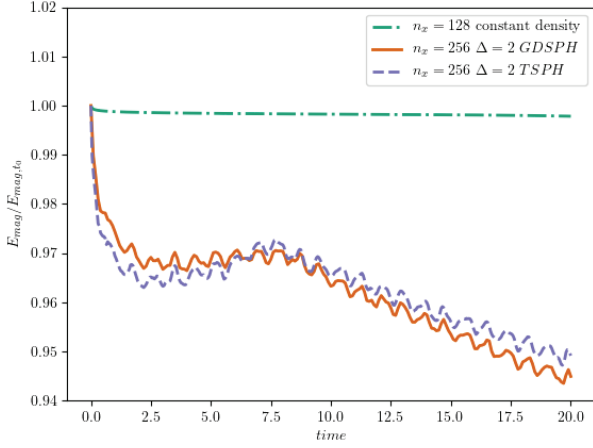

Fig. 2. Results from the advection loop test in 3D, showing a rendering of $|\boldsymbol{B}|$ in units of the initial value $|\boldsymbol{B_0}|$. *Top left panel*: initial setup (same rendering for $n_x = 128$ and $n_x = 256$, and *top right*: uniform density case for GDSPH with resolution $n_x = 128$ after twenty crossings $t = 20$. We can see that the current loop is conserved almost perfectly even with all the dissipation terms turned on. This shows an improvement comparing to the SPMHD results in PHANTOM, where dissipation is seen after five periods (Fig. 35 in Price et al. 2018), which plots the current density. The bottom two panels show the cases with a density gradient $\Delta \equiv \frac{\rho_{in}}{\rho_{out}} = 2$ between the inner loop and outer medium and with resolution of $n_x = 256$, after twenty crossings $t = 20$. The bottom left panel shows the GDSPH case and the bottom right show the TSPH case ($n_x = 256$). Both show similar dissipation of the magnetic field to the results from the MFM/MFV method in GIZMO (Hopkins & Raives 2016).

with uniform density can be sustained for thousands of periods, as shown in Rosswog & Price (2007). This shows a significant advantage for Lagrangian codes compared to Eulerian codes, which suffer from resolution-dependent advection errors when the configuration is not aligned to the grid. In the case of the density gradient, we can see that there is now a faster dissipation of the magnetic energy. The sudden reduction in magnetic energy is largely due to the reordering of the initial particle lattice near the density contrast. Comparing to Hopkins & Raives (2016), we can see that we have a similar reduction in magnetic energy as in the results from the MFM/MFV method at $t = 20$. There is a tiny difference ($<1\%$) between GDSPH and TSPH, however, this owes itself to the initial reordering, after that we can see that the rate of change in the two discretizations are practically the same. The averaged normalized divergence error, $\langle \epsilon_{divB} \rangle$, is around 10^{-2} for both the $\Delta = 1$ case and $\Delta = 2$ case.

3.3. Brio-Wu shocktube

The Brio-Wu shocktube (Brio & Wu 1988) is an MHD extension to the classic Sod shocktube test (the hydro setup is the same). It

Fig. 3. Results from the advection loop test in 3D, showing the time evolution of the magnetic field energy in units of the initial value. After $t = 20$ our uniform case has dissipated about 0.3%, while the cases with the density gradient $\Delta = 2$ have dropped around 5%, which is similar to the dissipation displayed by the MFM/MFV method in Hopkins & Raives (2016). There is a tiny difference between GDSPH and TSPH, but this owes itself to differences in the initial reordering.

tests how well the implementation can handle different MHD shocks, rarefactions, and contact discontinuities. We followed the setup from Hopkins & Raives (2016) and Price et al. (2018) and initialized a 3D thin periodic box, with a total region of $[n_x, n_y, n_z] = [1024, 24, 24]$ and an active region of $[256, 24, 24]$ particles on the left side $x_L = [-2, 0]$, and a total region of $[n_x, n_y, n_z] = [512, 12, 12]$ and an active region of $[128, 12, 12]$ on the right side $x_R = [0, 2]$. The left state was set to:

$$(\rho_L, P_L, v_x, v_y, v_z, B_x, B_y, B_z) = (1, 1, 0, 0, 0, 0.75, 1, 0),$$

and the right state was set to:

$$(\rho_R, P_R, v_x, v_y, v_z, B_x, B_y, B_z) = (0.125, 0.1, 0, 0, 0, 0.75, -1, 0).$$

The adiabatic index is set to $\gamma = 2$. We ran the simulation up to $t = 0.2$ and the results can be seen in Fig. 4. The GDSPH and TSPH results are shown with black and red dots, respectively, and the analytical solution is shown in blue lines. Our results are very similar to those from the PHANTOM code default case with the same resolution (Fig. 30 in Price et al. 2018). However, there is noticeable wall heating in the internal energy u in our test, due to the conservative thermal dissipation term used in this work. A more aggressive thermal dissipation can be added to smooth out the wall heating, which improves the results in the density, thermal and pressure profiles. However, this often leads to over dissipation in cases involving gravitational fields and is thus not a preferable choice. Divergence errors are kept low with a maximum value of $\sim 10^{-3}$ at the shock, and B_x remains close to constant, which also indicates excellent divergence control. Varying artificial resistivity parameter α_B from $\alpha_B = 0.5$ to $\alpha_B = 1$ only shows minimal differences, and as we can see from the results, $\alpha_B = 0.5$ is sufficient to capture the magnetic field structure. We also note that using constant artificial viscosity (AV) parameters decreases post-shock oscillations and improves the results in the velocity profile. From Fig. 4, we can see that there is very little difference between GDSPH and TSPH in this test.

3.4. Orszag-Tang vortex

The Orszag-Tang vortex test was introduced by Orszag & Tang (1979) and is a standard test of MHD schemes, as it involves

the development of super-sonic turbulence and the interaction of the different MHD shocks. We set up a 3D thin periodic box with $L = (1.0, 1.0, \frac{2\sqrt{6}}{n_x})$ at varying resolutions ($[n_x, n_y, n_z] = [128, 148, 12]$, $[256, 296, 12]$ and $[512, 590, 12]$). The test consists out of a velocity vortex:

$$[v_x, v_y, v_z] = v_0[-\sin(2\pi(y - y_{min})), \sin(2\pi(x - x_{min})), 0],$$

and a doubly periodic magnetic field:

$$[B_x, B_y, B_z] = B_0[-\sin(2\pi(y - y_{min})), \sin(4\pi(x - x_{min})), 0],$$

where $v_0 = 1$, $B_0 = 1/\sqrt{4\pi}$, $x_{min} = -0.5$ and $y_{min} = -0.5$. Setting the initial plasma beta $\beta_0 = 10/3$, the initial Mach number $M = v_0/c_s = 1$ and the adiabatic index $\gamma = 5/3$, we get the initial pressure $P_0 = B_0^2 \beta_0/2 = 0.133$ and density $\rho_0 = \gamma P_0 M_0 = 0.221$. We show the results of the different resolution runs in Fig. 5 after $t = 0.5$ (top row) and $t = 1$ (bottom row). The test was run with both GDSPH and TSPH, however, we found only very small differences between them, which is why we only show the result from GDSPH. This can additionally be seen in Fig. 6, which show the time evolution of the magnetic energy in all of our test cases. From the result at $t = 0.5$ we can see that we reproduce the shock structure well and capture the trapped dense filament in the centre of the domain for all resolutions. With increasing resolution, the shock structure and filament become more defined. At $t = 1$, a more turbulent flow has developed. Our simulations capture most of the key features and compare well with previous works (for example, Fig. 32 in Price et al. 2018). However, it appears that our method is unable to develop the central magnetic island, a feature that is supposed to form when the current sheet in the center becomes unstable and reconnects due to the tearing mode instability. This is the case for most previous implementations of SPMHD, however, in Wurster et al. (2017) the authors argue that with a less dissipative artificial resistivity switch the magnetic island can be reproduced, and this motivate them to use the signal speed $v_{sig,B}$ given in Eq. (19).

We use the same switch but the problem remains. Nevertheless, if we compare our evolution of the magnetic energy (the magenta curve in Fig. 6) to theirs (the grey curve) we can see that our simulations are actually less dissipative, likely because we use a smaller resistivity parameter $\alpha_B = 0.5$. Increasing α_B to 1 leads to more dissipation and brings the final energy closer to the Phantom run. It is thus likely that the development of the magnetic island also depends on the other dissipation terms such as AV and artificial conductivity. The mean normalized divergence error in the simulations are of the order $\langle \epsilon_{divB} \rangle = 10^{-3.5}$–$10^{-2.5}$, decreasing with higher resolution.

3.5. MHD rotor

The MHD rotor test was introduced by Balsara & Spicer (1999), which tests the propagation of Alfvén waves generated by a magnetized rotor. We followed the setup from Tóth (2000) and Price et al. (2018), and initialized a 3D thin periodic box of $L = (1.0, 1.0, \frac{2\sqrt{6}}{n_x})$ at two resolutions, $[n_x, n_y, n_z] = [128, 148, 12]$ and $[256, 296, 12]$. A rotating dense cylinder ($\rho = 10$) was initiated with cylindrical radius $R = 0.1$, within a surrounding medium ($\rho = 1$). The cylinder was put into rotation with an initial velocity of

$$v = \frac{v_0}{r_{cyl}}[-(y - y_0), (x - x_0), 0] \quad r_{cyl} < R,$$
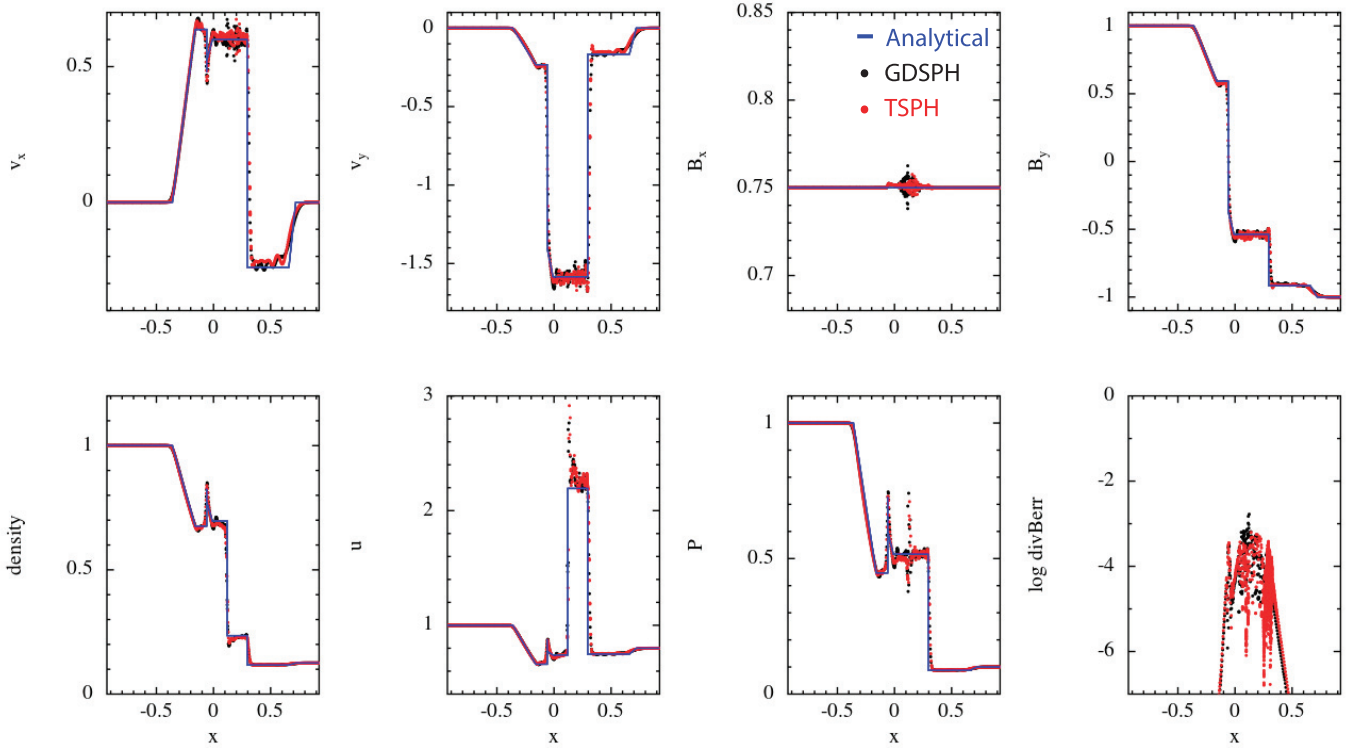
Fig. 4. Results from the Brio-Wu shocktube in 3D, with an initial left state $(\rho_L, P_L, v_x, v_y, v_z, B_x, B_y, B_z) = (1, 1, 0, 0, 0, 0.75, 1, 0)$ and right state $(\rho_R, P_R, v_x, v_y, v_z, B_x, B_y, B_z) = (0.125, 0.1, 0, 0, 0, 0.75, -1, 0)$. The figure shows the active region of the shock after $t = 0.2$, which contains about $n_x \approx 300-400$ particles across the x-direction. The blue line shows the reference solution and the black dots show the result from the GDSPH simulation, while red dots show the result from the TSPH simulation. There are minimal differences between the GDSPH and TSPH result.
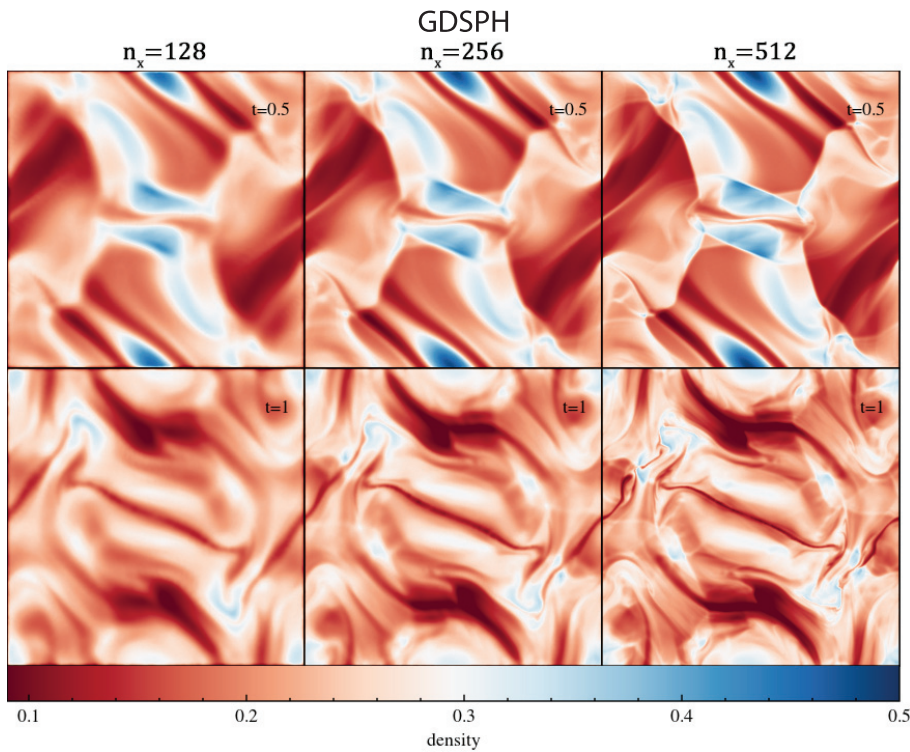
Fig. 5. Results from the Orszag-Tang vortex in 3D done with GDSPH, which shows rendered density slices ($z = 0$) at $t = 0.5$ (top) and $t = 1$ (bottom) for varying resolution $[n_x, n_y, n_z] = [128, 148, 12], [256, 296, 12]$ and $[512, 590, 12]$ (low to high from left to right). The simulations capture well most of the key features for all tested resolutions. With increasing resolution the flows are more defined and show increased complexity. There are no significant differences between GDSPH and TSPH in this case.

where $r_{cyl} = \sqrt{x^2 + y^2}$ and $v_0 = 2$. The initial pressure was set to $P = 1$, with an adiabatic index of $\gamma = 1.4$. The initial magnetic field was set to $B = [5/\sqrt{4}, 0, 0]$. The particles were set up on a closed packed lattice and the simulation were run until $t = 0.15$.

The density contrast was unsmoothed, which means that there will be some noise at the boundary initially, due to particle reordering. The results of the simulations done with GDSPH and TSPH can be seen in Fig. 7, which shows 30 contours and the

86
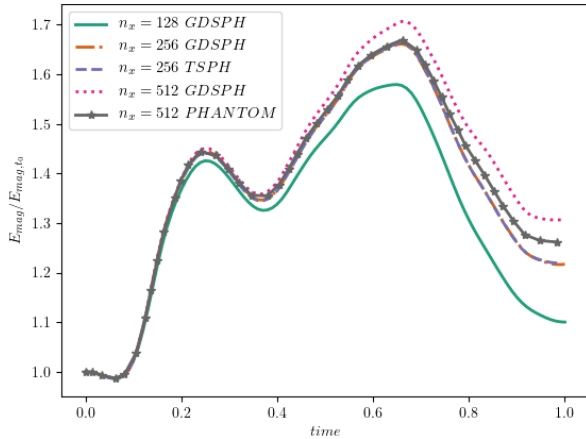
Fig. 6. Evolution of the total magnetic energy in units of the initial value for the 3D Orszag-Tang vortex test. We plot the result from three different tested resolutions $[n_x, n_y, n_z]$ = $[128, 148, 12], [256, 296, 12], [512, 590, 12]$ done in GDSPH. We also include a TSPH case with $n_x = 256$ and the $n_x = 512$ curve from Wurster et al. (2017) for comparison sake. We can see that there are no visible difference between the TSPH (purple curve) and GDSPH (brown curve) cases. From the figure, it is also clear that the GDSPH case of $n_x = 512$ (magenta curve) is less dissipative than the simulation from Wurster et al. (2017) (grey curve). Significant differences between resolutions can be seen to occur at later times during the evolution.

rendering of the magnetic pressure, with limits taken to be the same as in Tóth (2000) and Price et al. (2018). From the results, we can see that the difference between GDSPH and TSPH is generally small. However, we do find that in GDSPH there are notable increases in magnetic pressure at the pressure maxima compared to TSPH, which also seen in Hopkins & Raives (2016) when the authors compared MFM with SPH (their Fig. 15). In general, the key features of the test are captured by both methods. The mean normalized divergence errors in the simulations are of the order $\langle \epsilon_{\mathrm{div}B} \rangle = 10^{-4}$–$10^{-3}$.

3.6. Magnetized blastwave

The magnetized blastwave was introduced by Balsara & Spicer (1999) and Londrillo & Del Zanna (2000), in which a central over-pressurized region expands preferentially along the magnetic fields lines. We followed the setup from Stone et al. (2008) and Price et al. (2018), and initialized a 3D periodic box of $L = [1.0, 1.0, 1.0]$ with uniform density at a resolution of $N = 256^3$. An inner region of radius $R = 0.125$ was over-pressurized ($P_{\mathrm{in}} = 100$) to 100 times the outer pressure, which was set to $P_{\mathrm{out}} = 1$. The adiabatic index of the gas is set to $\gamma = 5/3$[5]. The initial magnetic field was set to:

$$B = [10/\sqrt{2}, 0, 10/\sqrt{2}].$$

This sets the initial plasma beta to $\beta_{\mathrm{in}} = 2$ in the inner region and $\beta_{\mathrm{out}} = 0.02$ in the outer region. The simulation was run for $t = 0.02$ and the result can be seen in Fig. 8. The rendering and limits in the figure were set to the same as the results presented in Tóth (2000) and Price et al. (2018), so that they can be directly compared. We can see that our results agree well with the previous authors, capturing the inner and outer structure of the blast well. There are minimal differences between the GDSPH and

---

[5] This is different from the choice in Price et al. (2018) ($\gamma = 1.4$), however, $\gamma = 5/3$ is more representative of gas in astrophysical applications
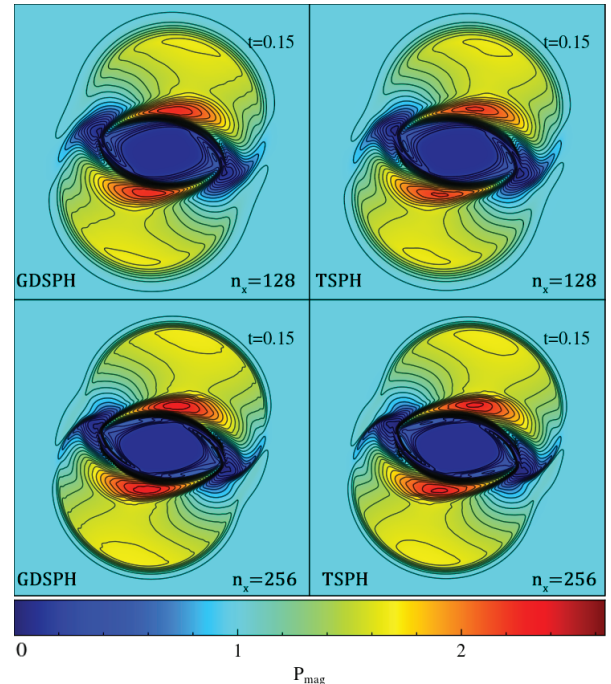

Fig. 7. Result from the magnetic rotor in 3D, which shows rendered magnetic pressure slices ($z = 0$) at $t = 0.15$, for varying resolution $[n_x, n_y, n_z]$ = $[128, 148, 12]$ and $[256, 296, 12]$ and for both GDSPH and TSPH. The plot also shows 30 contours with limits taken to be the same as Tóth (2000) and Price et al. (2018) ($P_{\mathrm{mag}} = [0, 2.642]$) for a more direct comparison. We can see that GDSPH develops a larger and broader magnetic pressure peak compared to TSPH.

TSPH results. The mean normalized divergence error in the simulations are of the order $\langle \epsilon_{\mathrm{div}B} \rangle = 10^{-5}$.

3.7. Kelvin-Helmholtz instability in MHD

Generation of the Kelvin-Helmholtz instability is crucial for efficient mixing in hydrodynamical simulations. Here, we look at the same problem but with a magnetic field applied parallel to the flow. This has a stabilizing effect on the shear flow due to the magnetic tension force. We followed the setup from McNally et al. (2012), but extend it to 3D, making a thin periodic box ($L = [1.0, 1.0, \frac{2\sqrt{6}}{n_x}]$), with a resolution of $[n_x, n_y, n_z]$ = $[256, 296, 12]$. We applied a uniform pressure of $P = 5/2$ with an adiabatic index of $\gamma = 5/3$. The hot outer stream has a density of $\rho_{\mathrm{out}} = 1$ and velocity $v_{\mathrm{out}} = [-0.5, 0, 0]$. The cold inner stream has a density of $\rho_{\mathrm{in}} = 2$ and velocity $v_{\mathrm{in}} = [0.5, 0, 0]$. A uniform magnetic field was added in the direction of the flow velocity $B = [0.1, 0, 0]$.

The results for TSPH and GDSPH at $t = 1.6$ and 3.2 can be seen in Fig. 9. And in Fig. 10 we show the particle distribution of the surface boundary at $t = 3.2$. The TSPH result exhibits a very gloopy behaviour and shows a decreased growth of the KH mode. A strong artificial surface tension effect can clearly be seen between the hot and the cold phase in Fig. 10. With GDSPH this effect is largely eliminated and the growth rate improves significantly. This large improvement in GDSPH lends itself mainly to the reduction of the leading order errors, which we discussed in Sect. 2.2. Adding turbulent diffusion (that is, with the code default parameters) further improves the result, because it allows particles to effectively mix or reorder (as shown clearly in the particle distribution near the boundary regions in
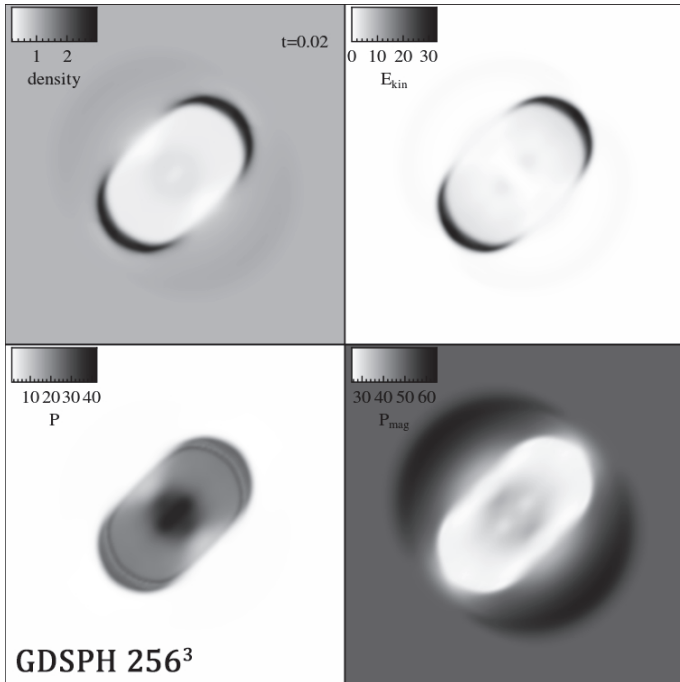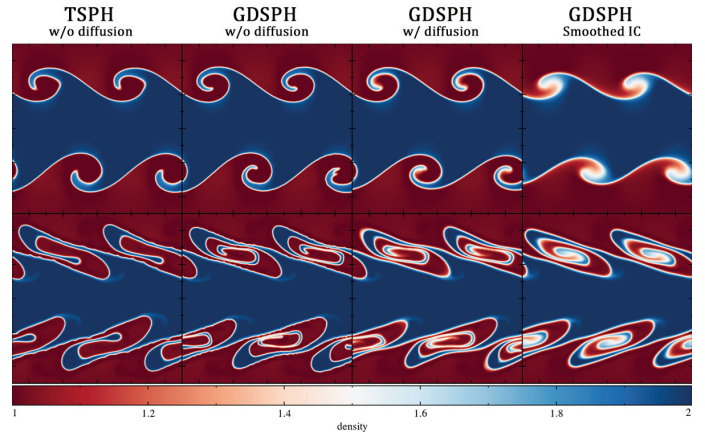
Fig. 8. Result from the magnetized blast in 3D in the 256³ GDSPH run, which shows rendered slices of different fluid quantities at $t = 0.02$. To the *top left* we can see the density rendering, *top right* the kinetic energy density, *bottom left* the thermal pressure and *bottom right* the magnetic pressure. The limits are taken to be the same as Stone et al. (2008) and Price et al. (2018) for a direct comparison: $\rho = [0.19, 2.98]$, $E_{kin} = [0, 33.1]$, $P = [1, 42.4]$ and $P_{mag} = [25.2, 65.9]$.

Fig. 9. Result from the magnetic Kelvin-Helmholtz instability in 3D, which shows rendered density slices ($z = 0$) at $t = 1.6$ (*top*) and $t = 3.2$ (*bottom*), for TSPH without diffusion (*left*), GDSPH without diffusion (*middle left*), GDSPH with diffusion (*middle right*) and GDSPH with an initial smoothed contact discontinuity (*right*). The TSPH result exhibits a very gloopy behaviour and shows decreased growth of the KH mode. This is mainly due to the artificial surface tension effect (see Fig. 10). GDSPH shows much better growth, the addition of diffusion only slightly improves the growth rate. The main effect from the magnetic field can be seen in all cases, which uncoils and stretches the vortex. The smoothed result closely resembles the MFM and grid result from Hopkins & Raives (2016).

Fig. 10), but the growth rate remains similar to the GDSPH-only case. We note that the sharp contact discontinuities in the initial condition are not smoothed, unlike in McNally et al. (2012). We choose this because it represents an extreme situation for SPH where the initial particle ordering is not optimal (that is, zeroth order errors are relatively high), and we show that GDSPH performs well even in this extreme case. We also ran the setup using a smoothed contact discontinuity, and this is shown in the rightmost column in Fig. 9. The magnetic field effectively uncoils and stretches the vortex, which is in good agreement to the results shown in Hopkins & Raives (2016) with the same setup. Here TSPH and GDSPH develop indistinguishably until later time, where at the end only small differences can be seen. The mean normalized divergence error in the simulations are of the order of $\langle \epsilon_{divB} \rangle = 10^{-3}$.

4. Collapse of a magnetized cloud

In this Section, we apply our method to an astrophysical problem and consider the collapse of a magnetized cloud. In this type of problem involving large dynamic scales, we see a substantial difference between GDSPH and TSPH. A rotating magnetized cloud is allowed to collapse under its own gravity. During the collapse, the cloud is compressed over several orders of magnitude, testing how the magnetic field develops and interacts with the gas during compression. The large-scale collapse is eventually halted by the formation of a pseudo-disk[6], which then starts to slowly contract via magnetic braking. The collapse continues

within the central region and as the first hydrostatic core starts to form, the magnetic field is twisted until it eventually launches a jet (Uchida & Shibata 1986; Lynden-Bell 1996; Ustyugova et al. 2000; Nakamura & Meier 2004). The formation and subsequent evolution of the first hydrostatic core stalls the collapse and a slow contraction phase begins. In this paper, we do not run the simulations far beyond the time of jet launching. The two main jet launching mechanisms are the magneto-centrifugal and the magnetic pressure driven mechanism. With a global poloidal magnetic field as in our model, both of these mechanisms play an important role. The resulting magnetic field structure of the jet consists of a poloidal dominated central core with a surrounding toroidal field which produces a strong current along the jet. We refer to this magnetic field structure as the magnetic tower throughout this paper. All these key aspects require the code to have excellent angular momentum conservation, small numerical dissipation and maintain low divergence errors ($\nabla \cdot B$).

We followed the setup outlined in Hennebelle & Fromang (2008) and Hopkins & Raives (2016) and set up a 3D periodic box $L = [0.15\,\text{pc}, 0.15\,\text{pc}, 0.15\,\text{pc}]$. A cloud was initiated with a radius of $R_c = 0.015\,\text{pc}$ and a mass of 1 solar mass ($M_c = 1\,M_\odot$), within a surrounding medium that has 360 times lower density than the cloud ($\rho_{out} = M_c/(360V_c)$). The cloud was put in rotation with an orbital time of $P = 4.7 \times 10^5\,\text{yr}$, which corresponds to a kinetic over potential energy ratio of about $E_K/E_P \approx 0.045$. This is a higher ratio compared to the peak value of 0.02 from the observed distribution of rotation rates in molecular clouds ($E_K/E_P \in (0.002, 1.4)$) (Goodman et al. 1993). A constant magnetic field B_0 was initialized in the direction of the angular momentum vector ($\hat{z}$), and we varied the strength in accordance to different mass-to-flux ratios. The mass-to-flux

---

[6] The disks formed in strong magnetic fields are primarily not supported by rotation, as magnetic braking quickly transfers angular momentum outwards. A pseudo-disk is however formed, which struc-
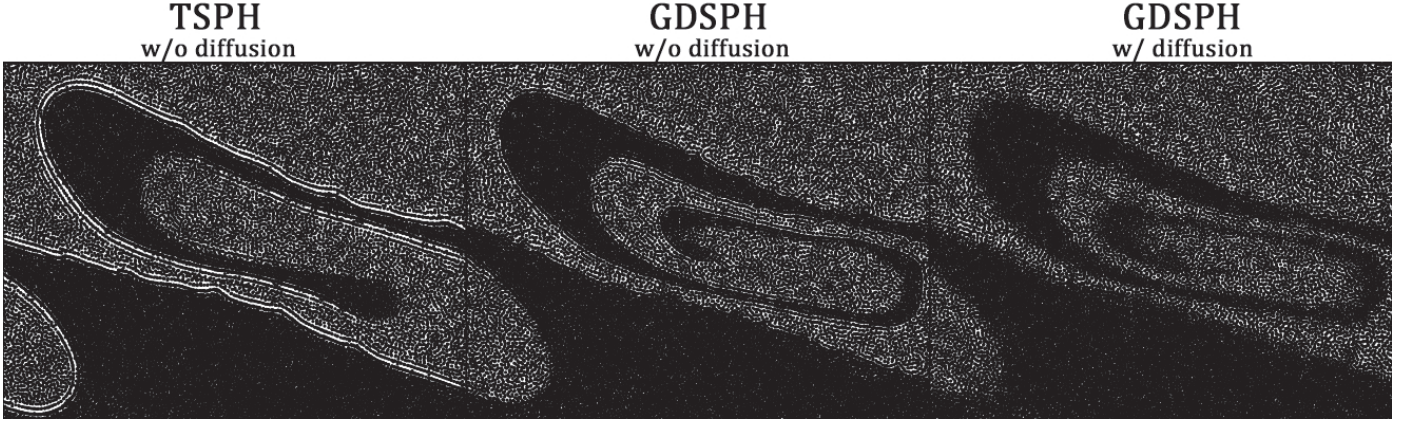
ture is a consequence of the anisotropy of the magnetic support against the gravitational collapse. Due to our high initial rotation rate, we are though more likely to retain a more rotationally supported disk compared to other studies which apply a lower ratio.

Fig. 10. Surface boundary between the high and low density region in the magnetic Kelvin-Helmholtz instability at $t = 3.2$. The effect of the numerical surface tension can clearly be seen in the TSPH case, while GDSPH does not suffer from this issue. Adding thermal diffusion allows for local mixing between the cold and hot phase.

ratio μ is relative to the critical mass-to-flux ratio, $(M_c/\Phi)_{\text{crit}}$, in which the cloud is fully supported by magnetic forces against gravity, that is,

$$\mu = \left(\frac{M_c}{\Phi}\right) \Big/ \left(\frac{M_c}{\Phi}\right)_{\text{crit}}, \tag{34}$$

$$\left(\frac{M_c}{\Phi}\right) = \frac{M_c}{\pi R_c^2 B_0}, \quad \left(\frac{M_c}{\Phi}\right)_{\text{crit}} = \frac{c_1}{3\pi}\sqrt{\frac{5}{G}}. \tag{35}$$

Here, $c_1 = 0.53$ is a parameter that can be determined numerically (Mouschovias & Spitzer 1976). We then get the corresponding initial magnetic field:

$$B_0 = \frac{610}{\mu} \, [\mu G]. \tag{36}$$

The thermal pressure is determined by the following barotropic EOS,

$$P = c_{s,0}^2 \rho \sqrt{1 + (\rho/\rho_0)^{4/3}}, \tag{37}$$

with $\rho_0 = 10^{-14}$ g cm^{-3} and $c_{s,0} = 0.2$ km s^{-1}. We looked at six different magnetic flux ratio values in our simulations, from weak to high ($\mu = \infty, 75, 20, 10, 5, 2$). These were run with a moderate resolution of 50^3 in the cloud, which corresponds to about 40^3 particles in the low density medium, same as in the setup of Hopkins & Raives (2016). These six cases were run with both GDSPH and TSPH until the core has fully collapsed, close after the time of jet launching, which typically occurs when the maximum density hits a value in between $\rho = 10^{-12} \leftrightarrow 10^{-11}$ g cm^{-3}. This occurs near the free fall time $t_{ff} = \sqrt{\frac{3}{2\pi G\rho}} \approx 4 \times 10^4$ yr, at around $t = 1.05 t_{ff} \leftrightarrow 1.3 t_{ff}$ depending on resolution/initial magnetic field strength. No sink particles were used in any of our simulations. The results of these simulations can be seen in Fig. 11 (GDSPH) and Fig. 12 (TSPH).

The pure hydrodynamic runs ($\mu = \infty$) of both GDSPH and TSPH become gravitationally unstable and the resulting evolution is very similar (see Figs. 11 and 12). For GDSPH, we see in Fig. 11 that jet launching can be seen in the weak field regime ($\mu = 75, 20, 10$), although it is very short-lived in the case of $\mu = 75$. It is clear from the poloidal magnetic field and the current density (the fourth and fifth row in Fig. 11) that we have a developed magnetic tower in all these three cases. This is a remarkable achievement, especially for SPMHD, since the

amplification of the magnetic field can easily be quenched by numerical dissipation. The jet strength, morphology and velocity structure resemble those in Hopkins & Raives (2016) with the same resolution using the MFM/MFV method with more complex gradient operators and Riemann solvers. In contrast, for TSPH (Fig. 14) we see neither jet launching nor a magnetic tower in the weak-field regime with the fiducial resolution of 50^3. This is largely due to numerical dissipation which suppresses field amplification and hinders the formation of a jet. At the time of jet launching, fragmentation of the disc occurs in the two weakest cases $\mu = 75$ and $\mu = 20$ for TSPH, as the magnetic field is too weak to support the disc. For GDSPH, it does not occur until a later time in the simulation, however, the exact time of fragmentation is heavily dependent on other dissipation terms such as artificial viscosity.

For the more magnetized case with $\mu = 5$ we can see that TSPH successfully develops a jet, however, closer inspection on $|B_z|$ in Fig. 12 shows that the central portion of the magnetic tower is much less developed, with an order of magnitude smaller strength than the same run with GDSPH. Jet launching is also seen in the GDSPH case with $\mu = 5$ with the magnetic tower intact, albeit weaker and less collimated than in the $\mu = 10$ case. For $\mu = 2$, the collapse proceeds differently in GDSPH and TSPH from an early stage. This can be seen in Fig. 15, which shows the density structure of the collapsing cloud in an early stage with different resolutions. As the magnetic field is very strong, accretion will occur primarily along the field lines, creating an elongated cloud structure. While at high resolution (250^3) both GDSPH and TSPH runs converge to the correct structure, at the fiducial resolution of 50^3, only GDSPH shows an elongated cloud. The cloud collapses faster in TSPH, likely due to excessive dissipation.

For $\mu = 2$, we can see that GDSPH does not produce a coherent jet (Fig. 11). This is mainly due to the disk being disrupted by the magnetic interchange instability. This instability occurs due to an accumulation of magnetic flux near the accreting protostar, where the magnetic flux that would have been dragged into the protostellar core is redistributed to the surrounding medium by dissipative effects (AR). This builds a large magnetic pressure gradient which, together with the twisted magnetic field, eventually launches highly magnetized bubbles in the azimuthal direction. A density rendering together with a velocity map of the $\mu = 2$ case after the launch of the magnetized bubbles is shown in Fig. 16. This is similar to the results seen in simulations using the

GDSPH 50³
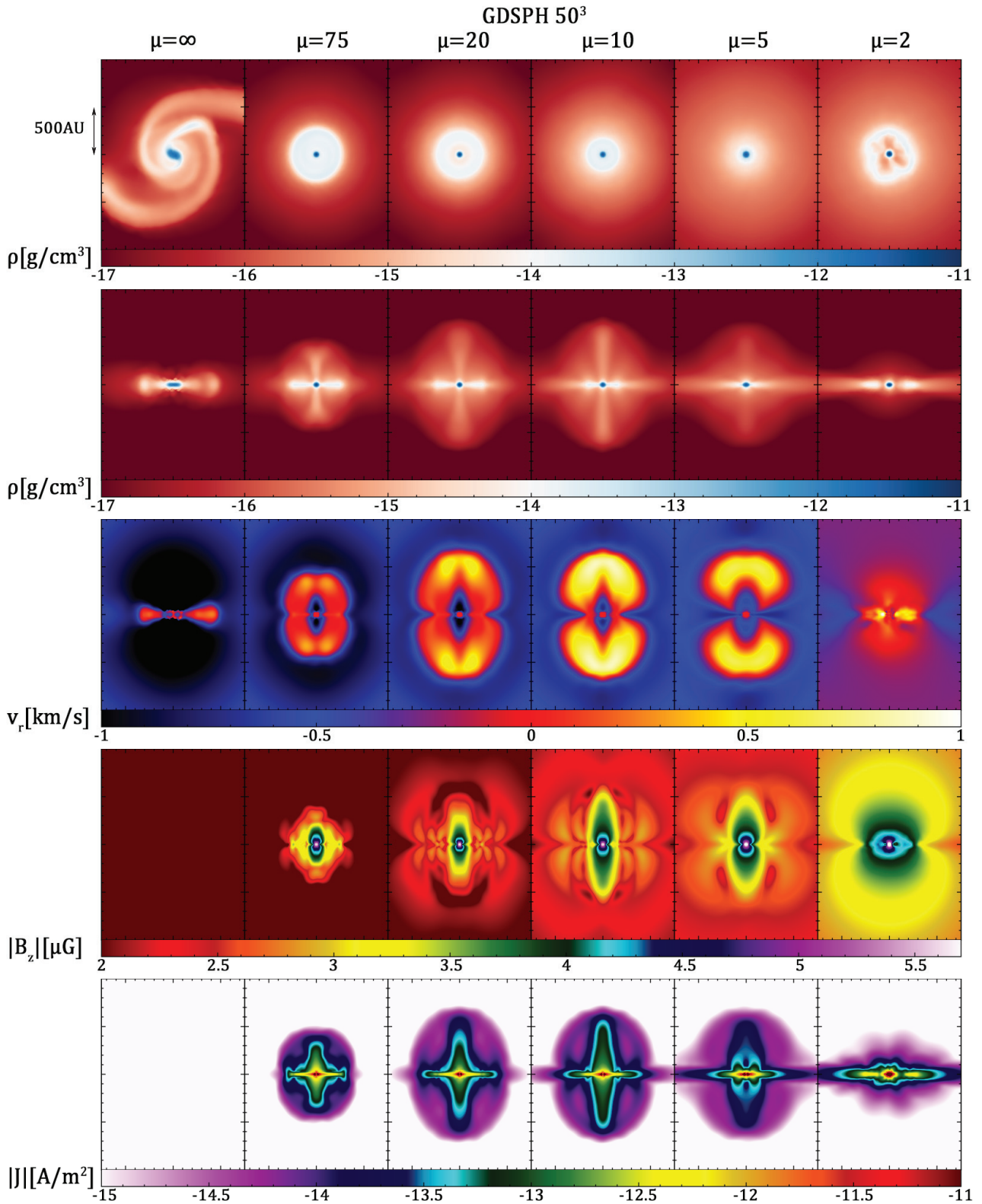
Fig. 11. Result of the magnetized cloud collapse for GDSPH at a resolution of 50^3 particles with varying magnetic flux ratio μ going *left to right from high to low*. We show figures at the time of jet formation (around $t = t_{ff}$), which occurs due to the winding of the magnetic field during the collapse, which produces a magnetic tower structure. The *top row* shows a rendered face-on slice ($L_{xy} = [2000\,\mathrm{AU}, 2000\,\mathrm{AU}]$) of the density [$\mathrm{g\,cm^{-3}}$], the rest of the rows show rendered slices through the rotation axis ($L_{xz} = [2000\,\mathrm{AU}, 2000\,\mathrm{AU}]$), where the *second* shows density [$\mathrm{g\,cm^{-3}}$], the *third* show radial velocity [$\mathrm{km\,s^{-1}}$], the *fourth* show the absolute poloidal magnetic field [μG] and the *fifth* shows the current density [$\mathrm{A\,m^{-2}}$], all quantities are shown in logarithmic scale. The pure hydrodynamic run ($\mu = \infty$) of GDSPH becomes gravitationally unstable and is very similar to that of TSPH in Fig. 12. We can see that a jet is launched in the cases of $\mu = 75, 20, 10, 5$ while in the case of $\mu = 2$ the interchange instability (see Fig. 16) disrupts the disk before jet launching.
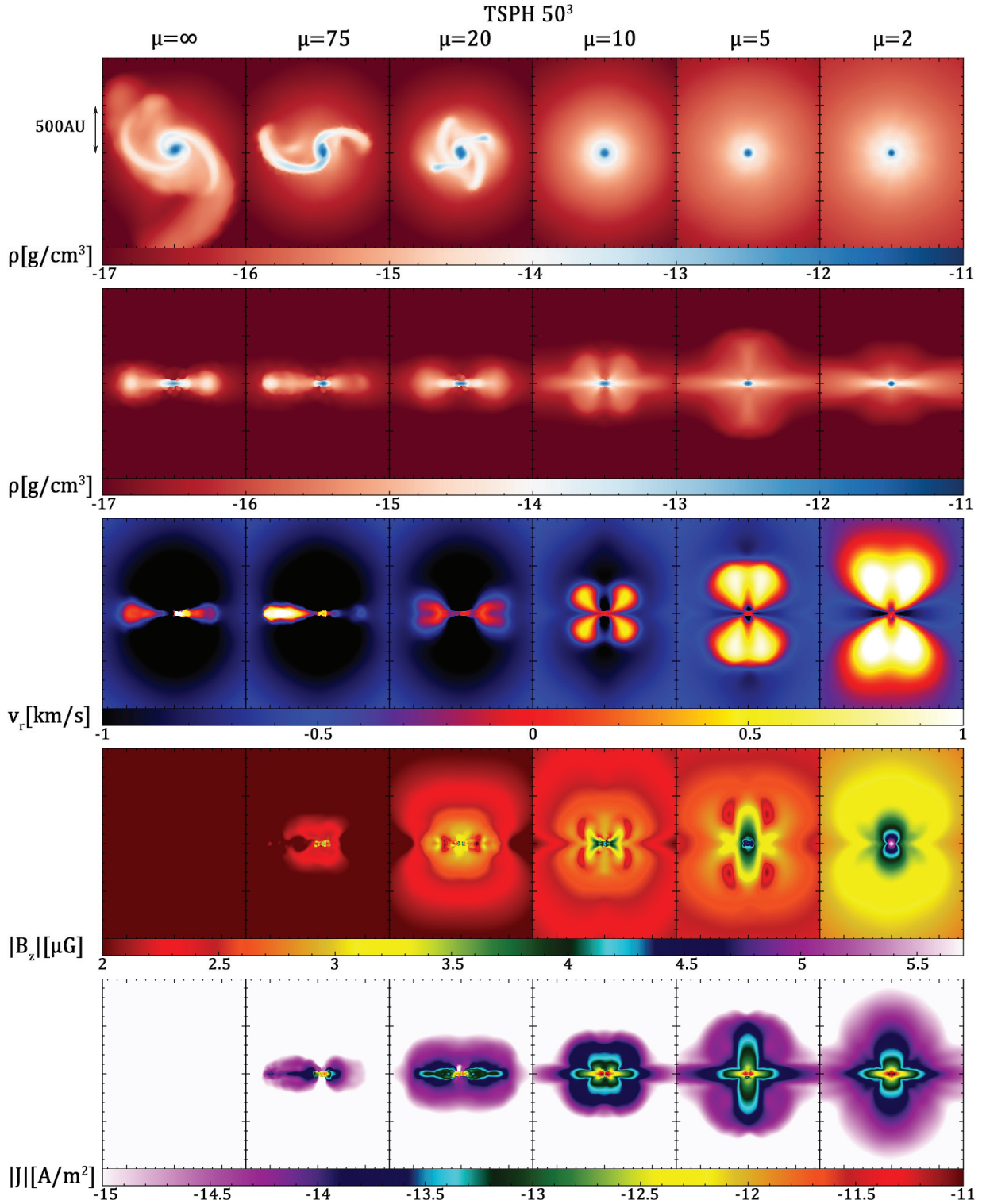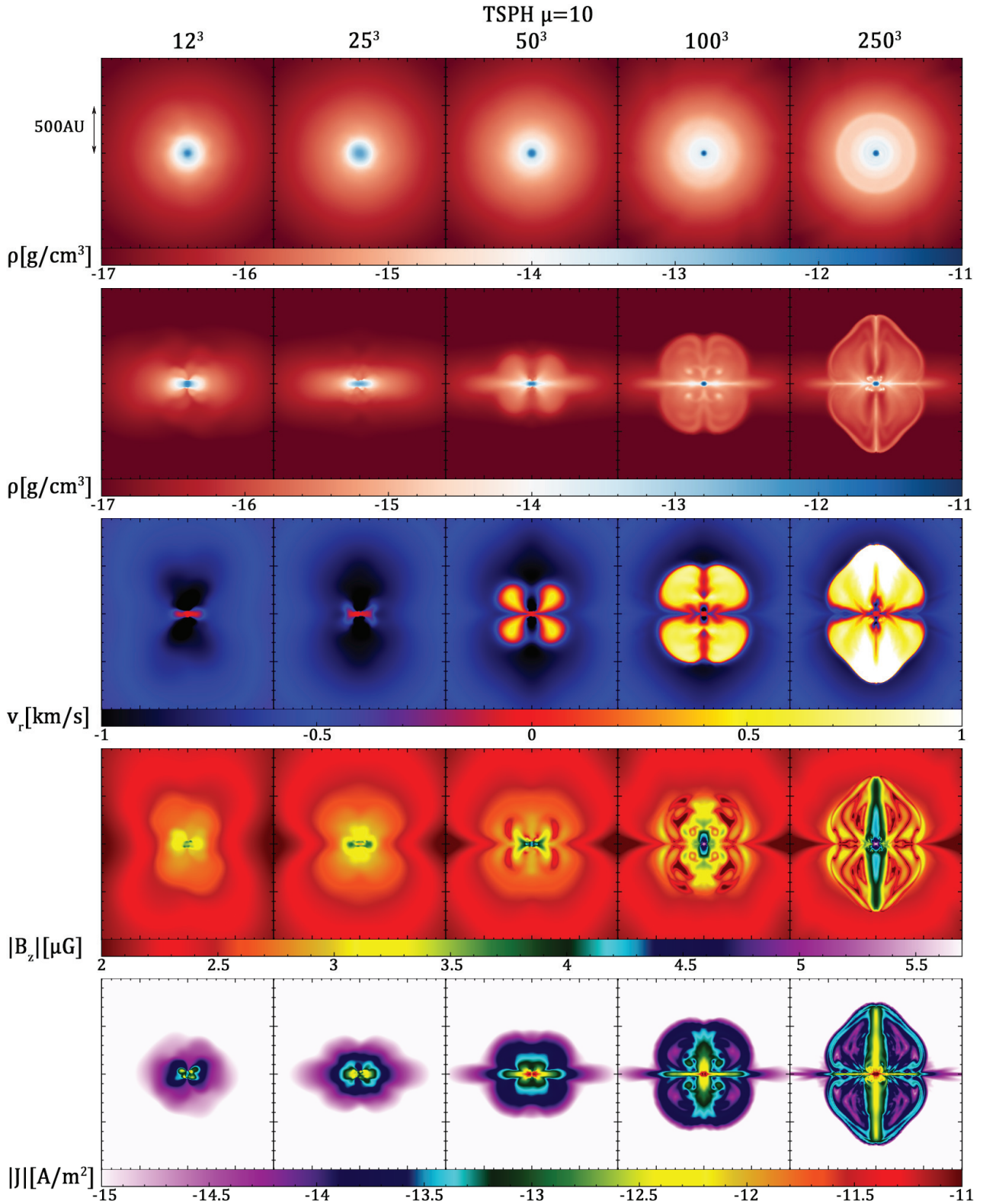
Fig. 12. Result of the magnetized cloud collapse for TSPH at a resolution of 50^3 particles with varying magnetic flux ratio μ going *left to right from high to low*. We show figures at the time of jet formation (around $t = t_{ff}$), which occur due to the winding of the magnetic field during collapse, which produces a magnetic tower structure. The *top row* shows a rendered face-on slice ($L_{xy} = [2000\,\text{AU}, 2000\,\text{AU}]$) of the density [g cm^{-3}], the rest of the rows show rendered slices through the rotation axis ($L_{xz} = [2000\,\text{AU}, 2000\,\text{AU}]$), where the *second* shows density [g cm^{-3}], the *third* show radial velocity [km s^{-1}], the *fourth* show the absolute poloidal magnetic field [μG] and the *fifth* shows the current density [A m^{-2}], all quantities are shown in logarithmic scale. The pure hydrodynamic run ($\mu = \infty$) of TSPH becomes gravitationally unstable and is very similar to that of GDSPH in Fig. 11. We can see that TSPH does not form a jet in any of the weak field cases ($\mu = 75, 20, 10$) and there is no sign of a magnetic tower being formed. In the case of $\mu = 5$, we can see a jet being launched, where a current dominated magnetic tower has formed, however, the central part of the tower has been completely quenched. The $\mu = 2$ case also launches a jet, but collapses faster than in the high resolution case, which effectively leads to easier jet formation.
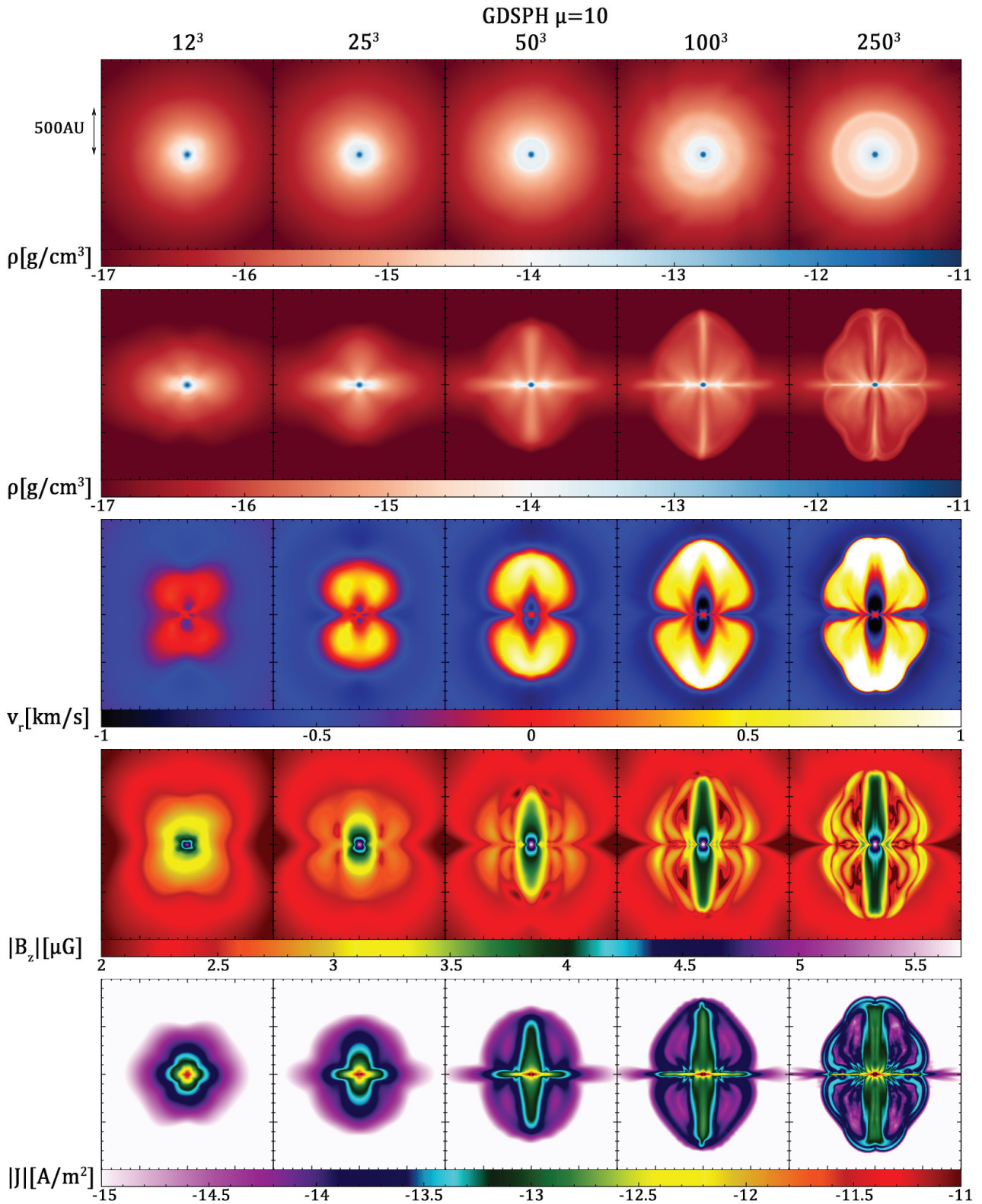
Fig. 13. Result of the resolution study of the magnetized cloud collapse for GDSPH with $\mu = 10$. We vary the resolution from left to right, in the initial cloud ($12^3, 25^3, 50^3, 100^3, 250^3$) and medium ($10^3, 20^3, 40^3, 80^3, 200^3$). We show figures at the time of jet formation (around $t = t_{ff}$), which occur due to the winding of the magnetic field during collapse, which produces a magnetic tower structure. The *top row* shows a rendered face-on slice ($L_{xy} = [2000\,\mathrm{AU}, 2000\,\mathrm{AU}]$) of the density [$\mathrm{g\,cm^{-3}}$], the rest of the rows show rendered slices through the rotation axis ($L_{xz} = [2000\,\mathrm{AU}, 2000\,\mathrm{AU}]$), where the *second* shows density [$\mathrm{g\,cm^{-3}}$], the *third* show radial velocity [$\mathrm{km\,s}$], the *fourth* show the absolute poloidal magnetic field [μG] and the *fifth* shows the current density [$\mathrm{A\,m^{-2}}$]; all quantities are shown in logarithmic scale. Jet formation and a proper magnetic tower can be seen to occur at very low resolution compared to TSPH. The jet structure and magnetic tower further increases in complexity as we increase the resolution.

Fig. 14. Result of the resolution study of the magnetized cloud collapse for TSPH with $\mu = 10$. We vary the resolution from left to right, in the initial cloud ($12^3, 25^3, 50^3, 100^3, 250^3$) and medium ($10^3, 20^3, 40^3, 80^3, 200^3$). We show figures at the time of jet formation (around $t = t_{ff}$), which occur due to the winding of the magnetic field during collapse, which produces a magnetic tower structure. The *top row* shows a rendered face-on slice ($L_{xy} = [2000 \text{ AU}, 2000 \text{ AU}]$) of the density [g cm^{-3}], the rest of the rows show rendered slices through the rotation axis ($L_{xz} = [2000 \text{ AU}, 2000 \text{ AU}]$), where the *second* shows density [g cm^{-3}], the *third* show radial velocity [km s^{-1}], the *fourth* show the absolute poloidal magnetic field [μG] and the *fifth* shows the current density [A m^{-2}], all quantities are shown in logarithmic scale. We can see that TSPH only forms a collimated jet and a proper magnetic tower at the highest resolution.

GDSPH   TSPH

50^3

250^3

$\updownarrow$2000AU

-19   -18   -17
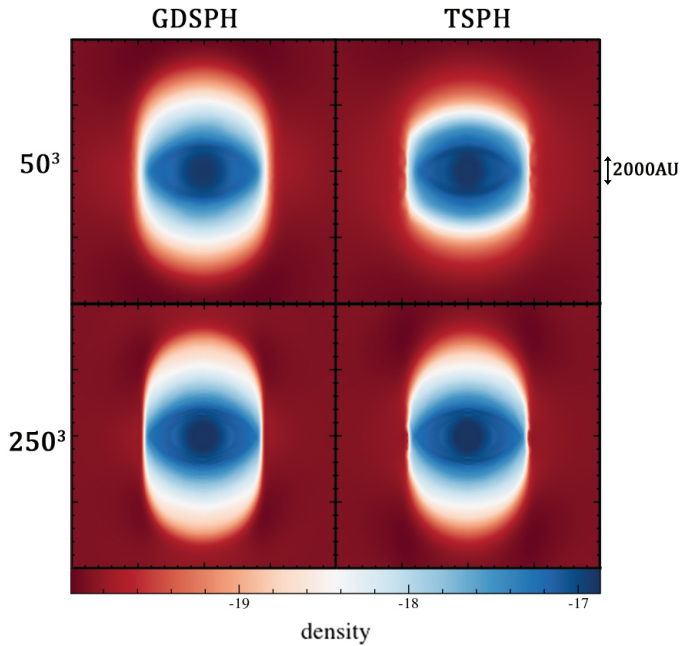
density

Fig. 15. Density rendered slice ($[\mathrm{g\,cm^{-3}}]$) through the rotation axis, showing the early cloud structure of the strong field case $\mu = 2$ before the formation of the disk. As the magnetic field is very strong, accretion will occur primarily along the field lines, creating an elongated cloud structure. Both high resolution cases (250^3) of TSPH and GDSPH creates an elongated cloud structure, while in the low-resolution case (50^3) only GDSPH forms the same cloud structure. TSPH instead forms a more compact central cloud, which as a consequence collapses faster than the GDSPH case and the high resolution cases.

AMR code ENZO (Krasnopolsky et al. 2012) and in SPH simulations with PHANTOM (Wurster et al. 2017). We would like to stress that, unlike the SPH runs in Hopkins & Raives (2016), the disk disruption is not due to divergence errors, but instead a consequence of the magnetic dissipation. At later times (for example, right panel of Fig. 16), we can see that the protostellar core remains centrally located, which indicates good divergence control and angular momentum conservation. As the formation of the interchange instability is driven by the redistribution of magnetic flux, it can depend heavily on the choice of AR prescription and the use of sink particles. Wurster et al. (2017) observed similar magnetic bubbles with the same AR prescription as ours, while other tested AR prescriptions did not launch magnetic bubbles. However, all other works that produce interchange instabilities use sink particles, which can artificially redistribute the flux as matter is accreted by the sink, while leaving the magnetic field close to the sink intact. The development of the interchange instability in our simulations without sink particles might indicate a more physical origin of the effect. Additional work will need to be done to determine if this is in fact a real effect or a consequence of the numerical scheme.

To investigate the convergence with resolution, we simulated the $\mu = 10$ case across different resolutions (12^3, 25^3, 50^3, 100^3 and 250^3) for both methods. The results are shown in Fig. 13 for GDSPH and Fig. 14 for TSPH. In GDSPH, resolved jet structures and fully developed magnetic towers are already evident in cases with 25^3 resolution, and which increase in complexity as we increase the resolution. A weak outflow appears even in the lowest resolution of 12^3. In contrast, the runs with TSPH shows slow convergence. The structure of the magnetic field is severely distorted, and magnetic tower and proper colli-
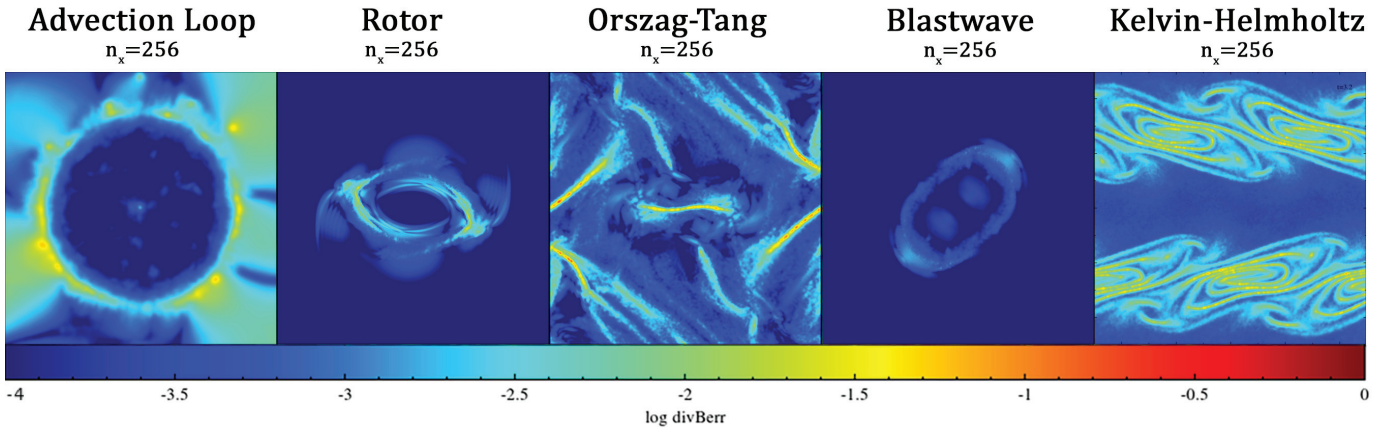
94
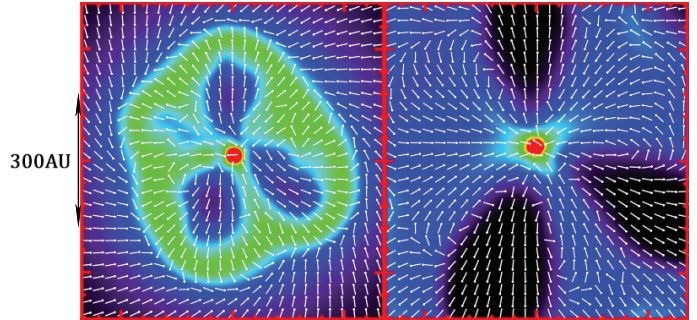
Fig. 16. Magnetic interchange instability in the strong field case ($\mu = 2$) for the GDSPH simulation with 50^3 resolution. *Left panel*: zoom-in of the disc structure seen face-on in Fig. 11 and *right panel*: same region at a later time. The white arrows show the direction of velocity and the colour scale indicates density. The instability launches magnetized bubbles in the azimuthal direction. At later times we can see that the central star starts to accrete again along the filamentary structure. These figures can be compared to the results from Krasnopolsky et al. (2012).

mated jet are not developed in all cases except the highest resolution. Again, we note that our GDSPH results are very comparable to the MFM/MFV runs in Hopkins & Raives (2016), both in terms of jet properties and converging speed. The magnetic tower structure is also qualitatively similar to the cloud collapse simulation in the weak field regime from the moving-mesh code AREPO (Pakmor et al. 2011), although with a slightly different initial setup. We should note that the collapse of the 12^3 is artificially suppressed and contract much slower then what is expected. This is because the local Jeans mass is not fully resolvable in these simulations. Bate & Burkert (1997) estimated that around 3×10^4 particles where required to correctly resolve the Jeans mass in similar collapse cases[7]. The effect can partly be seen in the 25^3 case as well, especially at later times. However, in this case, the cloud collapsing has a similar evolution up to the time of jet-launching as the higher resolution cases.

5. Discussion

In this paper, we present an SPMHD method, which utilizes the Geometric Density average force discretization (GDSPH) of the MHD equations. GDSPH has been shown in previous work to greatly improve the accuracy near density discontinuities and eliminate the surface tension problem. We show that MHD also benefits from this method. For a large part, the standard test problems (Sects. 3.1–3.6) both GDSPH and TSPH handle the problems very well, and the differences between the two methods are minimal. However, when the problem involves mixing such as in the case of Kevin-Helmholtz instabilities, GDSPH shows clear advantages. This is somewhat expected, and in agreement with earlier studies without magnetic fields (Wadsley et al. 2017). However, when we apply the method in the astrophysical test of a collapsing magnetized cloud, we see that GDSPH leads to a significant improvement. GDSPH not only realistically captures the development of a magnetic tower and jet launching in the weak field regime ($\mu \gtrsim 10$), but also exhibits a fast improvement in the complexity and structure of the jet with increased resolution. In contrast, TSPH only manages to launch jets in the strong field regime with a resolution

---

[7] The number of particles required to resolve the Jeans mass is presumably even higher in our simulation as Bate & Burkert (1997) used a smaller neighbour number ($N_{\mathrm{neigh}} = 50$) and neglected magnetic fields.

Advection Loop $n_x=256$ **Rotor** $n_x=256$ **Orszag-Tang** $n_x=256$ **Blastwave** $n_x=256$ **Kelvin-Helmholtz** $n_x=256$

Fig. 17. Normalized divergence error ($\epsilon_{\mathrm{div}B} \equiv h|\nabla \cdot \mathbf{B}|/|\mathbf{B}|$, Eq. (29)) of the different cases (all in 3D) with GDSPH. *From left to right*: *first*: advection of a current loop with a density ratio of $\Delta = 2$ at $t = 20$ (Sect. 3.2), *second*: MHD rotor ($n_x = 256$) at $t = 0.15$ (Sect. 3.5). *Third*: Orszag-Tang vortex ($n_x = 256$) at $t = 0.5$ (Sect. 3.4). The MHD blastwave ($n = 256^3$) at $t = 0.02$ (Sect. 3.5). The MHD Kelvin-Helmholtz instability ($n_x = 256$) with an initial sharp contact discontinuity at $t = 3.2$ (Sect. 3.7).

of 50^3 and only develop a collimated jet in the highest resolution runs of the $\mu = 10$ case. We also show that, in the strong field regime, GDSPH converges better than TSPH in accretion time and in the outer cloud structure. The results of TSPH is in agreement with previous studies using TSPH (Hopkins & Raives 2016; Bürzle et al. 2011) which used the same IC as this work, and other studies (Price & Bate 2007; Price et al. 2012) which employ a smaller initial cloud rotation ($E_K/E_P = 0.005$).

Overall, our new method shows improved or comparable results to previous SPMHD implementations such as in PHANTOM (Price et al. 2018) and in GIZMO (Hopkins & Raives 2016). In many test cases and particularly in the cloud collapse case, GDSPH produces qualitatively very similar result to that of the MFM/MFV method and achieves similar convergence speed. It is worth noting that all the simulations are run in 3D with the code default parameters listed in Sect. 3 without any adjustment by hand to specific problems. The success of GDSPH can most likely be attributed to the reduction of SPH "E_0 errors" (Eq. (10)) and linear errors by the geometric density average force formulation. As discussed in Sect. 2.2, the advantage of such discretization is more evident when the density gradient is large, such as in the cloud collapse case.

Using the constrained hyperbolic divergence cleaning scheme with variable cleaning speed from Tricco et al. (2016), we can keep the divergence error low in all cases. The mean normalized divergence error, $\langle\epsilon_{\mathrm{div}B}\rangle = \langle h|\nabla \cdot \mathbf{B}|/|B|\rangle$, is typically of order 10^{-5}–10^{-3}. In Fig. 17, we show the normalized divergence error maps for several test problems. Again we see that the divergence cleaning works extremely well here, the maximum error is generally around 10^{-2}. Comparing to Hopkins (2016, their Fig. 4), we find that the errors are smaller than their MFM simulations with the Dedner et al. (2002) cleaning in general, with an exception for the outskirt of the advection loop (where the magnetic field is essentially zero and thus not important for the result). The improvement is probably due to the more advanced constrained cleaning method (Tricco et al. 2016). The normalized divergence error for the $\mu = 10$ cloud-collapse case at the jet launching time is shown in Fig. 18. Here, the divergence cleaning still performs very well in the disc, along the jets and for the majority of the regions where the outflow interacts with the ambient gas, especially when the divergence error is compared to the total gas pressure (right panel). The result is similar to the Dedner cleaning in Hopkins (2016), although
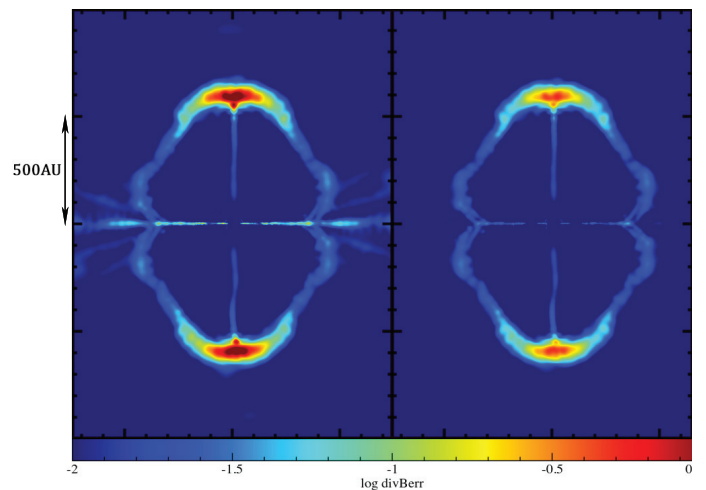
Fig. 18. Normalized divergence error of the magnetized cloud collapse simulation with GDSPH at the jet launching time, $t \approx t_{ff}$. The mass-to-flux ratio is $\mu = 10$ and the resolution is 100^3. *Left:* normalized divergence error as in (Eq. (29)), $\epsilon_{\mathrm{div}B} \equiv h|\nabla \cdot \mathbf{B}|/|\mathbf{B}|$; *right:* divergence error normalized to total gas pressure, $\epsilon_{\mathrm{div}B}/\sqrt{(1+\beta)} = h|\nabla \cdot \mathbf{B}|/\sqrt{(\mathbf{B}^2 + 2P)}$, where $\beta = 2P/\mathbf{B}^2$ is the plasma beta.

our error is somewhat larger at the tip of the jets where the gas is shocked. However, we note that the comparison is not direct in this case as the jets may develop differently. Overall, the result from cleaning is still worse than the constrained transport or constrained gradient schemes (Hopkins 2016). For SPMHD, as shown in Tricco & Price (2012), divergence errors can be reduced to machine precision (or more practically to a certain tolerance value) using cleaning, with the help of a sub-cycling routine. However, local adjustments are required to determine the number of iterations for each particle to efficiently subcycle the cleaning in the simulation. This is because certain regions are more affected than others and because divergence is spread to nearby neighbours. Conceivably, if vector potentials (Stasyszyn & Elstner 2015) could work for a wider range of problems this could be an interesting avenue as well. However, the exploration of these methods in detail is beyond the scope of this work.

From the tests, we can see that using a lower artificial resistivity coefficient ($\alpha_B = 0.5$) than ($\alpha_B = 1$) (Price et al. 2018) works well for all cases. However, the choice of artificial resistivity switch still remains somewhat ad-hoc as it is difficult to accurately detect the MHD discontinuity. A Godunov SPH scheme (Iwasaki & Inutsuka 2011) solves this problem by replacing artificial resistivity with Riemann solvers, which have been shown to produce minimal artificial diffusivity. However, this brings with it an increase in computational cost and it is unclear if the extra cost is worth it. Further improvements in the convergence of SPMHD may be found in the use of integral-based gradient estimates, which have been shown to be more accurate and less noisy than the standard SPH gradient estimate (García-Senz et al. 2012; Rosswog 2015; Cabezón et al. 2017). This could be especially beneficial for modeling subsonic turbulent flows (Valdarnini 2016). This gradient estimate can easily be implemented within the GDSPH framework and will be investigated in future work.

Meshless methods (SPH and MFM) were recently explored in local 3D simulations of the magnetorotational instability (MRI; Deng et al. 2019). The authors found that in the vertically stratified MRI simulations, SPH developed an unphysical state with strong toroidal field components and no sustained turbulence. In a forthcoming paper (Wissing et al., in prep.) we will show that GDSPH do not show this unphysical behavior and that they reproduce the characteristic periodic azimuthal magnetic field pattern (butterfly diagram) of the stratified MRI.

References

Balsara, D. S., & Spicer, D. S. 1999, J. Comput. Phys., 149, 270
Bate, M. R., & Burkert, A. 1997, MNRAS, 288, 1060
Beck, R., Brandenburg, A., Moss, D., Shukurov, A., & Sokoloff, D. 1996, ARA&A, 34, 155
Booth, C. M., Agertz, O., Kravtsov, A. V., & Gnedin, N. Y. 2013, ApJ, 777, L16
Børve, S., Omang, M., & Trulsen, J. 2001, ApJ, 561, 82
Børve, S., Omang, M., & Trulsen, J. 2004, ApJS, 153, 447
Boulares, A., & Cox, D. P. 1990, ApJ, 365, 544
Brandenburg, A. 2010, MNRAS, 401, 347
Brio, M., & Wu, C. C. 1988, J. Comput. Phys., 75, 400
Brookshaw, L. 1985, PASA, 6, 207
Bürzle, F., Clark, P. C., Stasyszyn, F., Dolag, K., & Klessen, R. S. 2011, MNRAS, 417, L61
Butsky, I. S., & Quinn, T. R. 2018, ApJ, 868, 108
Butsky, I., Zrake, J., Kim, J.-H., Yang, H.-I., & Abel, T. 2017, ApJ, 843, 113
Cabezón, R. M., García-Senz, D., & Figueira, J. 2017, A&A, 606, A78
Dedner, A., Kemm, F., Kröner, D., et al. 2002, J. Comput. Phys., 175, 645
Dehnen, W., & Aly, H. 2012, MNRAS, 425, 1068
Deng, H., Mayer, L., Latter, H., Hopkins, P. F., & Bai, X.-N. 2019, ApJS, 241, 26
Evans, C. R., & Hawley, J. F. 1988, ApJ, 332, 659
García-Senz, D., Cabezón, R. M., & Escartín, J. A. 2012, A&A, 538, A9
Gardiner, T. A., & Stone, J. M. 2005, J. Comput. Phys., 205, 509
Gardiner, T. A., & Stone, J. M. 2008, J. Comput. Phys., 227, 4123
Goodman, A. A., Benson, P. J., Fuller, G. A., & Myers, P. C. 1993, ApJ, 406, 528
Hennebelle, P., & Fromang, S. 2008, A&A, 477, 9
Hopkins, P. F. 2015, MNRAS, 450, 53
Hopkins, P. F. 2016, MNRAS, 462, 576
Hopkins, P. F., & Raives, M. J. 2016, MNRAS, 455, 51
Iwasaki, K., & Inutsuka, S.-I. 2011, MNRAS, 418, 1668
Jun, B.-I., Norman, M. L., & Stone, J. M. 1995, ApJ, 453, 332
Kale, L., & Krishnan, S. 1993, ACM SIGPLAN Not., 28, 91
Kotarba, H., Lesch, H., Dolag, K., et al. 2011, MNRAS, 415, 3189
Krasnopolsky, R., Li, Z.-Y., Shang, H., & Zhao, B. 2012, ApJ, 757, 77
Londrillo, P., & Del Zanna, L. 2000, ApJ, 530, 508
Lynden-Bell, D. 1996, MNRAS, 279, 389
McCourt, M., O'Leary, R. M., Madigan, A.-M., & Quataert, E. 2015, MNRAS, 449, 2
McNally, C. P., Lyra, W., & Passy, J.-C. 2012, ApJS, 201, 18
Menon, H., Wesolowski, L., Zheng, G., et al. 2015, Comput. Astrophys. Cosmol., 2, 1
Monaghan, J. J. 1992, ARA&A, 30, 543
Monaghan, J. J. 2000, J. Comput. Phys., 159, 290
Mouschovias, T. C., & Spitzer, L., Jr 1976, ApJ, 210, 326
Nakamura, M., & Meier, D. L. 2004, ApJ, 617, 123
Orszag, S. A., & Tang, C.-M. 1979, J. Fluid Mech., 90, 129
Pakmor, R., & Springel, V. 2013, MNRAS, 432, 176
Pakmor, R., Bauer, A., & Springel, V. 2011, MNRAS, 418, 1392
Pakmor, R., Pfrommer, C., Simpson, C. M., & Springel, V. 2016, ApJ, 824, L30
Pakmor, R., Gómez, F. A., Grand, R. J. J., et al. 2017, MNRAS, 469, 3185
Phillips, G. J., & Monaghan, J. J. 1985, MNRAS, 216, 883
Price, D. J. 2010, MNRAS, 401, 1475
Price, D. J. 2012, J. Comput. Phys., 231, 759
Price, D. J., & Monaghan, J. J. 2004, MNRAS, 348, 139
Price, D. J., & Monaghan, J. J. 2005, MNRAS, 364, 384
Price, D. J., & Bate, M. R. 2007, MNRAS, 377, 77
Price, D. J., Tricco, T. S., & Bate, M. R. 2012, MNRAS, 423, L45
Price, D. J., Wurster, J., Tricco, T. S., et al. 2018, PASA, 35, e031
Read, J. I., Hayfield, T., & Agertz, O. 2010, MNRAS, 405, 1513
Rieder, M., & Teyssier, R. 2016, MNRAS, 457, 1722
Rosswog, S. 2015, MNRAS, 448, 3628
Rosswog, S., & Price, D. 2007, MNRAS, 379, 915
Shen, S., Wadsley, J., & Stinson, G. 2010, MNRAS, 407, 1581
Springel, V., & Hernquist, L. 2002, MNRAS, 333, 649
Stasyszyn, F. A., & Elstner, D. 2015, J. Comput. Phys., 282, 148
Steinwandel, U. P., Beck, M. C., Arth, A., et al. 2019, MNRAS, 483, 1008
Stone, J. M., Gardiner, T. A., Teuben, P., Hawley, J. F., & Simon, J. B. 2008, ApJS, 178, 137
Su, K.-Y., Hopkins, P. F., Hayward, C. C., et al. 2017, MNRAS, 471, 144
Tóth, G. 2000, J. Comput. Phys., 161, 605
Tricco, T. S., & Price, D. J. 2012, J. Comput. Phys., 231, 7214
Tricco, T. S., & Price, D. J. 2013, MNRAS, 436, 2810
Tricco, T. S., Price, D. J., & Bate, M. R. 2016, J. Comput. Phys., 322, 326
Tsukamoto, Y., Iwasaki, K., & Inutsuka, S.-I. 2013, MNRAS, 434, 2593
Tsukamoto, Y., Iwasaki, K., Okuzumi, S., Machida, M. N., & Inutsuka, S. 2015a, ApJ, 810, L26
Tsukamoto, Y., Iwasaki, K., Okuzumi, S., Machida, M. N., & Inutsuka, S. 2015b, MNRAS, 452, 278
Uchida, Y., & Shibata, K. 1986, Can. J. Phys., 64, 507
Uhlig, M., Pfrommer, C., Sharma, M., et al. 2012, MNRAS, 423, 2374
Ustyugova, G. V., Lovelace, R. V. E., Romanova, M. M., Li, H., & Colgate, S. A. 2000, ApJ, 541, L21
Valdarnini, R. 2016, ApJ, 831, 103
Wadsley, J. W., Veeravalli, G., & Couchman, H. M. P. 2008, MNRAS, 387, 427
Wadsley, J. W., Keller, B. W., & Quinn, T. R. 2017, MNRAS, 471, 2357
Wang, P., & Abel, T. 2009, ApJ, 696, 96
Wendland, H. 1995, Adv. Comput. Math., 4, 389
Wurster, J., Price, D., & Ayliffe, B. 2014, MNRAS, 444, 1104
Wurster, J., Price, D. J., & Bate, M. R. 2016, MNRAS, 457, 1037
Wurster, J., Bate, M. R., Price, D. J., & Tricco, T. S. 2017, ArXiv e-prints [arXiv:1706.07721]

Magnetorotational instability with smoothed particle hydrodynamics

Wissing, R., Shen, S., Wadsley, J., Quinn, T.

II

Astronomy & Astrophysics

Magnetorotational instability with smoothed particle hydrodynamics

Robert Wissing, Sijing Shen, James Wadsley, and Thomas Quinn

Institute of Theoretical Astrophysics, University of Oslo, Postboks 1029, 0315 Oslo, Norway
e-mail: robertwi@astro.uio.no

ABSTRACT

The magnetorotational instability (MRI) is an important process in driving turbulence in sufficiently ionized accretion disks. It has been extensively studied using simulations with Eulerian grid codes, but remains fairly unexplored for meshless codes. Here, we present a thorough numerical study on the MRI using the smoothed particle magnetohydrodynamics method with the geometric density average force expression. We performed 37 shearing box simulations with different initial setups and a wide range of resolution and dissipation parameters. We show, for the first time, that MRI with sustained turbulence can be simulated successfully with smoothed-particle hydrodynamics (SPH), with results consistent with prior work with grid-based codes, including saturation properties such as magnetic and kinetic energies and their respective stresses. In particular, for the stratified boxes, our simulations reproduce the characteristic "butterfly" diagram of the MRI dynamo with saturated turbulence for at least 100 orbits. On the contrary, traditional SPH simulations suffer from runaway growth and develop unphysically large azimuthal fields, similar to the results from a recent study with meshless methods. We investigated the dependency of MRI turbulence on the numerical Prandtl number (P_m) in SPH, focusing on the unstratified, zero net-flux case. We found that turbulence can only be sustained with a Prandtl number larger than ∼2.5, similar to the critical values for the physical Prandtl number found in grid-code simulations. However, unlike grid-based codes, the numerical Prandtl number in SPH increases with resolution, and for a fixed Prandtl number, the resulting magnetic energy and stresses are independent of resolution. Mean-field analyses were performed on all simulations, and the resulting transport coefficients indicate no α-effect in the unstratified cases, but an active $\alpha\omega$ dynamo and a diamagnetic pumping effect in the stratified medium, which are generally in agreement with previous studies. There is no clear indication of a shear-current dynamo in our simulation, which is likely to be responsible for a weaker mean-field growth in the tall, unstratified, zero net-flux simulation.

Key words. methods: numerical – ISM: magnetic fields – magnetohydrodynamics (MHD)

1. Introduction

A popular mechanism for the generation of turbulence within accretion disks is the magnetorotational instability (MRI; Velikhov 1959; Chandrasekhar 1960; Fricke 1969; Balbus & Hawley 1991), which is a local linear instability that occurs for magnetic fields in Keplerian-like flows (e.g., accretion disks). The ensuing turbulence subsequently acts as a driver for angular momentum transport within the disk, allowing efficient mass accretion onto the central object (Shakura & Sunyaev 1973; Lynden-Bell & Pringle 1974). Due to its simple prerequisites of "activating" the instability (negative angular momentum gradient, weak magnetic field, and sufficiently ionized gas), the MRI is potentially a crucial component in many different astrophysical systems.

While the linear behavior of the MRI is well established (Balbus & Hawley 1991, 1992; Curry et al. 1994; Goodman & Xu 1994; Kersalé et al. 2004), the nonlinear phase is an active area of research. Modeling the full nonlinear behavior of the MRI requires numerical simulations, which for the past few decades have been readily applied to study the MRI in both global (Penna et al. 2010; Hawley et al. 2011, 2013; Parkin & Bicknell 2013; Deng et al. 2020) and local (Hawley et al. 1995) setups. While global simulations allow the inclusion of global properties such as winds, jets, and accre-

tion, they require extensive computational resources to properly resolve the MRI growth rates. Sano et al. (2004) found that a minimum of six grid zones per MRI wavelength (λ_{MRI}) was required to model the linear phase. This criterion was further extended to the nonlinear regime by Noble et al. (2010), where an effective quality parameter (Q) was used to gauge the resolution requirement for correct MRI behavior. On the other hand, local setups allow higher resolution and remain simple and well-posed for investigating the nonlinearity and saturation of the MRI under specific initial conditions. In general, local setups apply a shearing box approximation (Goldreich & Lynden-Bell 1965; Hawley et al. 1995), which models either a small unstratified block of gas within the disk (neglecting gravity) or a slice of the disk with a vertically stratified density field (including the vertical gravity component). The initial configuration of the magnetic field is an important factor for the behavior and saturation of the MRI, and most studies apply either a constant mean magnetic field through the box (often referred to as the net flux case NF; Hawley et al. 1995; Sano et al. 2004; Guan et al. 2009; Simon et al. 2009) or an initial magnetic field which has a zero mean-field value (often referred to as the zero net flux case ZNF; Hawley et al. 1996; Fromang & Papaloizou 2007; Simon & Hawley 2009; Bodo et al. 2011). Both cases are idealized setups. In reality, the mean-field within local patches of the disk (with sizes around the scale height of disk) varies in

time due to larger-scale current structures and nonideal magneto-hydrodynamic (MHD) effects. In general, the initial mean-field within local setups is either along an azimuthal or vertical direction, as any radial mean-field leads to a constant increase in the azimuthal mean-field due to the shear.

The turbulence generated by the MRI is subcritical, which means that it requires a self-sustaining process to remain active (Rincon et al. 2007; Herault et al. 2011; Riols et al. 2013). A physical explanation for the turbulence saturation in the vertical net-flux case was proposed by Goodman & Xu (1994), Pessah & Goodman (2009), and Latter et al. (2009), in which saturation is driven by parasitic (secondary) instabilities that break down the so-called channel modes (axisymmetric radial streaming motions) generated by the primary (fastest-growing) MRI modes. These correspond to both Kelvin-Helmholtz instabilities which feed off the shear in the velocity field and tearing mode instabilities which feed off the current density. The secondary instabilities themselves eventually decay into small-scale turbulence which then, in combination with the vertical net-flux, regenerate the MRI modes, creating a self-sustaining loop. The mechanism for saturation becomes more difficult to pinpoint when there is no global mean-field in the box (ZNF), since both the magnetic field and turbulence are required to sustain each other. In addition, the unstratified ZNF case is statistically symmetric, which means that there are no net helicities within the flow, and this makes the generation of local mean-fields more difficult. However, dynamo cycles and coherent local mean-field growth have been observed in previous simulations of the unstratified ZNF case (Shi et al. 2016). The underlying process of growth still remains uncertain, but the two primary theories are the stochastic alpha effect (Vishniac & Brandenburg 1997; Silant'ev 2000; Heinemann et al. 2011) and the magnetic shear current effect (Rogachevskii & Kleeorin 2003, 2004; Squire & Bhattacharjee 2015a), which we examine in more detail in the upcoming sections.

Adding stratification to the shearing box represents a more realistic view of the accretions disk and brings forth new mechanisms that act on the behavior and saturation of the system. The stratified case enables buoyancy instabilities, which transports magnetic fields from the outer central region upward. Beyond $|z| > 2H$, the gas is magnetically dominated, less turbulent and buoyantly unstable (e.g., Shi et al. 2010; Guan & Gammie 2011). Meanwhile, the sign of the field flips within the mid-plane and this becomes a cyclical behavior that occurs around every 10 orbits (producing the characteristic butterfly diagram). This behavior of the magnetic field indicates an active mean-field dynamo (e.g., Brandenburg et al. 1995a; Stone et al. 1996; Hirose et al. 2006; Gressel 2010; Davis et al. 2010; Simon et al. 2011). The stratified disk dynamo is complicated, likely involving several mechanisms acting together; as such the cyclic behavior observed within these simulations still remains unclear. While the buoyancy instabilities dominate the regions beyond the scale height, the central region remain buoyantly stable, requiring an alternative mechanism in this region (Shi et al. 2010; Gressel 2010). One such mechanism is through the alpha-effect, or more explicitly the outward transport of small scale magnetic helicity flux (Vishniac & Cho 2001; Subramanian & Brandenburg 2004). Another mechanism that can advect magnetic fields is turbulent pumping which can expel magnetic field from high turbulent regions to lower turbulent regions (Gressel 2010). In addition, the dynamo mechanisms in the unstratified case likely plays a role here too, as the unstratified case represents an approximation of the mid-plane in the disk (Lesur & Ogilvie 2008; Käpylä & Korpi 2011).

The stratified shearing box is also dependent on the strength and geometry of the global magnetic mean-field, showing a wide range of different behaviors. For example, compared to an azimuthal mean-field, the presence of a vertical mean-field greatly enhances the stress within the fluid and exhibits powerful outflows which can increase the removal of angular momentum from the disk (Suzuki & Inutsuka 2009; Guan & Gammie 2011; Simon et al. 2011, 2013; Bai & Stone 2011).

Seminal work by Fromang et al. (2007) showed that for the ZNF unstratified case the saturated turbulence level decreased with higher resolution. This highlighted the importance of small-scale dissipation for the MRI. Further work has shown that more or less all MRI cases are sensitive to the small-scale dissipation, where kinematic viscosity (ν) and magnetic resistivity (η) play a major role. The ratio between the two, the so-called magnetic Prandtl number ($P_m = \nu/\eta$), is shown to be fundamentally important in determining the MRI saturation and the stress, and in general the behavior of MHD turbulence in any system (Schekochihin et al. 2004a,b; Federrath et al. 2014; Federrath 2016). In nature, galaxies, galaxy clusters and molecular clouds have magnetic Prandtl numbers far greater than unity ($P_m \gg 1$). For example, in molecular clouds $P_m \approx 10^{10}$ (Federrath 2016). On the opposite extreme, protostellar disks and stars usually have magnetic Prandtl numbers much smaller than unity ($P_m \ll 1$) (Brandenburg & Subramanian 2005; Schekochihin et al. 2007). In MRI simulations, the Prandtl number can be either physical, where explicit dissipation is added to the system, or numerical, which is determined by the numerical dissipation of the numerical scheme. Higher Prandtl numbers generally increase the angular momentum transport (Fromang & Papaloizou 2007; Lesur & Longaretti 2007; Simon et al. 2009; Simon & Hawley 2009; Fromang et al. 2010). In the low Prandtl number limit, while the NF case still exhibits MRI turbulence and saturates at a low but finite value of angular momentum transport (Meheut et al. 2015), in the ZNF case turbulence cannot be sustained for Prandtl numbers below a certain critical value ($P_m < 2$ in Fromang et al. 2007)[1]. In addition, the convergence behavior of the MRI turbulence and the critical Prandtl number can also be sensitive to the vertical aspect ratio of the domain: while simulations with standard box (with vertical-over-radial aspect ratio, $L_z/L_x = 1$) exhibit decreased stress levels with increasing resolution, in the tall-box simulations ($L_z/L_x > 2.5$) the stress levels are converged. The stress saturation still depends on the Prandtl number in the tall boxes, albeit with a somewhat lower critical value and with longer lifetimes (Shi et al. 2016).

While a lot of the focus surrounding the Prandtl number has revolved around the physical Prandtl number, not many studies have been done on the numerical Prandtl number. Numerical dissipation acts differently compared to physical dissipation, depending heavily on the fluid flow and the resolution. How well the numerical Prandtl number relates to the observed dependency on the physical Prandtl number for MHD turbulence is still unclear, but a similar dependency is expected. The consequence of not knowing the numerical Prandtl number and its resolution dependency in MRI simulations is clear, as a low-order resistive scheme with a high-order viscosity scheme will eventually result in a low P_m value and can lead to misinterpretation in convergence studies. The numerical Prandtl number

---

[1] The critical Prandtl number is itself dependent on the Reynolds number, however no study have found a critical Prandtl number lower than $P_{m,c} = 2$ for the standard box.

has been investigated in several grid codes (Fromang et al. 2007 [with ZEUS] Lesaffre & Balbus 2007 [with ZEUS3D] Simon et al. 2009 [with ATHENA] Federrath et al. 2011 [with FLASH]), which have found a Prandtl number of around $P_m \sim 2$ with a very weak dependency on resolution. However, the true P_m value during nonlinear MRI simulation remains uncertain as the numerical dissipation is not readily available for grid codes and requires comparison to analytical work or analysis of Fourier transfer functions with certain assumptions and constraints. The estimates of the numerical Prandtl number in these papers are taken for subsonic flows and might significantly change for higher Mach flows. In this paper, we take a closer look at the numerical Prandtl number in SPH and see how it affects the turbulence within MRI simulations.

The vast majority of MRI simulations have been carried out with Eulerian grid-based codes. There have only been a handful of studies investigating the MRI with meshless methods in 2D (Gaburov & Nitadori 2011; Pakmor & Springel 2013; Hopkins & Raives 2016) and in 3D (Deng et al. 2019). The MRI is an especially difficult test for meshless codes due to the strong divergence-free constraint, which in Eulerian codes can be enforced to machine precision with the constrained transport method (Evans & Hawley 1988). However, improved divergence cleaning methods in recent years have been developed for meshless codes, which significantly reduce the divergence errors (Tricco & Price 2012; Tricco et al. 2016). A benefit of Lagrangian methods such as SPH is that they are always Galilean invariant and do not suffer from advection errors, which can otherwise be an issue for Eulerian codes in simulations with large bulk flows. In addition, SPH is naturally adaptive in resolution, making it ideal for simulations involving a wide range of spatial scales. Understanding the numerical aspects of the MRI in SPH is important, as SPH is widely used in astrophysical simulations where the MRI can be present.

In Deng et al. (2019) the authors investigated the MRI in 3D with the meshless finite mass (MFM) and the SPH methods for a wide array of different initial magnetic field configurations. For the unstratified NF case, it was shown that MFM and SPH showed similar behavior to Eulerian grid-based codes. However, for the unstratified ZNF case, both MFM and SPH showed rapid decay of the turbulence. This is likely related to the numerical dissipation schemes of the two methods, which we investigate for SPH in this paper. For the stratified azimuthal NF case, the MFM method could correctly produce the characteristic dynamo cycles for around 50 to 70 orbits before the turbulence eventually died out. SPH on the other hand could not develop sustained turbulence and instead developed unphysically strong azimuthal fields. This was attributed to a combination of discretization errors of the magnetic field in the radial component and divergence cleaning amplifying the vertical field component. In this paper, we further investigate this case with the newly developed geometric density SPH (GDSPH), which has been shown to improve the accuracy of SPH in problems involving large density gradients. Specifically, it allows grid-scale instabilities to grow that are suppressed in traditional SPH (Wadsley et al. 2017; Wissing & Shen 2020).

In this paper, we have performed MRI simulations of the unstratified NF case in the regular-sized box ($L_z/L_x = 1$) and the unstratified ZNF case in both regular and taller sized boxes ($L_z/L_x = 4$ as in Shi et al. 2016) with varying resolution and numerical dissipation parameters. We have investigated the numerical Prandtl number in SPH and its effect on the amplification and saturation of the MRI. We have also performed simulations on the stratified NF case with both the traditional

SPH method (TSPH)[2] and the GDSPH method to further investigate the unphysical growth in the azimuthal fields observed in Deng et al. (2019). For these simulations, we also vary the resolution and strength of the numerical dissipation. In addition, to all the simulations we also investigate the turbulent transport coefficients.

This paper is organized as follows. In Sect. 2, we go through the basics of dynamo theory, the simulation setup, and the post-process analysis. In Sect. 3, we present our result for the unstratified NF and ZNF cases and in Sect. 4 we present our result for the stratified case. In Sect. 5, we discuss our results and present some concluding remarks.

2. Theory

2.1. Dynamo theory

A magnetic dynamo describes the exponential growth and sustenance of magnetic fields due to being stretched, twisted, and folded by the underlying fluid motions. While specific velocity field configurations can lead to dynamo action (laminar dynamo), astrophysical fluids are usually highly turbulent, where motion is chaotic across a large range of spatial scales. Dynamo action can occur across all turbulent scales, but the magnetic field is stretched faster by the smaller scale motions than the larger-scale ones, leading to a faster growth on smaller scales (known as the small-scale dynamo) (Kulsrud & Anderson 1992; Kulsrud 1999). In ideal MHD, the growth rate is set primarily by the viscous scale of the fluid. However, for MHD with diffusion of the magnetic field (resistivity), this is no longer necessarily true, as the magnetic fields on small-scales can now be damped quickly. This makes the growth of the magnetic field more intricate, as it is determined by the relationship between the viscous scale l_v and the resistive scale l_η (Spitzer 1962). The ratio between these two, the magnetic Prandtl number $P_m = \frac{l_v}{l_\eta}$ is thus very important in the resulting characteristic and saturation of the turbulent dynamo (Schekochihin et al. 2004a). For $P_m > 1$ the quickest twisting and folding of the magnetic field is driven at the viscous scale, where the underlying velocity field is smooth as there are no smaller velocity structures in the flow at this scale. The chaotic but smooth motion at this scale lends itself to dynamo action, which means that magnetic fields can efficiently be generated (Vaĭnshteĭn & Zel'dovich 1972; Zeldovich 1983; Zeldovich et al. 1990). The cut-off scale of magnetic fluctuations will still be set by the resistive scale, which allows for a buildup of power within the subviscous range. With higher P_m values than one, more of the subviscous scale becomes available for magnetic field amplification (Kulsrud & Anderson 1992; Schekochihin et al. 2004a).

The small-scale dynamo has been shown to be a possible mechanism for amplifying the weak seed fields in the early universe to magnitudes observed in galaxies today (Boulares & Cox 1990; Beck et al. 1996; Kulsrud et al. 1997). However, magnetic fields in the universe exhibit a high degree of coherence at scales larger than the underlying turbulent motion (Beck et al. 2005; Beck 2015). Large-scale dynamo theory is an attempt to explain how these coherent large-scale magnetic field structures can be generated in highly turbulent environments. In essence, it

---

[2] By traditional SPH we mean the MHD equations that are derived directly from the Euler-Lagrange equations with the traditional SPH density estimate $\rho_a = \sum_b m_b W_{ab}$. See Price (2012) for more information.

investigates how the small-scale kinetic and magnetic fluctuations couple to the underlying large-scale field.

To figure out the effect of the small-scale field on the large-scale field, it is useful to introduce the formalism of mean-field theory (Moffatt 1978; Parker 1979; Krause & Raedler 1980; Ruzmaikin et al. 1988; Brandenburg & Subramanian 2005). Assuming a scale separation between the large-scale and small-scale, both the magnetic and velocity fields can be decomposed to a mean field component ($\overline{B}$ and $\overline{U}$) and a fluctuating component (b and u):

$$B = \overline{B} + b, \qquad U = \overline{U} + u. \tag{1}$$

Averaging the induction equation leads to the evolution equation for the magnetic mean-field:

$$\frac{\partial \overline{B}}{\partial t} = \nabla \times (\overline{U} \times \overline{B}) + \nabla \times \mathcal{E} + \eta \nabla^2 \overline{B}. \tag{2}$$

Here U represents the large-scale velocity structure, η the magnetic diffusivity and $\mathcal{E}$ is the electromotive force (EMF) produced by the fluctuating fields:

$$\mathcal{E} = \overline{u \times b}. \tag{3}$$

By studying how the fluctuating u and b fields reacts to an applied mean field, it can be shown that both u and b contain a component independent of the mean-field and an additional term which is linearly dependent on the applied mean-field:

$$b = b_0 + b_{\overline{B}}, \qquad u = u_0 + u_{\overline{B}}. \tag{4}$$

Assuming the independent terms b_0 and u_0 are uncorrelated ($\mathcal{E}_0 = \overline{u_0 \times b_0} = 0$) and the assumption of scale separation, we can expand $\mathcal{E}$ in a Taylor series in $\overline{B}$ and $\overline{U}$:

$$\mathcal{E}_i = \alpha_{ij} \overline{B}_j - \eta_{ij} \overline{J}_j + \gamma_{ij} \overline{\Omega}_j + \ldots \tag{5}$$

Here α, η and γ are the tensorial transport coefficients and $\overline{J} = \overline{\nabla \times B}$ is the mean-field current density and $\overline{\Omega} = \overline{\nabla \times U}$ is the mean-field vorticity. The first term of Eq. (5) is the α-effect in which the small-scale turbulence generates an EMF which is proportional to the mean-field itself. This effect, coupled together with differential rotation, can develop the well-known $\alpha\omega$ dynamo. The alpha-effect depends crucially on the small-scale helcities within the turbulent flow, which require the system to break statistical symmetry either by stratification or through having a net helicity (Pouquet et al. 1976; Moffatt 1978; Brandenburg & Subramanian 2005). The second term in Eq. (5) generates an EMF in proportion to the mean-current and can act to either amplify or diffuse the mean-field. The last term of Eq. (5) is the Yoshizawa effect, which acts without the need for a large-scale magnetic field and can be seen as a turbulent battery mechanism (Yoshizawa & Yokoi 1993; Yokoi 2013). In addition to a mean vortical velocity component, the effect requires small-scale cross-helicity between the turbulent fields $(\overline{u \cdot b})^3$.

In this paper, we are interested in the dynamo action that arises within shearing boxes (see Sect. 2.2 for coordinate definitions and simulation setup). We define our mean-field by taking a horizontal average:

$$\overline{X} = \frac{\int X \mathrm{d}x \mathrm{d}y}{\int \mathrm{d}x \mathrm{d}y}. \tag{6}$$

---

[3] A global magnetic field is probably required to create cross-helicity in a turbulent field. Cross-helicity is shown to occur when the mean-field is parallel to the direction of gravity in Rüdiger et al. (2011).

102

The turbulent field can then be calculated by removing the mean-field component from the total field (see Eq. (1)). For the velocity, the mean-field is determined from the shearing box approximation ($U_0 = -q\Omega x\hat{\boldsymbol{y}}$). Here Ω is the angular velocity and q is the shearing parameter, which for Keplerian disks is $q = 3/2$. Since the horizontal average is only a function of z, Eq. (5) and subsequently Eq. (2) simplifies greatly ($\overline{B_z} = 0$, $\overline{J_z} = 0$, and $\overline{\Omega_z} = 0$):

$$\mathcal{E}_x = \alpha_{xx} \overline{B}_x + \alpha_{xy} \overline{B}_y - \eta_{xx} \overline{J}_x - \eta_{xy} \overline{J}_y, \tag{7}$$

$$\mathcal{E}_y = \alpha_{yx} \overline{B}_x + \alpha_{yy} \overline{B}_y - \eta_{yx} \overline{J}_x - \eta_{yy} \overline{J}_y, \tag{8}$$

$$\frac{\partial \overline{B}}{\partial t}_x = -\partial_z(\alpha_{yx} \overline{B}_x) - \partial_z(\alpha_{yy} \overline{B}_y) + \partial_z(\eta_{yx} \overline{J}_x) + \partial_z((\eta_{yy} + \eta) \overline{J}_y), \tag{9}$$

$$\frac{\partial \overline{B}}{\partial t}_y = -q\overline{B}_x + \partial_z(\alpha_{xx} \overline{B}_x) + \partial_z(\alpha_{xy} \overline{B}_y) - \partial_z((\eta_{xx} + \eta) \overline{J}_x) - \partial_z(\eta_{xy} \overline{J}_y). \tag{10}$$

The γ terms from Eq. (5) become zero as our only component of $\overline{\Omega}$ is in the z direction. The diagonal components α_{xx} and α_{yy} are the main driver of the alpha effect, generating a feedback loop between the radial and azimuthal fields. The sign of diagonal components will depend on $\Omega \cdot g$ (here g is the gravitational acceleration) which will give us an odd symmetry around the midplane of our stratified box simulations. Depending on the gradient of the α parameter and structure of the magnetic field, it will either work in accordance or in discordance with the field. The antisymmetric components α_{xy} and α_{yx} can be related to the diamagnetic pumping term $\gamma_z = \frac{1}{2}(\alpha_{yx} - \alpha_{xy})$ and describes the transport of mean-fields due to the turbulence. In a similar fashion, the diagonal components η_{xx} and η_{yy} describe the diffusion of the mean-field due to the turbulence. Finally, we have the off-diagonal components η_{xy} and η_{yx} that are responsible for the dynamo produced by the $\Omega \times J$ effect (Rädler 1969) and the shear current effect (Rogachevskii & Kleeorin 2003). These equations provide a powerful tool to connect our simulation data to the mean-field theory. To calculate the transport coefficients we can fit Eqs. (7) and (8) to output data from our simulations. One starts by calculating

$$A_1 = \left[\overline{B}_x \mathcal{E}_x, \overline{B}_y \mathcal{E}_x, \overline{J}_x \mathcal{E}_x, \overline{J}_y \mathcal{E}_x \right], \tag{11}$$

and

$$A_2 = \left[\overline{B}_x \mathcal{E}_y, \overline{B}_y \mathcal{E}_y, \overline{J}_x \mathcal{E}_y, \overline{J}_y \mathcal{E}_y \right], \tag{12}$$

and the matrix

$$M = \begin{pmatrix} \overline{B_x B_x} & \overline{B_x B_y} & \overline{B_x J_x} & \overline{B_x J_y} \\ \overline{B_y B_x} & \overline{B_y B_y} & \overline{B_y J_x} & \overline{B_y J_y} \\ \overline{J_x B_x} & \overline{J_x B_y} & \overline{J_x J_x} & \overline{J_x J_y} \\ \overline{J_y B_x} & \overline{J_y B_y} & \overline{J_y J_x} & \overline{J_y J_y} \end{pmatrix}. \tag{13}$$

Then we solve the following matrix equations (using a least-square method):

$$A_1 = MC_1 \quad \text{and} \quad A_2 = MC_2 \tag{14}$$

for the transport coefficients:

$$C_1 = (\alpha_{xx}, \alpha_{xy}, -\eta_{xx}, -\eta_{xy}) \quad \text{and} \quad C_2 = (\alpha_{yx}, \alpha_{yy}, -\eta_{yx}, -\eta_{yy}). \tag{15}$$

Because the mean-field is not solely evolved by $\mathcal{E}$ but also by the shearing and dissipation of the field, significant errors can arise in the transport coefficients from the correlation between

different components. The main harmful error comes from correlations with $\overline{B}_x$ (due to the shear term). We can improve the signal and reduce the noise by minimizing the influence of $\overline{B}_x$ with the following two approximations. First, we set the diagonal transport coefficients to be equal ($\alpha_{xx} = \alpha_{yy}$ $\eta_{xx} = \eta_{yy}$), which have been shown to be an accurate approximation (Hubbard et al. 2009; Gressel 2010). The second approximation is to set $\alpha_{yx} = 0$, $\eta_{xy} = 0$ which is justified by the fact that $\overline{B}_x \ll \overline{B}_y$ (Squire & Bhattacharjee 2015b). However, we have seen that including α_{yx}, η_{xy} does not significantly change the result for the other transport coefficients. For comparison with previous studies, in the stratified case we allow a nonzero α_{yx} and η_{xy}, and allow α_{xx} and α_{yy} to be different.

What causes the dynamo growth within shearing box simulations of the MRI remains uncertain and remains an active area of research. The unstratified shearing box simulations develop a so-called nonhelical shear dynamo which cannot be generated by the α-effect (in the traditional sense) as there is no net kinetic/magnetic helicity or density stratification within the flow. This implies that the mean of the α coefficients will tend toward zero. However, the α coefficients for a finite-sized system will fluctuate in time. If the fluctuations are sufficiently large, this has shown to enable dynamo growth. This has been called the incoherent-α dynamo, which could explain the dynamo mechanism in unstratified shearing boxes (Vishniac & Brandenburg 1997; Silant'ev 2000; Heinemann et al. 2011). However, a potential issue with the incoherent-α dynamo is that the mean fluctuations in α becomes smaller as the size of the box is increased, which decreases the growth rate of the dynamo. Another potential mechanism for the dynamo is the magnetic shear-current effect, which depends crucially on the off-diagonal turbulent resistivity coefficient η_{yx} (Rogachevskii & Kleeorin 2003; Squire & Bhattacharjee 2015a,b,c). The idea of the magnetic shear-current effect is that a bath of magnetic fluctuations under the influence of an azimuthal field produces an EMF that generates radial fields which subsequently act to amplify the azimuthal field resulting in a dynamo instability. The instability can be shown to happen if $-\eta_{yx}\Omega_z < 0$ which means that dynamo action is possible from the shear-current effect if η_{yx} is negative. In this paper, we examine the shear-current effect and determine if it agrees well with previous results.

Furthermore, stratification adds several additional mechanisms that can affect the dynamo process. The α-effect can provide dynamo action and has been proposed to be a main driver of the dynamo together with the shear-current effect. Both of these effects can cause a phase-shift between the growing fields, explaining the cyclic nature of the radial and azimuthal fields seen in stratified shearing boxes. In addition, buoyancy instabilities expel the magnetic field outward.

2.2. Simulation setup

For all our simulations we use the MHD version of Gasoline2 with the same default set of code parameters as in Wissing & Shen (2020). The simulations are set up using a shearing box approximation (Goldreich & Lynden-Bell 1965; Hawley et al. 1995), in which a corotating patch of disk with angular velocity Ω at a distance R is used as the computational domain. The patch is assumed small such that curvature can be neglected and we can employ a local cartesian coordinate system with x as the radial direction, y as the azimuthal direction and z as the vertical direction. The additional terms added to the equations of motion are:

$$\left(\frac{dv}{dt}\right)_{\text{shearbox}} = 2q\Omega^2 x\,\hat{x} - 2\mathbf{\Omega} \times \mathbf{v} - \Omega^2 z\,\hat{z}, \quad (16)$$

$$q = -\frac{d\ln\Omega}{d\ln r}.$$

Where the term $2q\Omega^2 x\,\hat{x}$ represents the tidal acceleration, $2\mathbf{\Omega} \times \mathbf{v}$ represents the Coriolis force and $\Omega^2 z\,\hat{z}$ represents the vertical gravitational force from the central object. The equilibrium solution of Eq. (16) will be independent of time and follows a uniform shearing motion in the azimuthal direction

$$\mathbf{v}_y = q\Omega x\,\hat{y}. \quad (17)$$

If any mean radial velocity exists, the simulation box will start to oscillate with an epicyclic frequency of $\kappa = 2\Omega\sqrt{1 - q/2}$. This can be the case if set initially or if momentum is not tightly conserved. SPH conserves both momentum and energy very tightly and only suffers from nonconservation in the strong-field regime ($\beta < 2$) in the presence of large divergence errors. The shear parameter q is set to follow a Keplerian profile ($q = 3/2$) and the angular velocity is set to $\Omega = 1.0$. For our periodic boundaries we do not employ explicit ghost or boundary particles, the particles across the boundary interact and exchange forces as regular. Position and velocities are relative to the central particle and neighbors across the boundaries receive a position offset of one domain length (L_x, L_y, L_z). We do not allow for a compact kernel radius that is larger than the smallest domain length of the box, as this would lead to the particle interacting with itself. This could in principle be allowed but would require additional code and some extra overhead. The boundary in the x-direction is shear periodic, which means that particles passing/interacting across the boundary receives an additional velocity offset of $\Delta v = \pm q\Omega L_x\hat{y}$ in which L_x is the length of the domain in the x direction. This is simpler than for grid codes, where shear periodic boundaries require careful reconstruction to retain conservative fluxes across the boundary. While retaining fluxes due to boundary conditions remain simple in SPH, there are other potential flux errors. The main one comes from the divergence error and, more precisely, the removal of the monopole current $v(\nabla \cdot B)$ from the induction equation (Janhunen 2000; Dellar 2001; Price & Monaghan 2005). Removing this term from the induction equation ensures that the surface flux is conserved (which is crucial) and makes the magnetic field divergence become a passive scalar which is simply carried away with the flow. However, in doing this, it is no longer ensured that the volume integral of the magnetic field is conserved (the global mean-field). This issue is shared among the majority of numerical schemes and in this case the error will directly depend on the magnetic field divergence. The error is generally very small but can contaminate the solution, as MRI can be quite sensitive to any global radial mean-field. To avoid this we employ a correction to the flux, which ensures that no global radial mean-fields are generated. We do not employ this correction for simulations with outflow boundaries.

For the unstratified simulations, the last term of Eq. (16) is not included and the domain is periodic in both the y and z directions. For the stratified simulations, all terms are included and the domain is periodic in y and has outflow boundaries in z. The outflow boundary in z is set to remove any element with a smoothing length greater than $h = 0.5 L_x$ to avoid the double-counting of elements across the computational domain. The stratified simulations acquire a density profile of $\rho = e^{-zH}$ with a scale height of $H = c_s/\Omega$ where c_s is the speed of sound. We use an isothermal

equation of state ($P = \rho c_s^2$), with $c_s = 1.0$ set for all simulations. Before simulations are run, the initial particle distribution is relaxed to a glass distribution, then random velocity perturbations of around 5% of the sound speed are added to the shear flow to quickly initiate the MRI.

To determine how well the MRI is resolved , we use the resolution metric developed by Noble et al. (2010) which defines an effective quality parameter (number of resolution elements per MRI wavelength):

$$Q = \frac{\lambda_{\mathrm{MRI}}}{h} = \frac{2\pi v_{\mathrm{A},z}}{\Omega h}, \tag{18}$$

where λ_{MRI} is the characteristic wavelength and is roughly equal to the fastest growing MRI mode, and $v_{\mathrm{A},z}$ is the vertical component of the Alfvén velocity, and h is the resolution length. We follow the example from Deng et al. (2019) where, instead of setting the resolution length to the smoothing length, it is based on the standard deviation of the smoothing kernel. For the Wendland C4 kernel, it gives an effective resolution element length $h_{\mathrm{eff}} = 0.9h$. To properly resolve the linear MRI roughly only $Q > 6$ is required, however, the stress is highly resolution-dependent until a value of roughly $Q_z > 10$ and $Q_y > 20$ is reached (for the stratified NF case Hawley et al. 2011).

As mentioned in the introduction, the magnetic Prandtl number plays a large role in the growth of turbulent dynamos. To gauge the effective Prandtl number from a numerical scheme, the numerical dissipation needs to be determined and translated into an effective kinematic viscosity (ν) and physical resistivity (η). In Eulerian schemes, dissipation comes partly from advection of the fluid which introduces diffusion due to truncation errors in the flux reconstruction. This error will be proportional to both the resolution and the fluid velocity. For shear periodic boundary conditions this means that there will be uneven dissipation due to larger velocities near the edge than the center of domain. Moreover, additional dissipation is added to maintain numerical stability, this is often done through Riemann solvers in grid codes. Estimating the numerical diffusion in Eulerian schemes is not straightforward and often requires comparison to analytical solutions for an accurate estimate.

Compared to Eulerian grid codes, SPH does not suffer from these advection errors and artificial dissipation terms[4] are added to handle flow discontinuities (e.g., shocks). These are primarily discretized from physical dissipation laws, but with diffusion parameters that depend on the resolution and potentially on flow properties. In Monaghan (1985) it was shown that the linear coefficient (α_{AV}) in the artificial viscosity corresponds to a resolution-dependent physical viscosity in the continuum limit, which has been confirmed by several authors (Artymowicz & Lubow 1994; Lodato & Price 2010; Meru & Bate 2012). However, extrapolating to the continuum limit in this case underestimates the physical viscosity/resistivity. It becomes more difficult to estimate the physical dissipation when using particle-pair dependent signal velocities (as is done for our artificial resistivity). In this paper, we opt for another way to estimate the physical dissipation. By recording the energy lost due to artificial dissipation terms, we can directly estimate the parameters from the equivalent physical dissipation equations. From the Navier-Stokes equation we can estimate the shear viscosity with:

$$\nu_{\mathrm{AD}} = \frac{\left(\frac{\mathrm{d}u}{\mathrm{d}t}\right)_{\mathrm{AV}}}{\frac{1}{2}\left(\frac{\partial v^i}{\partial x^j} + \frac{\partial v^j}{\partial x^i}\right)^2 + (\nabla \cdot \boldsymbol{v})^2}. \tag{19}$$

---

[4] The artificial dissipation terms can be seen as approximate Riemann solvers as they functionally produce similar dissipation (Monaghan 1997).

104

Here, we have assumed the fixed ratio between the bulk viscosity and the shear viscosity, which follows from the continuum limit derivation ($\zeta_{\mathrm{AV}} = \frac{5}{3}\nu_{\mathrm{AV}}$) (Lodato & Price 2010). We estimate the physical resistivity from the Ohmic dissipation law:

$$\eta_{\mathrm{AD}} = \frac{\rho}{J^2}\left(\frac{\mathrm{d}u}{\mathrm{d}t}\right)_{\mathrm{AR}}. \tag{20}$$

Taking the ratio of the two equations then gives us the numerical Prandtl number:

$$P_{\mathrm{m,AD}} = \frac{\nu_{\mathrm{AD}}}{\eta_{\mathrm{AD}}}. \tag{21}$$

For some of our simulations we force a certain average numerical Prandtl number $\langle P_{\mathrm{m,AD}}\rangle = \frac{\langle \nu_{\mathrm{AD}}\rangle}{\langle \eta_{\mathrm{AD}}\rangle}$. This is done by adjusting either $\left(\frac{\mathrm{d}u}{\mathrm{d}t}\right)_{\mathrm{AV}}$ and $\left(\frac{\mathrm{d}v}{\mathrm{d}t}\right)_{\mathrm{AV}}$ or $\left(\frac{\mathrm{d}u}{\mathrm{d}t}\right)_{\mathrm{AR}}$ and $\left(\frac{\mathrm{d}B}{\mathrm{d}t}\right)_{\mathrm{AR}}$ by a constant factor such that $\langle P_{\mathrm{m,AD}}\rangle$ corresponds to the desired value. This is the same as changing the artificial dissipation coefficients (α_B, α_{AV}) by a constant factor at each time step.

2.3. Post-process analysis

After the SPH simulations are done, the particle data is interpolated to uniform grid data for post-analysis. To obtain statistical properties of our simulations, we average our data in a few different ways. The first is the horizontal average given in Eq. (6). The second is the volume average:

$$\langle X \rangle = \frac{\int X \mathrm{d}V}{\int \mathrm{d}V} \tag{22}$$

and the final one is the time average:

$$\langle X \rangle_t = \frac{\int X \mathrm{d}t}{\int \mathrm{d}t}. \tag{23}$$

All the averages are in general applied over the whole spatial/time domain of the simulation if not stated otherwise. To quantify the angular momentum transport and the saturation of the MRI, it is useful to calculate the stresses in the fluid. The total stress together with its magnetic and hydrodynamic component is given by:

$$\alpha_{\mathrm{stress}} = -\frac{B_x B_y}{P_0} + \frac{\rho(v_x - \bar{v}_x)(v_y - \bar{v}_y)}{P_0}, \tag{24}$$

where P_0 is the initial pressure(in our case $P_0 = 1$) and ρ is the density and here the first term in the equation represent the Maxwell stress (α_{MW}) and the second term the Reynolds stress (α_{Rey}). A related quantity that we look at is the normalized magnetic stress:

$$\alpha_{\mathrm{mag}} = -2\frac{\langle B_x B_y \rangle}{\langle B^2 \rangle}. \tag{25}$$

In addition to looking at the effect of the total field, we also investigate the contributions from the mean-field ($\overline{B}$) and turbulent component ($\boldsymbol{b}$) in the magnetic energy and the stress. We define their respective normalized stress as in Shi et al. (2016):

$$\alpha_{\mathrm{mag,mean}} = -2\frac{\langle \overline{B}_x \overline{B}_y \rangle}{\langle \overline{B}^2 \rangle}, \qquad \alpha_{\mathrm{mag,turb}} = -2\frac{\langle b_x b_y \rangle}{\langle B^2 - \overline{B}^2 \rangle}. \tag{26}$$

Net-flux standard case (n_x=48)

From α_B= 0.25 to α_B= 4.0
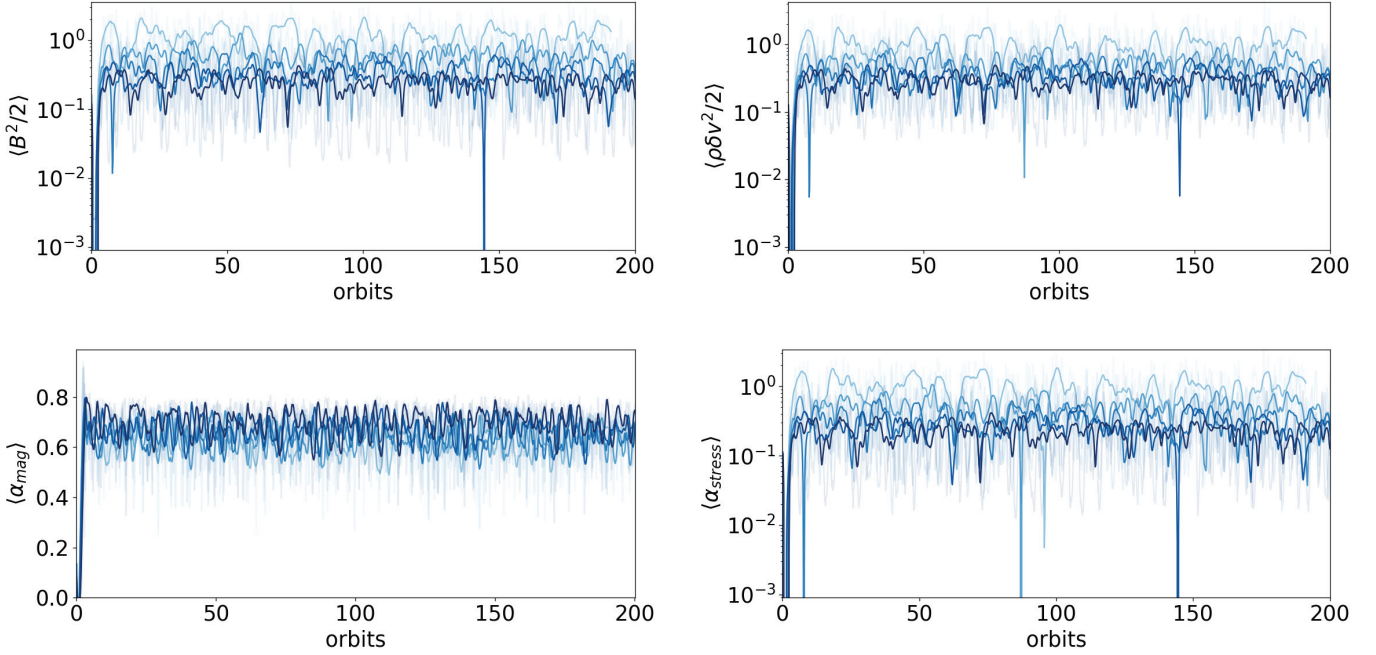
Fig. 1. Time evolution of several volume-averaged quantities over 200 orbits. Magnetic energy (*top left*), kinetic energy (*top right*), normalized Maxwell stress (*bottom left*) and the total stress (*bottom right*). The darkness of the curves is determined by the strength of the artificial resistivity parameter, $\alpha_B = 0.25, 0.5, 1.0, 2.0, 4.0$. Due to the high oscillatory nature of the simulation we have smoothed the curves using a Savitzky–Golay filter, the unsmoothed curves can still be seen as very transparent curves. The oscillations are related to the formation and destruction of channel modes.

Another useful quantity is the Elsasser number, which describes the relative strength of the magnetic dissipation term:

$$\Lambda = \frac{v_A^2}{\eta_{AD}\Omega}. \tag{27}$$

Here, v_A is the Alfvén speed. For a $\Lambda < 1$ the linear properties of the MRI will change significantly and hinder saturation (Blaes & Balbus 1994; Wardle 1999; Balbus & Terquem 2001).

Finally, it is important to track the divergence error in numerical simulations to make sure it remains small and does not severely effect the results:

$$\epsilon_{divB} = \frac{h|\nabla \cdot \boldsymbol{B}|}{|B|}. \tag{28}$$

The mean of this quantity should preferably remain below 10^{-2} but higher values can still be acceptable (depending on the system).

3. Unstratified simulation results

3.1. Net-flux simulations

We setup our simulation with a shearing box of size $L = (1.0, \pi, 1.0)$ with a resolution of $[n_x, n_y, n_z] = [48, 150, 48]$. The magnetic field is initialized with a constant vertical component

$$B = \sqrt{\frac{2P_0}{\beta}}\hat{z}. \tag{29}$$

With a plasma beta of $\beta = 400$ and pressure equal to $P_0 = 1.0$. Using Eq. (18) we can see that we resolve λ_{MRI} with a vertical quality parameter of $Q_z = [22, 30, 45]$. We carry out several

simulations with various artificial resistivity coefficients $\alpha_B = [0.25, 0.5, 1.0, 2.0, 4.0]$, where $\alpha_B = 0.5$ is the code default. The simulations are run for about 200 orbits or until the turbulence dies out. The results of the simulations are shown in Figs. 1–5.

In Fig. 1 we can see that the turbulent dynamo in all the simulations reach a saturated state with a heavily fluctuating magnetic energy density, which is what we expect from the unstratified NF case (Hawley et al. 1995)[5]. From Fig. 2, we can see that as we decrease the resistivity, the magnetic energy and stress increases rapidly, where the total stress goes from $\alpha_{stress} = 0.25$ to 0.9. For the normalized magnetic stress (α_{mag}), we can see that the average lies around 0.65 with only a weak dependency on the resistivity. The normalized magnetic stress is, in general, higher than what has been seen in previous Eulerian grid simulations, where $\alpha_{mag} \approx 0.4$ to 0.6. The magnetic energy and Maxwell stress vary widely in the literature ($\alpha_{stress} = 10^{-2} \rightarrow 10^0$) and our values are similar to the ones reported in Hawley et al. (1995) and Simon et al. (2009). From Fig. 2, the ratio between the Maxwell stress and Reynolds stress(α_{MW}/α_{rey}) shows a value of around 4.0 with an increasing trend for lower resistivity. This is also similar to values reported in Hawley et al. (1995) but somewhat lower than Simon et al. (2009) ($\alpha_{MW}/\alpha_{rey} \approx 7.6$).

The higher α_{mag} can likely be explained by the use of a smaller box size $L = (1.0, \pi, 1.0)$ compared to most other studies, which use $L = (1.0, 2\pi, 1.0)$. A smaller aspect ratio in the NF case does in general show stronger fluctuations in the turbulent state (Bodo et al. 2008; Lesaffre et al. 2009). The stronger fluctuations are a result of suppressing larger MRI modes that

---

[5] We have also performed simulations with excessively strong dissipation $\Lambda < 1$ and simulations with a very weak magnetic field (such that MRI is unresolved) to ensure that the MRI does not grow in these situations.

Net-flux standard case (n_x = 48)
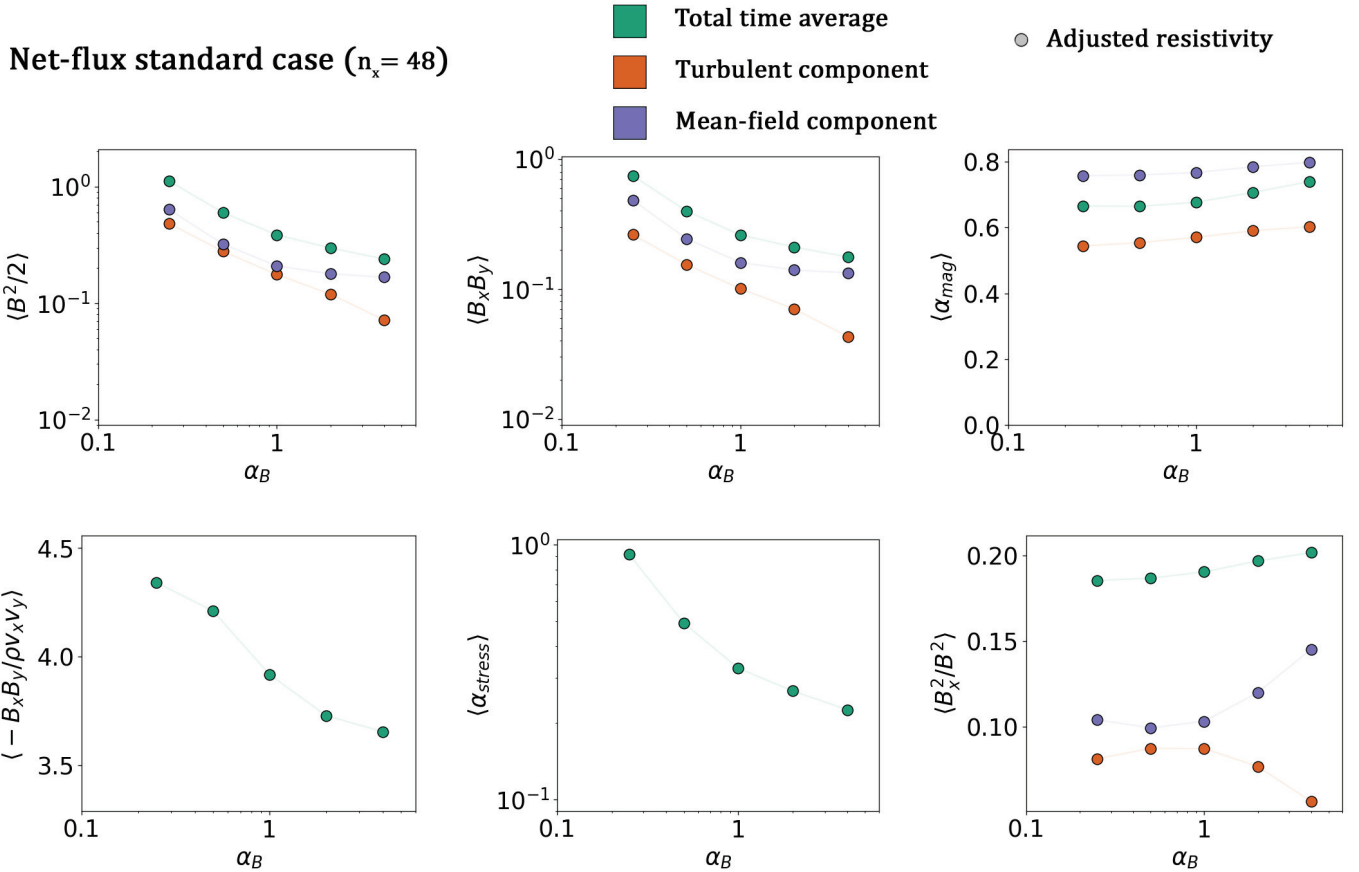
Fig. 2. Time-averaged values of several quantities as a function of the artificial resistivity coefficient, for all our unstratified net-flux simulations. *From the top left to bottom right*: magnetic energy density, Maxwell stress, normalized Maxwell stress, ratio between Reynolds and Maxwell stresses, total stress, ratio between radial and total magnetic field energy. For some quantities we have plotted the total time average (shown in green), the time average of the turbulent component (shown in orange) and the time average of the mean-field component (shown in blue).

would otherwise participate in the nonlinear dynamics, which heavily effect the growth and decay of channel modes. In Fig. 3, we can see an example of the formation and destruction of such a channel mode; during this process the magnetic energy and stress will peak. In addition to being dependent on the aspect ratio of the box, the growth and destruction of these channel modes will depend on the dissipation. This can clearly be seen in Fig. 4 where we see the evolution of the horizontal averaged azimuthal field and stress over a period of thirty orbits for two different resistivities ($\alpha_B = 0.5$ and $\alpha_B = 4$). We can see that during this time channel modes are subsequently formed and destroyed, but with different frequency and behavior. In the high resistivity case, the magnetic energy peaks during channel mode formation but most of the small-scale magnetic fluctuations are quickly suppressed after channel mode breakdown. This means that less of the stress within this case comes from the turbulent component. This can also be seen in Fig. 2, where the mean-field component dominates over the turbulent component at $\alpha_B = 4$ while becoming almost equal at $\alpha_B = 0.5$. Interestingly, the normalized mean-field and turbulent magnetic stresses stays fairly constant $\alpha_{mag,mean} \approx 0.8$ and $\alpha_{mag,turb} \approx 0.55$.

The average divergence error remains either below or close to $\epsilon_{div,err} \approx 10^{-2}$. For the simulations with $\alpha_B = [0.25, 0.5, 1.0, 2.0, 4.0]$ the corresponding time-averaged Prandtl numbers is $\langle\langle P_m \rangle\rangle_t = [1.95, 1.42, 0.96, 0.60, 0.35]$. The standard default value of $\alpha_B = 0.5$ has a $P_m \approx 1.5$. The Elsasser
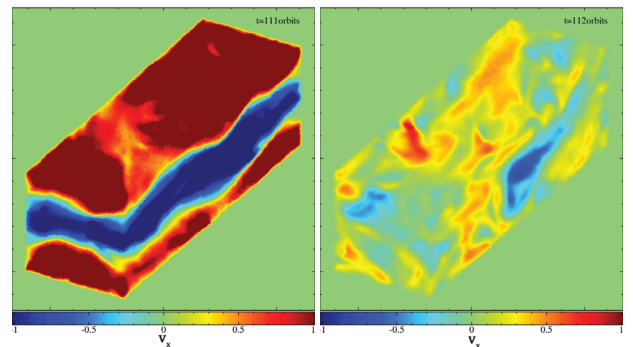

Fig. 3. Generation and break down of a channel mode during the unstratified net-flux run with $\alpha_B = 0.5$. The figure depicts a surface rendering of the radial velocity within the shearing box. The two-channel flow is clearly seen in the left picture which over an orbit is quickly broken down into turbulence, as seen in the right figure. The generation of the channel mode coincides with a peak in the magnetic energy and as the channel flow is destroyed the magnetic energy will decrease. The formation and destruction of these channel flows occur continuously throughout the simulation.

number remains far above 1 for all the cases and the average plasma beta rises linearly with α_B with value between $\beta \approx 5 \rightarrow 20$.

Net-flux case $\alpha_B = 0.5$ Net-flux case $\alpha_B =$
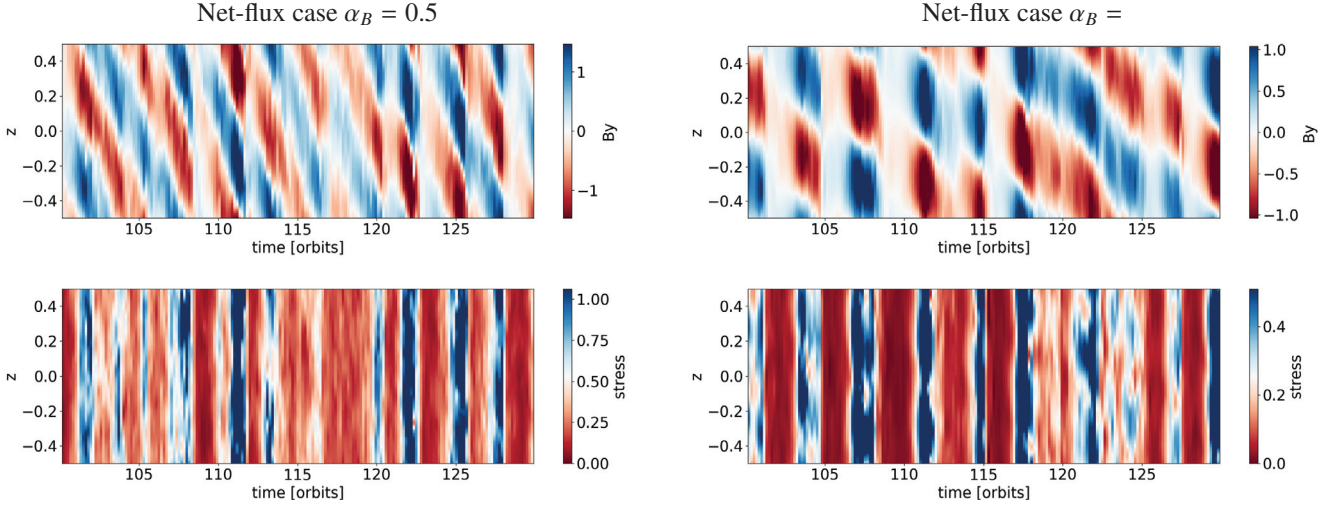
Fig. 4. Spacetime diagrams showing the azimuthal magnetic field at the top and the total stress at the bottom. The *left figures* shows the simulation with an artificial resistivity coefficient $\alpha_B = 0.5$ and the *right figures* show the simulation with $\alpha_B = 4$. The figures clearly show the peaks related to the continuous creation and destruction of channel modes. Increasing the resistivity leads to a suppression of small scale magnetic fluctuation, and this means that more of the stress will be generated by the mean-field component.
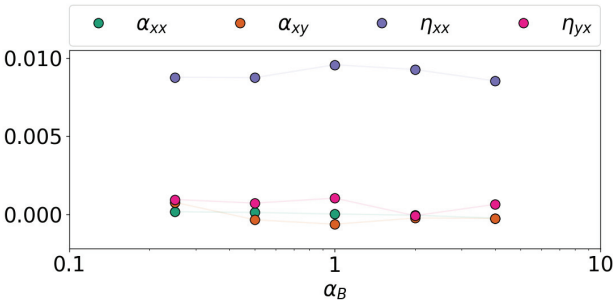
Fig. 5. Time-averaged turbulent transport coefficient from the unstratified net-flux cases. To minimize noise/bias we have set $\alpha_{xx} = \alpha_{yy}$, $\eta_{xx} = \eta_{yy}$, $\alpha_{yx} = 0.0$ and $\eta_{xy} = 0.0$. We can see that only the turbulent resistivity η_{xx} has a consistent value above 0.0, with a value of about 0.008.

Figure 5 shows the time-averaged values of the transport coefficients α_{xx}, α_{xy}, η_{xx} and η_{yx} for all the simulations. From the figure, we can see that both α coefficients have values very close to zero which is to be expected from the unstratified case. η_{yx} does also not have a significant value and remains close to zero. The only value that has a significant value above zero is the turbulent diffusivity which has a value of around $\eta_{xx} \approx 0.008$.

3.2. Zero net-flux simulations

The setup follows from Deng et al. (2019), in which a shearing box together with a varying vertical magnetic field is initialized

$$B = B_0 \hat{z} \sin(2\pi x). \tag{30}$$

Here, B_0 is the initial magnetic field strength and is set such that the volume averaged plasma beta is $\beta = 2P/B^2 = 400$. We run the simulations at three different resolutions $[n_x, n_y, n_z] = [48, 150, 48], [64, 200, 64], [96, 300, 96]$ with a standard box with length $L = (1.0, \pi, 1.0)$. To test the effect of a taller box within SPH, we also run with a domain size of $L = (1.0, \pi, 4.0)$ (same as in Shi et al. 2016), with a resolution of $[n_x, n_y, n_z] = [48, 150, 192]$. Using Eq. (18), we can see that we resolve λ_{MRI} with an initial quality parameter of

$Q_z = [22, 30, 45]$ in each respective resolution. We carry out several simulations at each resolution by varying the artificial resistivity coefficient $\alpha_B = [0.25, 0.5, 1.0, 2.0, 4.0]$ (blue curves in Figs. 6 and 7), where $\alpha_B = 0.5$ is the default value. The corresponding time-averaged Prandtl numbers in the $n_x = 96$ standard box is $\langle\langle P_{\mathrm{m}}\rangle\rangle_t = [2.54, 2.17, 1.35, 0.83, 0.54]$ and in the $n_x = 48$ tall box $\langle\langle P_{\mathrm{m}}\rangle\rangle_t = [1.84, 1.47, 1.11, 0.67, 0.34]$. In addition, we run four cases where we force a certain average numerical Prandtl number by adjusting either the artificial viscosity or the artificial resistivity (see Sect. 2.2). One case is run by adjusting the artificial resistivity, where we force the Prandtl number to be equal to $P_{\mathrm{m,AR}} = 3$ (the red curve in Figs. 6 and 7). Two of the cases adjust the artificial viscosity with $\alpha_B = 0.5$, forcing a Prandtl number of $P_{\mathrm{m,AV}} = 3$ and $P_{\mathrm{m,AV}} = 6$ and one case adjust the artificial viscosity with $\alpha_B = 0.25$, forcing a Prandtl number of $P_{\mathrm{m,AV}} = 0.25$ (green curves in Figs. 6 and 7). The simulations are run for about 200 orbits or until the turbulence dies out. The results of the simulations are shown in Figs. 6–13.

In Fig. 6 we show the time evolution of the magnetic energy, kinetic energy, normalized Maxwell stress, and the total stress for our high-resolution standard box cases with $n_x = 96$. Only four of the nine cases reach a saturated state ($\alpha_B = 0.25$, $P_{\mathrm{m,AR}} = 3$, $P_{\mathrm{m,AV}} = 3$, $P_{\mathrm{m,AV}} = 6$), which all have a Prandtl number of $P_{\mathrm{m}} > 2.5$. The $\alpha_B = 0.5$ case sustain turbulence for about 50 orbits before decaying, and most of the other cases have their turbulence eliminated within the first 30 orbits, similar to what was seen in Deng et al. (2019), where the longest living case was about 20 orbits. An outlier is the evolution of $P_{\mathrm{m,AV}} = 0.25$, where small stress oscillation can still be seen for a long time after the initial decay. This is simply caused by numerical noise, as we force a very low AV for this case together with a low AR coefficient $\alpha_B = 0.25$. In Fig. 7, we show the time evolution of the same quantities for the tall-box simulations with resolution $n_x = 48$. We find that the same four cases reach a saturated state for the tall box ($\alpha_B = 0.25$, $P_{\mathrm{m,AR}} = 3$, $P_{\mathrm{m,AV}} = 3$, $P_{\mathrm{m,AV}} = 6$). The $\alpha_B = 0.5$ case sustain turbulence for a longer time, decaying after around 120 orbits. Most of the other cases have their turbulence eliminated within the first 20 orbits.

In Figs. 8 and 9 we show the time-averaged quantities of the high-resolution ($n_x = 96$), standard box runs and the lower resolution ($n_x = 48$), tall box cases, respectively. For the tall
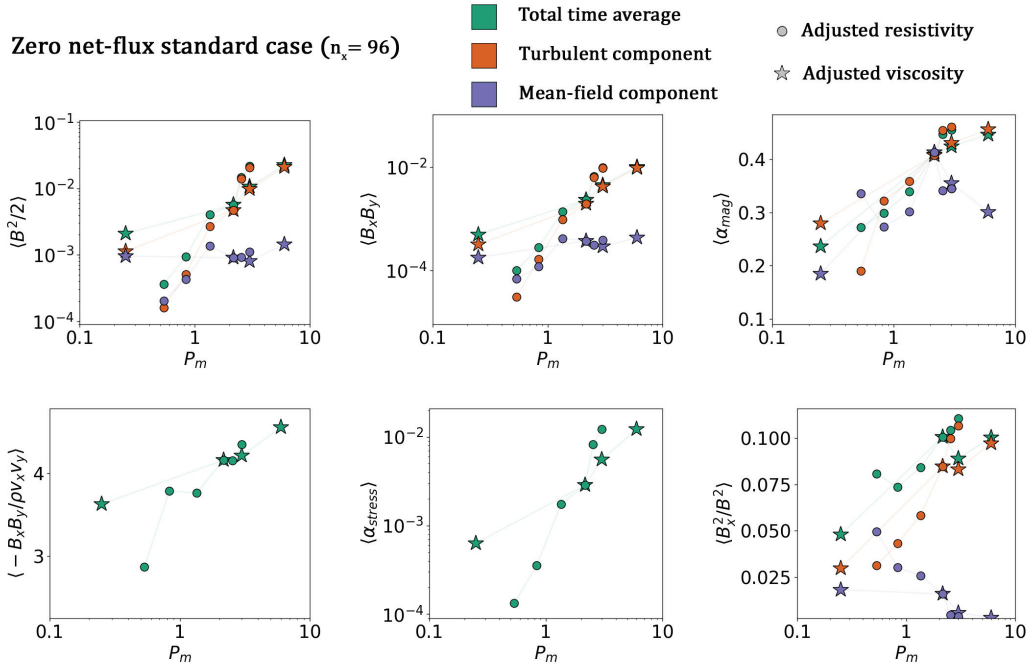
Zero net-flux standard case (n$_x$=96)

P$_{m,AV}$= 0.25, P$_{m,AV}$= 3 and P$_{m,AV}$= 6

From α_B= 0.25 to α_B= 4

P$_{m,AR}$= 3
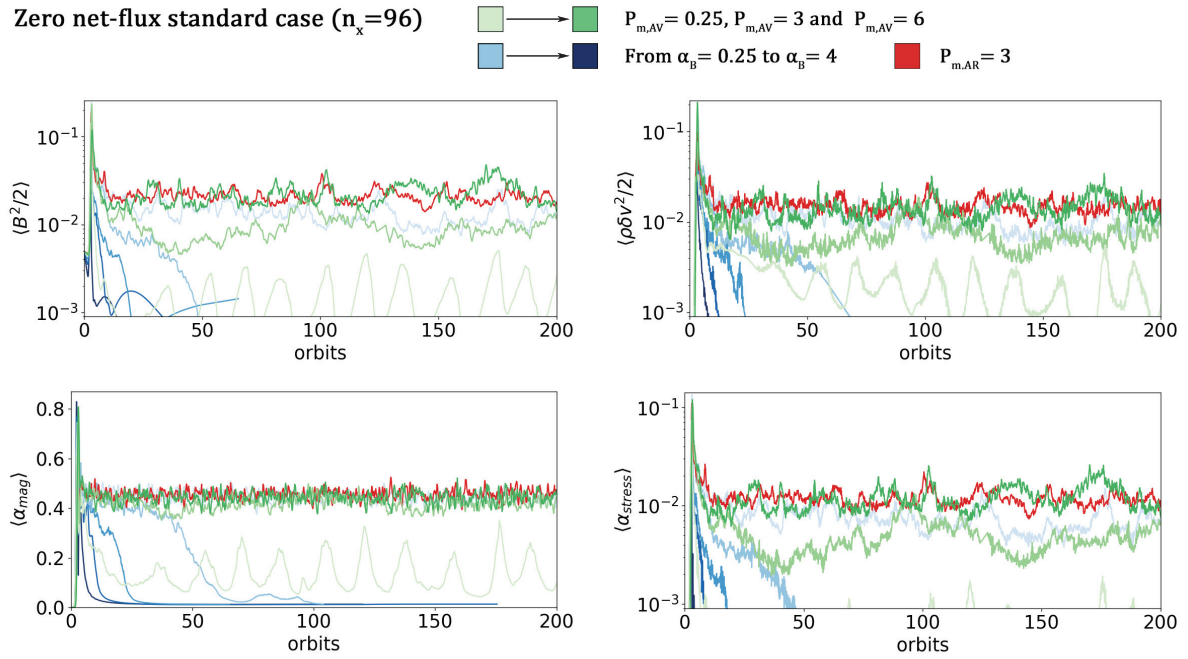
Fig. 6. Time evolution of several volume-averaged quantities for the standard box, unstratified ZNF cases at as resolution of n_x = 96: magnetic energy (*top left*), kinetic energy (*top right*), normalized Maxwell stress (*bottom left*) and the total stress (*bottom right*). The red line show the case of $P_{m,AR}$ = 3.0 where we set the Prandtl number by altering the AR strength. The green lines show the case where we set the Prandtl number by altering the AV strength, the darkness of the curve is determined by the value of the set Prandtl number, $P_{m,AV}$ = [0.25, 3.0, 6.0]. The blue curves represent the cases with a set AR coefficient without forcing the Prandtl number, where the darkness is determined by the strength of the artificial resistivity parameter, α_B = [0.25, 0.5, 1.0, 2.0, 4.0]. Four of the nine cases reach a saturated state (α_B = 0.25, $P_{m,AR}$ = 3.0, $P_{m,AV}$ = 3.0, $P_{m,AV}$ = 6.0) The code default value of α_B = 0.5 sustains turbulence for around 50 orbits before decaying.
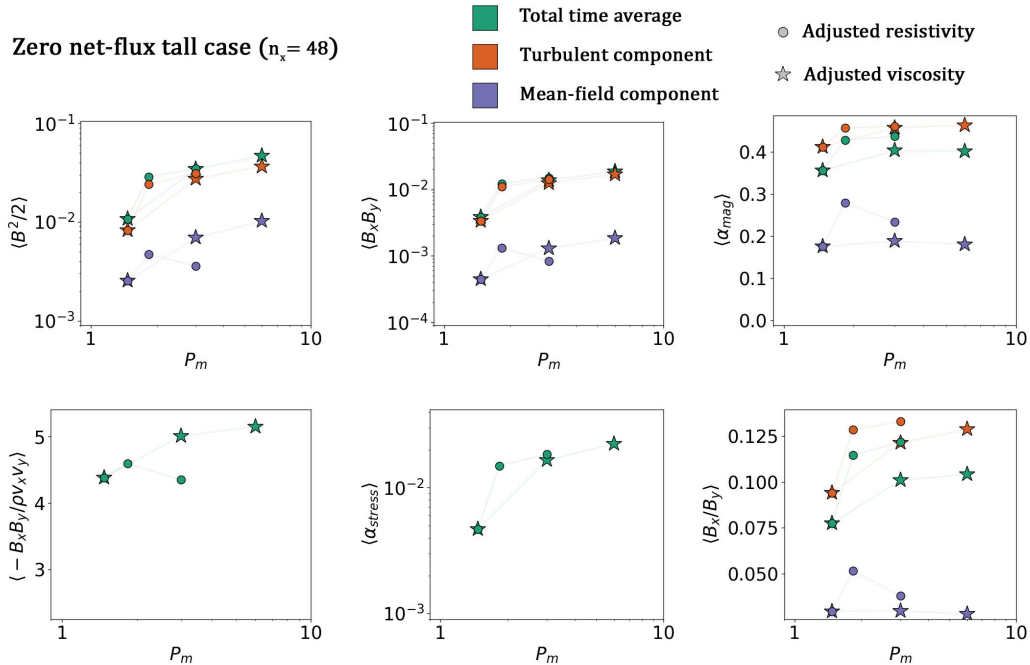
Zero net-flux tall case (n$_x$=48)

P$_{m,AV}$= 0.25, P$_{m,AV}$= 3 and P$_{m,AV}$= 6

From α_B= 0.25 to α_B= 4

P$_{m,AR}$= 3
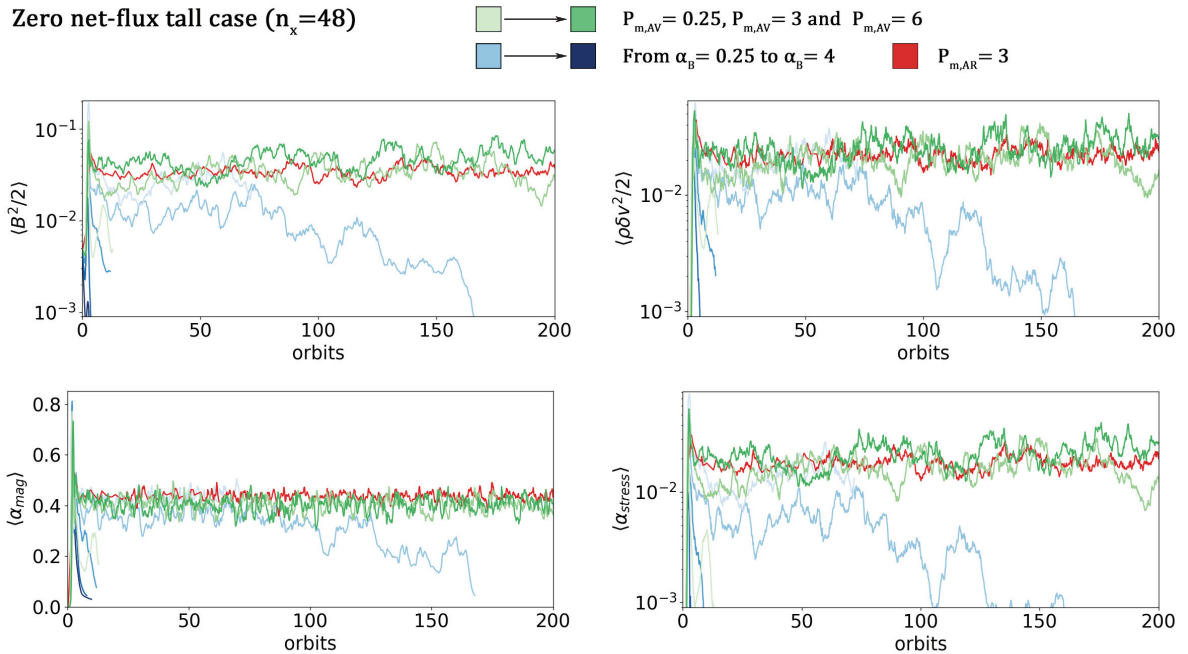
Fig. 7. Time evolution of several volume-averaged quantities for the tall box, unstratified ZNF cases at a resolution of n_x = 48: magnetic energy (*top left*), kinetic energy (*top right*), normalized Maxwell stress (*bottom left*) and the total stress (*bottom right*). The red line show the case of $P_{m,AR}$ = 3.0 where we set the Prandtl number by altering the AR strength. The green lines show the case where we set the Prandtl number by altering the AV strength, the darkness of the curve is determined by the value of the set Prandtl number, $P_{m,AV}$ = [0.25, 3.0, 6.0]. The blue curves represent the cases with a set AR coefficient without forcing the Prandtl number, where the darkness is determined by the strength of the artificial resistivity parameter, α_B = [0.25, 0.5, 1.0, 2.0, 4.0]. Four of the nine cases reach a saturated state (α_B = 0.25, $P_{m,AR}$ = 3.0, $P_{m,AV}$ = 3.0, $P_{m,AV}$ = 6.0).The code default value of α_B = 0.5 sustains turbulence for a long time but starts to decay after around 120 orbits.
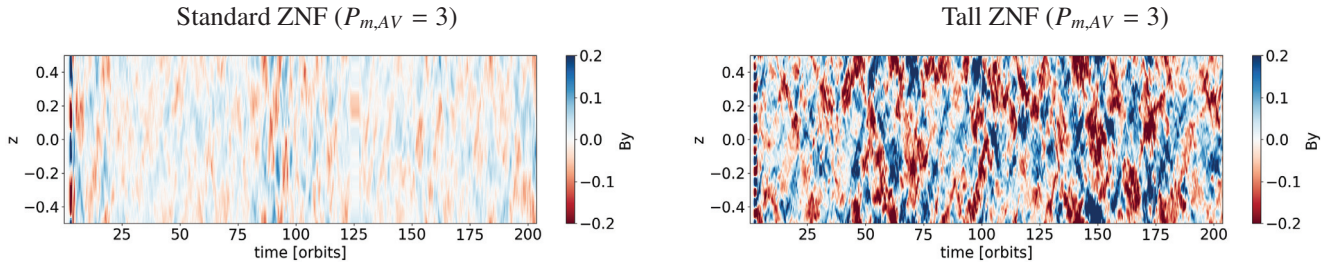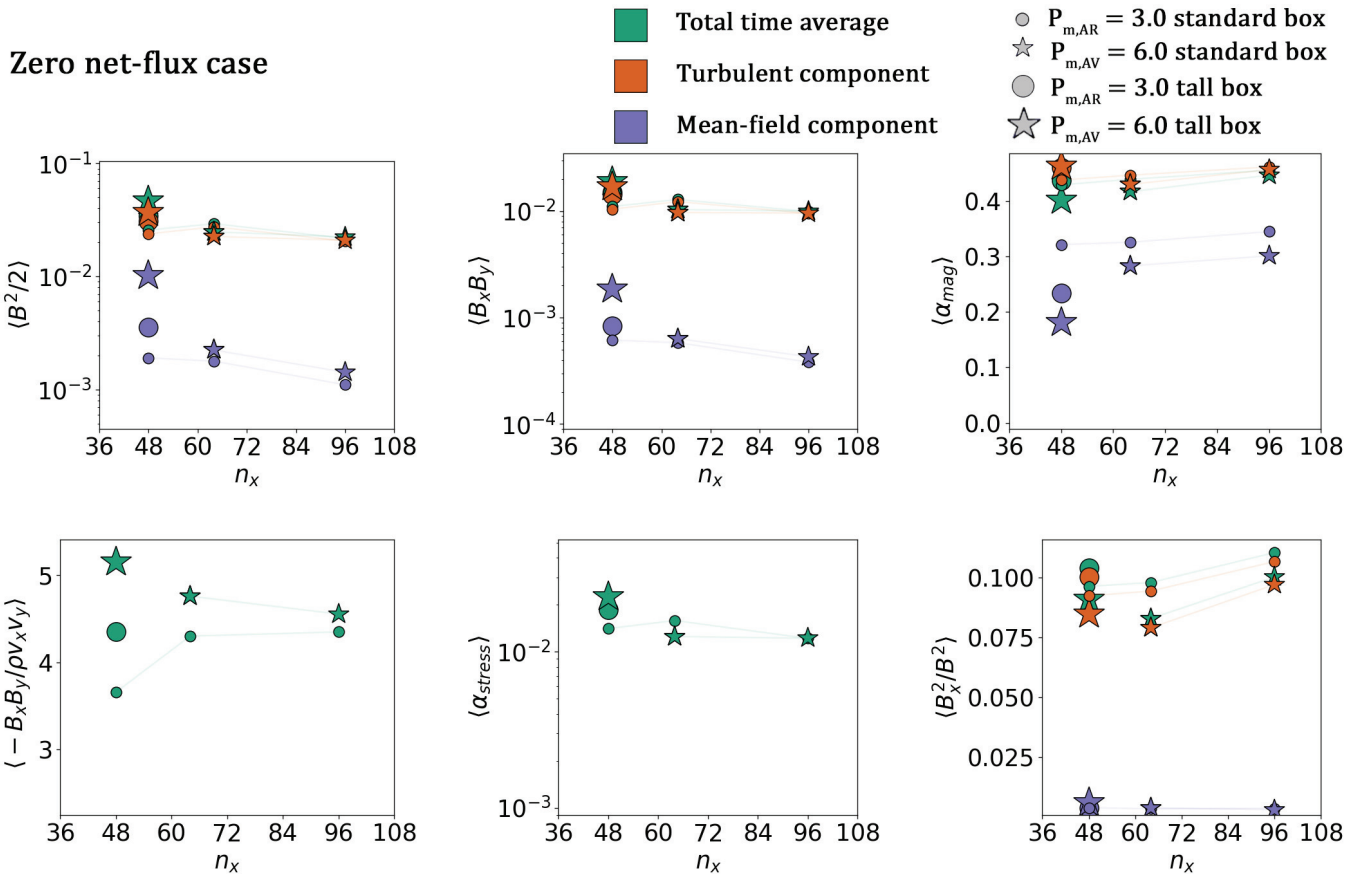
108

Fig. 8. Time-averaged values of several quantities for all our unstratified, zero net-flux simulations with standard box size ($L = [1.0, \pi, 4.0]$) and resolution $n_x = 96$. *From the top left to bottom right*: magnetic energy density, Maxwell stress, normalized Maxwell stress, ratio between Reynolds and Maxwell stresses, total stress, ratio between radial and total magnetic field energy. The x-axis shows the time-averaged effective Prandtl number of the simulation. For some quantities we have plotted the total time average (shown in green), the time average of the turbulent component (shown in orange) and the time average of the mean component (shown in blue). The circles represent the simulations where we have adjusted the strength of the artificial resistivity, while the star symbols represent the simulations where we have adjusted the artificial viscosity.

Fig. 9. Time-averaged values of several quantities for all our unstratified, zero net-flux simulations with tall box size ($L = [1.0, \pi, 4.0]$) and resolution $n_x = 48$. *From the top left to bottom right*: magnetic energy density, Maxwell stress, normalized Maxwell stress, ratio between Reynolds and Maxwell stresses, total stress, ratio between radial and total magnetic field energy. The x-axis shows the time-averaged effective Prandtl number of the simulation. For some quantities we have plotted the total time average (shown in green), the time average of the turbulent component (shown in orange) and the time average of the mean component (shown in blue). The circles represent the simulations where we have adjusted the strength of the artificial resistivity, while the star symbols represent the simulations where we have adjusted the artificial viscosity.

Standard ZNF ($P_{m,AV} = 3$) Tall ZNF ($P_{m,AV} = 3$)

Fig. 10. Spacetime diagrams showing the horizontal-averaged azimuthal magnetic field for the unstratified, zero net flux case ($P_{m,AV} = 3$). We can see that the tall box has larger structured mean-fields than the standard box. Compared to Shi et al. (2016) the rendered pattern of the mean-fields are similar, however, they produce much stronger mean-fields in their tall box simulations.

Fig. 11. Time-averaged values of several quantities for our resolution study of the unstratified, zero net-flux cases with $P_{m,AR} = 3.0$ and $P_{m,AV} = 6.0$, which includes tall box and standard box simulations. *From the top left to bottom right*: magnetic energy density, Maxwell stress, normalized Maxwell stress, ratio between Reynolds and Maxwell stresses, total stress, ratio between radial and total magnetic field energy. For some quantities we have plotted the total time average (shown in green), the time average of the turbulent component (shown in orange) and the time average of the mean component (shown in blue). The circles represent the simulations where we have adjusted the strength of the artificial resistivity, small circles represent standard box cases and large circles represent tall box. While the star (standard box size) and large stars (tall box size) represent the simulations where we have adjusted the artificial viscosity.

box case, we only show the time averages of the saturated runs as all the other runs are killed after their initial turbulence die out. For the standard box, we can see that as we increase the Prandtl number the magnetic energy and stress increases rapidly until we reach a high enough P_m for saturation. The saturated cases reaches a total stress of around $\alpha_{stress} = 0.01$ and a normalized magnetic stress of $\alpha_{mag} = 0.4$, which is consistent with previous studies of the MRI (Hawley et al. 1995; Simon et al. 2009). From these figures, we can see that the total magnetic field energy and stresses are largely dominated by the turbulent component, with only a very weak mean-field

component. The mean-field energy and stress do not change significantly as the Prandtl number is increased. We can also see that there is not a one to one correlation between energies and stresses for $P_{m,AR}$ and $P_{m,AV}$ simulations with the same Prandtl number. The resulting stress levels are higher when lowering the artificial resistivity compared to increasing the artificial viscosity. While saturation is mainly governed by the Prandtl number, stress levels will depend on both the Prandtl number and the strength of the resistivity (Simon & Hawley 2009). In addition, as shown in Fromang et al. (2007) the critical Prandtl number does have a dependence on the Reynolds number
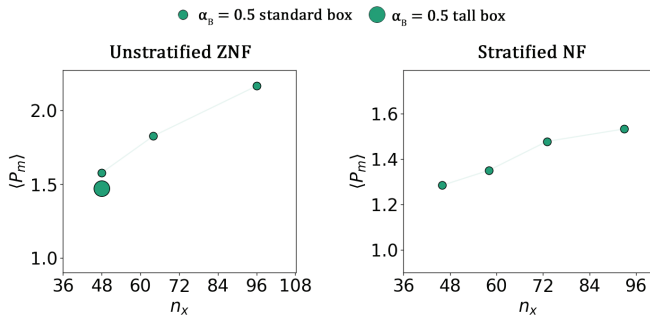
Fig. 12. Resolution dependence of the numerical Prandtl number for the unstratified, zero-flux cases on the left (Sect. 3.2) and for the stratified, net-flux cases to the right (Sect. 4). This shows cases with an AR coefficient set to $\alpha_B = 0.5$, which is our code default. We can see that we have an almost linear increase with higher resolution for both cases.

which also can have an effect on the amplitude of the saturated stress.

Comparing this to the time average results from the tall box shown in Fig. 9, we can see that similar to the standard box, magnetic energy and stress increases with P_m, reaching albeit higher values but with similar normalized magnetic stress values. From the magnetic energy density, it is clear that the turbulent part of the energy is dominant similar to the standard box case. This is quite different from the results presented in Shi et al. (2016) where the mean-field contributes most to the energy density.

In fact, they showed a rapid increase in mean-field energy density as the vertical aspect ratio of the domain was increased. We do see that the mean-field energy density of our tall box is larger than the standard box, however, it remains relatively weak. A visual comparison of the mean-fields can be seen in Fig. 10, where we see that the tall box has larger structured mean-fields than the standard box. The rendered pattern of the mean-fields are reminiscent of the result presented in Shi et al. (2016). The lack of significant mean-fields can be seen in the resulting stress levels of our simulations, which are only slightly larger than the ones from the standard box case and nowhere near the $\alpha_{stress} = 10^{-1}$ presented in Shi et al. (2016).

We can see from Figs. 8 and 9 that, in general, there is a small increase in the ratio between Maxwell stress and Reynolds stress as Prandtl number is increased and seem to converge towards a value of roughly $\alpha_{MW}/\alpha_{rey} \approx 4.5$ for the standard box and $\alpha_{MW}/\alpha_{rey} \approx 5$ in the tall box. For the standard box, this is slightly higher than the typical values from Eulerian grid simulations, which report values of around $\alpha_{MW}/\alpha_{rey} \approx 3 \leftrightarrow 4$ (Hawley et al. 1995, 1999; Abramowicz et al. 1996; Stone et al. 1996; Sano et al. 2004). However the tall box values are in accordance with those presented in Shi et al. (2016).

The average divergence error remains either below or close to $\epsilon_{div,err} \approx 10^{-2}$. As expected, the divergence error is kept lower by increasing the artificial viscosity to reach a certain Prandtl number than by decreasing the resistivity. For the majority of cases, the Elsasser number remains far above 1, however, for the high resistivity cases ($\alpha_B = 4, \alpha_B = 2$) the number drops below one, which is likely why we see such a rapid decay of turbulence in these cases. We also show the relative radial energy ratio (B_x^2/B^2), which shows a steep increase with P_m and for our saturated runs it reaches values around $B_x^2/B^2 \approx 0.1$. This is similar to the values reported by Hawley et al. (1996) but is somewhat lower than the higher resolution simulation performed by Simon et al. (2009) and Shi et al. (2016), which reports values of around $B_x^2/B^2 \approx 0.14$. Looking at Fig. 11, this is consistent

with the increasing trend with resolution that we see. Increasing the vertical domain size slightly increases the value from about $B_x^2/B^2 \approx 0.09$ for the standard box to around $B_x^2/B^2 \approx 0.11$ for the tall box. This is opposite to what is found in Shi et al. (2016), which see a consistent decrease in this value as the vertical domain size is increased, going from $B_x^2/B^2 \approx 0.14$ for the standard box to $B_x^2/B^2 \approx 0.12$ for the 4 times vertical ratio and $B_x^2/B^2 \approx 0.09$ for the 8 times vertical ratio.

We also performed a resolution study on the standard box case to see how different time-averaged quantities change with resolution. We primarily look at the two cases where we set $P_{m,AV} = 6$ and $P_{m,AR} = 3$. From Fig. 11, we can see that for the saturated cases there is no strong resolution dependence on the total stress as reported by studies using Eulerian grid codes (Fromang et al. 2006). Instead, the stress saturates at around $\alpha_{stress} = 0.01$. This resolution independence is of course only for the cases where we force a certain numerical Prandtl number, as increasing the resolution for a fixed resistivity coefficient will alter the numerical Prandtl number. The resolution dependency of the numerical Prandtl number can be seen in Fig. 12, which shows that P_m has an almost linear increase with resolution. The normalized turbulent stress ratio remains fairly constant at around $\alpha_{mag} \approx 0.42$ with a slight increase with resolution. The relative radial energy ratio (B_x^2/B^2) show a steady increase with resolution and have not converged for our highest resolution case. The divergence error is also reduced with increasing resolution, which is consistent with our cleaning scheme implementation.

Figure 13 shows the time-averaged values of the transport coefficients α_{xx}, α_{xy}, η_{xx} and η_{yx} for all the unstratified simulations. From the figures, we can see that both α coefficients have values very close to zero which is to be expected from the unstratified case. η_{yx} can be seen to have a slightly positive value for all cases exhibiting sustained turbulence, which is more significant in the tall box. The turbulent diffusivity can be seen to have a consistent positive value, which is around $\eta_{xx} \approx 0.006$ for the standard box and $\eta_{xx} \approx 0.015$ in the tall box. The nonnegative value in η_{yx} might explain why we do not see the generation of large mean-fields within our simulations as Shi et al. (2016) shows a consistent negative value for η_{yx} which as we explained in the introduction can act to generate local mean-fields through the shear-current effect. However, the lack of shear-current effect is consistent with other previous studies of the MRI (Brandenburg et al. 1995a; Brandenburg 2008; Gressel 2010).

4. Stratified simulation results

The stratified NF simulations represent a more realistic and complex situation than the unstratified case, as it includes the vertical tidal component (final term in Eq. (16)), which results in the following density stratification:

$$\rho = \rho_0 e^{-\frac{z^2}{H^2}}. \tag{31}$$

Here, H is the scale height and is set by $H = c_s/\Omega = 1.0$. As we adopt an isothermal equation of state we do not have to worry about the scale height changing during the simulation. In previous studies, the developed MRI turbulence shows a periodic dynamo cycle, where large-scale magnetic fields emanate from the central region and migrate outwards to the disk corona, growing in strength as they do so. This flips the sign of the field within the central region and the process is repeated. As we mentioned in the introduction, recently it has been shown that SPH develops unphysically strong azimuthal fields in simulations of the stratified shearing box (Deng et al. 2019). In this section, we further
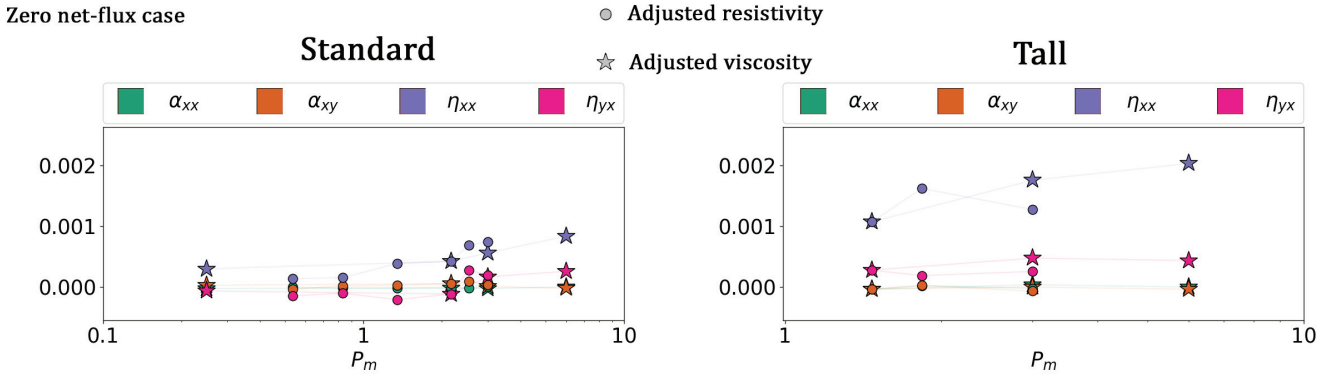
Fig. 13. Time-averaged turbulent transport coefficients from the unstratified, zero net-flux cases, with the standard box size cases ($L = [1.0, \pi, 1.0]$, $n_x = 96$) to the *left* and the tall box cases ($L = [1.0, \pi, 4.0]$, $n_x = 48$) to the *right*. The circles represent the simulations where we have adjusted the strength of the artificial resistivity, while the star symbols represent the simulations where we have adjusted the artificial viscosity. To minimize noise we have set $\alpha_{xx} = \alpha_{yy}$, $\eta_{xx} = \eta_{yy}$, $\alpha_{yx} = 0.0$ and $\eta_{xy} = 0.0$. We can see that the α coefficients have values of around zero as expected for the unstratified case and η_{xx} with a consistent positive value. For the standard box η_{yx} remain close to zero while for the tall box we see a consistent positive value which is contrary to what was seen by Shi et al. (2016).

investigate this case with a larger array of different numerical dissipation parameters and resolutions. In addition, we compare the results from TSPH to the newly developed GDSPH, which has been shown to improve performance in cases involving large density gradients (Wissing & Shen 2020). We set up the simulation following Deng et al. (2019), in which they use a shearing box of length $L = (\sqrt{2}, 4\sqrt{2}, 24)$ together with an azimuthal magnetic field:

$$ B = \sqrt{\frac{2P}{\beta}} \hat{y}. \tag{32} $$

Here, the initial plasma beta is set to $\beta = 25$ throughout the box and, as the pressure will vary with density as $P = \rho c_s^2$, we begin with a magnetic field that varies in the vertical direction. We run the simulations at four different resolutions $[n_x, N] = [46, 1.6 \times 10^6], [58, 3.1 \times 10^6], [73, 6.2 \times 10^6], [93, 12.8 \times 10^6]$, where the two lower resolution cases are the same as the ones run in Deng et al. (2019). As the resolution is adaptive, we have more resolution in the inner region of the disk (which is where the MRI turbulence is sustained) and less resolution outside in the disk corona. Using Eq. (18) we can see that we resolve λ_{MRI} with an average initial quality parameter of $Q_{mid} = [43, 55, 68, 90]$ in the midplane for each respective resolution. We carry out several simulation at a resolution of $n_x = 58$, where we vary the artificial resistivity coefficient $\alpha_B = [0.3, 0.5, 1.0, 2.0]$, where $\alpha_B = 0.5$ is the code default value. For all the simulation cases we run one with TSPH and one with GDSPH for comparison. Due to the outflow boundaries, there is mass loss from the simulation, which leads to a flattening of the density profile. This means that resolution will gradually be reduced as time goes on, which is why we at most run our simulation for about 100 orbits. The high-resolution cases are also very computationally costly and are stopped at a somewhat earlier time. The results of the simulations are shown in Figs. 14–21.

In Fig. 14 we can see the time evolution of the magnetic energy, kinetic energy, normalized Maxwell stress, and the total stress for a resolution with $n_x = 58$. From this figure, we can see that all of the TSPH simulations exhibit an unphysical growth in the magnetic energy density, similar to what was seen in Deng et al. (2019). These simulations are stopped when they reach roughly an average plasma beta value of $\beta = 1$, which acts as a confirmation of erroneous growth. On the other hand, all the

GDSPH simulations remain stable and those runs with moderate artificial resistivities all reach saturated magnetic energy and stress levels that are similar to what has been seen in the literature (Shi et al. 2010; Simon et al. 2011). To get a closer look at what is going on, we have in Fig. 15 plotted the time-space evolution of the horizontal averaged radial and azimuthal fields for both GDSPH and TSPH in the case of $\alpha_B = 0.3$ with a resolution $n_x = 58$. Both GDSPH and TSPH develop the characteristic butterfly diagram, where the azimuthal fields are buoyantly transported outward and periodically flip signs in the central region. However, while the GDSPH case stably continues this behavior for over 100 orbits, the TSPH case quickly becomes unstable and exhibits a runaway growth. Increasing the resistivity to $\alpha_B = 1.0$ does not help stabilize the TSPH scheme, as can be seen in Fig. 16. The butterfly diagram is gone and instead, a strong positive azimuthal field permeates the disk corona ($|z| > 2$). The azimuthal field is additionally amplified as the simulation goes on and starts to propagate into the central disk region. The failure of buoyantly ejecting the positive fields in the disk corona is due to the magnetic field growing strong enough to stabilize the region (magnetic tension suppresses the bending of field lines). The time-space diagram of the TSPH case in Fig. 16 is reminiscent of the result presented in Deng et al. (2019) where a similar magnetic field growth was observed. The GDSPH case, on the other hand, still exhibits the butterfly diagram at higher resistivity, but with a longer periodic cycle for the flipping of the magnetic field (especially at early times). The TSPH case still has a very active and fluctuating radial field within the central region, and this is also reflected in the normalized Maxwell stresses in Fig. 14, where the values of the TSPH cases remain similar to the GDSPH runs with the same α_B. This is further highlighted in Fig. 17, where we can see a rendering of the magnetic field and density within the box for both the TSPH and GDSPH cases. Both simulations exhibit a very similar central region, while the TSPH have significantly stronger azimuthal fields in the outskirts. As TSPH and GDSPH mainly differ at density gradients, it makes sense that the issue of the unphysical growth seems to lie in the outer region of the disk (beyond $|z| > 1$) where we have lower resolution and a significant density gradient.

Figure 18 shows time averages of different quantities. In general, as we decrease the resistivity, the magnetic energy and stress increases for both the TSPH and GDSPH runs. The total stress reaches a time-averaged value of around $\alpha_{stress} \approx 10^{-2}$
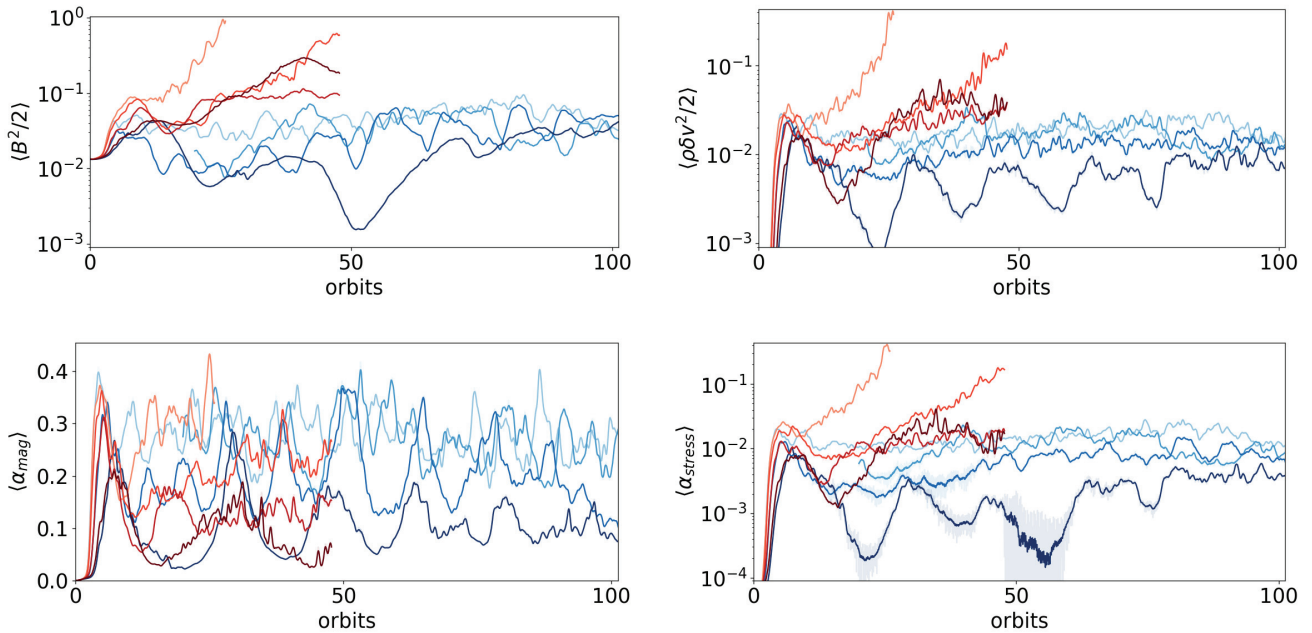
Fig. 14. Time evolution of several volume-averaged quantities for the stratified net-flux simulations with varying artificial resistivity (α_B = [0.3, 0.5, 1.0, 2.0]) at a resolution of n_x = 58. Magnetic energy (*top left*), kinetic energy (*top right*), normalized Maxwell stress (*bottom left*) and the total stress (*bottom right*). The red lines show the simulations run with TSPH and blue lines show the runs with GDSPH where the darkness of the line represents the strength of the artificial resistivity. We have smoothed the curves using a Savitzky–Golay filter, the unsmoothed curves can still be seen as very transparent curves.
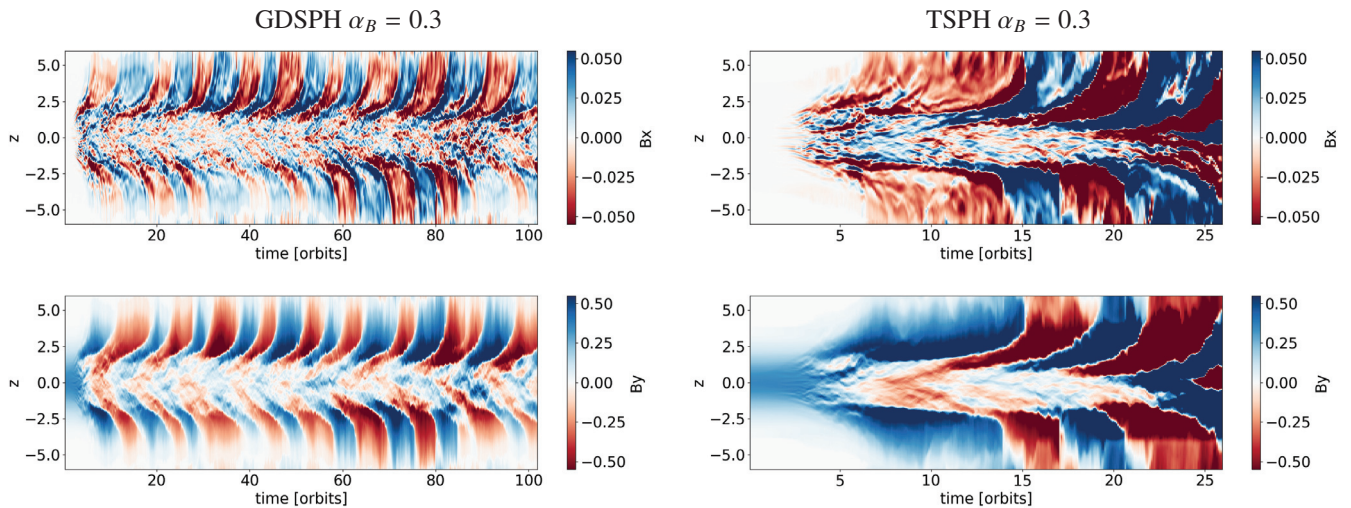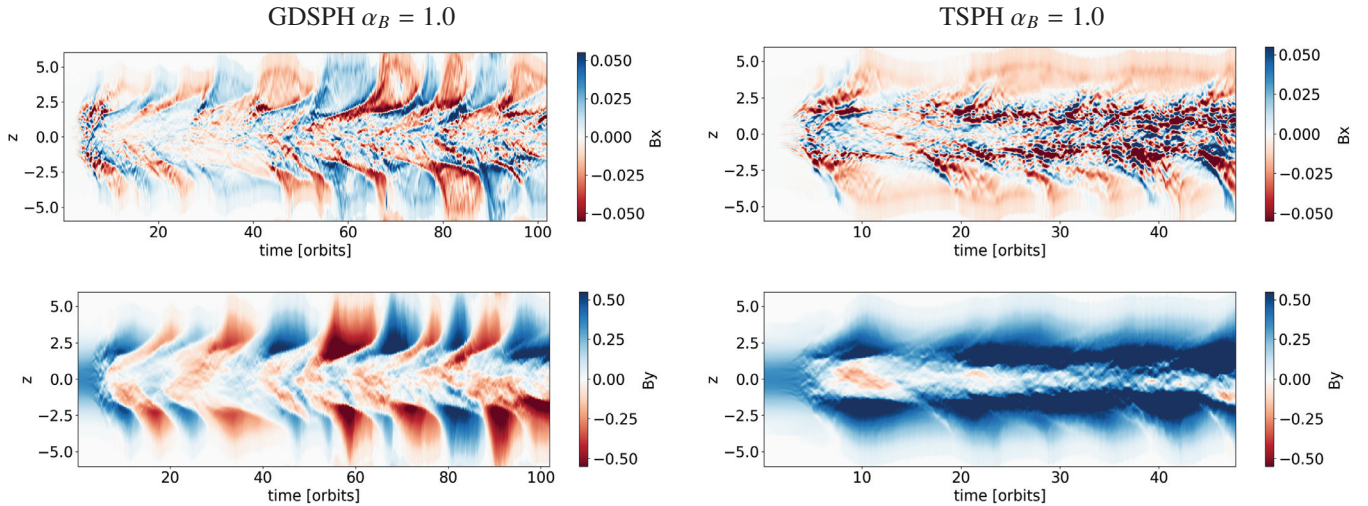

Fig. 15. Spacetime diagrams of the stratified net flux simulations, showing the evolution of the horizontal averaged radial (*top*) and azimuthal (*bottom*) fields for both GDSPH (*left*) and TSPH (*right*) in the case of α_B = 0.3 with a resolution n_x = 58. Both GDSPH and TSPH develop the characteristic butterfly diagram. However, the TSPH simulation quickly becomes unstable and exhibits a runaway growth in the magnetic field.

and a normalized Maxwell stress of around α_{mag} = 0.3 for the low resistivity cases, similar to previous result from the literature (Shi et al. 2010; Simon et al. 2011). Looking at the mean and turbulent components of the magnetic energy density, we can see that the mean-field component is the dominant part, but with an increasing fraction from the turbulent field as we decrease the resistivity. The TSPH runs develop a much higher magnetic energy density than the GDSPH cases, with a highly dominating mean-field component, which comes mainly from the strong azimuthal fields in the corona. For the Maxwell stress, in our

GDSPH simulations the turbulent and mean-field components contribute a similar amount to the total Maxwell stress. The normalized Maxwell stresses have similar values for both GDSPH and TSPH, with the turbulent component of around 0.45 and largely independent of the resistivity, but the mean-field component increases with decreasing resistivity.

From Fig. 18 we can also see that the ratio between the Maxwell stress and Reynolds stress show a value of around 5.0 for the GDSPH cases with an increasing trend for lower resistivity. For the TSPH runs, this ratio shoots up for the low resistivity

Fig. 16. Spacetime diagrams of the stratified net flux simulations, showing the evolution of the horizontal averaged radial (*top*) and azimuthal (*bottom*) fields for both GDSPH (*left*) and TSPH (*right*) in the case of $\alpha_B = 1$ with a resolution $n_x = 58$. At this resistivity only GDSPH reproduce the butterfly diagram, where for TSPH a strong positive azimuthal field permeates the disk corona ($|z| > 2$). The azimuthal field is additionally amplified as the simulation goes on and starts to propagate into the central disk region.
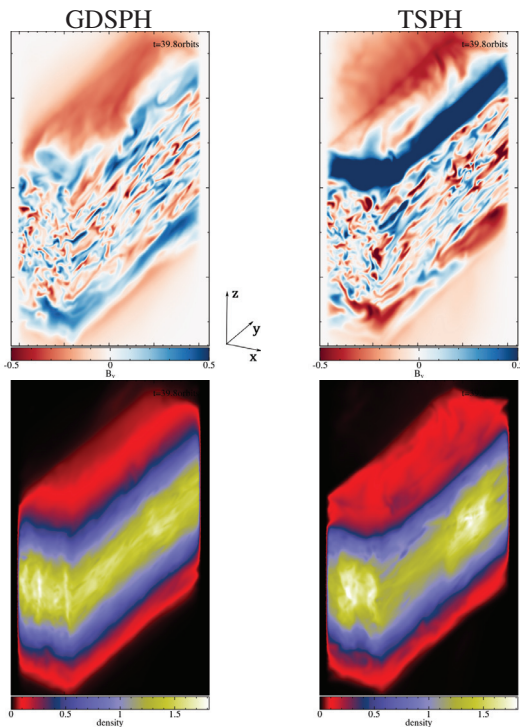
Fig. 17. Stratified shearing box simulation with net-flux, shows the surface rendering of the azimuthal field (*top*) and the density (*bottom*). *Left*: case for GDSPH and *right*: case with TSPH. In the TSPH case we can see that there is excessive growth in the magnetic field in the outer part of the disk.

cases to a value of around 8. The numerical Prandtl number has a steady increase as we decrease the resistivity. For GDSPH it goes from a value of around 0.7 for $\alpha_B = 2.0$ to a value of 1.6 for $\alpha_B = 0.25$. In TSPH the numerical Prandtl number is larger but not by much. The average divergence error for both GDSPH and TSPH remains close or below a value of $\epsilon_{\mathrm{div,err}} \approx 10^{-2}$.

To investigate the effect of resolution in the stratified simulations, we perform a resolution study with the following radial resolutions $n_x = [48, 58, 73, 93]$. In these simulations, we use
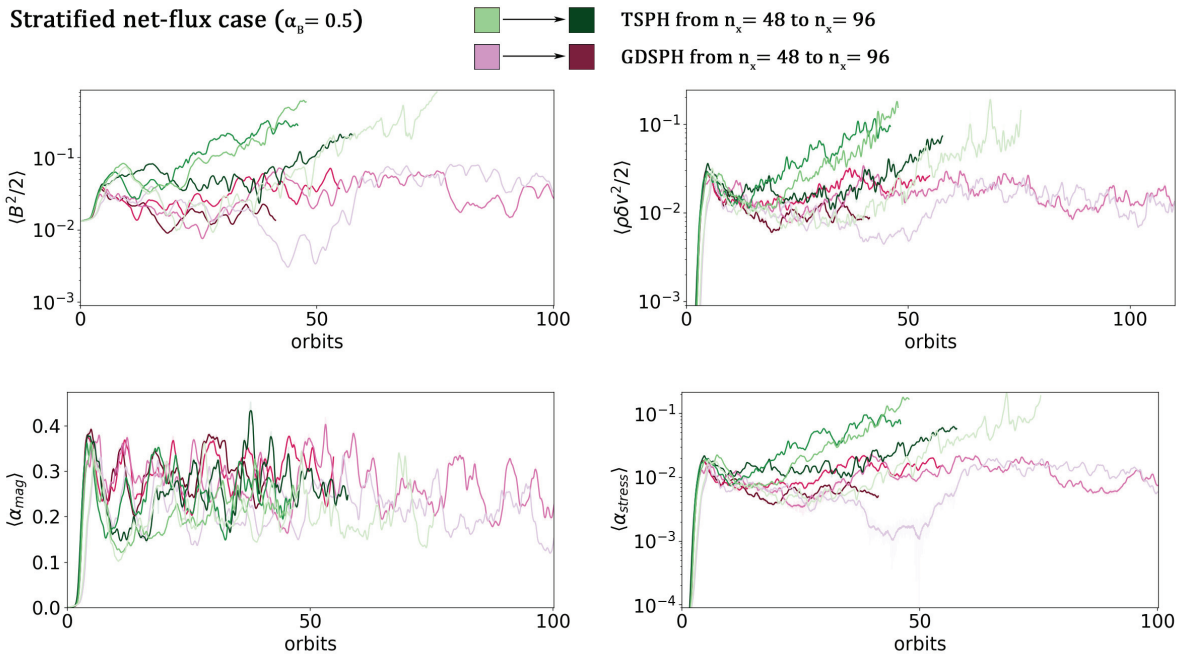
the code default artificial resistivity coefficient of $\alpha_B = 0.5$. The high-resolution cases ($n_x = 73, 93$) are very costly, so we have only run them for about 60 orbits. In Fig. 19 we can see the time evolution of the magnetic energy, kinetic energy, normalized Maxwell stress, and the total stress for TSPH and GDSPH at different resolutions. From this figure, we can see that all the TSPH cases eventually become unstable, and the lowest resolution cases "survives" the longest. All of the GDSPH cases show a stable behavior, with only the lowest resolution case having a period of low stress before increasing to similar levels as the higher resolution cases. A significant early difference that can be seen between TSPH and GDSPH is shown in the magnetic energy density, where all the TSPH have a much larger initial "bump" than the GDSPH curves which flatten out after the initial increase. This larger initial bump correlates to stronger magnetic fields near the density contrast at around $|z| \approx 1$.

In Fig. 20 we can see that the values of magnetic energy density and stress remain fairly flat, with a slight initial increase with resolution but then a slight decrease for our highest resolution. It is not clear to why we see a decrease in the stress for the highest resolution. It could simply be a stochastic phenomena that would flatten out if we ran it for longer. However, both GDSPH and TSPH follow a similar curve, pointing towards a real effect. We can see that the turbulent component does become a more dominant part in both the energy density and in the stress as we increase resolution. The normalized Maxwell stress has a slight increase with resolution, going from around $\alpha_{\mathrm{mag}} = 0.2$ to $\alpha_{\mathrm{mag}} = 0.3$ and the total stress for GDSPH lies between $\alpha_{\mathrm{stress}} = 10^{-3} \leftrightarrow 10^{-2}$ which is in accordance to the values presented by Stone et al. (1996) and Shi et al. (2010). We can see that the ratio between the Maxwell stress and Reynolds stress is almost independent of resolution giving a value of 5.0 for the GDSPH cases and around 7.0 for TSPH. Similar to the unstratified case, we can in Fig. 12 see that we have a slow but linear increase in the numerical Prandtl number with resolution, going from around $P_m = 1.3$ to $P_m = 1.5$ for the GDSPH cases. The average divergence error slightly decreases with resolution for both TSPH and GDSPH with values around $\epsilon_{\mathrm{div,err}} \approx 10^{-2}$.

In Fig. 21 we show the horizontal time-averaged turbulent coefficients as a function of z. As we mentioned in the

114

Stratified net-flux case ($n_x = 58$)
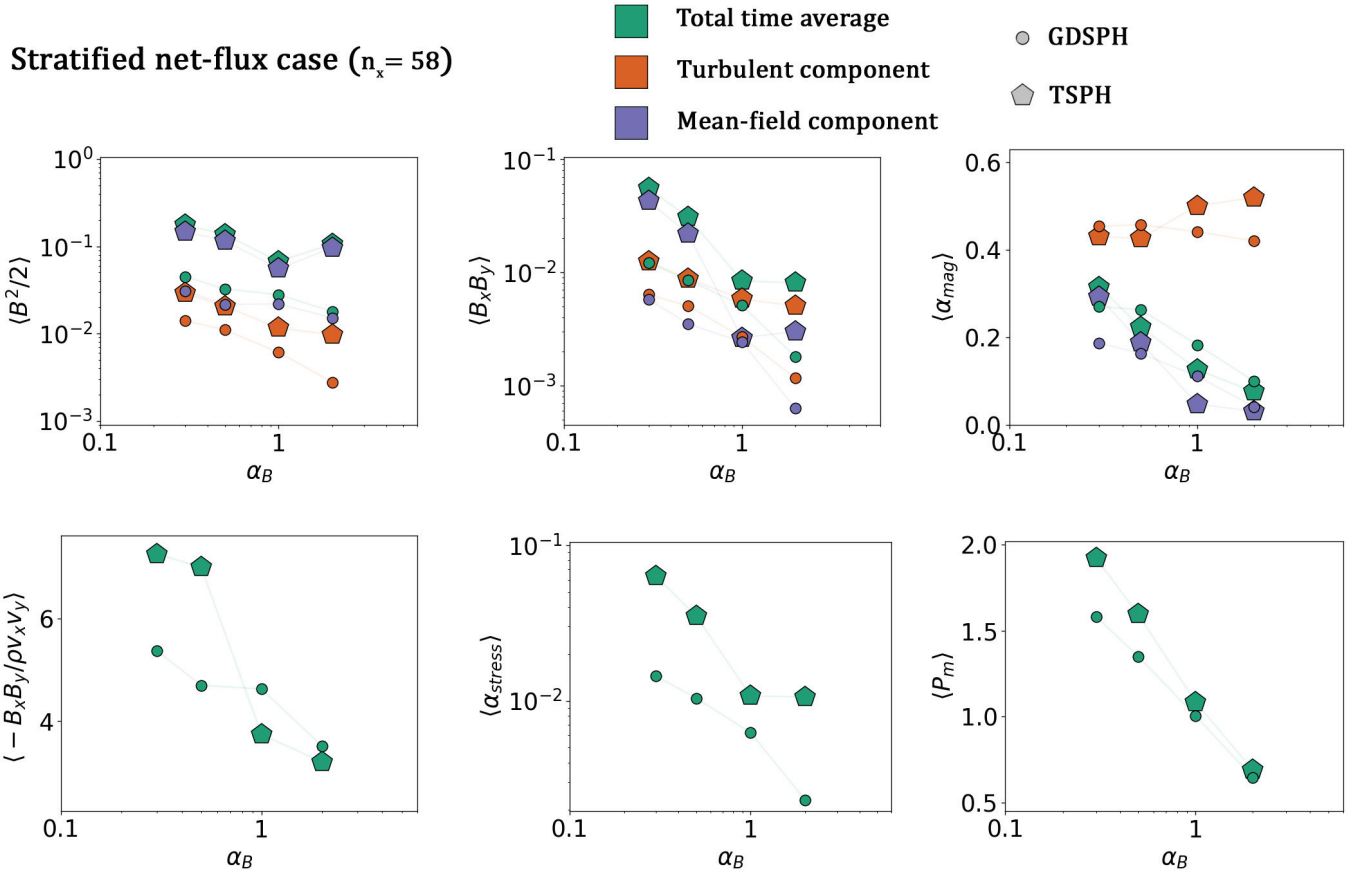
Fig. 18. Time-averaged values of several quantities for all our stratified net-flux simulations as a function of the artificial resistivity (α_B) at a resolution of $n_x = 58$. *From the top left to bottom right*: magnetic energy density, Maxwell stress, normalized Maxwell stress, ratio between Reynolds and Maxwell stresses, total stress, estimated numerical Prandtl number. For some quantities we have plotted the total time average (shown in green), the time average of the turbulent component (shown in orange) and the time average of the mean component (shown in blue). The circles represent the simulations run with GDSPH while the diamonds represent the simulations run with TSPH.

Fig. 19. Time evolution of several volume averaged quantities for the stratified net-flux simulations with varying resolution ($n_x = [48, 58, 74, 93]$) and the artificial resistivity coefficient set to $\alpha_B = 0.5$. Magnetic energy (*top left*), kinetic energy (*top right*), normalized Maxwell stress (*bottom left*) and the total stress (*bottom right*). The green lines show the simulations run with TSPH and purple lines show the runs with GDSPH. The darkness of the line indicate the resolution, where the darkest line represents the highest resolution.
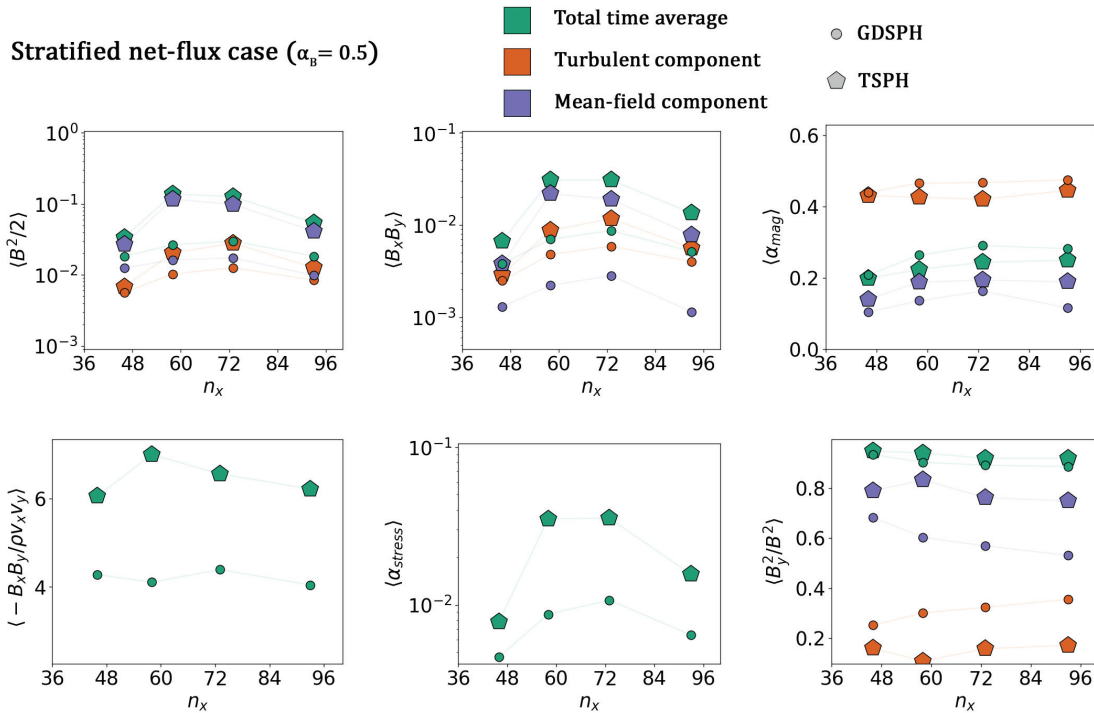
Fig. 20. Time-averaged values of several quantities for all our stratified net-flux simulations with artificial resistivity coefficient set to $\alpha_B = 0.5$, plotted over the resolution (particles along the *x*-axis). *From the top left to bottom right*: magnetic energy density, Maxwell stress, normalized Maxwell stress, ratio between Reynolds and Maxwell stresses, total stress, ratio between azimuthal and total magnetic field energy. For some quantities we have plotted the total time average (shown in green), the time average of the turbulent component (shown in orange) and the time average of the mean component (shown in blue). The circles represent the simulations run with GDSPH while the diamonds represent the simulations run with TSPH.

introduction, the dynamo action within stratified disks includes several mechanisms that can act in different sections of the disk. We find that the α_{xx}, α_{yy}, α_{xy} and α_{yx} all have a continuous gradient, with anti-symmetric behavior around the mid-plane. The behavior of α_{yy} determines the effectiveness of the $\alpha\omega$-dynamo, as it operates on the radial mean fields (see Eq. (9)). We can see that α_{yy} has a negative gradient with negative values above the midplane, this is consistent with Brandenburg et al. (1995b), Brandenburg & Sokoloff (2002), Brandenburg (2008), Shi et al. (2016), and is indicative of an effective alpha effect for turbulent shear flows. The α_{xx} has a positive gradient and will act against the shear term, however, the shear term is the dominant part of the induction equation for the toroidal mean field. The off diagonal terms of α is often interpreted as a turbulent/diamagnetic pumping term $\gamma_z = \frac{1}{2}(\alpha_{yx} - \alpha_{xy})$. For our case, γ_z is positive above the mid-plane and negative below, meaning that we have a net transport of mean-fields away from the mid-plane. The α_{xy} and α_{yx} coefficients have the opposite sign, which is similar to the results from Shi et al. (2016), but different from other works by Brandenburg (2008), Gressel (2010), where the two have the same sign. However, α_{xy} and α_{yx} usually have similar magnitude in earlier works which is not observed in our cases. The η_{xx} coefficient and η_{yx} are generally positive, which is similar to what was found by Brandenburg (2008), Gressel (2010) but contrary to Shi et al. (2016).

5. Discussion

In this paper, we performed 23 simulations of the unstratified shearing-box MRI and 14 simulations of the stratified shearing-box MRI using SPH. For the unstratified NF case, we reproduced the results from previous studies in the literature, albeit

with slightly larger α_{mag} values and in general larger mean-field stresses. We attribute this primarily to the use of a smaller box, which increases the amplitude and frequency of channel modes and causes large bursts of magnetic energy and stress levels.

We demonstrate that the saturation of the unstratified ZNF simulations is highly dependent on the numerical Prandtl number. Our simulations with a Prandtl number above 2.5 achieve saturation for at least 200 orbits. To further illustrate that the MRI saturation depends on the numerical Prandtl number, rather than simply on the resistivity, we ran a simulation with a forced Prandtl number of $P_{m,AV} = 0.25$ but with a low artificial resistivity coefficient $\alpha_B = 0.25$. This simulation does not saturate even though having a very low numerical resistivity. This confirms that the dependencies on the Prandtl numbers found in Fromang & Papaloizou (2007) still holds true for numerical Prandtl numbers within SPH. The saturation levels in energies and stresses are also mainly dependent on the Prandtl number. However, for saturated simulations with the same Prandtl number, the magnetic energy and stress are slightly higher in cases with varying artificial resistivity than the ones with varying artificial viscosity. This is also shown in Figs. 6 and 7: when comparing the $P_{m,AR} = 3$ case with $P_{m,AV} = 3$ run, the latter exhibit larger oscillations and lower saturation levels.

We do not observe a decrease in stress with increasing resolution as found in previous studies with Eulerian codes. Although the stresses are highly dependent on numerical Prandtl number, they have a weak dependency on the resolution at a fixed Prandtl number, either increasing or staying roughly at the same stress level with increasing resolution. A possible explanation is that the numerical Prandtl number in Eulerian codes is not independent of resolution. This is contrary to studies by Fromang et al. (2007) and Simon et al. (2009), where the authors

116

Stratified case (n$_x$=58)

From α$_B$= 0.3 to α$_B$= 2.0
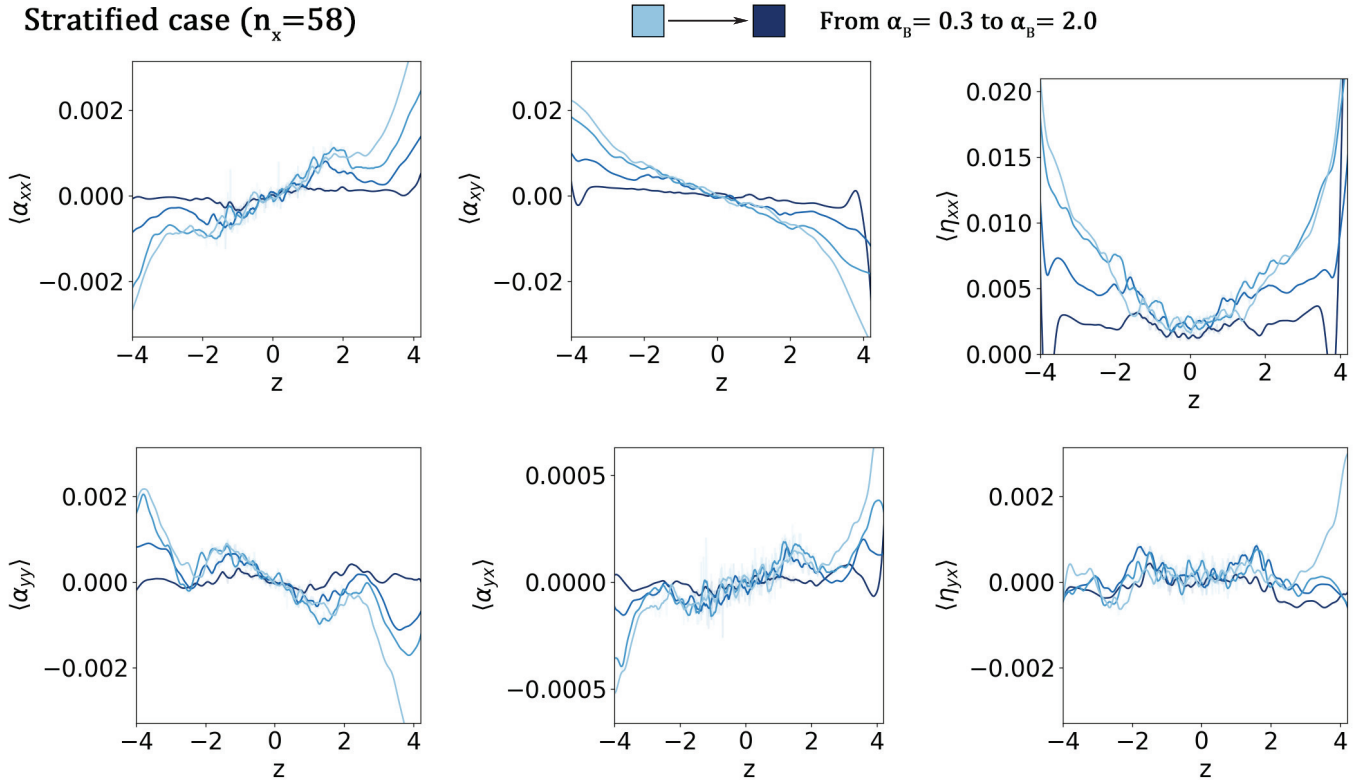
Fig. 21. Horizontal time-averaged turbulent transport coefficient in the z direction from the stratified net-flux cases. The darkness of the curves is determined by the strength of the artificial resistivity parameter, $\alpha_B = 0.3, 0.5, 1.0, 2.0$. We can see that we have a negative α_{yy} effect that is negative (positive) in the *top* (*bottom*) half of the box. This enables the $\alpha\omega$-dynamo to operate efficiently within the central region. α_{xx} on the other hand has a positive gradient and will act against the shear term. Turbulent pumping advects magnetic fields outwards from the central region with velocity $\gamma_z = \frac{1}{2}(\alpha_{yx} - \alpha_{xy})$. However, the α_{xy} magnitudes differ significantly to what is expected, which is likely caused by correlations with $\overline{B}_x$ due to the shear term as explained in Sect. 2.1. In the central region we find that at all resistivities we have a positive value for η_{xx} and η_{yx}, which is similar to our result of the unstratified case. In general we find that the behavior of the transport coefficients are similar to previous simulations of the stratified MRI (Brandenburg et al. 1995b; Brandenburg & Sokoloff 2002; Brandenburg 2008; Shi et al. 2016; Gressel 2010).

found the numerical Prandtl number to be almost independent of resolution ($P_m \approx 1.6$). These studies utilized Fourier transfer functions to compute the energy transfer between different scales. They found that an active MRI can exist in their simulations even though the numerical Prandtl number is lower than the critical value determined in studies with physical dissipation ($P_m \sim 2$). Thus, it was concluded that numerical dissipation acts differently to physical dissipation. In this paper, we however find that active turbulence still requires similar critical Prandtl numbers found in studies using physical dissipation. It is likely that the numerical dissipation in SPH is more closely related to physical dissipation than in grid codes, as SPH does not suffer from advection errors. This difference seems to be the reason to why grid codes see a significant reduction in stress with resolution.

Ideally, one would like the numerical Prandtl number to remain independent of resolution, as this would ensure the correct dynamo behavior if one can resolve the turbulent medium. The Prandtl numbers in our simulations increase with resolution for a fixed artificial resistivity coefficient ($\alpha_B = 0.5$) ranging from $\langle P_m \rangle \sim 1.5$ for $n_x = 48$ to $\langle P_m \rangle \sim 2.1$ at $n_x = 96$. Although not independent, an increase of P_m with resolution ensures that it increases along with the other fluid parameters (e.g., Reynolds number and magnetic Reynolds number). This means that we have convergent results when modeling most astrophysical fluids. A worse result would have been if the Prandtl number decreased with resolution which could result in a lowering of

stress with resolution and finally in the decay of the MRI. In addition, as mentioned in the introduction, the Prandtl number plays a major role in several dynamo mechanisms and is crucial for the saturation of the small-scale dynamo, which for example can be important for correctly simulating the growth and saturation of magnetic fields within galaxies. Our results highlight the importance of studying the numerical Prandtl number for all numerical schemes beyond MRI, for instance in turbulent boxes at different Mach numbers.

The main difference in our tall boxes compared to Shi et al. (2016) is the lack of significant mean-fields, which leads to stress levels that are only slightly larger than the ones in the standard box cases, but much smaller than $\alpha_{\text{stress}} = 10^{-1}$ seen in Shi et al. (2016). Our simulations do develop similar large-scale patches in the toroidal field, but they are significantly weaker. The small-scale turbulent components are consistent with the Shi et al. (2016) results. The lack of mean-fields is likely due to the difference seen in η_{yx}, which was consistently negative for Shi et al. (2016) but for all our simulations are either zero or positive. This would effectively lead to less coherent mean-field growth within the box. However, the positive value of η_{yx} is consistent with previous studies with the quasi-kinematic approach (Brandenburg et al. 1995a; Brandenburg 2008; Gressel 2010). For future work, it is worth exploring higher resolutions and different aspect ratios for SPH, to see if higher mean-field growth can be observed.

We demonstrated, for the first time, that the new GDSPH can successfully sustain the turbulence in the stratified shearing boxes for at least 100 orbits without decaying, similar to the simulations using the Gizmo code with the meshless finite-mass (MFM) method (Deng et al. 2019). However, the TSPH runs remain unstable for all cases, which confirms the result from Deng et al. (2019). Isolating each MHD term and looking at the effect of the GDSPH weighing on each of them reveals that the unstable growth is governed by the TSPH induction and cleaning equation. The major effect comes from the TSPH induction equation, which always leads to larger growth rates at the outskirts of a disk ($|z| > H$) following the end of the linear phase. This leads to larger regions of the simulation being magnetically dominated, and consequently results in larger mass outflows and momentum oscillations within the box. The TSPH cleaning equations increases the oscillations of the magnetic energy in the outskirt, leading to quicker instability if paired together with the TSPH induction equation. The unphysical growth rate is possibly due to a magnetic flux error, as the energy is continuously increasing together with the magnetic field getting either more and more positive or negative. Global mean-field such as this can either be generated by the outflow boundaries or the monopole currents. Since outflow boundaries tend to expel flux roughly equally, the error is more likely to be caused by monopole currents, together with the gradient errors of TSPH near the density gradient. These fields eventually become so strong that they can no longer be buoyantly transported outward, because the critical wavelength is larger than the radial size of box. The negative radial fields in the outskirts will continue to increase the azimuthal field and subsequently the total magnetic energy. To be clear, this is not an intrinsic nonconservation of energy in the method (as seen in Lewis et al. 2015 due to an integrator bug), for either GDSPH or TSPH, both show excellent momentum and energy conservation for a wide range of tests shown in Wissing & Shen (2020). Kinetic energy will naturally transfer to magnetic energy due to the shear of net radial fields. In Deng et al. (2019) this unphysical increase of the azimuthal field was partly attributed to the divergence cleaning. While the divergence cleaning can increase the energy oscillations in the outskirt, the cleaning scheme is in itself guaranteed to decrease the overall magnetic energy and can not generate global mean-fields within the box. Because the hyperbolic divergence cleaning is conservative, which means that the spreading of the magnetic flux due to the cleaning is always symmetrical.

In addition, in our simulations the MRI turbulence is sustained longer than the MFM simulation presented in Deng et al. (2019), in which the turbulence decays around 40 orbits in their fiducial run. Our code has the ability to sustain long-term MRI turbulence similar to the Eulerian codes in previous MRI studies (Shi et al. 2010; Davis et al. 2010). However, as the simulations were terminated earlier in Deng et al. (2019), it is unclear if the MRI has actually fully died down in that work. We do also observe that the MRI can temporarily dip down to similar values before eventually being reenergized.

We also performed an analysis of the turbulent coefficients for all the simulations presented in this paper. We showed that no α-effect was present for the unstratified case as expected. For the stratified case, we have a negative α_{yy} effect that is negative (positive) in the top (bottom) half of the box, which indicates an effective $\alpha\omega$-dynamo. This is similar to what was found in Brandenburg (2008) and Shi et al. (2016). We find a turbulent pumping that transports the mean-fields away from the central region. However, we note that there is a significant uncertainty in the calculated α_{yx} coefficients due to correlations with the shear term, as explained in Sect. 2.1. The turbulent resistivity η_{xx} and η_{yx} are found to be positive in all of our simulations, and are consistent with previous quasi-kinematic studies employing the test-field method (Brandenburg et al. 1995b; Brandenburg & Sokoloff 2002; Brandenburg 2008).

Using the constrained hyperbolic divergence cleaning scheme with variable cleaning speed from Tricco et al. (2016), we can keep the divergence error low in all cases. The mean normalized divergence error, $\langle \epsilon_{\mathrm{div}B} \rangle = \langle h |\nabla \cdot \boldsymbol{B}|/|\boldsymbol{B}| \rangle$, is typically of order 10^{-2}.

In conclusion, we find that

- SPH can effectively develop the MRI and reproduce many of the values and dependencies seen in previous studies with grid-based codes.
- The geometric density SPH (GDSPH) successfully develops the characteristic "butterfly" diagram of the stratified MRI, showing saturated turbulence for at least 100 orbits. The results are similar to MRI simulations with the MFM method, and the turbulence is sustained longer.
- The numerical dissipation in SPH is found to act in a similar fashion to physical dissipation. We find a critical Prandtl number of around $P_{\mathrm{m}} \approx 2.5$, which is similar to what grid codes find with physical dissipation.
- The saturated stress for a certain numerical Prandtl number is found to be nearly independent of resolution, which is contrary to grid codes where stress is reduced with increased resolution. The results highlight the importance in determining the general behavior of the numerical Prandtl number in different turbulent flows, to ensure a more accurate saturation of the magnetic field.
- A major difference can also be seen in the tall, unstratified, zero net-flux case, where the mean-fíelds are much weaker than a previous study. From the mean-field analysis, we speculate that this might be due to a lack of shear-current effect our simulations. Nevertheless, we find that our transport coefficients are consistent with many previous studies that also do not find an effective shear-current effect.

References

Abramowicz, M., Brandenburg, A., & Lasota, J.-P. 1996, MNRAS, 281, L21
Artymowicz, P., & Lubow, S. H. 1994, ApJ, 421, 651
Bai, X.-N., & Stone, J. M. 2011, ApJ, 736, 144
Balbus, S. A., & Hawley, J. F. 1991, ApJ, 376, 214
Balbus, S. A., & Hawley, J. F. 1992, ApJ, 400, 610
Balbus, S. A., & Terquem, C. 2001, ApJ, 552, 235
Beck, R. 2015, A&ARv, 24, 4
Beck, R., Brandenburg, A., Moss, D., Shukurov, A., & Sokoloff, D. 1996, ARA&A, 34, 155
Beck, R., Fletcher, A., Shukurov, A., et al. 2005, A&A, 444, 739
Blaes, O. M., & Balbus, S. A. 1994, ApJ, 421, 163
Bodo, G., Mignone, A., Cattaneo, F., Rossi, P., & Ferrari, A. 2008, A&A, 487, 1
Bodo, G., Cattaneo, F., Ferrari, A., Mignone, A., & Rossi, P. 2011, ApJ, 739, 82
Boulares, A., & Cox, D. P. 1990, ApJ, 365, 544
Brandenburg, A. 2008, Astron. Nachr., 329, 725
Brandenburg, A., & Sokoloff, D. 2002, Geophys. Astrophys. Fluid Dyn., 96, 319
Brandenburg, A., & Subramanian, K. 2005, Phys. Rep., 417, 1
Brandenburg, A., Nordlund, A., Stein, R. F., & Torkelsson, U. 1995a, ApJ, 446, 741

Brandenburg, A., Nordlund, Å., Stein, R. F., & Torkelsson, U. 1995b, in Dynamo Generated Turbulence in Discs, eds. M. Meneguzzi, A. Pouquet, & P. L. Sulem, 462, 385

Chandrasekhar, S. 1960, Proc. Natl. Acad. Sci., 46, 253

Curry, C., Pudritz, R. E., & Sutherland, P. G. 1994, ApJ, 434, 206

Davis, S. W., Stone, J. M., & Pessah, M. E. 2010, ApJ, 713, 52

Dellar, P. J. 2001, J. Comput. Phys., 172, 392

Deng, H., Mayer, L., Latter, H., Hopkins, P. F., & Bai, X.-N. 2019, ApJS, 241, 26

Deng, H., Mayer, L., & Latter, H. 2020, ApJ, 891, 154

Evans, C. R., & Hawley, J. F. 1988, ApJ, 332, 659

Federrath, C. 2016, J. Plasma Phys., 82, 535820601

Federrath, C., Chabrier, G., Schober, J., et al. 2011, Phys. Rev. Lett., 107, 114504

Federrath, C., Schober, J., Bovino, S., & Schleicher, D. R. G. 2014, ApJ, 797, L19

Fricke, K. 1969, A&A, 1, 388

Fromang, S., & Papaloizou, J. 2007, A&A, 476, 1113

Fromang, S., Hennebelle, P., & Teyssier, R. 2006, A&A, 457, 371

Fromang, S., Papaloizou, J., Lesur, G., & Heinemann, T. 2007, A&A, 476, 1123

Fromang, S., Papaloizou, J., Lesur, G., & Heinemann, T. 2010, in EAS Pub. Ser., eds. T. Montmerle, D. Ehrenreich, & A. M. Lagrange, 41, 167

Gaburov, E., & Nitadori, K. 2011, MNRAS, 414, 129

Goldreich, P., & Lynden-Bell, D. 1965, MNRAS, 130, 125

Goodman, J., & Xu, G. 1994, ApJ, 432, 213

Gressel, O. 2010, MNRAS, 405, 41

Guan, X., & Gammie, C. F. 2011, ApJ, 728, 130

Guan, X., Gammie, C. F., Simon, J. B., & Johnson, B. M. 2009, ApJ, 694, 1010

Hawley, J. F., Gammie, C. F., & Balbus, S. A. 1995, ApJ, 440, 742

Hawley, J. F., Gammie, C. F., & Balbus, S. A. 1996, ApJ, 464, 690

Hawley, J. F., Balbus, S. A., & Winters, W. F. 1999, ApJ, 518, 394

Hawley, J. F., Guan, X., & Krolik, J. H. 2011, ApJ, 738, 84

Hawley, J. F., Richers, S. A., Guan, X., & Krolik, J. H. 2013, ApJ, 772, 102

Heinemann, T., McWilliams, J. C., & Schekochihin, A. A. 2011, Phys. Rev. Lett., 107, 255004

Herault, J., Rincon, F., Cossu, C., et al. 2011, Phys. Rev. E, 84, 036321

Hirose, S., Krolik, J. H., & Stone, J. M. 2006, ApJ, 640, 901

Hopkins, P. F., & Raives, M. J. 2016, MNRAS, 455, 51

Hubbard, A., Del Sordo, F., Käpylä, P. J., & Brandenburg, A. 2009, MNRAS, 398, 1891

Janhunen, P. 2000, J. Comput. Phys., 160, 649

Käpylä, P. J., & Korpi, M. J. 2011, MNRAS, 413, 901

Kersalé, E., Hughes, D. W., Ogilvie, G. I., Tobias, S. M., & Weiss, N. O. 2004, ApJ, 602, 892

Krause, F., & Raedler, K. H. 1980, Mean-field Magnetohydrodynamics and Dynamo Theory (Oxford: Pergamon Press)

Kulsrud, R. M. 1999, ARA&A, 37, 37

Kulsrud, R. M., & Anderson, S. W. 1992, ApJ, 396, 606

Kulsrud, R. M., Cen, R., Ostriker, J. P., & Ryu, D. 1997, ApJ, 480, 481

Latter, H. N., Lesaffre, P., & Balbus, S. A. 2009, MNRAS, 394, 715

Lesaffre, P., & Balbus, S. A. 2007, MNRAS, 381, 319

Lesaffre, P., Balbus, S. A., & Latter, H. 2009, MNRAS, 396, 779

Lesur, G., & Longaretti, P. Y. 2007, MNRAS, 378, 1471

Lesur, G., & Ogilvie, G. I. 2008, A&A, 488, 451

Lewis, B. T., Bate, M. R., & Price, D. J. 2015, MNRAS, 451, 288

Lodato, G., & Price, D. J. 2010, MNRAS, 405, 1212

Lynden-Bell, D., & Pringle, J. E. 1974, MNRAS, 168, 603

Meheut, H., Fromang, S., Lesur, G., Joos, M., & Longaretti, P.-Y. 2015, A&A, 579, A117

Meru, F., & Bate, M. R. 2012, MNRAS, 427, 2022

Moffatt, H. K. 1978, Magnetic Field Generation in Electrically Conducting Fluids (Cambridge: Cambridge University Press)

Monaghan, J. J. 1985, Comput. Phys. Rep., 3, 71

Monaghan, J. J. 1997, J. Comput. Phys., 136, 298

Noble, S. C., Krolik, J. H., & Hawley, J. F. 2010, ApJ, 711, 959

Pakmor, R., & Springel, V. 2013, MNRAS, 432, 176

Parker, E. N. 1979, Cosmical Magnetic Fields. Their Origin and their Activity (New York: Oxford University Press)

Parkin, E. R., & Bicknell, G. V. 2013, MNRAS, 435, 2281

Penna, R. F., McKinney, J. C., Narayan, R., et al. 2010, MNRAS, 408, 752

Pessah, M. E., & Goodman, J. 2009, ApJ, 698, L72

Pouquet, A., Frisch, U., & Leorat, J. 1976, J. Fluid Mech., 77, 321

Price, D. J. 2012, J. Comput. Phys., 231, 759

Price, D. J., & Monaghan, J. J. 2005, MNRAS, 364, 384

Rädler, K. H. 1969, Monatsber. Deutsch. Akad Wissenschaftliche Berlin, 11, 194

Rincon, F., Ogilvie, G. I., & Proctor, M. R. E. 2007, Phys. Rev. Lett., 98, 254502

Riols, A., Rincon, F., Cossu, C., et al. 2013, J. Fluid Mech., 731, 1

Rogachevskii, I., & Kleeorin, N. 2003, Phys. Rev. E, 68, 036301

Rogachevskii, I., & Kleeorin, N. 2004, Phys. Rev. E, 70, 046310

Rüdiger, G., Kitchatinov, L. L., & Brandenburg, A. 2011, Sol. Phys., 269, 3

Ruzmaikin, A. A., Sokolov, D. D., & Shukurov, A. M. 1988, Magnetic Fields of Galaxies (Dordrecht: Kluwer Academic Publishers), 133

Sano, T., Inutsuka, S.-I., Turner, N. J., & Stone, J. M. 2004, ApJ, 605, 321

Schekochihin, A. A., Cowley, S. C., Taylor, S. F., Maron, J. L., & McWilliams, J. C. 2004a, ApJ, 612, 276

Schekochihin, A. A., Cowley, S. C., Maron, J. L., & McWilliams, J. C. 2004b, Phys. Rev. Lett., 92, 054502

Schekochihin, A. A., Iskakov, A. B., Cowley, S. C., et al. 2007, New J. Phys., 9, 300

Shakura, N. I., & Sunyaev, R. A. 1973, A&A, 500, 33

Shi, J., Krolik, J. H., & Hirose, S. 2010, ApJ, 708, 1716

Shi, J.-M., Stone, J. M., & Huang, C. X. 2016, MNRAS, 456, 2273

Silant'ev, N. A. 2000, A&A, 364, 339

Simon, J. B., & Hawley, J. F. 2009, ApJ, 707, 833

Simon, J. B., Hawley, J. F., & Beckwith, K. 2009, ApJ, 690, 974

Simon, J. B., Hawley, J. F., & Beckwith, K. 2011, ApJ, 730, 94

Simon, J. B., Bai, X.-N., Stone, J. M., Armitage, P. J., & Beckwith, K. 2013, ApJ, 764, 66

Spitzer, L. 1962, Physics of Fully Ionized Gases (New York: Interscience Publishers)

Squire, J., & Bhattacharjee, A. 2015a, Phys. Rev. Lett., 114, 085002

Squire, J., & Bhattacharjee, A. 2015b, Phys. Rev. Lett., 115, 175003

Squire, J., & Bhattacharjee, A. 2015c, Phys. Rev. E, 92, 053101

Stone, J. M., Hawley, J. F., Gammie, C. F., & Balbus, S. A. 1996, ApJ, 463, 656

Subramanian, K., & Brandenburg, A. 2004, Phys. Rev. Lett., 93, 205001

Suzuki, T. K., & Inutsuka, S.-I. 2009, ApJ, 691, L49

Tricco, T. S., & Price, D. J. 2012, J. Comput. Phys., 231, 7214

Tricco, T. S., Price, D. J., & Bate, M. R. 2016, J. Comput. Phys., 322, 326

Vaĭnshteĭn, S. I., & Zel'dovich, Y. B. 1972, Sov. Phys. Usp., 15, 159

Velikhov, E. 1959, Sov. Phys. JETP, 36, 995

Vishniac, E. T., & Brandenburg, A. 1997, ApJ, 475, 263

Vishniac, E. T., & Cho, J. 2001, ApJ, 550, 752

Wadsley, J. W., Keller, B. W., & Quinn, T. R. 2017, MNRAS, 471, 2357

Wardle, M. 1999, MNRAS, 307, 849

Wissing, R., & Shen, S. 2020, A&A, 638, A140

Yokoi, N. 2013, Geophys. Astrophys. Fluid Dyn., 107, 114

Yoshizawa, A., & Yokoi, N. 1993, ApJ, 407, 540

Zeldovich, Y. B. 1983, Magnetic Fields in Astrophysics (Heidelrberg: Springer-Verlag)

Zeldovich, Y. B., Ruzmaikin, A. A., & Sokoloff, D. D. 1990, The Almighty Chance (Singapore: World Scientific Publishing)